In vitro Micro Particle Image Velocimetry Measurements in the Hinge Region of a Bileaflet Mechanical Heart Valve

A Thesis
Presented to
The Academic Faculty

by

Brian H. Jun

In Partial Fulfillment
Of the Requirements for the Degree
Master of Science in Bioengineering

Georgia Institute of Technology
May, 2014

In vitro Micro Particle Image Velocimetry Measurements in the Hinge Region of a Bileaflet Mechanical Heart Valve

Dr. Ajit P. Yoganathan, Advisor
Department of Biomedical Engineering
Georgia Institute of Technology

Dr. Don P. Giddens
Department of Biomedical Engineering
Georgia Institute of Technology

Dr. J. Brandon Dixon
School of Mechanical Engineering
Georgia Institute of Technology

Date Approved: February, 2014

ACKNOWLEDGMENTS

I would like to acknowledge the following people whose significant support and contributions have assisted me in completing my master's thesis. First of all, I would like to thank my advisor Dr. Ajit Yoganathan for affording me the opportunity to work as a member of the Cardiovascular Fluid Mechanics Lab, and perform academic research in the field of biomedical engineering. Similarly, I would like to thank Dr. Don Giddens and Dr. Brandon Dixon for serving on my thesis committee.

I am grateful for the financial support I received from the National Heart, Lung and Blood Institute (RO1-HL-07262) and the School of Mechanical Engineering (Graduate Teaching Assistantship) at the Georgia Institute of Technology during my graduate studies. I would like to thank the graduate coordinators of the Bioengineering Program and the School of Mechanical Engineering, especially Mr. Chris Ruffin, Ms. Glenda Johnson, and Dr. Wayne Whiteman for their dedication in helping students.

It has been my privilege to work and share valuable experiences with all the members of the Cardiovascular Fluid Mechanics Lab: Neela, Min, Shiva, Andrew, Ikay, Arvind, Yap, Elaine, Reza, Swetha, JP, Maria, Lucia, Brandon, Milan, Eric, Mike, Vrishank, Prem, Paul, Charley, Thomas, Shahrokh, and Sandra.

Finally, my sincere thanks must go to my family, Duk Bin Jun, Yeonhee Lee, Hwail Kim, Hyoung Lak Jun, and Jihyeon Kim, for their endless encouragement and support toward taking the opportunity I was granted at Georgia Tech to advance my education.

TABLE OF CONTENTS

LIST OF TABLES

LIST OF FIGURES

NOMENCLATURE

PIV	Particle Image Velocimetry
μPIV	Micro Particle Image Velocimetry
LDV	Laser Doppler Velocimetry
μm	micrometer
μs	microsecond
BMHV	Bileaflet Mechanical Heart Valve
CFD	Computational Fluid Dynamics
Vel	Velocity magnitude
RSS	Reynolds Shear Stress
RSS_{app}	Apparent Reynolds Shear Stress
VSS	Viscous Shear Stress
Vel_{peak}	Peak Velocity magnitude
RSS_{peak}	Peak Reynolds Shear Stress magnitude
VSS_{peak}	Peak Viscous Shear Stress magnitude
SJM	St. Jude Medical
CM	Carbomedics
cSt	Centi-stokes
RBC	Red Blood Cells
TAT	Thrombin-Antithrombin III
FLAT plane	Flat level
195µm plane	195µm above flat level

390µm plane	390µm above flat level
585µm plane	585µm above flat level
δ_{corr}	Depth of Correlation
Re	Reynolds Number
µ	Dynamic viscosity
ρ	Fluid density

SUMMARY

A number of clinical, *in vitro* and computational studies have shown the potential for thromboembolic complications in bileaflet mechanical heart valves (BMHV), primarily due to the complex and unsteady flows in the valve hinges. These studies have focused on quantitative and qualitative parameters such as velocity magnitude, turbulent shear stresses, vortex formation and platelet activation to identify potential for blood damage. However, experimental characterization of the whole flow fields within the valve hinges has not yet been conducted. This information can be utilized to investigate instantaneous damage to blood elements and also to validate numerical studies focusing on the hinge's complex fluid dynamics.

The first objective of this study was therefore to develop a high-resolution imaging system to characterize the flow fields and global velocity maps in a BMHV hinge. In this study, the steady leakage hinge flow fields representing the diastolic phase during the cardiac cycle in a 23 mm St. Jude Medical (SJM) Regent BMHV in the aortic position were characterized using a two-dimensional Micro Particle Image Velocimetry (μPIV) system. Diastolic flow was simulated by imposing a static pressure head on the aortic side. Under these conditions, a reverse flow jet from the aortic to the ventricular side was observed with velocities in the range of 1.47 to 3.24 m/s, whereas low flow regions were observed on the ventricular side of the hinge with viscous shear stress (VSS) magnitude up to 60 N/m^2. High velocities and viscous shearing may be associated with platelet activation & hemolysis, while low flow zones can cause thrombosis due to increased residence time in the hinge.

The second objective of this study was to characterize the global velocity maps under pulsatile conditions to fully understand the blood damage potential of BMHVs. The current study hypothesized that the hinge gap width will affect flow fields in the hinge region. Accordingly, the blood damage potential of three St. Jude Medical (SJM) BMHVs with different hinge gap widths was investigated under pulsatile flow conditions, using a μPIV system. The results demonstrated that the hinge gap width had a significant influence during the leakage flow phase in terms of washout and shear stress characteristics. During the leakage flow, the largest hinge gap generated the highest RSS_{app} magnitudes (~1000 N/m^2) among the three valves at the ventricular side of the hinge. At this location, all three valves indicated VSS greater than 30 N/m^2. The smallest hinge gap exhibited the lowest level of shear stress values, but had the poorest washout flow characteristics among the three valves, demonstrating propensity for flow stasis and associated activated platelet accumulation potential. The results from this study indicate that the hinge is a critical component of the BMHV design, which needs to be optimized to find the appropriate balance between reduction in fluid shear stresses and enhanced washout during leakage flow, to ensure minimal thrombotic complications.

Overall, this study has shown the fully pulsatile flow characteristics of the three BMHV models with intricate hinge flow structures, such as variations in velocity, VSS, and RSS_{app}. In addition, the study has demonstrated the application of the high-resolution μPIV system, which can be extended to investigate micron-scale flow domains in various prosthetic devices under different hemodynamic conditions.

CHAPTER 1

INTRODUCTION

According to the World Health Organization, nearly 17 million people died from cardiovascular disease in 2008, representing 30% of all global deaths. Cardiovascular disease can affect native heart valve function, which may be treated with medication but often involves valve replacement. When a patient requires a heart valve replacement, two types are available that include mechanical heart valves (MHV) or biological heart valves made from animal or human tissue. Today, over 55% of heart valve replacements utilize MHVs, with the bileaflet mechanical heart valve (BMHV) currently the most popular design (Yoganathan, 2003). BMHVs consist of two leaflets that insert into recessed hinges within an external housing and have been shown to be extremely durable with satisfactory bulk flow characteristics (Blackman, 2007). But despite its widespread use, the BMHV's hinge and pivot regions have been cited by many researchers for their potential to cause hemolysis and thrombosis due to high fluid shear stresses and low flow recirculation regions imposed on blood constituents (Giersiepen, 1990).

Characterization of hemodynamics in the hinge region is a critical step to improve valve design. However, the small spatial scales involved pose a major challenge to obtaining detailed fluid flow measurements in this region. Previous *in vitro* studies have sought to quantify fluid flow parameters in the BMHV hinge using Laser Doppler Velocimetry (LDV) (Simon, 2004a; Leo, 2006). The major limitations with LDV experiments are the low spatial resolution and significantly long data acquisition period since it is a point measurement technique. To obtain 2D velocity fields in the BMHV hinge using LDV, a number of measurement locations and velocity measurements up to 130 and 21,500 were required, respectively (Simon, 2004b).

Among the different designs of BMHVs investigated in these LDV studies, the leakage flow phase has been shown to have the highest thromboembolic potential of any phase of the cardiac cycle (Leo, 2002; Simon, 2004; Leo, 2006). Simon *et al*. reported that the maximum velocity and turbulent shear stress measured in the hinge when the leaflets were fully closed were two magnitudes or more higher than during any other phase (Simon, 2004). Subsequently, Fallon *et al.* and Travis *et al.* conducted *ex vivo* studies to assess platelet activation and markers of platelet damage within different hinge designs during the leakage flow using a steady flow loop system (Travis, 2001; Fallon, 2006). The studies concluded that clotting in BMHVs is most likely due to leakage flow through the hinge area and that hinge gap width had a significant effect on platelet secretion initiated by leakage flow.

To improve the spatial resolution required to assess hinge flow characteristics, numerical simulations under transaortic hemodynamic conditions have been conducted. The improved spatial resolution allowed for the determination of 3D velocity flow maps under pulsatile flow (Simon, 2010; Yun, 2012). These studies have enabled more detailed characterization of these flow fields. While computational simulations exhibit significant potential, these models still require benchmark validation. Although previous *in vitro* flow visualization techniques have been unable to offer the spatial resolution required for such a validation, advances in particle image velocimetry can now allow for such studies to be conducted.

Particle Image Velocimetry (PIV) can provide whole flow fields with enhanced spatial resolution in hinge flows, overcoming limitations of previous experimental and computational techniques. PIV has been utilized to study regurgitant flow fields across and perpendicular to the B-datum

line in the 27mm SJM BMHV under physiological conditions (Manning, 2003). More recently, Bellofiore *et al.* used a scale-up model representative of an SJM BMHV to investigate the unsteady flow fields at the trailing edge of the leaflet with enhanced spatial and temporal resolution (Bellofiore, 2011). Nevertheless, PIV techniques used in these studies are designed for spatial resolution on the order of 1mm, which is too large for investigating the hinge flows, where the entire geometry has a width of about 3-4 mm.

By contrast, Micro Particle Image Velocimetry (μPIV) is a well-established technique to quantitatively measure flow behavior in small domains down to the nanometer scale (Meinhart, 1999). This meets the spatial resolution demands for experimental studies in BMHV hinge flow fields. Typical μPIV studies are performed at low Reynolds numbers, with steady flow conditions in micron-scale uniform flow domains such as rectangular microchannels (Wereley, 2010). In addition, the total fluid volume of such systems is typically less than 20 ml.

There are unique challenges to utilizing μPIV in the BMHV hinge. The fluid volume required to generate physiologic pressure across the human aortic valve ranges from 4 L to 10 L in *in-vitro* heart simulators used in relevant LDV and PIV studies (Manning, 2003; Simon, 2004; Leo, 2006; Saikrishnan, 2012).Despite this macro-scale flow domain, the hinge recess (1.5μL in volume) is orders of magnitude smaller, making it difficult to achieve a good seeding density when flow passes through the entire valve region. In addition, the choice of an appropriate objective lens is limited since magnification larger than 5× will only resolve smaller areas of the hinge region, and magnification smaller than 3× will have depth of field greater than the hinge recess gap.

To this end, this study sought to accomplish two goals to assess the challenges in quantifying BMHV hinge flow. The first goal was to develop a custom-designed μPIV system to characterize the flow fields within a BMHV hinge. This goal was accomplished through experiments conducted under steady leakage flow conditions, representing aortic hemodynamic conditions during diastole. The second goal of this study was to investigate the influence of hinge gap width on flow fields within BMHV hinges using the established μPIV system under pulsatile flow conditions and to relate these results to the potential for blood damage of these valves. This goal focuses on the performance and blood damage potential in BMHVs, by quantifying fluid mechanic parameters such as the velocity magnitude and the Reynolds and viscous shear stresses from the measured flow fields.

The broader objective of this study is to provide an improved methodology that can be extended to different MHV designs and other implantable cardiovascular devices, where micro-scale flow studies may be critical to assessing the potential for hemolytic and thromboembolic complications.

CHAPTER 2

BACKGROUND

2.1 The Heart

The human heart is composed of four cardiac chambers, two atria and ventricles acting as a double pump. The right side of the heart collects de-oxygenated blood in the right atrium from the superior and inferior vena cavae and then pumps the blood into the lungs by pressure that builds up in the right ventricle along the pulmonary arteries. The left side of the heart collects oxygenated blood in the left atrium from the lungs and then blood flows to the left ventricle, which pumps the blood throughout the body along the aorta. The heart has four cardiac valves that maintain uni-directional flow of blood across the heart. In the left side of the heart, the mitral valve is located between the left atrium and the left ventricle, and the aortic valve is located between the left ventricle and the aorta. In the right side of the heart, the tricuspid valve is located between the right atrium and the right ventricle, and the pulmonary valve is located between the right atrium and the pulmonary artery. These heart valves can be categorized into two groups that differ with regards to the location and the size of the valve. The atrioventricular valves include the mitral and tricuspid valves composed of two and three leaflets, respectively. The semilunar valves include the aortic and pulmonary valves, both composed of three leaflets and smaller than the atrioventricular valves.

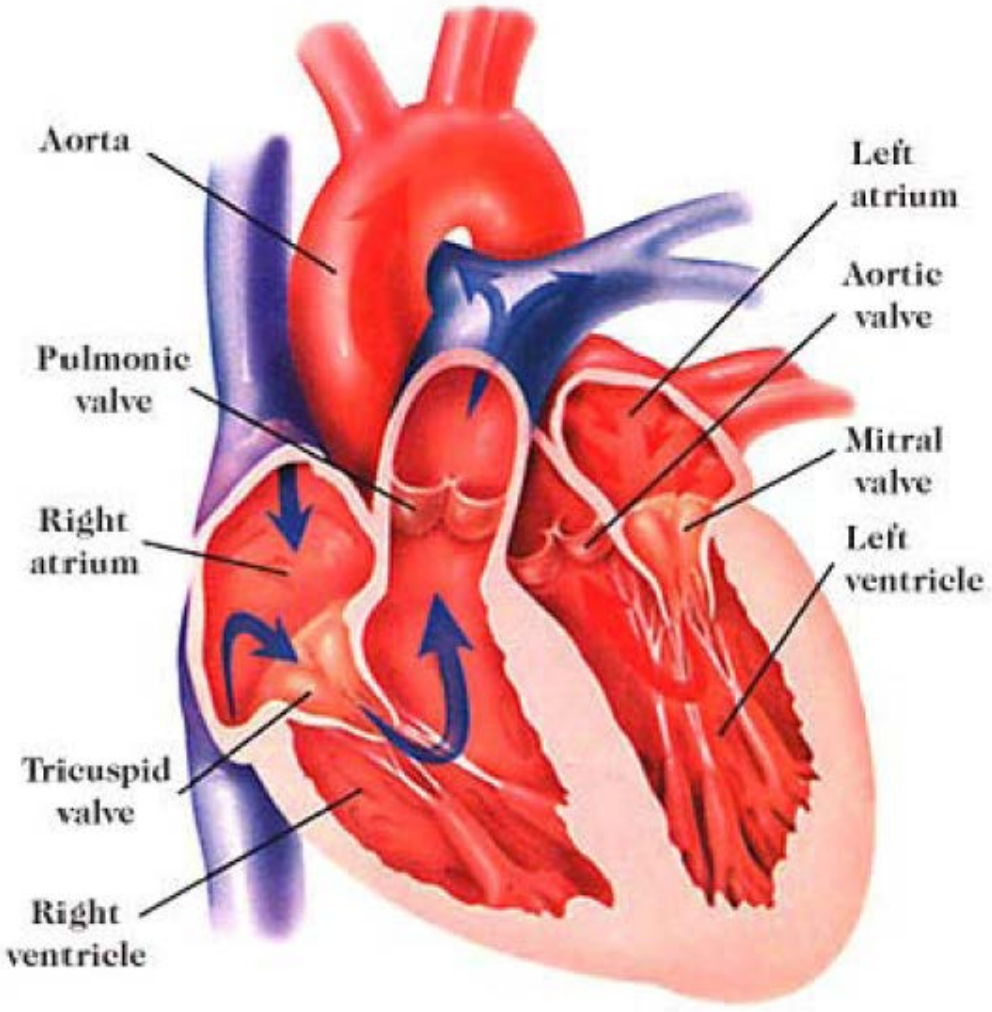

Figure 2.1: Anatomy of the human heart (Courtesy of Leo, 2005)

2.2 The Cardiac Cycle

The heart contracts and expands periodically, which increases or decreases blood pressure in the cardiac chambers. This process, referred to as the "cardiac cycle," is divided into two phases: the systole and diastole phases. During the diastole phase, heart muscles are relaxed and blood is passively filling the atria and then it flows into the ventricles while the atrioventricular valves are open. During this phase, the pressure in the ventricles is low, keeping the semilunar valve closed. At the end of the ventricular filling phase, the atrium contracts, referred to as the "atrial

systole," part of the end of the diastole phase that ensures maximum ejection of blood from the atrium to the ventricle. During the systole phase, ventricular muscles contract and eject the blood through the aorta and the pulmonary artery. The high pressure generated from the ventricles at this phase forces the semilunar valves to open and atrioventricular valves to close.

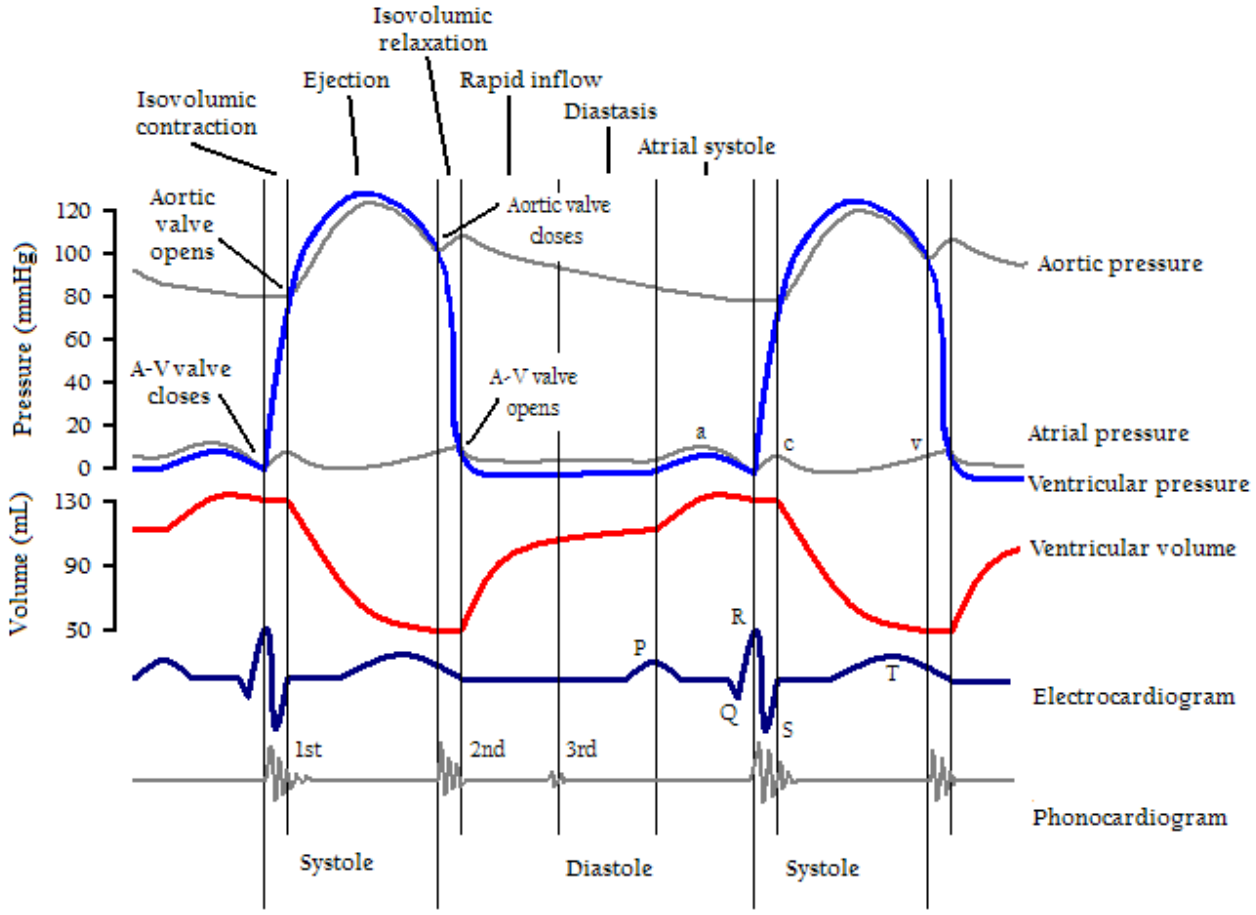

Figure 2.2: The Wiggers Diagram representing the cardiac cycle in the left heart (http://en.wikipedia.org/wiki/Cardiac_cycle)

2.3 Valvular Heart Disease

Any malfunction of one or more heart valves, which can be congenital or acquired during one's lifetime, indicates valvular heart disease. Two major types of heart valve disease are valvular stenosis and regurgitation, which can be caused by many different factors including calcification

of the leaflets, rheumatic fever, and congenital heart defects such as the bicuspid aortic valve. In valvular stenosis, leaflets are stiff or fused together, allowing a smaller opening area for the blood to pass through than a normal valve. In valvular regurgitation, also termed “insufficiency” or “incompetence,” leaflets do not seal tightly during the valve closure phase, permitting the backflow of blood. Subsequently, the heart has to work harder to compensate for the decrease in blood delivered to the rest of the body. Valvular stenosis can also result in a regurgitation problem because the calcification of the leaflets can cause ineffective sealing during the closure of the valve. Since the higher loading condition in the left ventricle provides much more pumping power then the right ventricle, valvular disease is most commonly found in the aortic and mitral valves, which undergo a pressure load ranging from 0 to 120mmHg and 80 to 120mmHg, respectively. Prevalence of valve disease increases with aging. For the elder population over the age of 75, more than one in eight people are diagnosed with valve disease (Nkomo, 2006)

2.4 Prosthetic Heart Valves

A prosthetic heart valve is a device implanted in the heart of a patient to replace malfunctioned native valves. When a patient requires a heart valve replacement, two types are available, including a mechanical heart valve or a valve made of animal or human tissue (biological valves). Each replacement valve is preferred for different attributes. Modern mechanical heart valve models nowadays can last a lifetime but require lifelong treatment with anticoagulants to prevent thromboembolic complications. On the other hand, bioprosthetic heart valves do not require prolonged use of anticoagulants, but have limited lifespan of up to 15 years (Black, 1994; Baudet, 1995; Vongpatanasin, 1996). To improve these limitations associated with durability and

thrombogenicity, effort is currently being made to develop a polymeric valve, which can adapt the best features from both mechanical and bioprosthetic valves. Within these two categories of prosthetic heart valves, various types exist in terms of different designs and materials.

2.4.1 Mechanical Heart Valves

After four decades of study, more than 50 mechanical heart valve designs have been implanted in humans. These different designs can be categorized into three major types; caged-ball, tilting disk and bileaflet. A caged-ball type valve was the first mechanical heart valve implanted in a human by Dr. Charles A. Hufnagel in 1952. Subsequently, a similar valve was developed which was referred as the Starr-Edwards ball-and-cage valve in 1960 (Figure 2.3) (Starr, 2002). However, the caged-ball valve design experienced a high tendency of forming blood clots primarily due to the flow obstruction caused by the ball. Consequently, the production of the Starr-Edwards valve is currently discontinued. The tilting-disc was the next emerging mechanical heart valve design in 1969, which works by the free floating disc supported by the metal strut (Figure 2.3). The Bjork-Shiley and Medtronic-hall were the representative tilting-disc models in US. The bileaflet mechanical heart valve (BMHV) was first introduced in 1979 by St. Jude Medical, Inc. (SJM). BMHVs are currently the most popular design and comprise 75% of implanted mechanical heart valves. The valve consists of two leaflets that insert into recessed hinges within an external housing. The primary improvement with BMHV includes larger orifice area, superior durability and functional safety. Nowadays, many different designs of BMHV have been developed including On-X valve, CarboMedics valve and Sorin Bicarbon valve (Yoganathan, 2003; Chandran, 2007).

Carpentier-Edwards S.A.V.
Aortic Bioprosthesis

Aortech trileaflet
Aortic polymeric Valve

Starr-Edwards Silastic Ball
Valve Prosthesis

Medtronic Hall Valve

St Jude Medical
Regent Valve

CarboMedics Standard
Aortic Valve

Figure 2.3: Types of artificial heart valves (Courtesy of Simon, 2004)

2.4.2 Bioprosthetic Valves

Biological valves are made of animal or human tissue which can provide natural hemodynamics closer to a human valve. On the first attempt, antibiotic or cryo-treated human aortic valves (homografts) were excised from cadavers for implantation into the patient's heart in 1962 by Ross (Ross, 1969). Although these homografts showed a great outcome, the supply of these valves were extremely limited due to the small number of donors. Soon after, a porcine bioprosthetic valve became popular in 1970, known as the Hancock Porcine Xenograft. This valve consists of porcine leaflets mounted on a rigid ring with three flexible supporting stents. Subsequently, a bovine bioprosthetic valve was also developed which was known as the Carpentier-Edwards valve (Figure 2.3). The overall design was similar to a porcine bioprosthetic valve, except with the completely flexible supporting frame. Biological valves provide more natural hemodynamics than mechanical valves due to their larger unobstructed opening area and deformable characteristics of tissue.

2.4.3 Complications of Prosthetic Heart Valves

Despite the increase in implantation of artificial heart valves and improvements in valve design, many complications still exist. Major complications associated with prosthetic heart valves include hemorrhage, thrombosis, embolism and structural deterioration. Mechanical heart valves are especially prone to thromboembolic complications such as hemolysis, platelet activation and thrombosis caused by non-physiological flow through manmade valve materials. A few mechanical valve designs in the past were withdrawn from the market due to a high degree of thrombosis and structural failure, including Star-Edwards, Medtronic Parallel Bileaflet and Bjork-Shiley Convexo-Concave valves (Chandran, 2007). For patients with mechanical heart

valves, lifelong treatments with anticoagulants are required to prevent complications. Nevertheless, patients could potentially suffer from an excess bleeding due to these treatments.

On the other hand, biological valves provide less risk of thromboembolic complications with use of living tissue material, which do not require an intensive treatment with anticoagulants. However, these valves primarily suffer from structural deterioration of tissue materials. This occurs progressively due to the wearing, tearing and calcification of leaflets which result in valvular stenosis and regurgitation. Subsequently, patients with biological valves require reoperations after 5-15 years, with a high risk of mortality and a long recovery period (Vongpatanasin, 1996; Blackman, 2000). The risk of reoperation increases with aging, where the mortality rate is 32% with 80 years of age (On-X Life Technologies Inc, 2013).

2.5 Blood Damage

To understand the complications associated with prosthetic heart valves, it is important to review biological and mechanical properties of blood, which can lead to identifying potential factors inducing blood damage.

2.5.1 Blood

Blood is a fluid that circulates in the arteries and veins of a human body, delivering essential nutrients and oxygen to the surrounding cells and tissues. Blood is composed of 55% liquid and 45% solid parts. The liquid part is called plasma, which consists mainly of water (~92%) in addition to a number of organic and inorganic substances; proteins, hormones, minerals, glucose and carbon dioxide. The solid part consists of red blood cells (erythrocytes), white blood cells

(leukocytes) and platelets (thrombocytes). Red blood cells have a biconcave disk-shaped structure with diameter of 7.8μm and thickness of 2.8μm. The membrane of the red blood cells carries enzymes and hemoglobin which help to deliver oxygen to surrounding tissues. Red blood cells are the most abundant cells in blood, comprising 40-45% of blood volume for a healthy adult. White blood cells only comprise of about 1% of blood volume and primarily function to protect the body from infections and parasites. Platelets are discoid-shaped cell fragments that are 1-2 μm in diameter, occupying approximately 0.6% of blood volume. Platelets are involved in hemostasis to prevent bleeding by forming blood clots, which is known as coagulation cascade. Normal adult typically has 4.2 – 6.1 million red blood cells, 4,500 – 10,000 white blood cells and 150,000 to 40,000 platelets per microliter of blood (MedlinePlus, 2013).

2.5.2 Properties of Blood

Since blood consists of both liquid and solid components, it exhibits characteristics of non-Newtonian fluid. Therefore, viscosity of blood can be changed drastically depending on factors such as the hematocrit level, aggregation of red blood cells and shear rates (Baskurt and Meiselman, 2003; Murphy, 2009). The apparent blood viscosity approaches an asymptotic value of 3.5 cSt at tube diameters and shear rates larger than about 0.5 mm and 50 sec^{-1}, respectively, at whole blood temperature of 37ºC. Therefore, blood can be assumed to behave as a Newtonian fluid within the human aorta, large arteries, and large veins where high shear rates greater than 80 sec^{-1} are experienced with large vessel diameters above 1mm (Chandran, 2007).

2.5.3 RBCs and Hemolysis

Hemolysis refers to the rupturing RBCs and release of their contents such as hemoglobin into surrounding plasma. As a result, hemolytic anemia can occur in which there are insufficient numbers of hemoglobin to transport oxygen from the lungs to the tissues in the body (Steegers, 1999). Hemolysis can be caused predominantly by the shear stress-induced damage to blood elements, especially with the presence of prosthetic heart valve.

2.5.4 Platelet Activation and Thrombosis

Platelets are considered critical element of hemostasis, eventually leading to the formation of thrombus (blood clots). When the platelets are in contact with subendothelium factors such as collagen, von Willibrand Factor (vWF), and other tissue factors, they become activated to initiate the coagulation cascade, which is a process to stop bleeding when injury occurs. Platelets can also be activated by factors that arise outside the subendothelium layer, such as interactions with thrombin, foreign material, and non-physiological flow conditions. Examples of such conditions include flow through artificial devices or arterial stenosis where high magnitudes of the shear stresses are experienced.

2.5.5 Shear Stress and Blood Elements

Many complications associated with circulatory diseases such as thrombosis, atherosclerosis, and embolism can be explained through fluid mechanics. Number of studies reported that the formations of plaques in arteries tend to develop at particular locations exhibiting curvatures and bifurcations where regions of high shear stresses and flow stasis are commonly observed (Ku, 1985). Manufacturers of artificial devices such as blood pumps and mechanical heart valves continuously seek to design a better product with reduced prevalence of high shear stresses, flow

separation, and regurgitation volume. As a result, determination of threshold levels for the shear stresses and exposure time of the blood elements to stresses are important steps to investigate in order to understand rheological behavior of human blood under circulatory diseases.

Two types of shear stresses including viscous and Reynolds shear stresses (RSS) can affect blood elements to potentially initiate hemolysis and platelet activation. The viscous shear stress indicates the shearing between adjacent layers of fluid, which represents the loading experienced by the fluid on blood elements. The Reynolds shear stress indicates turbulence in fluid momentum due to the fluctuating velocity component (Truskey, 2004; Murphy, 2009). Consequently, previous researchers have sought to determine the effect of VSS and RSS on RBCs and platelets. Leverett *et al*. demonstrated that red blood cell (RBC) damage can be affected predominantly by viscous shear stress alone at thresholds of 150 N/m^2 by using a rotational viscometer device (Leverett, 1972). Subsequently, shear stress damage under turbulent flow was investigated by Lu *et al*. using 2D Laser Doppler Anemometry, where a Reynolds shear stress level of 800 N/m2 was defined as an estimated threshold for hemolysis (Lu, 2001). Similarly, platelet activation threshold was also investigated, and viscous shear stress levels ranging from 30-100 N/m2 with exposure times of 25 – 1650 ms were shown to lead to platelet activation. The Reynolds shear stress threshold for platelet activation on a physiological time scale is still not clearly known (Murphy, 2009).

2.6 Bileaflet Mechanical Heart Valves

2.6.1 Design Characteristics of BMHV

BMHVs are currently the most successful and popular MHV design, consisting of two semicircular leaflets that insert into four recessed hinges within an external housing (DeWall, 2000; Yoganathan, 2003; Chandran, 2007). Two leaflets of a BMHV can be fully opened and closed passively due to the transvalvular pressure that is generated from the contraction and relaxation of the heart, in order to maintain unidirectional flow of blood. As represented on Figure 2.4, the external housing of the valve is enclosed with a sewing cuff (Dacron cloth) to aid the suturing of the BMHV to the valve annulus. The leaflets of the valve were made from pyrolytic carbon with a graphite substrate containing tungsten.

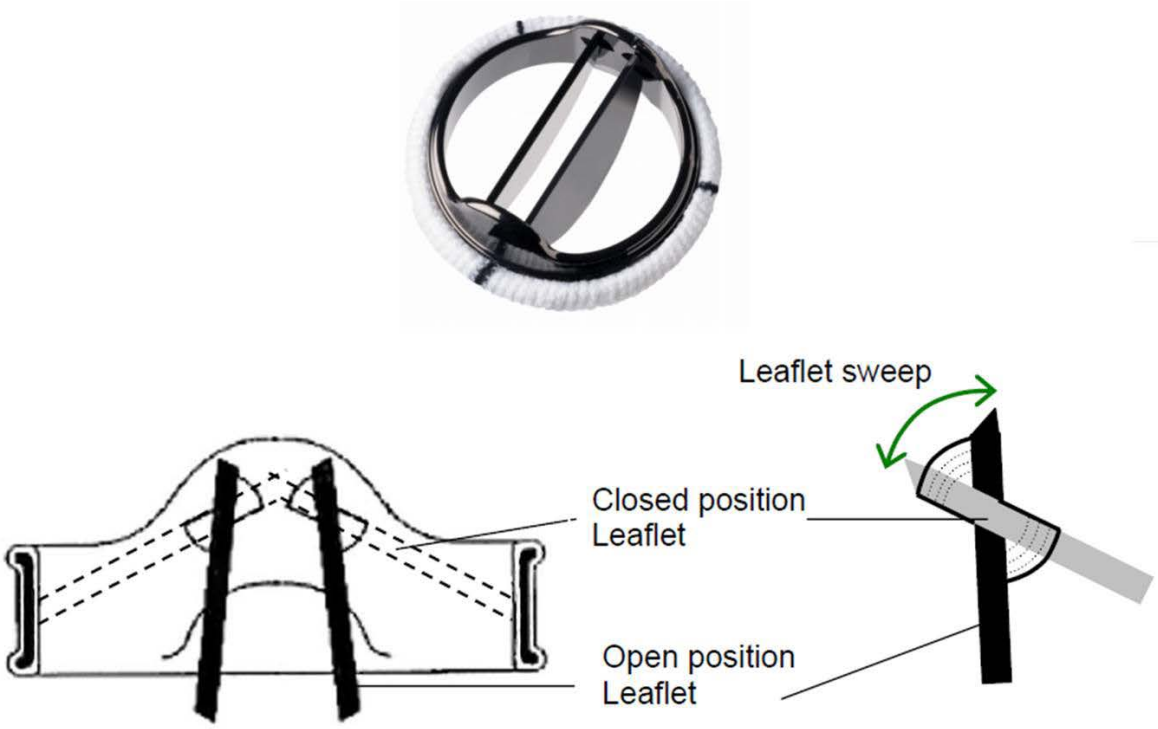

Figure 2.4: BMHV pivot mechanism (Courtesy of Simon, 2004)

During the forward flow phase while leaflets are opened, blood predominantly flows through three orifices as represented on Figure 2.4, including the central rectangular and two lateral orifices. Subsequently, blood flow through hinges during the forward flow phase is minimal.

While leaflets are fully closed, reverse flow occurs through the B-datum plane, four hinges, and peripheral leakage regions located in the neighborhood of the hinge. These gaps are also a critical part of the BMHV design, allowing strong leakage flow to washout blood elements that can be trapped in these regions.

2.6.2 BMHV Complications

BMHVs have been shown to be extremely durable with satisfactory bulk flow characteristics (Black, 1994; Baudet, 1995; Blackman, 2000). However, despite its widespread use and improvements over other MHV designs, BMHVs are still not considered ideal due to their susceptibility to backflow, which may give rise to the likelihood of blood element damage. In particular, hinge and pivot regions have been cited by many researchers for their potential to cause hemolysis and thrombosis due to high fluid shear stresses and low flow recirculation regions imposed on blood constituents (Giersiepen, 1990). Among different gaps allowing leakage flow in the BMHV design, the hinge regions of the BMHV have been known to cause most substantial blood element damage due to the complex and unsteady nature of flow within these regions. The clinical trials of the Medtronic Parallel BMHV in 1995 reported unacceptable levels of thrombus formation when implanted in the mitral position. Subsequently, many of the thrombi were observed in the hinge regions which lead to series of investigations in an effort to characterize the hinge flows (Ellis, 1996).

2.7 Previous Investigations

2.7.1 *In-vitro* studies of BMHVs

Previous *in-vitro* studies evaluated the performance and blood damage potential in BMHVs by quantifying parameters such as velocity magnitude, Reynolds shear stress and viscous shear stress from measured flow fields. In vitro LDV studies were conducted to evaluate performance of various BMHV models. Leo et al. compared hinge flow dynamics of CarboMedics (CM), SJM, and Medtronic Parallel BMHVs. The study was conducted in a pulsatile mitral flow condition in which two dimensional LDV was used to measure velocity and RSS fields (Leo, 2002). It was found that the hinge flow dynamics of the CM valve lies in between the SJM Regent and the MP BMHV designs with peak phased-averaged leakage velocity (3.17 m/s) and TSS (5640 dynes/cm^2) observed at the flat level and 190μm above flat level, respectively, in the hinge recess. It was concluded that the different performance observed among three valves were mainly attributed to the geometrical differences of the hinge.

Subsequently, similar LDV studies were conducted by Simon et al. comparing SJM and 23 mm CM BMHVs under physiological aortic and mitral valve conditions (Simon, 2004). The hinge flow fields were found to be more complex and unsteady in the CM valve than in the SJM valve, where higher velocities and RSS levels were registered with CM valve. The study reported that the superior hemodynamic performance of the SJM valve may be due to the smooth streamlined hinge geometry of the SJM valve. In addition, the results obtained under the aortic position indicated stronger forward flow than the mitral position which could ensure an efficient washout preventing the blood element buildup in the hinge region. These findings indicate that the implant position should also be considered as another critical design parameter in addition to the geometrical feature.

Leo et al. investigated the hinge flow fields in vitro using laser Doppler velocimetry (LDV) inside 27mm standard St. Jude Medical (SJM) BMHV prototypes with three different hinge gap widths. It was shown that thromboembolic potential was higher in prototypes with either a smaller and larger gap width than in the standard model. The highest RSS magnitude of 13,315 dynes/cm^2 was observed from the prototype with largest gap width. The prototype with the smallest hinge gap width exhibited highest velocity magnitude of 2.08 m/s among the three valves during the forward flow (Leo, 2006).

In addition to in-vitro LDV studies, the Particle Image Velocimetry (PIV) technique has also been utilized to study whole-flow fields in BMHVs. Manning et al. investigated leakage flows through B-datum line and peripheral gaps in 27mm SJM BMHV under pulsatile mitral flow condition. Strong regurgitant jets and twin vortices near the leaflets were observed. In this study, phase-averaged velocity fields were obtained upstream of the valve annulus at specific phases of the cardiac cycle including 5ms before the valve closure and 5, 50, and 100ms after the valve closure. Subsequently, flow fields revealed strong regurgitant jets and twin vortices near the B-datum plane immediately 5ms after the occlude impact, which persisted for about 20ms. Once valve leaflets were fully closed, sustained regurgitant flows were observed near hinges and peripheral leakage regions. The study reported that the vortex formation observed along the B-datum plane may potentially trap damaged blood elements resulting in thromboembolism (Manning, 2003).

Dasi et al. investigated the effects of a passive flow control device on leakage flow hemodynamics when applied to BMHV leaflets. In this study, PIV was used to examine flow

fields in 25mm SJM BMHVs with rectangular and hemispherical vortex generator (VG) arrays mounted near the B-datum leaflet edge. The results from this study demonstrated significantly improved hemodynamics with VG elements, in which spatially more dispersed and lower magnitude vorticity were observed than the BMHV with no VG. The maximum RSS levels were also 400 Pa lower with the presence of VGs with rectangular configuration (Dasi, 2008)

More recently, Bellofiore et al. used a scale-up model representative of an SJM BMHV to investigate the unsteady flow fields at the trailing edge of the leaflet with enhanced spatial and temporal resolution. This study enabled flow velocity maps with increased spatial and temporal resolutions of up to 120µm and 560µs, respectively, representing significantly smaller discretization errors than in physiological-scale experiments. Subsequently, the results from this study illustrated the leaflet wake flow evolution and vortex shedding in the systolic phase, representing the lower limit for initiating thrombosis (Bellofiore, 2011)

2.7.2 *Ex-vivo* studies of BMHVs

Ex-vivo studies were also conducted by researchers in conjunction with *in-vitro* studies in an attempt to make a direction correlation between the observed flow structures and blood element damage in BMHVs. Fallon et al. measured the effects of blood flow through small orifices resembling a leakage flow through MHVs. In this study, recalcified blood continuously flowed through 200, 400, 800, and 1200µm round orifices and 200, 400, and 800 µm wide slit orifices, each resembling the hinge region and B-datum line, respectively. The results reported a significantly increased thrombin–antithrombin III (TAT) levels in 200 and 400µm round orifices, indicating a critical threshold level with these geometries representing activation of coagulation

and thrombus formation. The study suggested that thrombus formation in MHVs is most likely due to leakage flow through the hinges than the B-datum plane. In addition, platelets were found to play a critical role under high shear stress conditions for the activation of coagulation cascade (Fallon, 2006).

Travis et al. studied the effects of different hinge geometries on markers of platelet damage including platelet secretion and anionic phospholipid expression. A steady flow pump was used to circulate the blood through BMHVs. Four BMHV models used in this study were 27mm MP, 27mm SJM Standard regular leaker, 27mm SJM high leaker, 27mm SJM low leaker, and 20mm SJM regular leaker representing hinges with different geometry, gap width, and valve diameter. The results from this study showed a significantly increased level of platelet secretion and anionic phospholipid expression from the 27mm SJM high leaker valve than the 27mm SJM regular leaker valve. However, no significant differences were observed between the 27mm SJM Standard regular leaker, 20mm SJM regular leaker, and 27mm MP valve. Subsequently, this study demonstrated that the hinge gap width had more significant effect on platelet damage than the other parameters such as hinge pivot geometry, and valve diameter (Travis, 2001).

2.7.3 Computational studies of BMHVs

More recently, numerical simulations of hinge flow fields under pulsatile flow conditions have been conducted to overcome limitations associated with experimental techniques, primarily due to the complex geometry and physiological conditions in the BMHV hinge region. Simon et al. enabled three-dimensional hinge flow simulations under pulsatile aortic flow conditions. The methodology used a Cartesian sharp-interface immersed-boundary method in conjunction with a

second-order accurate fractional-step method in order to simulate the flow through the hinge geometries constructed from the micro-CT scans of SJM BMHV hinges. The results from this study revealed the presence of a strong out-of-plane vertical velocity magnitude of up to 2.42m/s and peak shear stress magnitude of 6115 dynes/cm^2 during leakage flow that maybe detrimental to blood elements. The computational results from this study showed a good qualitative agreement with the previous LDV studies conducted under pulsatile aortic flow conditions. Flow fields obtained from both LDV and computational techniques demonstrated presence of vortical flow structure adjacent to the leaflet ear and vertical jet parallel to the forward flow direction in systole. A strong diastolic jet at the lateral and ventricular corners of the hinge was also observed from both studies. Overall, the results from the computational study highlighted the need to perform three-dimensional characterization of the hinge flows to fully assess the blood element damage potential of a BMHV (Simon, 2011).

Subsequently, another computational study on a BMHV hinge was performed by Yun et al, using realistically modeled blood elements within the hinge region to quantify blood damage associated with different hinge designs including the SJM and CM BMHVs. A novel feature of this study included the quantification of shear stresses experienced by individual platelets. The computational simulation was performed by using the lattice-Boltzmann method (LBM) in conjunction with the external boundary force (EBF) method. The results had shown that 0.4 percent and 3.2 percent of the released platelets in the SJM BMHV and CM BMHV, respectively, exceeded platelet activation threshold level of 34 dynes/cm^2 for a blood damage index (BDI). This study reported that the SJM BMHV showed better performance than the CM BMHV in terms of the blood damage potential, which may be attributed to a smoother transition geometries

of the SJM BMHV. Overall, the numerical method presented by Yun et al. allowed for a more realistic calculation of blood element damage by tracking the shear stress history of individual platelets, which was challenging to derive from previous experimental and numerical techniques (Yun, 2012).

CHAPTER 3

HYPOTHESIS AND SPECIFIC AIMS

Despite the clinical success and widespread use of bileaflet mechanical heart valves (BMHVs), hinge and pivot regions of BMHVs are known to cause blood element damage due to the complex and unsteady nature of flow within these regions (Giersiepen, 1990). Blood element damage is primarily caused by adverse fluid flow characteristics, such as high shear stress and recirculation regions (Gross, 1996). However, characterization of flow fields in the hinge region is difficult due to complex three-dimensional geometry and small spatial scales involved, which is estimated as a depth and volume of 500μm and 1.5μL, respectively. This requires multi-scale approaches to investigate small hinge region which exists in a macro-scale fluid volume. Previously, a point measurement technique such as Laser Doppler Velocimetry (LDV) was used to obtain velocity fields in the BMHV hinge (Simon, 2004; Leo, 2006). However, major limitations with LDV experiments are the low spatial resolution (~203μm) and significantly long data acquisition period. Conventional Particle Image Velcoimetry (PIV) techniques also do not have sufficient spatial resolution to study BMHV hinge flows where measurement depth is approximately 1mm (Manning, 2003; Bellofiore, 2011). To date, no study has focused on investigating the whole-flow fields within the valve hinges. Such information would provide new insight into the roles that hinge gaps have on the instantaneous damage to blood elements.

The hypothesis of this study is that:

Detailed characterization of flow fields in the hinge region of a bileaflet mechanical heart valve can lead to a better understanding of the effect of hinge gaps on thromboembolic potential.

This hypothesis was addressed by the three following specific aims:

<u>Specific Aim 1</u>: Establish a methodology to characterize global velocity maps within the hinge of a bileaflet mechanical heart valve.

To accomplish this goal, a high spatial resolution experimental technique based on Micro Particle Image Velocimetry will be developed to obtain a whole-flow field in the St. Jude Medical (SJM) BMHV hinge. Critical components of this system such as the camera, objective lens magnification, laser illumination, tracer particles, and composition of the working fluid will be carefully selected and integrated in order to map the fluid velocity at four different planes within the hinge recess. Instantaneous two-dimensional velocity fields will be measured inside the hinge under steady and physiological pulsatile flow conditions. This methodology will represent a significant improvement from the previous experimental technique by providing high-resolution whole-flow field information in the hinge, in comparison to single point time-averaged Laser Doppler Velocimetry techniques.

<u>Specific Aim 2</u>: Characterization of hinge flow fields of a bileaflet mechanical heart valve under steady diastolic leakage flow conditions using the Micro Particle Image Velocimetry system.

To accomplish this goal, two-dimensional global flow fields in a SJM BMHV hinge under steady flow conditions will be investigated. A steady flow loop system will be used to mimic the aortic valve leakage flow in diastolic phase. It has been shown that this particular phase has the highest thromboembolic potential of any phase of the cardiac cycle (Leo, 2002; Simon, 2004; Leo, 2006). This specific aim will include characterization of the whole-flow and viscous shear stress fields, and a representation of the mating between the leaflet and hinge housing. These results

will enable identification of the high velocity regions, the viscous shearing and the low flow zones associated with blood element damage in the hinge region of BMHVs.

<u>Specific Aim 3</u>: Investigate the influence of gap-width on hinge flow fields of bileaflet mechanical heart valves using the Micro Particle Image Velocimetry system under physiological pulsatile aortic flow conditions, and relate these results to blood damage potential.

To accomplish this, a pulsatile flow loop system simulating physiological aortic flow will be used in conjunction with the methodology proposed in specific aim 1. A pulsatile experimental setup will incorporate dynamic acceleration effects of leaflet motion on the hinge flow fields. This cannot be achieved from the steady flow loop setup where the valve leaflets are in a static position throughout the experiment. Subsequently, flow fields within SJM BMHV hinges with varying gap widths will be characterized, in order to fully investigate the blood damage potential from a fluid mechanics point of view. In this specific aim, parameters such as velocity, Reynolds shear stress, and viscous shear stress will be quantified from measured flow fields. This will allow a close examination of the effect of gap width on the flow characteristics in the hinge region of SJM BMHVs. These results will be related to the blood damage potential of these valves.

CHAPTER 4

EQUIPMENT AND MATERIALS

4.1 Valve Models

A 23 mm St. Jude Medical (SJM) Regent bileaflet mechanical heart valve (BMHV) with transparent body was directly obtained from the valve manufacturer for steady flow experiments. All parts of the clear housing valve were manufactured with tolerances identical to those of clinical models (Figure 4.1-a). This transparent acrylic replica of the valve allows visualization of the hinge region. The leaflets of the valve were made from pyrolytic carbon with a graphite substrate containing tungsten. Figure 4.1-b shows two different views of the BMHV and Figure 4.1-c,d represent the hinge geometry and leaflets in the fully opened and closed positions.

The hinge cavity is 3.5 by 3.5 mm in area and has a depth of approximately 600 μm (Figure 4.1-c,e), as shown in the micro-CT scan image of the BMHV hinge conducted by Simon (Simon, 2009). The SJM hinge geometry has a smooth butterfly-shaped cavity that retains semicircular leaflet ears. The opening and closing angles of the leaflet relative to the horizontal axis indicated in Figure 4.1-d are 84° and 29°, respectively.

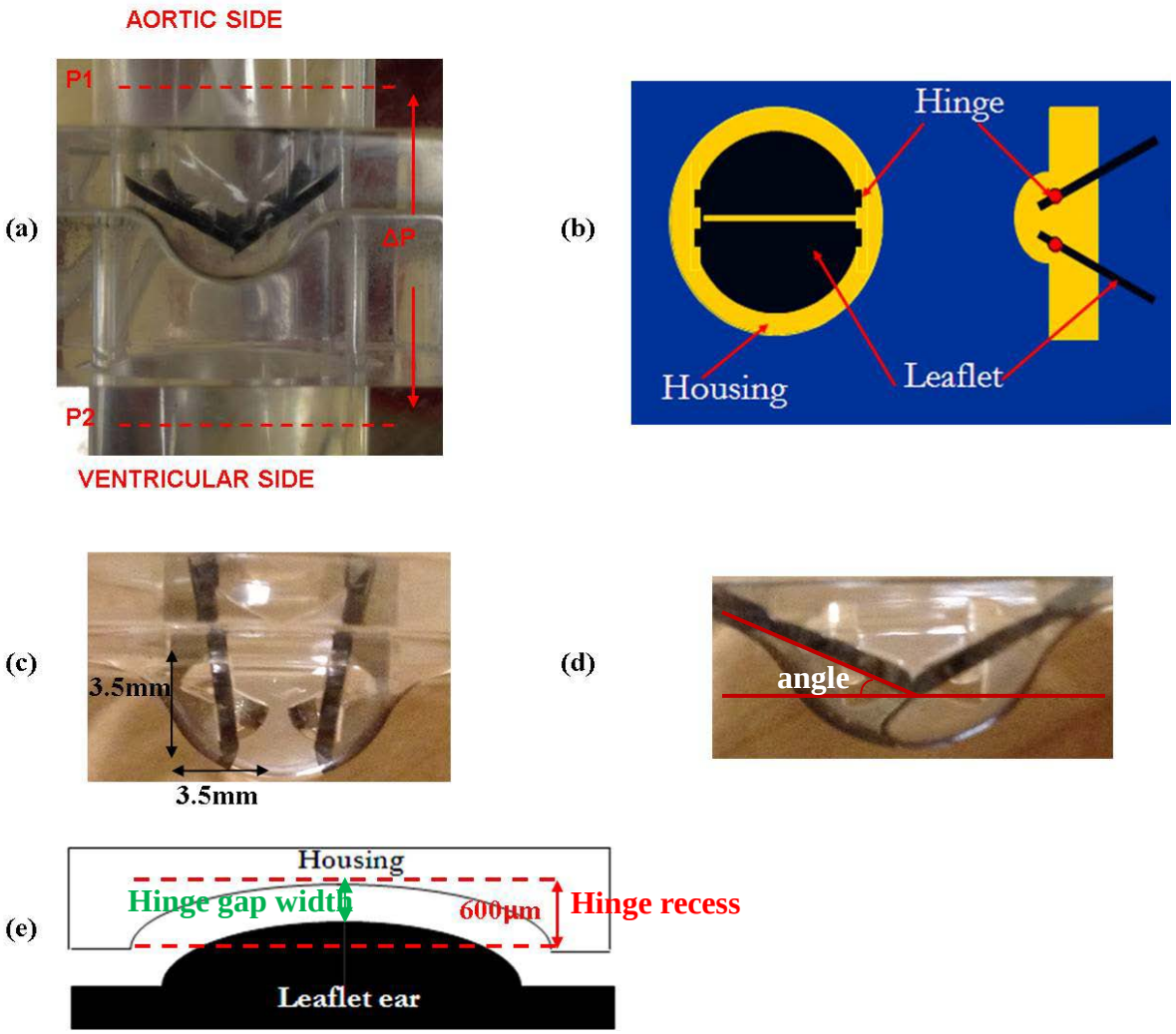

Figure 4.1: (a) St. Jude medical bileaflet mechanical heart valve clear housing model, (b) general components of BMHV (Leo, 2002) (c) leaflets in fully opened position, (d) leaflets in fully closed position, and (e) side view of hinge recess.

In order to study the effect of hinge gap width in pulsatile flow experiments, three additional BMHV prototypes with clear housings and different hinge gap widths were provided by St. Jude Medical Inc. (St. Paul, MN, USA). The term 'hinge gap width' was defined as the distance between the deepest point of recess and the tip of the leaflet ear (Figure 4.1-e). A 23mm SHP SJM BMHV with a gap width of ~100µm was used as a standard prototype (Standard) (Figure 4.3). All parts of the clear housing Standard valve were manufactured with tolerances identical to

those of clinical SJM valves. The hinge gap widths of two modified 27mm SJM BMHVs were ~50µm and ~200µm, which are referred to as a low leaker prototype (LLP) and a high leaker prototype (HLP), respectively (Figure 4.1-c,d). Unlike the Standard valve, the LLP and HLP valves were manufactured with tolerances outside the range of clinical SJM models. In these valves, hinge dimensions do not vary among adult sized valves (23mm, 25mm and 27mm) (Simon, 2009). The hinge gap width from these models was scanned and measured with micro-CT (Figure 4.2 and Table 4.1). Detailed instructions on measurement steps in the micro-CT scan software can be found in Appendix B-2.

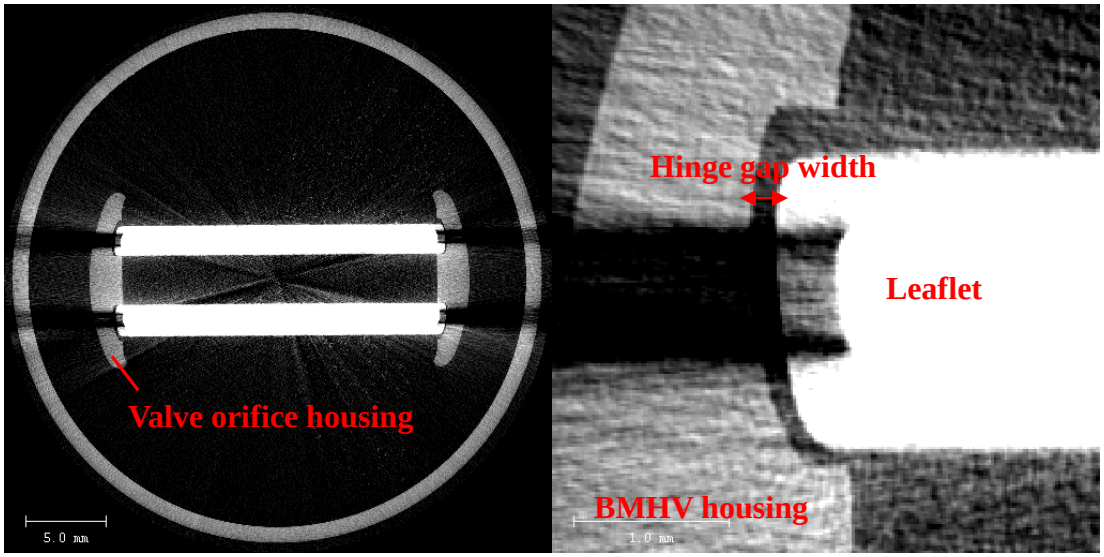

Figure 4.2: Representative micro-CT scan image of BMHV prototype. (a) micro-CT scan slice across the BMHV showing the leaflets and the acrylic housing, and (b) an enlarged view of the hinge gap width near the leaflet edge

Table 4.1: Measured gap width from the micro-CT scan images from valve models

	LLP	**Standard**	**HLP**
Gap width (µm)	52	104	196

4.2 Valve Mounting Chambers

Figures 4.1a, 4.3, and 4.4 show the transparent chambers for the valve models used in this study. For the 23mm SJM Regent and SHP BMHVs, leaflets were retained in a single housing provided directly by the valve manufacturer. The HLP and LLP valves were mounted in the chamber shown in Figure 4.4, used by Leo (2005). This chamber consists of four transparent acrylic pieces that are fastened together with four socket cap screws, and securely position the valve.

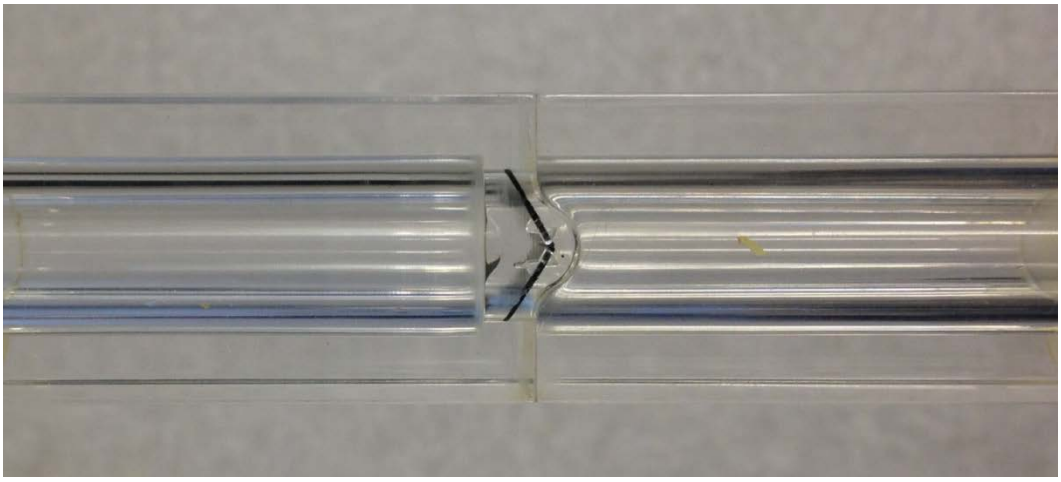

Figure 4.3: Valve housing for the Standard valve

Figure 4.4: Mounting chamber for the HLP and LLP valves

4.3 Flow Loop

4.3.1 Steady Flow Loop

To ensure adequate particle seeding in the hinge region without excessive particle aggregation or saturation, a low fluid volume system (500 ml) relative to *in vitro* heart simulators (Manning, 2003; Simon, 2004; Leo, 2006; Saikrishnan, 2012) was designed (Figure 4.5). This system maintained a steady backpressure on the BMHV leaflets to study diastolic leakage flow. The fluid reservoir was mounted on a rigid tube oriented vertically with height of 1 m and inner diameter of 10 mm, creating the desired hydrostatic pressure. A peristaltic pump (Cole-Parmer Company, IL, USA) was used to generate continuous circulation of fluid in the loop in order to maintain the necessary backpressure. Pressure transducers (Deltran transducers, Utah Medical Inc, UT, USA) were located 2.54 cm upstream and downstream of the BMHV model. These were paired with a custom LabVIEW Virtual Instrument (VI) to acquire real-time pressure measurements. A flow control valve controlled the steady leakage transvalvular pressure (**dP**) for the experiment.

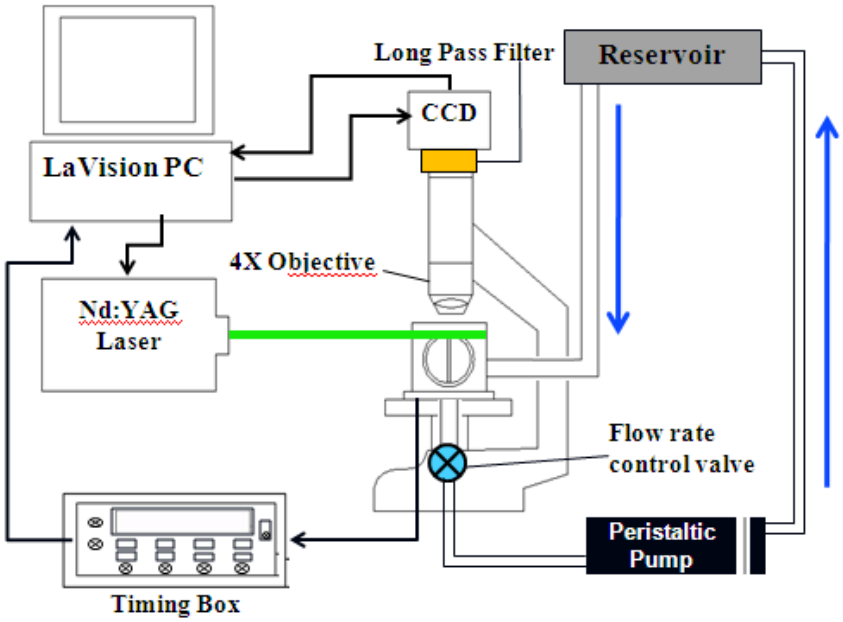

Figure 4.5: Schematic of steady flow experimental system.

4.3.2 Pulsatile Flow Loop

The valve model was mounted in an *in-vitro* left heart simulator (Fig 4.6) to replicate pulsatile physiological aortic flow. The physiological pulsatile flow was driven by a piston mounted to a linear actuator. During systole, the rapid upward movement of the piston in its cylinder forces the fluid to flow from the ventricle side to the aortic side across the aortic valve. In diastole, downward motion of the piston imposes back pressure on the aortic side, forcing the aortic valve leaflets to close. The fluid then circulates back to the ventricular side via a bypass loop with a one way valve that acts as a mitral valve. The motion of the piston was programmed to reproduce normal adult aortic flow conditions with a cardiac output of 5L/min, a 35% systole duration and a heart rate of 70bpm (total cardiac cycle time of 860ms). Compliance and resistance in the loop were adjusted during the experiment in order to achieve accurate physiological pressures.

An electromagnetic flow meter (Model 501, Carolina Medical Electronics Inc, NC, USA) was attached at the output of the piston/cylinder and two pressure transducers (Deltran transducers, Utah Medical Inc, UT, USA) were placed 2.54cm upstream and downstream of the valve model. These were used to measure the real-time flow rate and pressure using a custom LabVIEW VI. The LabVIEW VI was triggered by the linear actuator system, ensuring that the hemodynamic measurements were synchronized with the start of the cycle.

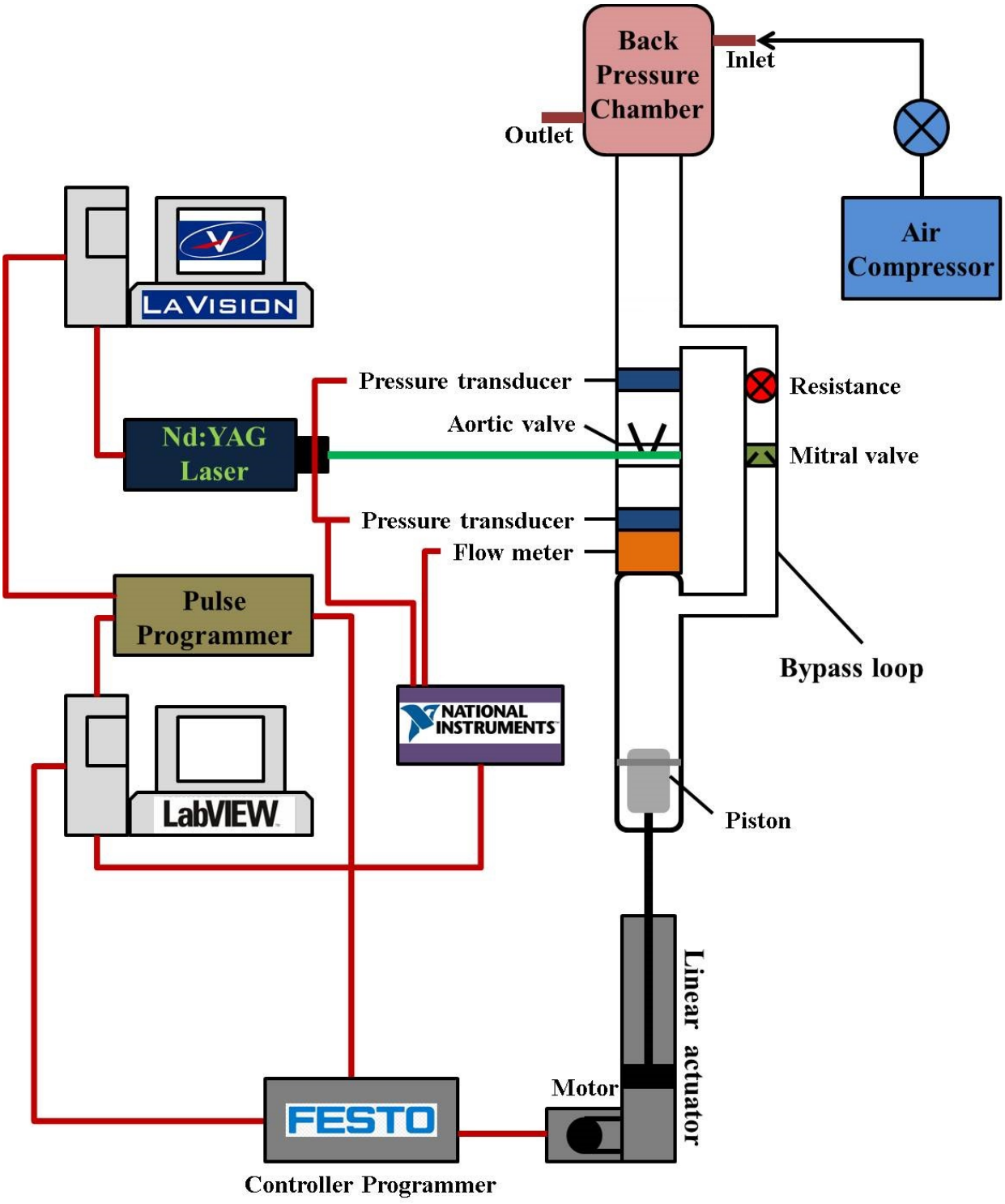

Figure 4.6: Schematic of pulsatile flow experimental system

The *in vitro* left heart simulator was operated by the motor (EMMS-AS-55-S-TSB, Festo Corporation, Hauppauge, NY) driven linear-actuator system (DGE-25-300-ZR-R, Festo Corporation, Hauppauge, NY) as represented on Figures 4.7 and 4.8, where the polyether ether ketone (PEEK) piston slides in and out of the titanium cylinder (Figure 4.6). A silicone O-ring was used to ensure a seal between the piston and the inner wall of the titanium cylinder. The motion of the piston was driven by a programmed motion profile created using the Festo Configuration Tool (FCT) software, where the position, velocity and acceleration of the linear actuator were defined in order to simulate physiological aortic flow. These parameters were calculated within the maximum working length (300mm) of the linear actuator, in order to generate physiological systolic and diastolic aortic flow from the upward and downward stroke motions, respectively.

Figure 4.7: FESTO linear-actuator system

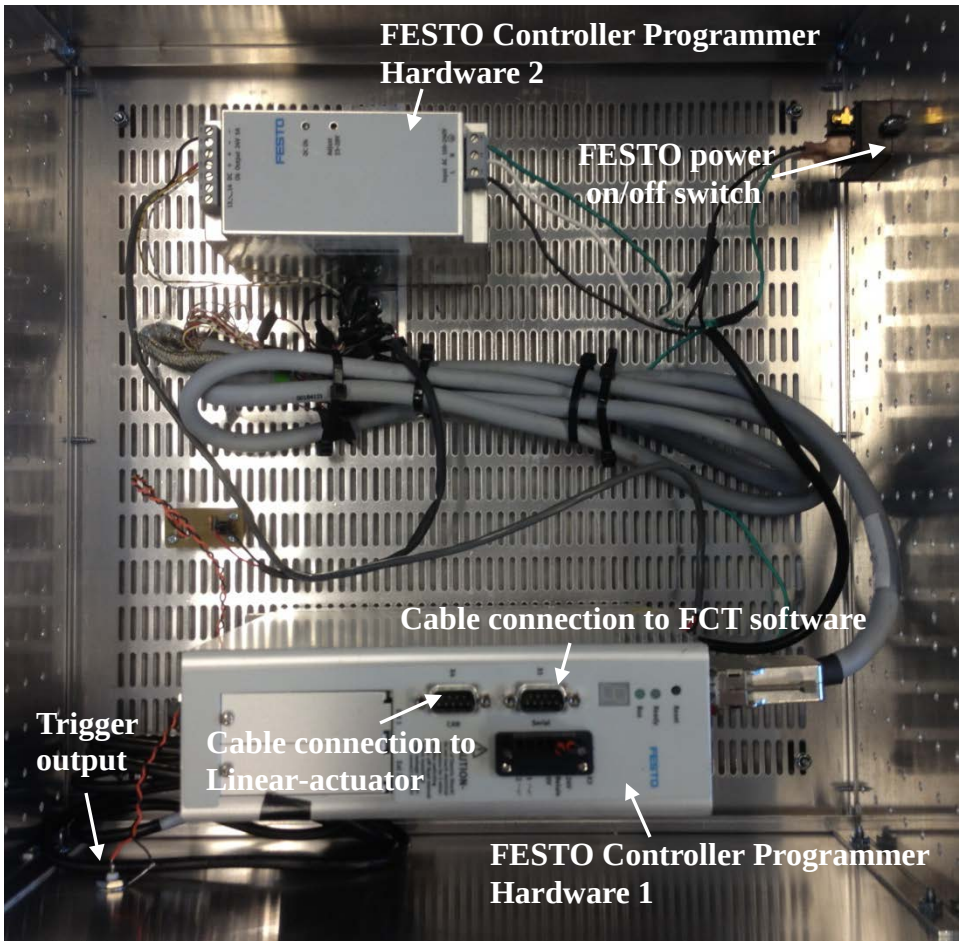

Figure 4.8: FESTO Controller Programmer

4.4 Micro Particle Image Velocimetry System

4.4.1 General Principle

Particle Image Velocimetry (PIV) is a quantitative method of optical flow visualization that provides global fluid velocity fields in a region of interest. This technique is non-intrusive and measures the velocities of tracer particles suspended in the flow (Figure 4.9).

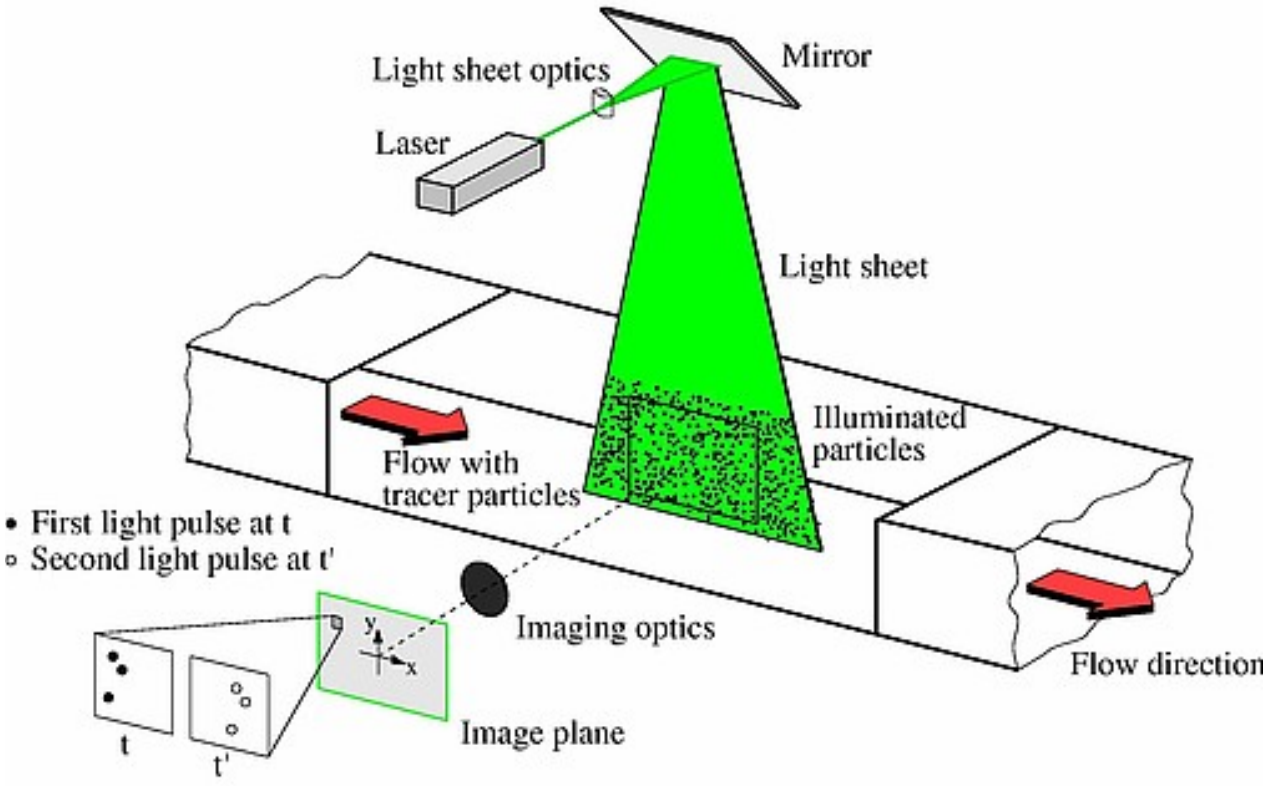

Figure 4.9: Principle of PIV

(http://www.dlr.de/as/en/desktopdefault.aspx/tabid-183/251_read-12796)

For typical PIV setups (Figure 4.9), lasers with a set of optics are used to generate high-power laser sheets with short pulse durations. Subsequently, the fluid seeded with fluorescent particles is illuminated so that particles are detectable from an imaging system. This technique measures whole-field velocity by quantifying the displacement of particles between image frames in a number of very small regions called interrogation windows. A cross-correlation technique is normally used to represent spatially averaged velocity vectors in these interrogation windows (Figure 4.10). This results in a two-dimensional velocity field of the fluid at the plane of interest.

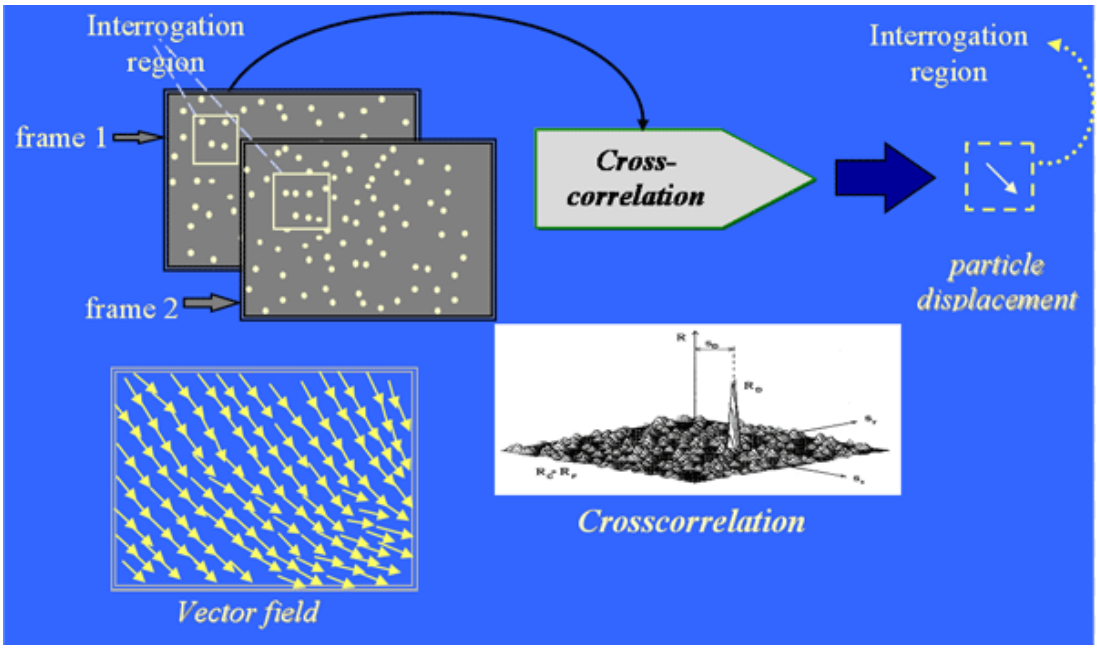

Figure 4.10: Illustration of PIV cross-correlation (https://www.erc.wisc.edu/piv.php)

PIV has been used to measure flow domains in BMHVs, prosthetic valves and tissue valves *in vitro* (Manning, 2003; Leo, 2005; Bellofiore, 2011; Saikrishnan, 2012). However, these conventional PIV techniques do not have sufficient spatial resolution to study BMHV hinge flows. Micro Particle Image Velocimetry (µPIV) is a well-established technique to quantitatively measure flow behavior in small domains down to the nanometer scale (Meinhart, 1999). A µPIV system (Figure 4.11-a) integrates a microscope with a CCD camera. In contrast to PIV, the entire volume of fluid is illuminated by the laser to capture maximum emission light from the tracer particles in the test section. Subsequently, the depth-of-correlation of the µPIV system determines the measurement depth where particles are effectively focused and contributes significantly to the velocity measurement (Meinhart, 2000; Wereley, 2010).(Figure 4.11-b) This allows for flow field spatial resolution at the micron level.

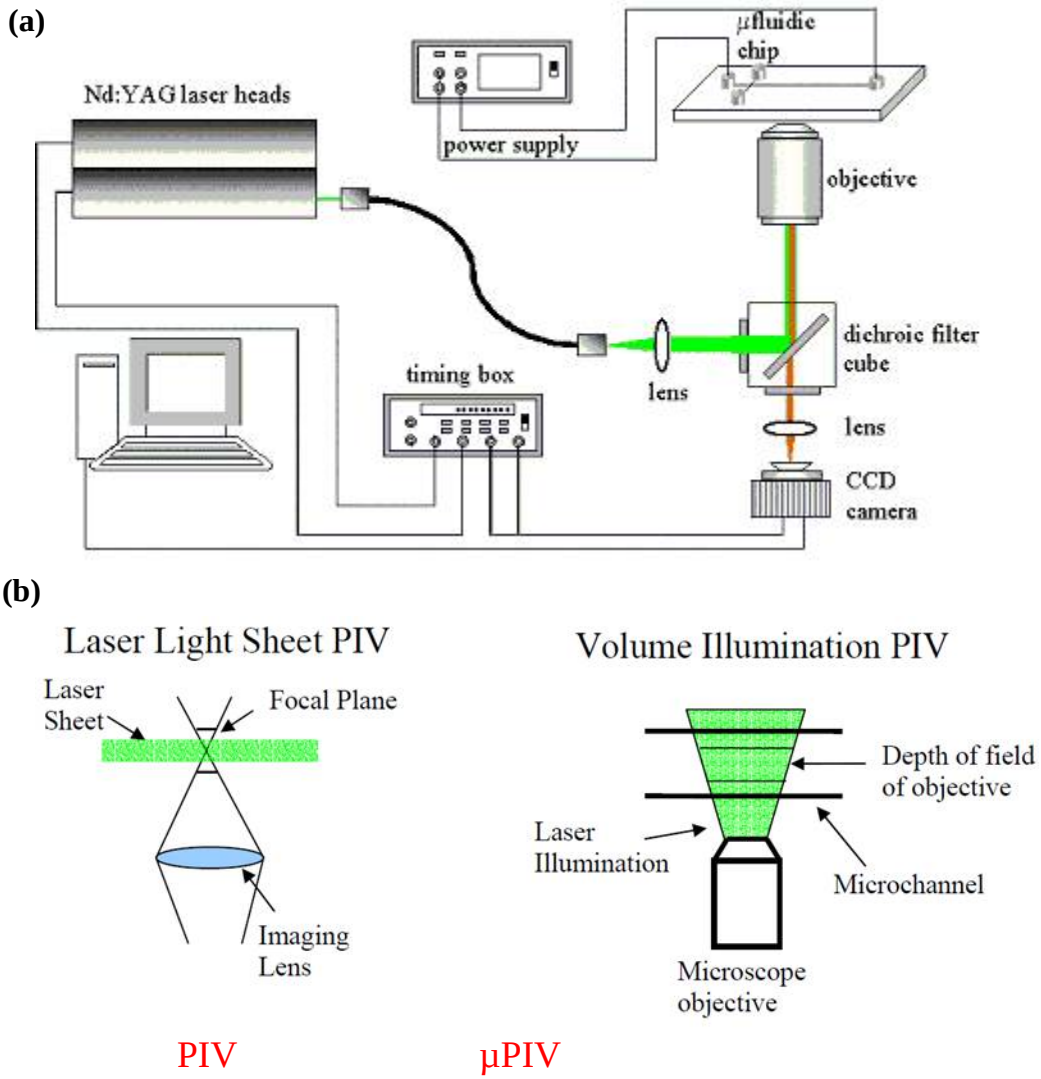

Figure 4.11: (a) General configuration of the Micro Particle Image Velocimetry system and (b) the Laser illumination system for conventional PIV and μPIV systems (http://microfluidics.stanford.edu/Projects/Archive/piv.htm)

4.4.2 Laser and Optics

A dual cavity pulsed 50mJ Nd:YAG laser (*ESI Inc., Portland, OR*) ($\lambda = 532$ nm, pulse duration = 9 ns) with a maximum repetition rate of 15Hz was used to generate a laser beam. This laser beam, with a diameter of approximately 4mm, was oriented vertically by two high energy

mirrors (16MFB415, Melles Griot) mounted on an optical rail (Figure 4.12). This arrangement allowed the laser beam to illuminate the hinge region of a BMHV mounted on a flow loop.

Figure 4.12: Optical setup used to direct the laser beam.

4.4.3 Imaging System

A LaVision Digital Particle Image Velocimetry (DPIV) system was adapted for this study. The flow was imaged with a CCD camera (LaVision, Germany, Imager Intense 1376 × 1040 pixels) connected to a microscope (Edmund Scientific Microscope – 156939) with a 4x magnification objective, numerical aperture NA = 0.1 and a long pass filter with λ = 570 nm (NT62-984, Edmund Optics, NJ) as represented on Figure 4.13. To be mounted with the CCD camera focus on the field of view, the 4X objective lens and the focal tube were partially detached from the microscope frame. The long pass orange filter was coupled with the CCD lens to effectively

capture the emitted light from the fluorescent particles while eliminating scattered or reflected light from the valve model.

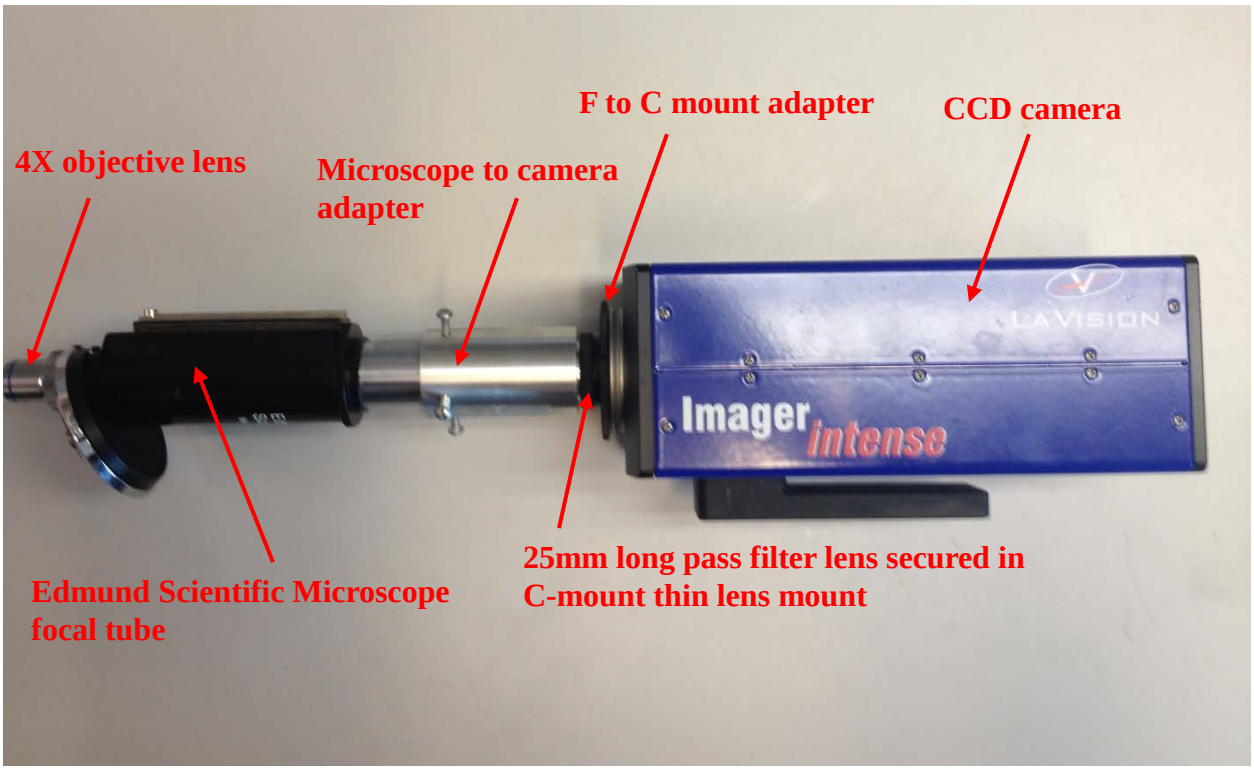

Figure 4.13: Camera setup for the Micro-PIV experiment

4.4.4 Traverse System

The imaging system described in section 4.4.3 was mounted on a motor-driven traverse system (BiSlide, Velmex Inc, USA) (Figure 4.14) to ensure accurate spatial positioning. During the experimental setup, the objective lens position was adjusted by the traverse system to known distances corresponding to the various measurement planes and spatial locations in the hinge region of a BMHV. The linear actuator motor was controlled by FlowSizer software (TSI Inc, MN, USA) and the motion of each traverse was programmed. Detailed instructions on launching

the software and setting up the traverse motions can be found in Appendix A-1. The resolution of the traverse system was 6.36μm.

Figure 4.14: Motor-driven traverse system

4.4.5 Working fluid and Tracer particles

Polymethyl methacrylate (PMMA) particles coated with fluorescent Rhodium-B dye (D = 1-20 μm) with density of 1.19 g/cm^3 were used as seeding particles (Dantec Dynamics, Denmark).

The working fluid was a mixture of 100% saturated Sodium Iodide solution, glycerin and water (79:20:1 by volume) with a density of 1.62 g/cm^3. This matched the kinematic viscosity of blood (3.5 cSt) and had an identical index of refraction to acrylic (n = 1.49). Detailed instructions on preparation and maintenance of the Sodium Iodide solution can be found in Appendix A-2.

4.4.6 Depth of Correlation

In the current study, the depth of correlation determines the measurement depth where particles are effectively focused and contributes significantly to the correlation function. According to Olson *et al*., a depth of correlation can be defined by the theoretical equation below (Olson, 2000).

$$\delta_{\text{corr}} = 2\left[\frac{1-\sqrt{\varepsilon}}{\sqrt{\varepsilon}}\left(\left(\frac{1}{2NA}\right)^2 {d_p}^2 + \frac{5.95(M+1)^2\lambda^2\left(\frac{1}{2NA}\right)^4}{M^2}\right)\right]^{1/2} \qquad \text{Equation } 4-1$$

Using the values for magnification (M = 4) and numerical aperture (NA = 0.1) of the objective lens, the seeding particle diameter (d_p = 1-20μm), the value for threshold weighting function (ε = 0.1, where the contribution of the particle becomes insignificant), and the wavelength of the emitted light (λ = 532 nm), the minimum and maximum measurement depth (δ_{corr}) were estimated to be 120.2 μm and 317.4 μm, respectively.

The two experimental parameters that directly affect the depth of correlation are the magnification of the objective lens and the diameter of the seeding particle. In an experimental trial of 1 μm seeding particles, it was determined that, due to insufficient illumination of the small seeding particles, the signal-to-noise ratio of the PIV data was too low. Using a higher magnification lens (10x or 20x) would avoid this difficulty and reduce the depth of correlation to under 100 μm. However, this reduced depth of correlation would lead to a significantly increased number of measurement locations (8 to 15 subsections), and obtaining sufficient seeding density at such high magnifications is not possible in the current system. Consequently, the

representative instantaneous field would only cover a small portion (7 to 13%) of the hinge region, giving no significant advantage over previously established LDV techniques.

Subsequently, to produce global velocity maps in the hinge region, and to keep the number of imaging locations below four, the magnification of the objective lens cannot exceed 4x. The choice of an appropriate objective lens is limited since magnification larger than 5x will only resolve smaller areas of the hinge region, and magnification smaller than 3x will have depth of field greater than the hinge recess gap.

It must be noted that the theoretical maximum measurement depth is meant to be a very conservative estimate, assuming a uniform particle diameter of 20 μm and no image pre-processing. The image pre-processing and masking were used in this study during the PIV cross-correlation to subtract unfocused particles and background illumination. In addition, the geometry that we are attempting to image in the current scenario is extremely complex, and is much more complicated than the idealized geometries that are typically studied using μPIV; hence the depth of correlation is greater than those observed in typical μPIV studies.

4.4.7 PIV Measurement Locations

As illustrated in Figure 4.15-a, four measurement planes separated by 195 μm were chosen with the bottom flat surface of the hinge selected as a reference plane. The four measurement planes and hemodynamic conditions were selected for the purpose of comparison with previous experimental and computational studies of hinge flows (Simon, 2004; Leo, 2005; Simon, 2010; Yun, 2012).

These planes are referred to as FLAT, 195 µm, 390 µm and 585 µm planes, based on their distance from the reference plane (flat level). The FLAT and 195 µm planes are referred to as the lower measurement planes, while the 390 µm and 585 µm planes are referred to as the upper measurement planes. In order to image the entire hinge region with the microscope lens, 2D-PIV images were acquired at three distinct sections (Figure 4.15-b). These were labeled as aortic, center or ventricular, according to their spatial location.

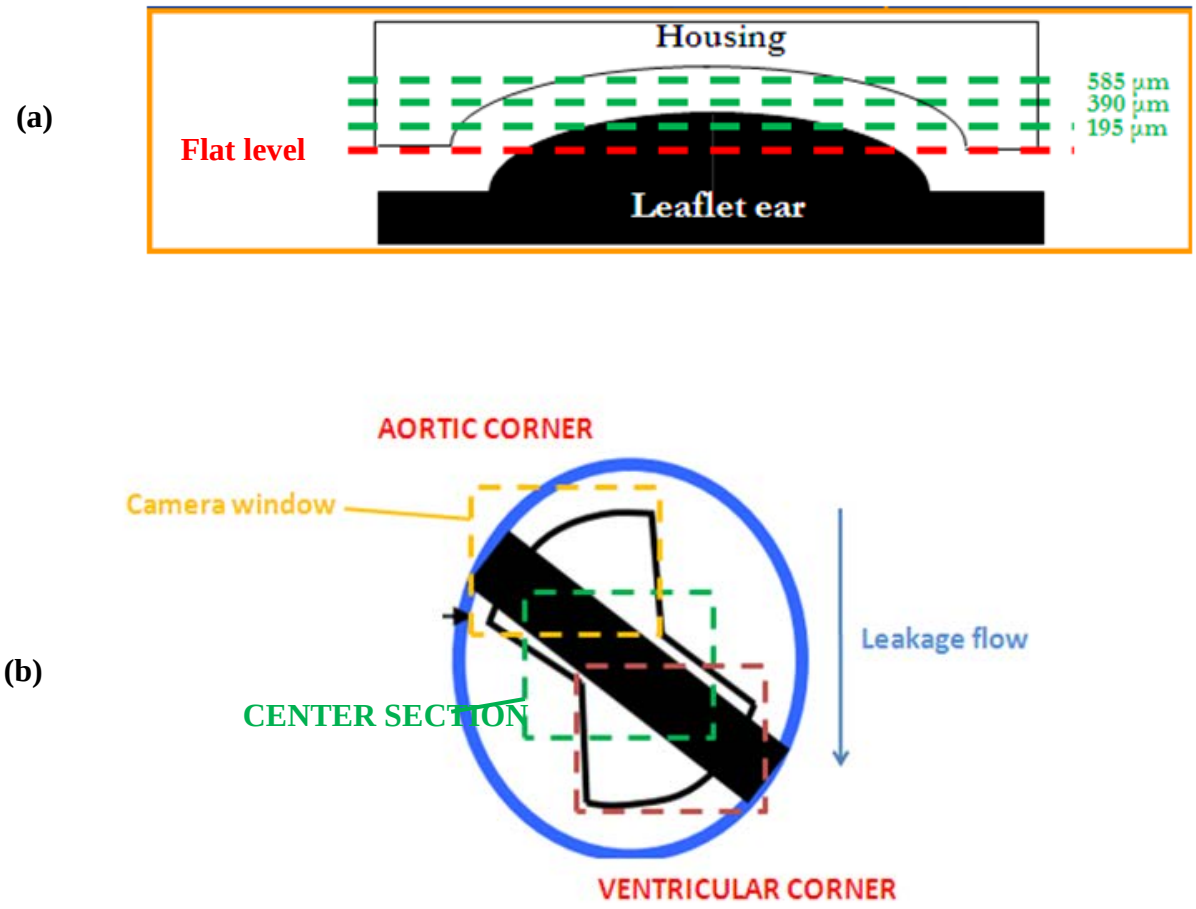

Figure 4.15: (a) Measurement planes in the hinge recess gap, (b) Measurement locations in the hinge.

4.4.8 PIV calibration

PIV calibration was performed using a series of precision-machined acrylic blocks (±0.0007 in) of varying thickness (Table 4.2), equal to the depth of material through which the PIV plane was imaged. This depth was measured from a micro-CT scan of the valve model. Due to accurate refractive index matching between the working fluid and acrylic housing of the BMHV model, accurate *in situ* calibration was performed using this method. During the calibration process (Figure 4.16), the traverse position at which the objective lens and acrylic block surfaces were flush was set as the zero position. Subsequently, the objective lens was positioned away from the zero position until the calibration target was in focus. The distances that the objective lens had to be translated to focus at each measurement plane in the hinge region are represented on Table 4.2. The position error was estimated to be 3.18 μm based on the resolution of the traverse system. Table 4.2 below represents the thickness of acrylic blocks used for calibration of each experiment.

Table 4.2: Calibration block dimensions and traverse positions for each valve model

	FLAT	**195 μm**	**390 μm**	**585 μm**
LLP & HLP	0.3500 in (13.0 mm)	0.3423 in (13.3 mm)	0.3346 in (13.6 mm)	0.3269 in (13.9 mm)
Standard	0.4433 in (13.3 mm)	0.4356 in (13.6mm)	0.4279 in (13.9mm)	0.4202 in (14.2mm)

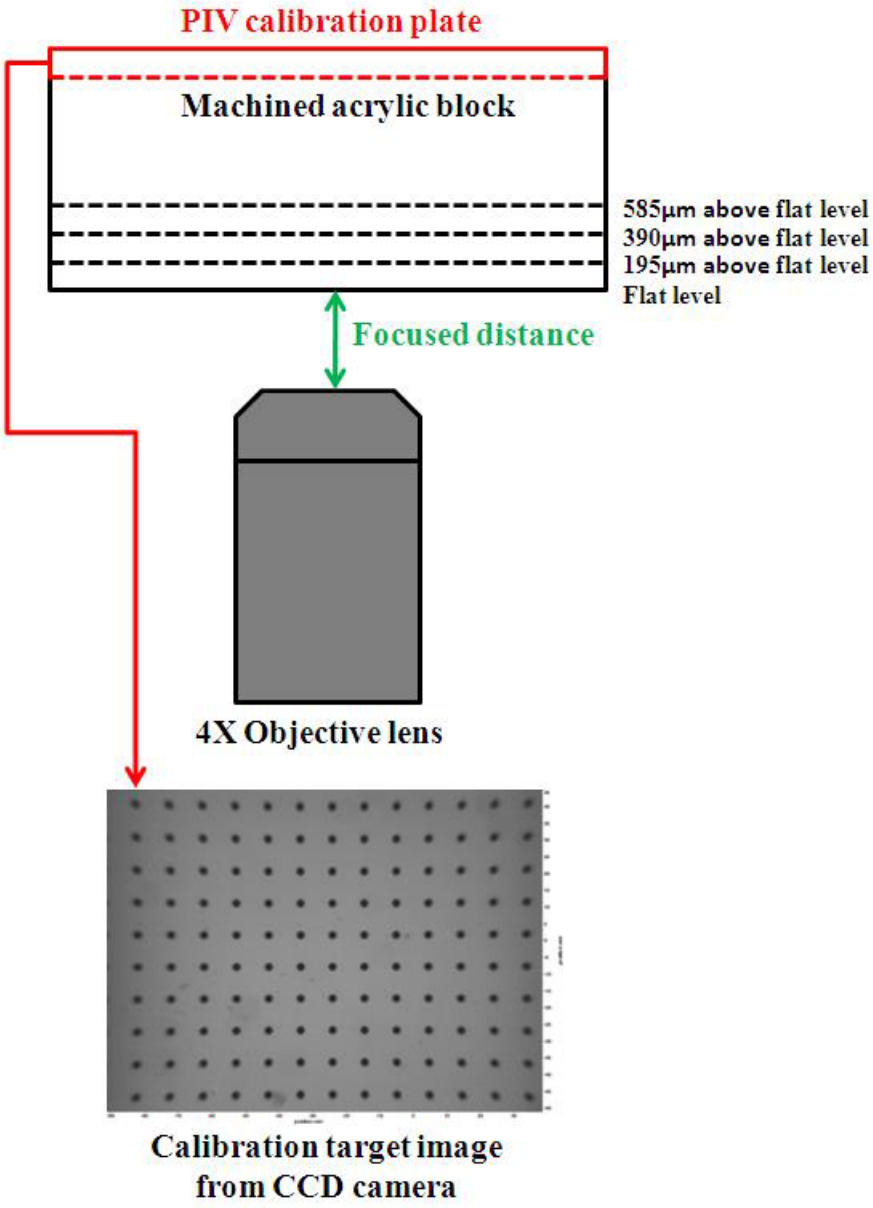

Figure 4.16: Micro-PIV calibration setup

CHAPTER 5

EXPERIMENTAL PROTOCOLS

The previous chapter described the materials, methods and various flow loops used in these studies. This chapter is organized to give a description of each experimental procedure, including the experimental protocols for the hinge studies, and the data processing techniques.

5.1 Camera and Laser beam alignment

The camera setup described in section 4.4.3 was mounted on a three-way traverse system as represented in Figure 5.1. Traverse components 2 and 3 allowed positioning of the camera at the aortic, center and ventricular spatial locations in the BMHV hinge. Traverse component 1 was used to position the camera at the FLAT, 195, 390 and 585μm measurement planes in the hinge. Unlike traverse components 1 and 2, which are automated and motor-driven, traverse component 3 was positioned manually by adjusting the displacement knob. The objective lens and the exterior surface of the valve model were positioned in a way that the two surfaces are flush and consequently parallel (Figure 5.2a). Subsequently, the camera position was adjusted by the traverse system to known distances (Chapter 4: Experimental Protocol – Table 4.2) corresponding to the various measurement planes.

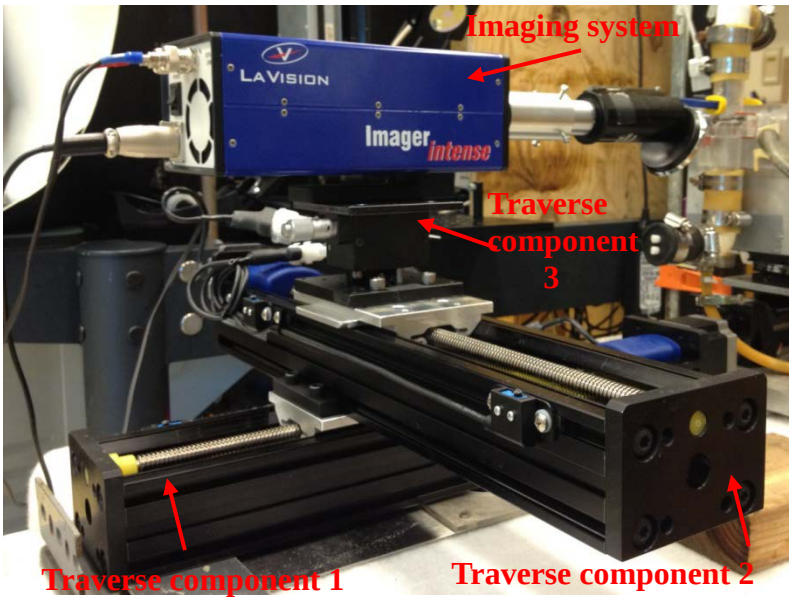

Figure 5.1: Complete assembly of the imaging system.

Unlike a conventional PIV system, where a thin laser sheet needs to be produced with combination of several optical lenses, the current Micro Particle Image Velocimetry (μPIV) system required only two high-energy mirrors and an optical rail to adjust the position of the laser beam produced directly from the laser head. Once the laser beam (under low energy level) was positioned appropriately near the hinge region, as represented in Figure 5.2b, it is necessary to visually assess the illuminated hinge region to ensure laser beam was not blocked by the leaflet. Proper safety procedures were maintained during visual assessment.

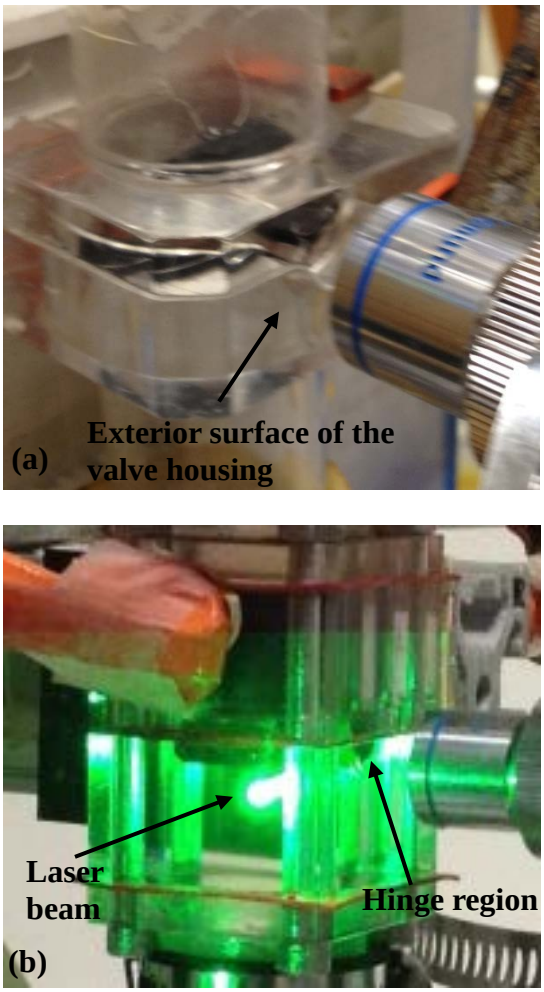

Figure 5.2: (a) Positioning objective lens, (b) Laser beam illumination in the hinge region

5.2 Static Leakage Test

To ensure that an increased leakage volume corresponded with increased gap width, a static leakage flow rate was measured from the SJM valves prior to the µPIV experiment. The static leakage flow setup (Figure 5.3) uses a 1.5 m vertical column filled with water-glycerin solution to impose a static pressure head of 120 mmHg on the aortic side of the valve. Each valve remained under the pressure head for one minute and the accumulated volume was collected and measured. This static leakage test was repeated five times per valve to calculate the average leakage flow rate.

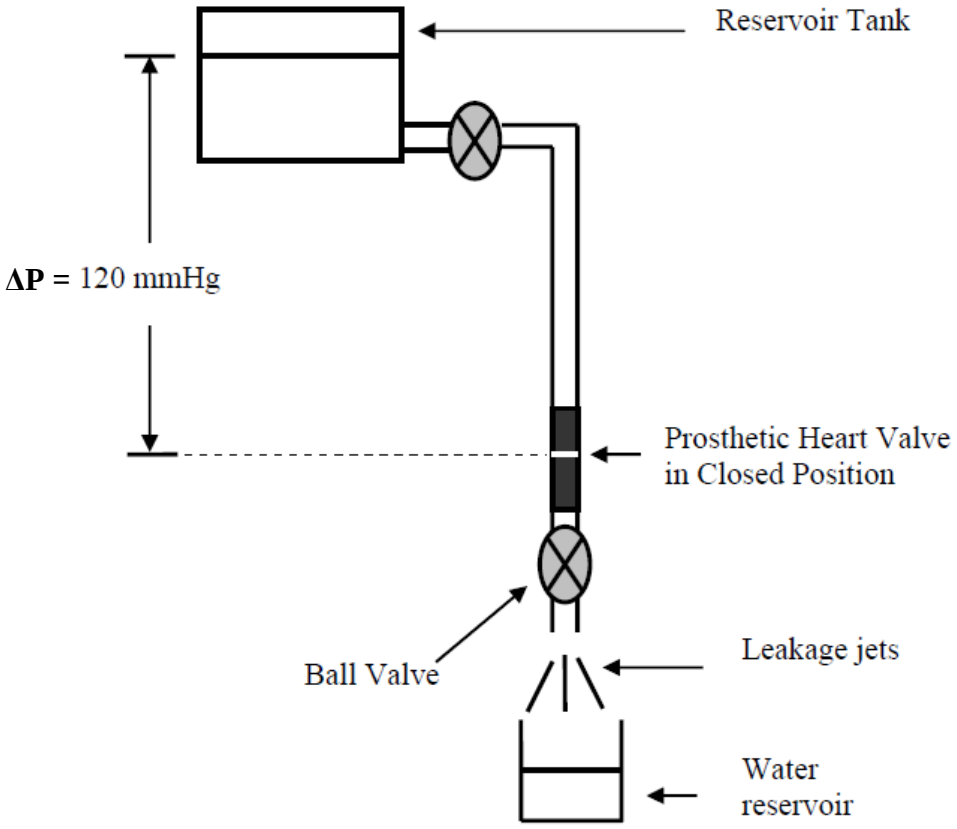

Figure 5.3: Static Leakage Test Circuit (Courtesy of Simon, 2004)

5.3 Steady Flow Experiment

For steady flow measurements, 50 PIV image pairs were obtained at **dP** = 80 mmHg and **dP** = 120 mmHg. These two values were chosen to simulate the flow during two different time points during diastolic leakage flow, based on previously acquired pulsatile hemodynamic waveforms (Simon, 2004). Table 5.1 represents the PIV pulse separation value used at each interrogation site.

Table 5.1: Pulse separation setting for the steady flow experiments

Measurement plane	Location	dt (in µs)	Velocity Uncertainty (m/s)
FLAT	Aortic	100	0.00197
	Center	100	0.00197
	Ventricular	50	0.00394
195µm	Aortic	100	0.00197
	Center	100	0.00197
	Ventricular	20	0.00985
390µm	Aortic	100	0.00197
	Center	20	0.00985
	Ventricular	10	0.0197
585µm	Aortic	50	0.00394
	Center	20	0.00985
	Ventricular	20	0.00985

The steady loop assembly is shown in Figure 5.4. This loop is filled with a sodium iodide solution and circulated back to the top reservoir via a peristaltic pump. The length of the vertical column was customized to 1 m to create a transvalvular pressure up to 140mmHg across the valve model. Lower transvalvular pressures, such as 80 and 120 mmHg, were achieved by adjusting the flow rate control valve.

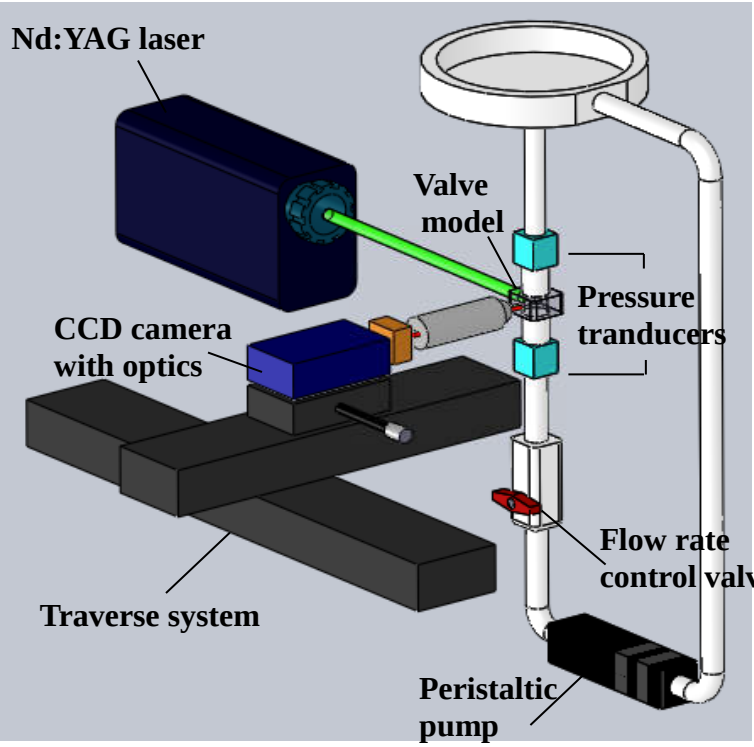

Figure 5.4: Schematic of steady flow experimental setup.

5.3.1 Data acquisition steps

With the camera position and laser optics fixed, as described in section 5.1, PIV data were acquired using DaVis 7.2 (LaVision, Germany). Acquisition employed the laser's internal trigger and utilized the maximum camera (Imager Intense) framing rate (4 Hz). The data acquisition procedure was as follows:

1. Adjust the flow rate control valve to achieve steady transvalvular pressure of 120 mmHg.
2. Position the camera to view the ventricular section of the hinge at the FLAT plane
3. Acquire 50 image pairs using DaVis 7.2 as well as real-time pressure tracings from the custom LabView program.
4. Position the camera to 195μm plane, and then acquire 50 image pairs.
5. Repeat step 3 for 390 and 585 μm planes.
6. Position the camera to view the center section of the hinge at the FLAT plane.
7. Repeat steps 3-5
8. Position the camera to view the aortic section of the hinge at the FLAT plane.
9. Repeat steps 3-5
10. Adjust the flow rate control valve to achieve steady transvalvular pressure of 80 mmHg.
11. Repeat steps 2-9

5.4 Pulsatile Flow Experiment

5.4.1 Replicating physiological conditions

The motion profile of the linear actuator was created using the Festo Configuration Tool (FCT) software, in order to simulate physiological aortic flow condition represented on Table 5.2 Detailed descriptions on each FESTO system component can be found in section 4.3.2 of Chapter 4: Equipment and Materials.

Table 5.2: Hemodynamic condition for the pulsatile flow experiment

Cardiac Output	**Mean aortic pressure**	**Peak flow rate**	**Heart rate**	**Cardiac cycle duration**	**Systolic duration**	**Ventricular pressure range**	**Aortic pressure Range**
5 L/min	100 mmHg	25 L/min	70 bpm	860 ms	300 ms	-40 to 130 mmHg	80 to 120 mmHg

The forward stroke of the piston motion closely mimicked a physiological aortic forward flow. The backward stroke of the piston motion forced the fluid to flow across the bypass loop while maintaining aortic valve leaflets to be closed. Table 5.3 represents the input velocity, acceleration, deceleration and position used for the forward and backward motions of the piston. Figure 5.5 represents the volumetric flow rate across the titanium tube (Figure 5.6), produced from the piston motion with parameters represented on Table 5.3. A detailed spreadsheet with each variable during the entire cardiac cycle can be found in Appendix B-1.

Table 5.3: Parameters used for the motion profile

	Velocity (mm/s)	**Acceleration (m/s^2)**	**Deceleration (m/s^2)**	**Position (mm)**
Forward stroke	1300	20	11	0
Backward stroke	400	8	8	220

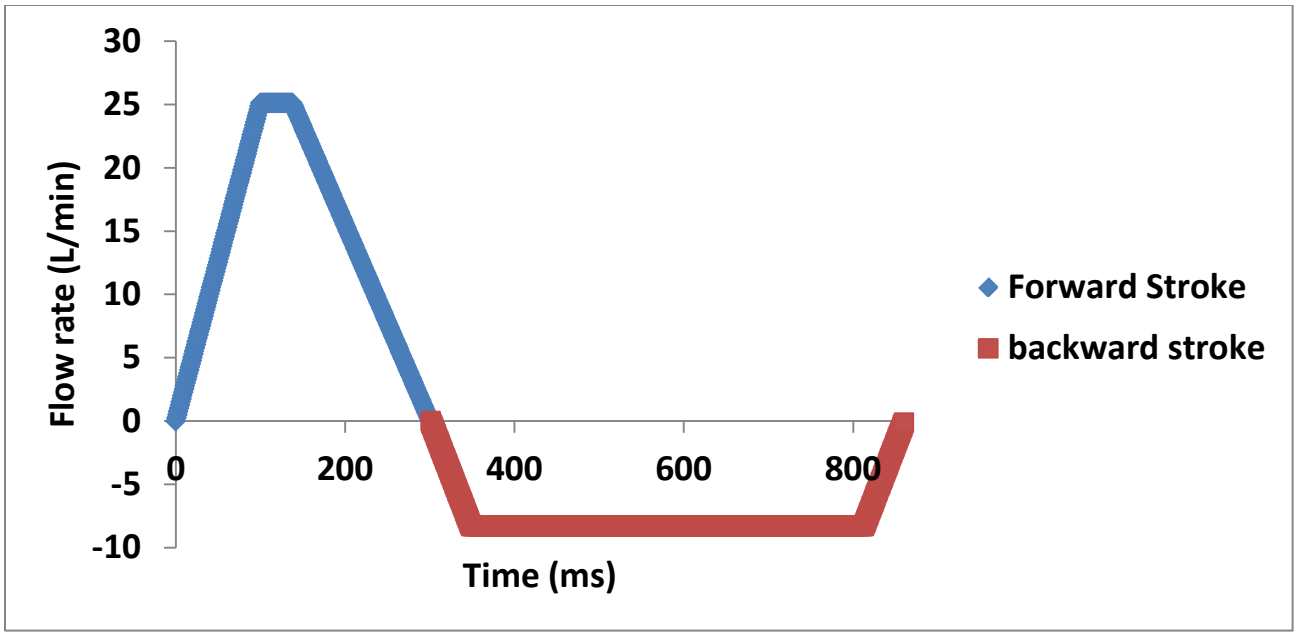

Figure 5.5: Volumetric flow rate produced based on the piston motion

These parameters can also be displayed in real-time by using the motion trace option from the FCT software. This feature proved useful when parameters needed to be adjusted to replicate different hemodynamic conditions. Detailed instructions on tracking the motion profile from the FCT software can be found in Appendix B-2.

The aortic and ventricular pressure conditions indicated on Table 5.2 were regulated by compliance and resistance elements illustrated in Figure 5.6. An inlet port with the external compressed air (30 psi) was connected to the back pressure chamber to replicate the aortic pressure ranging from 80 of 120 mmHg. A resistance clamp was used to control ventricular pressure ranging from -40 to 130 mmHg. Both the aortic and ventricular pressure ranges were selected based on the previous *in vitro* aortic flow and pressure conditions used by Simon *et al*. for the purpose of comparison with the LDV study (Simon, 2004).

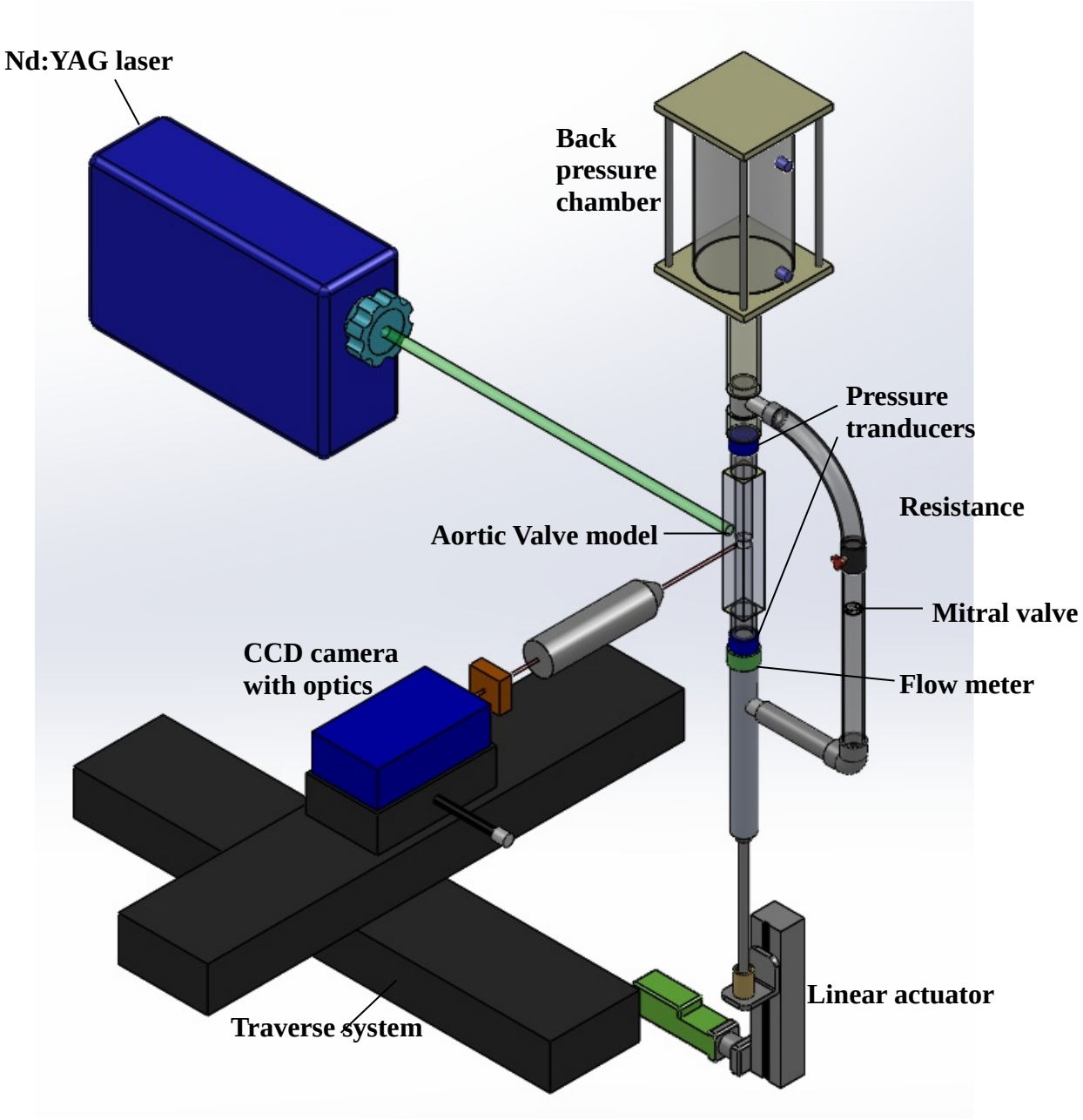

Figure 5.6: Schematic of pulsatile flow experimental setup.

5.4.2 Trigger setup

In order to synchronize the hemodynamic measurements as well as the PIV data acquisition with the motion of the piston, the FCT software was programmed to output a triggering signal at the start of the piston motion. The frequency of this signal was 1.161 Hz, which is equivalent to the frequency of a beating normal heart (cardiac cycle time of 860ms). A detailed instruction of trigger setup in the FCT software and trigger signals recorded during the experiments can be found in Appendix B-3.

5.4.3 Experimental conditions

In pulsatile flow measurements, 200 PIV image pairs and 100 PIV image pairs were obtained at 24 time points throughout the cardiac cycle for FLAT and other (195μm, 390μm, and 585μm) measurement planes, respectively. A larger number of image pairs were acquired at the FLAT plane for the purpose of statistical analysis using an ensemble averaging. The other measurement planes, at deeper hinge levels and a smaller cross-sectional area, experienced poor seeding density. In these cases, ensemble correlation was used to calculate the average flow field (Jun, 2013). The time spacing for both steady and pulsatile flow experiments were determined for each condition per location, such that the average particle displacement was about 16 pixels between pulses (Kean, 1992). Table 5.4 below represents the pulse separation used at each time point during the cardiac cycle.

Table 5.4: Pulse separation (μs) setting for the pulsatile flow experiments

	AORTIC				CENTER				VENTRICULAR			
Time (ms)	0μm	195 μm	390 μm	585 μm	0 μm	195 μm	390 μm	585 μm	0μm	195 μm	390 μm	585 μm
0	**50**	**50**	**50**	**50**	**50**	**50**	**50**	**50**	**20**	**50**	**50**	**50**
40	**50**	**50**	**50**	**50**	**50**	**50**	**50**	**50**	**20**	**50**	**50**	**50**
80	**50**	**50**	**50**	**50**	**50**	**50**	**50**	**50**	**20**	**50**	**50**	**50**
120	**200**	**200**	**100**	**200**	**40**	**200**	**50**	**50**	**20**	**100**	**50**	**50**
160	**1000**	**1000**	**400**	**600**	**400**	**400**	**150**	**450**	**150**	**400**	**250**	**800**
200	**900**	**900**	**800**	**900**	**1000**	**1200**	**800**	**1400**	**1000**	**1200**	**1500**	**1600**
240	**250**	**250**	**250**	**250**	**400**	**800**	**300**	**400**	**400**	**800**	**400**	**400**
280	**20**	**20**	**20**	**20**	**20**	**50**	**20**	**20**	**20**	**20**	**20**	**20**
300	**20**	**20**	**20**	**20**	**20**	**50**	**15**	**15**	**20**	**20**	**20**	**20**
320	**20**	**20**	**20**	**20**	**20**	**30**	**15**	**15**	**20**	**20**	**20**	**20**
340	**20**	**20**	**20**	**20**	**20**	**20**	**15**	**15**	**20**	**20**	**20**	**20**
360	**20**	**20**	**20**	**20**	**20**	**20**	**15**	**15**	**20**	**20**	**20**	**20**
380	**20**	**20**	**20**	**20**	**20**	**20**	**15**	**15**	**20**	**20**	**20**	**20**
400	**20**	**20**	**20**	**20**	**20**	**20**	**15**	**15**	**20**	**20**	**20**	**20**
420	**20**	**20**	**20**	**20**	**20**	**20**	**15**	**15**	**20**	**20**	**20**	**20**
440	**20**	**20**	**20**	**20**	**20**	**20**	**15**	**15**	**20**	**20**	**20**	**20**
460	**20**	**20**	**20**	**20**	**20**	**30**	**20**	**20**	**20**	**20**	**20**	**20**
480	**20**	**20**	**20**	**20**	**20**	**30**	**20**	**20**	**20**	**20**	**20**	**20**
520	**20**	**20**	**20**	**20**	**20**	**30**	**20**	**20**	**20**	**20**	**20**	**20**
560	**20**	**20**	**20**	**20**	**20**	**25**	**20**	**20**	**20**	**20**	**20**	**20**
600	**20**	**20**	**20**	**20**	**20**	**25**	**20**	**20**	**20**	**20**	**20**	**20**
640	**20**	**20**	**20**	**20**	**20**	**25**	**20**	**20**	**20**	**20**	**20**	**20**
680	**20**	**20**	**20**	**20**	**20**	**25**	**20**	**20**	**20**	**20**	**20**	**20**
720	**20**	**20**	**20**	**20**	**20**	**20**	**20**	**20**	**20**	**20**	**20**	**20**
760	**20**	**20**	**20**	**20**	**20**	**20**	**20**	**20**	**20**	**20**	**20**	**20**
800	**20**	**20**	**20**	**20**	**30**	**20**	**20**	**20**	**20**	**20**	**20**	**20**
840	**250**	**250**	**250**	**250**	**400**	**300**	**150**	**450**	**240**	**400**	**180**	**450**
860	**150**	**150**	**150**	**150**	**100**	**150**	**150**	**100**	**50**	**150**	**180**	**100**

5.4.4 Data acquisition steps

The following summarizes the pulsatile flow data acquisition procedure:

1. Position the camera to view the ventricular section of the hinge at the FLAT plane
2. In DaVis 7.2, verify the trigger rate of 1.161Hz
3. In DaVis 7.2, enter values for the time point (0ms) and the corresponding pulse separation as indicated on Table 5.4.
4. Acquire image pairs under experimental conditions explained in section 5.4.3 in DaVis 7.2 as well as real-time aortic flow and pressure waveforms from the custom LabView program.
5. Enter the next time point and the corresponding pulse separation as indicated on Table 5.4.
6. Repeat steps 4-5 until data acquisition for the entire cardiac cycle is completed.
7. Position the camera at the 195µm plane.
8. Repeat steps 3-6.
9. Position the camera at the 390µm plane.
10. Repeat steps 3-6.
11. Position the camera at the 585µm plane.
12. Repeat steps 3-6
13. Position the camera to view the center section of the hinge at the FLAT plane.
14. Repeat steps 3-12.
15. Position the camera to view the aortic section of the hinge at the FLAT plane.
16. Repeat steps 3-12.

5.5 Data Processing

The images were processed using DaVis 7.2, with a chosen interrogation window of 64 × 64 pixels in size and 50 percent overlap between subsequent windows. This resulted in 64 μm vector spacing. Figure 5.7 shows a representative raw PIV image with seeding particles visible in the center section of the hinge region prior to the data processing.

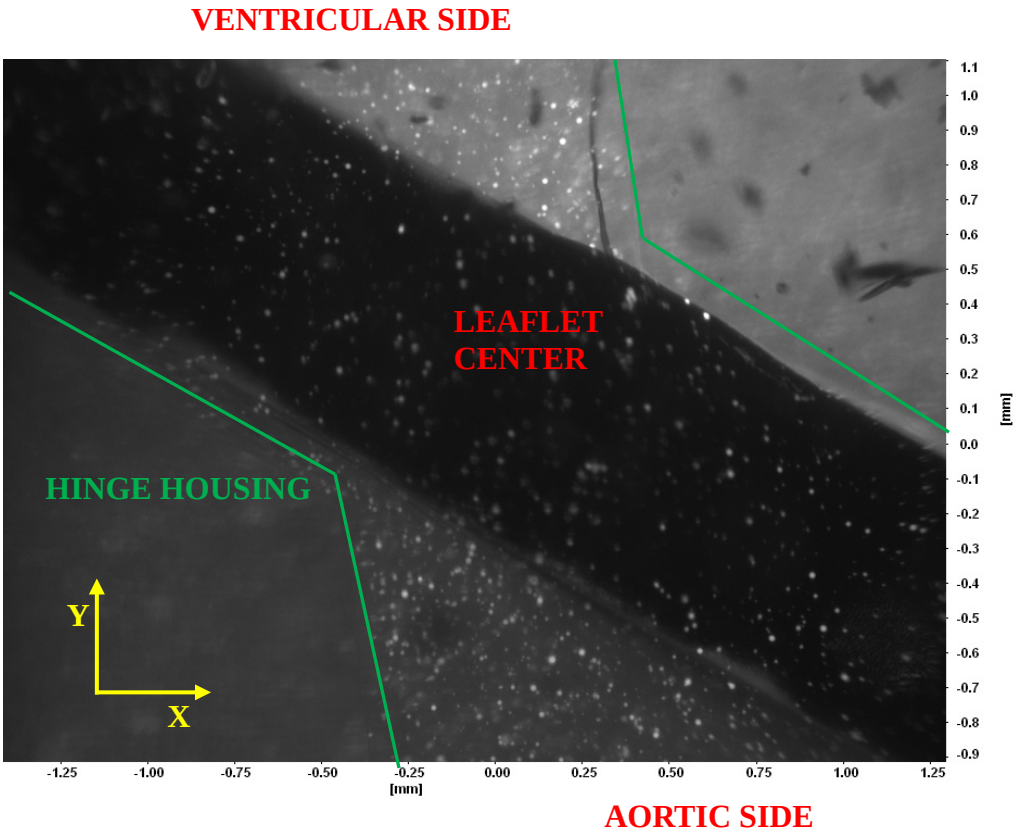

Figure 5.7: Raw PIV image at the center location in the hinge with seeding particles visible on the leaflet surface and ventricular and aortic corners. Fluorescent particles illuminate light from the laser beam.

Images were pre-processed using a sliding background subtraction filter and masking to eliminate defocused particles and background illumination during the PIV cross-correlation. Detailed instructions on image pre-processing in DaVis 7.2 can be found in Appendix B-4.

.

Ensemble averaging and ensemble correlation methods were used in this study to represent the dominant flow features in the flow fields. In conventional PIV studies, a large number of processed vector fields are ensemble averaged to identify the dominant flow structures (Manning, 2003; Bellofiore, 2011, Saikrishnan, 2013). Alternatively, this µPIV study computed a single vector field from the summed-up correlation planes using an ensemble correlation technique. Ensemble correlation is particularly advantageous for µPIV studies because seeding density is poor. This method detects the peak correlation after averaging all instantaneous cross correlation functions, thereby minimizing the number of erroneous measurements (Meinhart, 2000).

Equations 5.1 to 5.3 represent the algorithm used to compute ensemble averaging in image pairs.

$$C(x_0, y_0) = I_1(t_1, x_0, y_0) \otimes I_2(t_2, x_0, y_0) \quad \text{Equation 5.1}$$

where I_1 and I_2 represent the image interrogation windows at two different times t_1 and t_2. C refers to the correlation plane at image position x_o and y_o. The maximum correlation peak represents to the most likely displacement of the particle ensemble in the interrogation window, as indicated on equation 5.2.

$$V(x_0, y_0) = Position\ of\ highest\ peak\ in\ C(x_0, y_0) \quad \text{Equation 5.2}$$

where vector V refers to the displacement vector (Vx, Vy) at image position. Equations 5.1 and 5.2 indicate the cross-correlation of a single pair of interrogation windows which computes a single displacement vector V (Figure 5.8).

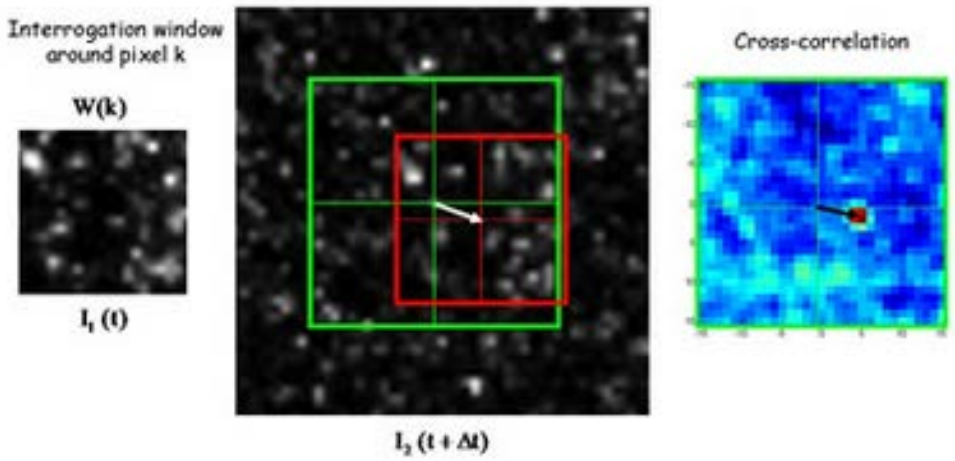

Figure 5.8: Illustration of cross-correlation between two images at t and t+Δt (ONERA, 2011)

Accordingly, all vectors are combined to create a whole two-dimensional vector field of the image. Equation 5.3 represents the ensemble averaging technique where vector fields are locally averaged from a large number of acquired image pairs to compute an average 2D vector field.

$$V_{avg}(x_0, y_0) = \frac{\sum V(x_0, y_0)}{n} \qquad \text{Equation 5.3}$$

where n refers to the number of images acquired.

In contrast, the ensemble-correlation algorithm computes the average displacement for a sequence of images. Equation 5.4 below represents the correlation plane using the cross-correlation of the individual interrogation windows from the image i.

$$C_i(x_0, y_0) = I_1(t_1, x_0, y_0) \otimes I_2(t_2, x_0, y_0) \qquad \text{Equation 5.4}$$

Subsequently, all correlation planes computed from a sequence of images are summed up to lead to a single ensemble of correlation planes as represented in equation 5.5.

$$C_{avg}(x_0, y_0) = \sum C_i(x_0, y_0) \qquad \text{Equation 5.5}$$

Finally, a single vector field is computed from all the summed-up correlation planes (Figure 5.9).

$$V_{avg}(x_0, y_0) = Position\ of\ highest\ peak\ in\ C_{avg}(x_0, y_0) \qquad \text{Equation 5.6}$$

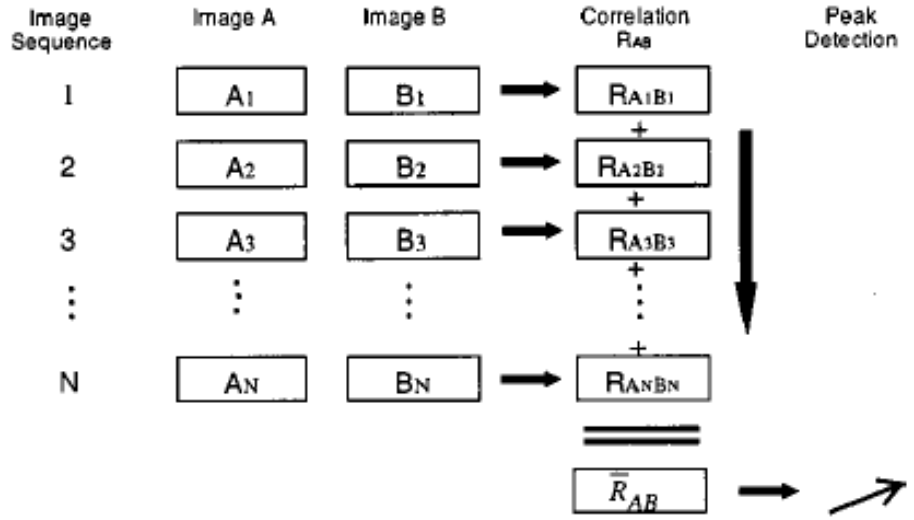

Figure 5.9: Illustration of ensemble correlation method (Meinhart, 2000)

Details of the theories on standard cross-correlation and ensemble correlation can be found in other studies (Raffel, 2007; Wereley, 2010). In this study, the standard ensemble averaging technique was only used for images acquired at the FLAT plane of the BMHV hinges under pulsatile flow conditions, enabling the calculation of apparent Reynolds shear stress (RSS_{app}).

The vector fields were post-processed with a median filter to remove erroneous vectors and recursive interpolation was used to fill-up empty spaces in the vector field. In the PIV system erroneous vectors typically originate from interrogation windows exhibiting insufficient seeding particle density, which appear with unexpected velocity magnitude and direction relative to the neighboring vectors (Westerweel, 2005). These erroneous vectors are detected and removed during the post-processing step based on threshold values set for the correlation peak ratio factor (Q) and median filter. Q refers to the ratio between the height of the first and the second correlation peak. In this study, Q > 1.3 was used, which allowed for elimination of spurious

vectors calculated from the weak correlation peak. The median filter allows for rejection of a vector when it is outside the defined deviation range of the neighboring vectors (RMS > 1.5).

Lastly, the flow fields acquired at three locations in the hinge were superimposed on the corresponding raw PIV images of the hinge using Tecplot (Tecplot Inc, Bellevue, WA, USA) to represent global velocity maps with background images of the leaflet and hinge geometry. Detailed instructions on this step can be found in Appendix B-5.

5.6 Uncertainty Analysis

5.6.1 Uncertainty of velocity measurements

In PIV systems, the total uncertainty can be described as a sum of bias and precision errors (Raffel, 2007). In the current μPIV system, precision errors for estimating repeatability cannot be quantified due to the use of ensemble correlation, where only a single vector field was computed from summed up correlation planes (Meinhart, 2000). Bias errors can be caused by experimental limitations, including sensor artifacts and pixel displacement gradients.

An uncertainty analysis was performed to estimate bias errors in the current μPIV system following the error analysis conducted by Cooper *et al.* (Cooper, 2008). The velocity uncertainty can be calculated by dividing the smallest measurable distance by the pulse separation (Δt) during the data acquisition. The highest resolution used in this system was 1.97 μm/pixel, and the smallest displacement can be quantified as 0.1-0.2 times the resolution, due to sub-pixel interpolation during the PIV processing.

5.6.2 Steady Flow Experiments

Table 5.5 represents uncertainties in velocity measurements at each location of acquisition, where the maximum value was 0.00985 m/s (0.3% of maximum velocity of 3.2m/s). Subsequently, uncertainty in velocity gradients can be calculated following the error propagation analysis suggested by Kline and McClintock (Kline, 1953). The uncertainty in VSS was calculated to be 2.47 N/m^2, which is proportional to the velocity uncertainty divided by the in-plane spatial resolution of 64μm.

Table 5.5: Uncertainty of velocity measurements at each location in the hinge.

Measurement plane	dt (in μs)	Velocity Uncertainty (m/s)
FLAT	20 – 100	0.00197 - 0.00985
195μm	20 – 100	0.00197 - 0.00985
390μm	20 - 50	0.00394 - 0.00985

5.6.3 Normalized Median Test

The reliability of velocity vectors obtained from ensemble correlation was evaluated using a normalized median test (Westerweel, 2005). To estimate the maximum possible errors caused by invalid velocity vectors, a flow field location featuring both low flow region and peak velocity jet (390μm plane, ventricular side) was analyzed. Figure 5.10 shows the percent valid vectors as a function of number of image pairs processed, constructed similarly to previous μPIV studies (Meinhart, 2000; Vennemann, 2006). The MATLAB code used for the normalized median test can be found in Appendix B-6.

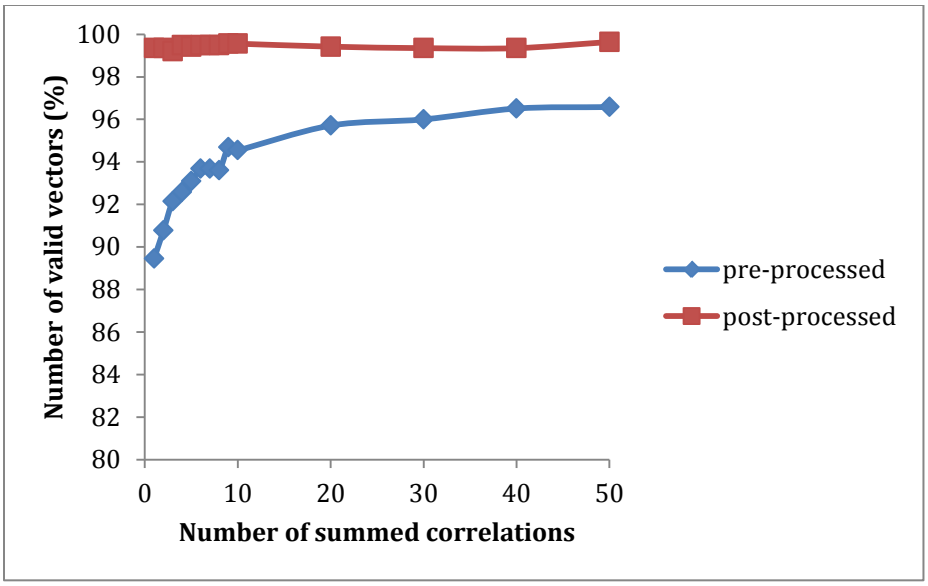

Figure 5.10: Normalized median test at the measurement plane of 390 µm above flat level on the ventricular side, representing a fraction of valid vectors.

The normalized median test showed that the lowest percent of valid vectors from a single post-processed image pair was 99.4%, and by averaging 50 image pairs with ensemble correlation, a validity ratio of 99.6% was reached. The pre-processed image pairs, which were unaffected by median filtering and interpolation in the post-processing steps, were also tested using this method. A single image pair had a validity ratio of 89.5%, and at 50 image pairs a validity ratio of 96.6% was reached. This analysis demonstrated that the final post-processed velocity field across the entire geometry is expected to have a reliability of velocity vectors close to 100%, indicating high fidelity of the data acquired.

5.6.4 Pulsatile Flow Experiments

Table 5.6 represents the range of pulse separation (Δt) during the data acquisition and calculated velocity uncertainty for each measurement plane. The maximum value of velocity uncertainty was 0.0394 m/s. Subsequent uncertainty in velocity gradients can be calculated following the

same analysis conducted from the previous section. The uncertainty in VSS and RSS_{app} was calculated to be 4.94 N/m^2 and 8.45 N/m^2, respectively.

Table 5.6: Uncertainty of velocity measurements at each location in the hinge.

Measurement plane	Cardiac phase	dt (in μs)	Velocity Uncertainty (m/s)
FLAT, 195, 390, and 585μm planes	Diastole	5 - 20	0.0003 – 0.0394
	Systole	200 - 700	

5.6.5 Leaflet Sliding Motion Analysis

The sliding motion was identified by tracking a small region (yellow circle on Figure 5.11) of the leaflet across all cycles during diastole at FLAT plane, and vector fields were classified based on the location of the tracked region with respect to the image. Figure 5.12 below represents two dominant modes of leaflet "resting" with corresponding flow fields. First, it is necessary to toggle through post-processed 200 image pairs from DaVis 7.2 and bin them into two groups of distinct patterns, as illustrated on Figure 5.11. Secondly, all instantaneous velocity vectors (DAT format) should be exported from DaVis 7.2 in order to be processed from MATLAB (Appendix-B6) to obtain the velocity, VSS, and RSS_{app} values within each group. Finally, these fluid dynamic parameters calculated from the two distinct groups were compared to investigate the variations in the hinge flow field due to different resting locations of the leaflet ear.

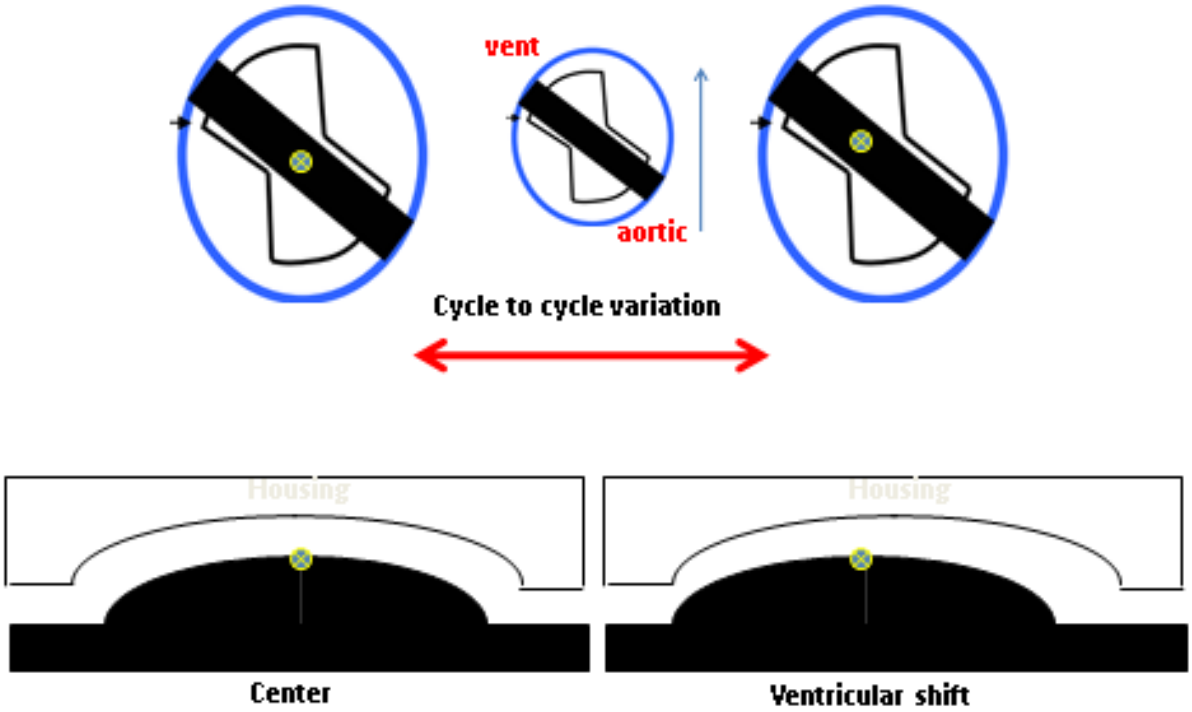

Figure 5.11: BMHV leaflet ear sliding motion during diastole

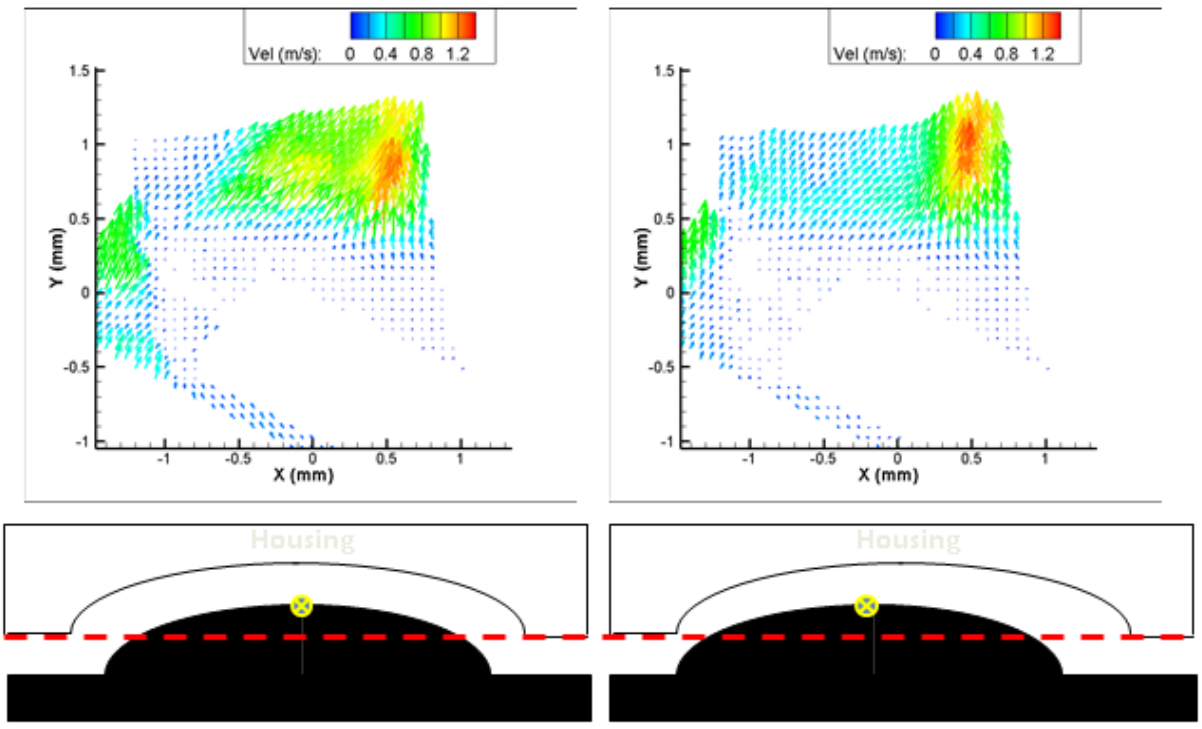

Figure 5.12: Two dominant modes of leaflet resting with corresponding velocity field

5.7 Definitions of Calculated Quantities

The 2D velocity fields presented in this study use the reference system shown in Figure 5.7, where interrogation is in the X-Y plane. The whole field velocity components are U and V in the X and Y directions, respectively.

To evaluate the thromboembolic potential of flow within the BMHV hinge, velocity magnitude ($\text{Vel} = \sqrt{U^2 + V^2}$), maximum velocity ($\text{Vel}_{\text{peak}}$), viscous shear stress (VSS) and apparent Reynolds shear stress (RSS_{app}) were quantified from 2D PIV measurements. In areas of flow stasis (Vel <0.03 m/s), activated platelets can endure a longer residence time, accelerating thromboembolism. Alternatively, a high velocity jet (Vel >1 m/s) can potentially cause shear stress to blood elements above threshold values, resulting in hemolysis and platelet activation (Simon, 2004; Leo, 2005; Yun, 2012).

The VSS indicates the shearing between adjacent layers of fluid, which can be used as a metric to assess the loading experienced by the fluid on blood cells transitioning through the hinge region. The in-plane VSS can be defined as:

$$VSS = \mu\left(\frac{\partial U}{\partial Y} + \frac{\partial V}{\partial X}\right) \qquad \text{Equation 5.7}$$

Reynolds shear stress (RSS) indicates the average momentum flux due to the fluctuating velocity component, representing turbulent stress which could initiate the process of platelet activation and hemolysis in artificial heart valves (Sallam and Hwang, 1984; Lu, 2001).

The in-plane RSS is defined as:

$$RSS = \rho\sqrt{\left(\frac{\overline{u'u'} - \overline{v'v'}}{2}\right)^2 + \left(\overline{u'v'}\right)^2} \qquad \text{Equation 5.8}$$

where u' and v' represent instantaneous velocity fluctuation in the X and Y direction, respectively. However, it must be noted that the RSS computed from the measured velocity fluctuations in this study is not a true representation of the rigorous definition of Reynolds stress arising due to turbulent velocity fluctuations. The cycle-to-cycle velocity fluctuations measured in this study are a result of variations in the flow, pressure, and leaflet dynamics in addition to the turbulent velocity fluctuations. Consequently, the RSS computed using equation 5.8 is referred to as an apparent Reynolds shear stress (RSS_{app}).

5.8 Important Considerations for µPIV Experiments

5.8.1 Seeding particle density

The biggest challenge when conducting Micro-PIV experiments in the BMHV hinges is a poor seeding particle density. To yield a good PIV signal, both seeding particle density and illumination strength must be sufficient, as represented in Figure 5.7. The current study used fluorescent polymer particles with a diameter ranging from 1 to 20 µm, which was an optimal choice considering the experimental limitations described in section 4.4.6. It is recommended that the fluid volume used in both steady and pulsatile flow experiments should be minimized (< 600mL). The fluid volume used has a significant effect on the quality of a µPIV data due to the particle seeding density required to get high fidelity vectors. The amount of tracer particle solution used in the current study was less than 0.5 mL, to ensure adequate particle seeding in the hinge region without excessive particle aggregation or saturation.

5.8.2 Air bubbles in the flow loop

In a steady or pulsatile flow loop setups with mechanical heart valves, existence of air bubbles prevent acquisition of high quality PIV images by blocking or altering the flow paths of tracer particles. Therefore, it is an important step to ensure the elimination of air bubbles before acquiring PIV images. In this study both the steady and pulsatile flow loops were oriented vertically, which helped rising air bubbles to the surface of a fluid. Nevertheless, several different approaches are available to eliminate air bubbles from the region of interest. For example, during the steady flow experiments, a high compliance tube was installed upstream of the clear housing valve chamber, which was squeezed manually by hand to induce sweeping motion of leaflets to wash out the hinge region. This was useful for preventing any clogging in the hinge region by small air bubbles or lumped particles that may exist in the loop. In pulsatile flow experiments, the minimum and maximum fluid levels during the piston motion was maintained within the tube section located upstream of the back pressure chamber (Figure 5.6). This prevents introducing air bubbles in the loop when fluid convects across the loop section with a sudden contraction or expansion. Furthermore, it was always helpful to let the flow loop run for about 10 minutes prior to the PIV acquisition to flush out the small or large air bubbles that may exist in the system.

5.8.3 Evaluation of preliminary results

In both steady and pulsatile flow experiments it is extremely important to test-process the acquired image pair during an initial stage of the PIV acquisition. An imaging artifacts or a blockage in the hinge region could influence the velocity field. Therefore, two precautionary steps were taken to prevent encountering problems which could affect the velocity magnitude in the hinge region. Firstly, prior to the experiment the BMHV model was visually assessed to

verify that hinge recess and leaflet ears are clear and undamaged. Secondly, a static leakage test described in section 5.2 was conducted to verify that an adequate amount of leakage volume is flowing through the valve hinges. A static leakage volume for several BMHV models was reported from Simon et al and Leo et al. (Simon, 2004; Leo, 2005). This test method allows identification of any external factors such as acrylic deformation or a damaged leaflet ear, which will directly affect the velocity magnitude in the hinge region.

CHAPTER 6

RESULTS

6.1 Static Leakage Test

To ensure that an expected amount of leakage volume was flowing through the valve hinges, a static leakage flow rate was measured from the three SJM valves prior to the μPIV experiment. A 1.5 m vertical column filled with water-glycerin solution was used to impose a static pressure head of 120 mmHg on the aortic side of the valve. Subsequently, the leakage volume was measured over one minute for each valve and repeated five times to calculate the average leakage flow rate. The SJM Regent, HLP, Standard and LLP valves had static leakage flow rates of 440±20 mL, 490±25 mL, 450±14 mL and 51±6 mL, respectively. The leakage flow rate increased with hinge gap width. These measured flow rates were very close to the static leakage rates measured in previous studies [Simon, 2004; Leo, 2005].

6.2 Steady Flow Results

6.2.1 Pressure measurements

Figure 6.1 shows the transvalvular pressure measurement during the time of Micro Particle Image Velocimetry (μPIV) data acquisition. Table 6.1 reports the mean and standard deviation of this measurement. To ensure adequate μPIV particle seeding density, an in-line flow meter was not used in the loop setup for minimizing the volume of the blood analog as much as possible. The flow across the valve occurs primarily through the four hinges and the B-datum line of leaflets during the leakage flow phase, resulting in a flow rate of less than 0.5 L/min [Simon,

2004] under a transvalvular pressure of 120 mmHg. This experiment controlled the transvalvular pressure such that it mimics diastolic leakage flow.

Table 6.1: Mean pressure and standard deviation for steady flow experiments

Conditions (sampling rate = 1 kHz)	Mean (mmHg)	Standard deviation (mmHg)
ΔP at 80 mmHg	80.606	0.214
ΔP at 120 mmHg	120.431	0.505

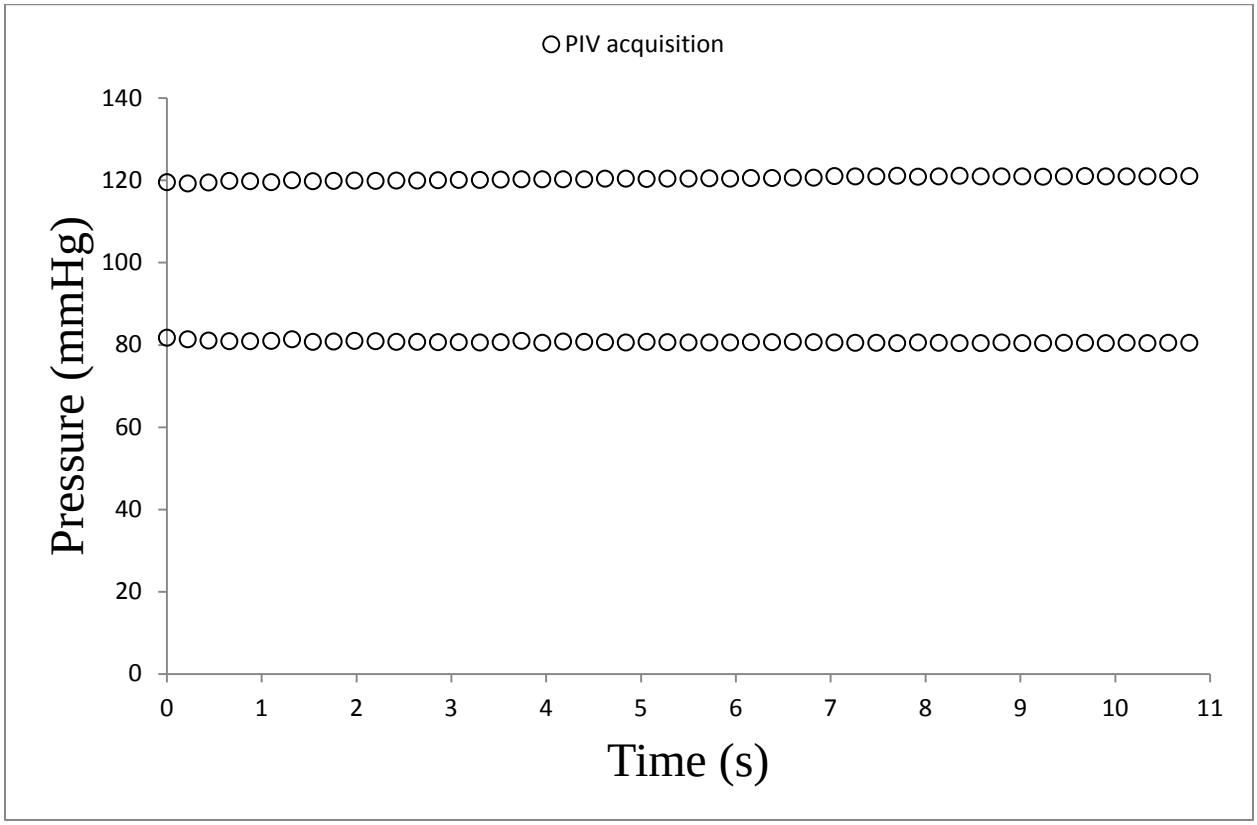

Figure 6.1: Pressure measurements during the PIV acquisition.

6.2.2 Velocity Vector Fields

The nomenclature used in the results section can be found in Chapter 4: Equipment and Materials and Chapter 5: Experimental Protocol. Figures 6.2 and 6.3 represent the global velocity

fields in the hinge collected from the aortic, center and ventricular sections with a representative PIV raw image of the hinge used as a background to display the location of the leaflet. Table 6.2 presents the values of V_{peak} at all planes for the two dP conditions.

Table 6.2: V_{peak} (in m/s) from ensemble correlation of 50 image pairs.

	FLAT plane	**195µm** plane	**390µm** plane	**585µm** plane
dP = 80mmHg	1.47	2.73	2.68	2.69
dP = 120mmHg	2.62	3.21	3.24	3.11

6.2.2.1 FLAT plane

Figures 6.2-a and 6.3-a represent the leakage velocity fields inside the hinge region in the FLAT plane at dP = 80 mmHg and dP = 120 mmHg, respectively. At dP = 80 mmHg, a reverse flow entered from the arc of the hinge housing between the aortic and lateral corners. This incoming flow exhibited a low velocity magnitude ranging from 0.03 to 0.05 m/s. Here, the velocity was lower near the lateral corner, as flow collided with the leaflet ear and diverged away from the aortic corner. The rest of the incoming flow near the aortic corner continued to flow towards the narrow gap between the leaflet and sharp corner of the hinge recess located in the center region, where velocity reached 0.88 m/s at the smallest gap.

In the adjacent corner, a high velocity jet was observed ranging from 1 to 1.47 m/s (V_{peak}), following the path along the arc of the housing. This sharp increase in velocity was likely caused by particles exiting from the smaller flow domain in the adjacent corner between the leaflet ear and hinge housing.

In the ventricular corner near the center region, the flow velocity was lowest, ranging from 0 to 0.03 m/s. The leaflet ear obstructing the reverse flow entering from the aortic corner likely

caused this low flow region. Increased flow velocity of up to 0.37 m/s was observed near the ventricular corner as a high velocity jet from the adjacent corner continued to flow towards this location. At higher transvalvular pressure (dP = 120 mmHg) as represented in Figure 6.3-a, qualitatively similar flow with increased velocity magnitude was observed at all locations of the hinge. The most significant increases in velocity were observed near the adjacent and ventricular corners, where the velocity magnitude rose from 1.23 to 2.62 m/s (V_{peak}) and 0.86 to 1.67 m/s, respectively.

6.2.2.2 195 μm plane

In the 195 μm plane (Figure 6.2-b and Figure 6.3-b), qualitatively similar flow fields were observed with a slight reduction in the flow area as the two-dimensional plane was located deeper into the hinge recess. In the top section of the hinge where reverse flow entered at dP = 80 mmHg, flow divergence towards the lateral corner was more apparent than at the FLAT level as obstruction from the leaflet ear was smaller. Low flow (0.03 m/s) was observed near the aortic corner and gradually increased up to 0.32 m/s and 0.21 m/s as particles flowed towards the lateral corner and narrow gap near the center region, respectively.

In the adjacent corner, a jet with velocity magnitude ranging from 1.08 to 2.73 m/s occurred and continued to flow along the arc of the housing directed towards the ventricular corner. Similar to the FLAT plane, a low flow region with velocity magnitude ranging from 0.01 to 0.03 m/s was observed near the ventricular corner closer to the center of the hinge, due to the obstruction from the leaflet ear. At dP = 120 mmHg, a qualitatively similar flow field was observed with increased velocity magnitude up to 3.21 m/s (V_{peak}) at the adjacent corner.

6.2.2.3 390 μm plane

The flow field inside the hinge in the 390 μm plane appeared different than the other two lower measurement planes (Figure 6.2-c and 6.3-c), due to the smaller cross-sectional area and velocity vectors resolved from particles flowing over the leaflet ear. Further reduction in the flow field was observed at the aortic and ventricular side of the hinge. For the reverse flow at the aortic side, velocity magnitude gradually increased from 0.03 m/s to 0.65 m/s (dP = 80 mmHg) and 0.83 m/s (dP = 120 mmHg) as flow approached the narrower center region of the hinge. This reverse flow at the aortic corner convected over the leaflet ear towards the ventricular side, where velocity magnitude continued to increase from 1.66 m/s to 2.02 m/s.

The location of V_{peak} in the hinge was at the ventricular side near the center, which was different from lower measurement planes. On the ventricular side, V_{peak} = 2.68 m/s (dP = 80 mmHg) and 3.24 m/s (dP = 120 mmHg). The low flow region in the hinge was also observed from the ventricular side closer to the center but the area was smaller than the lower measurement planes, as particles flowed across the leaflet ear.

6.2.2.4 585μm plane

This measurement plane was the deepest inside the hinge recess (Figure 6.2-d and 6.3-d). As expected, reduction in the hinge flow region was greatest compared to other measurement planes. The velocity magnitude appeared similar to the 390 μm plane, but the orientation of the velocity jet was more uniform towards the ventricular corner. On the aortic side, reverse flow entered the flow domain with ~0.11 m/s, then gradually increased as flow passed through the narrower gap near the center region directed towards the ventricular corner. The highest velocity

jet was located near the center in the ventricular side, which was similar to the 390 μm plane, where V_{peak} = 2.69 m/s (dP = 80 mmHg) and 3.11 m/s (dP = 120 mmHg).

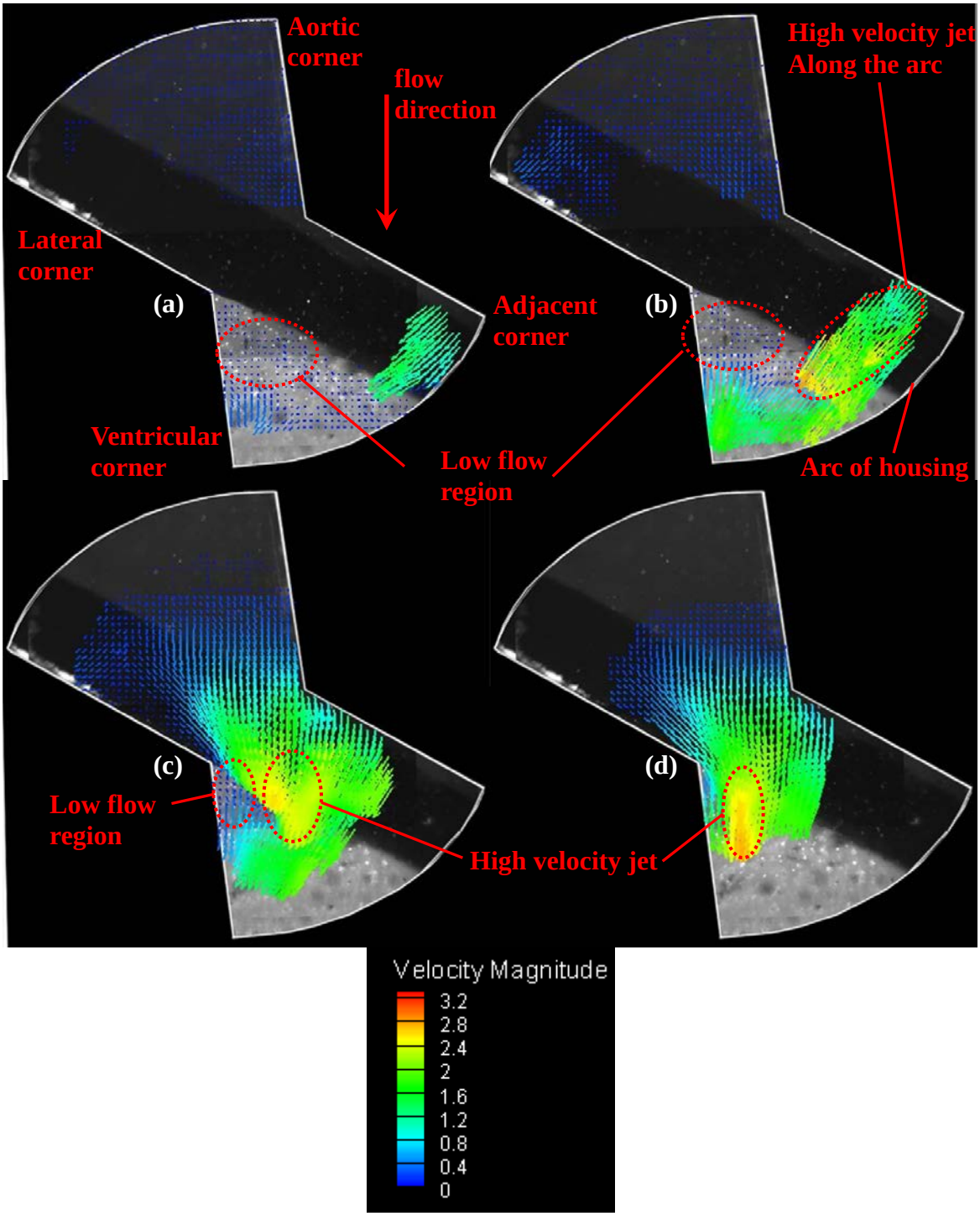

Figure 6.2: Global velocity map in the hinge at transvalvular pressure of 80 mmHg. Measurement plane at (a) flat level, (b) 195 μm above flat level, (c) 390 μm above flat level, (d) 585 μm above flat level.

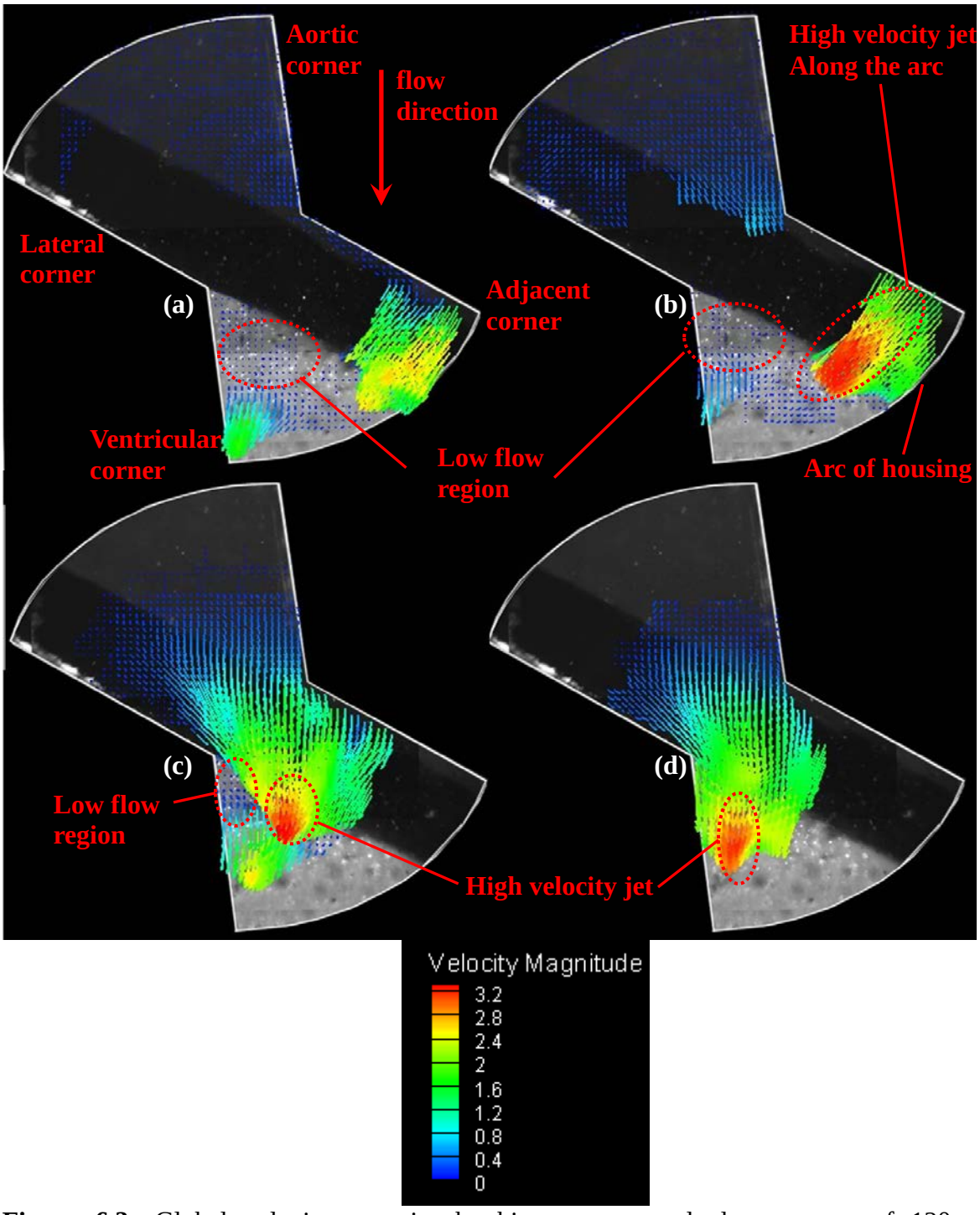

Figure 6.3: Global velocity map in the hinge at transvalvular pressure of 120 mmHg. Measurement plane at (a) flat level, (b) 195 μm above flat level, (c) 390 μm above flat level, (d) 585 μm above flat level.

6.2.2.5 Reynolds number

The dimensionless Reynolds number of the hinge flow was estimated using the following equation:

$$Re = \frac{\rho \cdot V \cdot D}{\mu}$$

where V (m/s) is the peak velocity observed in the hinge, D (m) is the length scale which is equivalent to the hinge gap width of 100μm, ρ (kg/m^3) is the density of the working medium and μ (m^2/s) is the kinematic viscosity of the working medium. Using the observed peak velocities, hinge gap width and kinematic viscosity of the working medium, the peak Reynolds number for the 23mm SJM BMHV was 78 and 93 at dP = 80 mmHg and 120 mmHg, respectively.

6.2.3 Viscous Shear Stress Fields

Figure 6.4 and 6.5 represent the VSS fields at each dP condition across all measurement planes. At the FLAT plane under dP = 80 mmHg (Figure 6.4-a), VSS values ranged from 0.07 to 0.48 N/m^2 near the aortic corner where reverse flow entered through the hinge. This gradually increased up to 7.21 N/m^2 near the leaflet and wall of the hinge housing closer to the center region as flow was passing through the narrower gap. In the adjacent corner of the hinge, regions of maximum VSS value (~55 N/m^2) correlated with the edge of the jet, as expected. The next highest region of VSS (~23 N/m^2) was at the intersection between the ventricular corner jet and low flow region. The VSS plots for the FLAT plane at dP = 120 mmHg (Figure 6.5-a) and 195 μm plane for all conditions (Figure 6.4-b and 6.5-b) were very similar to those of the FLAT level, with larger regions of high velocity gradient (VSS > 50 N/m^2) at the adjacent and ventricular corners due to the increased V_{peak} and jet area. The maximum VSS value remained close to ~60 N/m^2 for each plot.

At 390 µm (Figure 6.4-c, dP = 80 mmHg), the highest VSS (~60 N/m^2) was observed along the edge of the jet located near the center region represented in blue, directed towards the ventricular corner from both dP = 80 mmHg and 120 mmHg. This blue velocity gradient line represents the intersection between the low flow region and the high velocity jet (V > 1 m/s), which was expected to experience the highest level of VSS. A similar VSS plot can be seen at dP = 120 mmHg (Figure 6.5-c) as well, with more noticeable high VSS regions near the center of the leaflet, due to the increased velocity magnitude at this condition. At the 585 µm plane (Figure 6.4-d and 6.5-d), the highest VSS was observed near the edge of the jet, similar to the 390 µm plane.

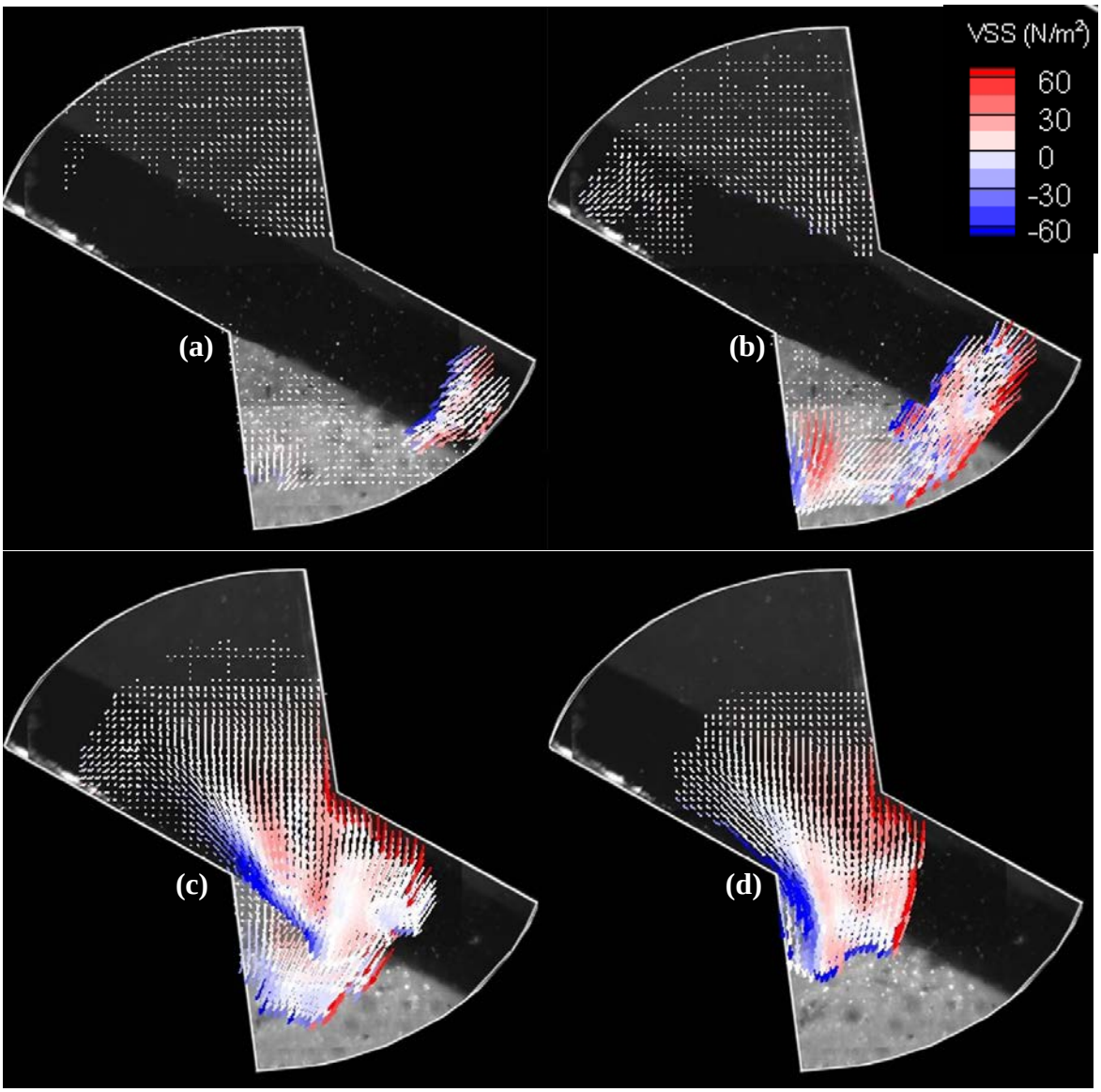

Figure 6.4: Viscous shear stress fields in the hinge at transvalvular pressure of 80 mmHg. Measurement plane at (a) flat level, (b) 195 μm above flat level, (c) 390 μm above flat level, (d) 585 μm above flat level.

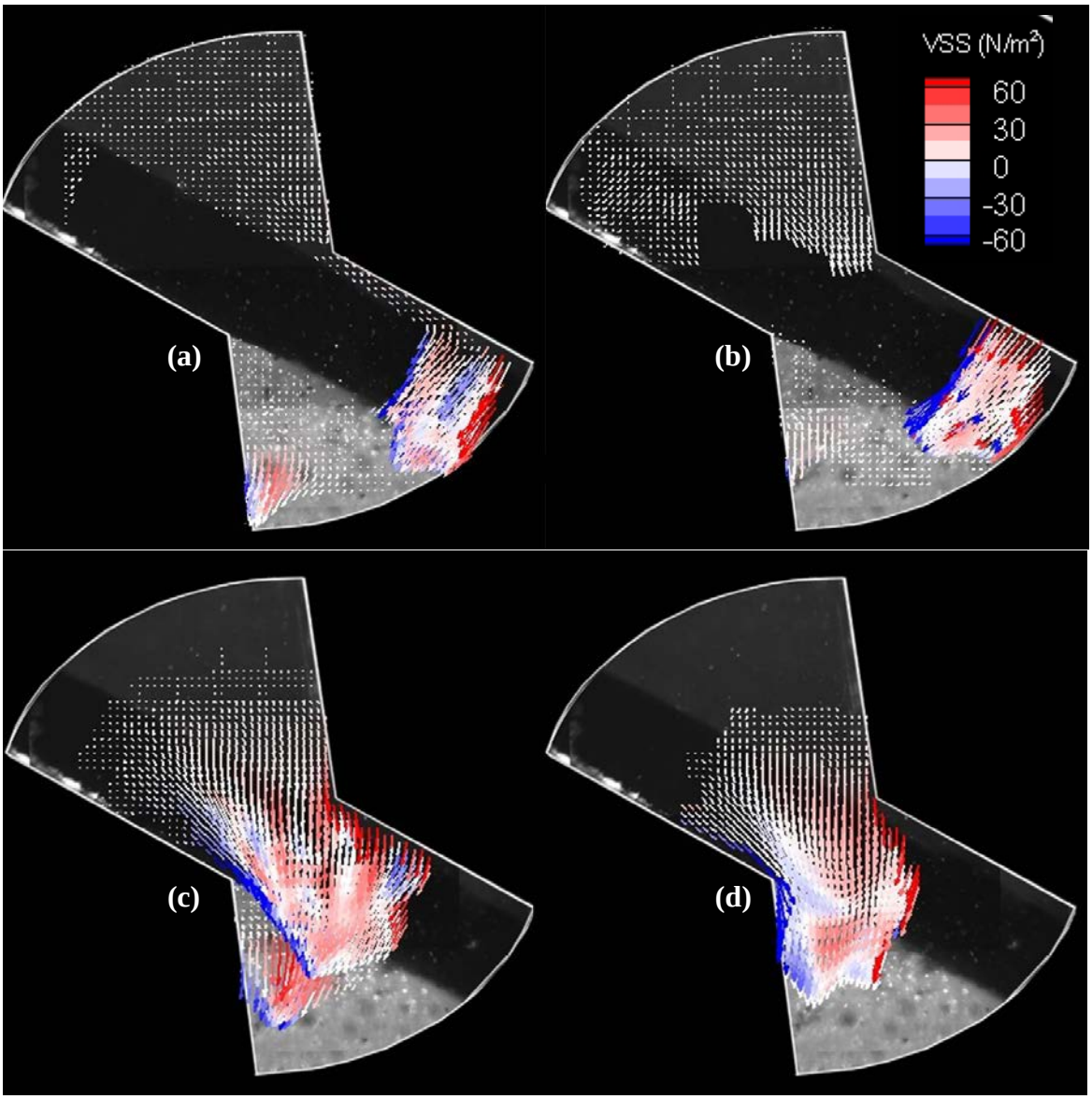

Figure 6.5: Viscous shear stress fields in the hinge at transvalvular pressure of 120 mmHg. Measurement plane at (a) flat level, (b) 195 μm above flat level, (c) 390 μm above flat level, (d) 585 μm above flat level.

6.3 Pulsatile Flow Results

6.3.1 Hemodynamics

Pressure and flow waveforms obtained from the three BMHV models under pulsatile aortic conditions are shown in Figure 6.6. Compliance and resistance elements were tuned such that the cardiac output, ventricular, and aortic pressure waveforms were comparable across the three valve models. The magnitude of diastolic leakage flow rate increased with respect to the hinge gap width, as described in section 6.1.

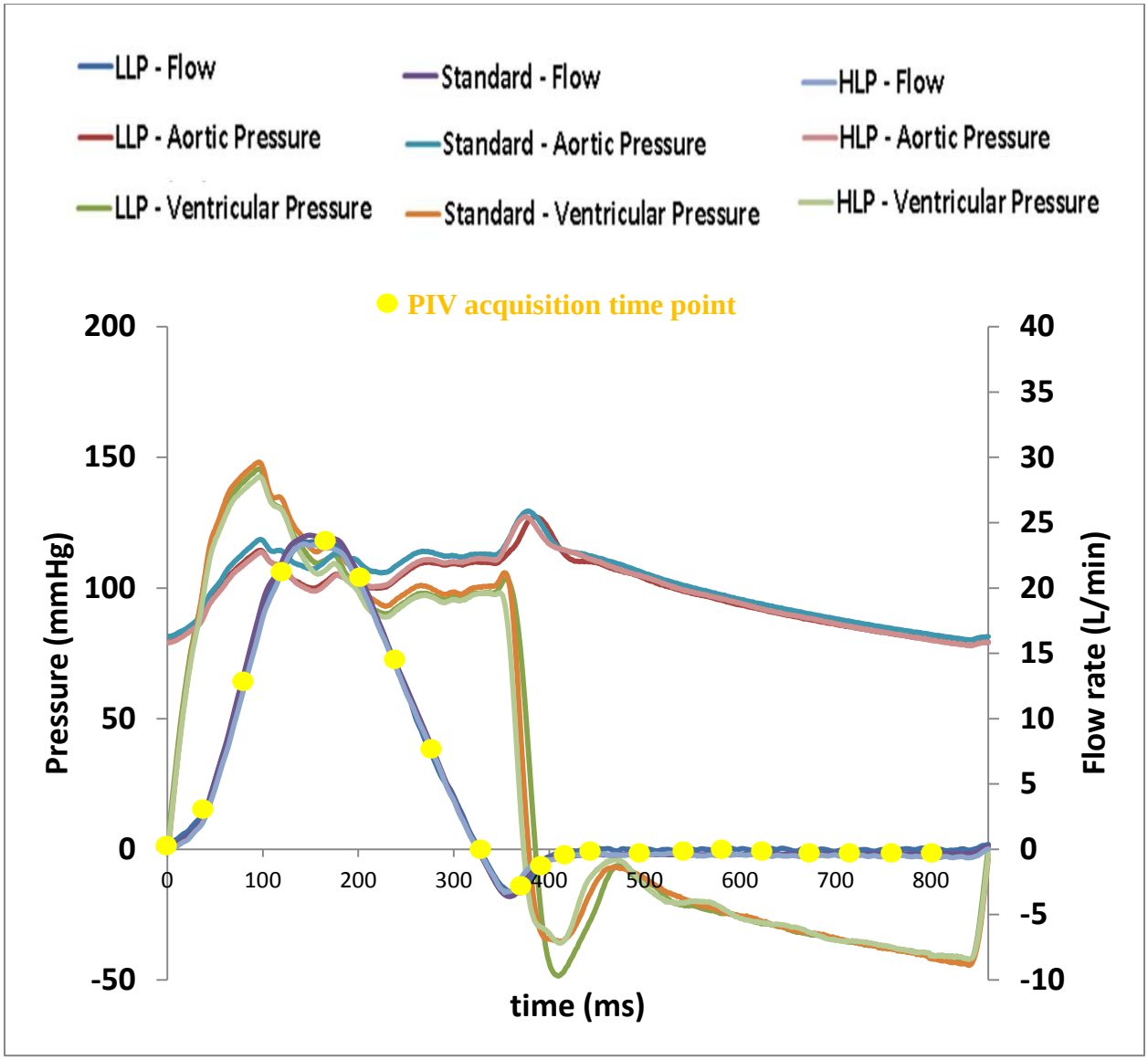

Figure 6.6: Aortic flow and pressure waveforms from the three valve types

6.3.2 Pulsatile flow features of Standard valve

Animations (AVI format) of the velocity flow fields obtained within the SJM hinge region are given in appendix C. During the beginning of systole at 120ms, an increase in forward flow velocity (Vel ~0.5m/s) was seen at the FLAT plane. A recirculating flow structure was observed from the lateral and adjacent corners closer to the leaflet center, as was an onset of strong forward flow with fully opened leaflets at the FLAT plane. Recirculating flow from the lateral corner transitioned to a jet directed towards the aortic side at 160 ms. Peak forward flow was reached at 200 ms, where a coherent jet (Vel_{peak} = 1.08 m/s) and recirculating flow (Vel_{peak} = 1.0 m/s) was seen at the lateral and adjacent corners, respectively (Fig. 6.7b). Flow fields from 280 to 360ms showed low velocity (Vel < 0.1m/s) across the hinge domain without any coherent recirculation zones. Leaflets were fully closed at 380 ms at the end of systole. Similar flow fields were observed during systole at the 195 µm plane, with lower velocity magnitude (Vel_{peak} = 0.5m/s at peak systole) and weaker velocity jets and recirculation zones. Subsequently, the 390µm and 585 µm planes showed flow stasis (Vel < 0.01m/s) across the hinge domain during systole.

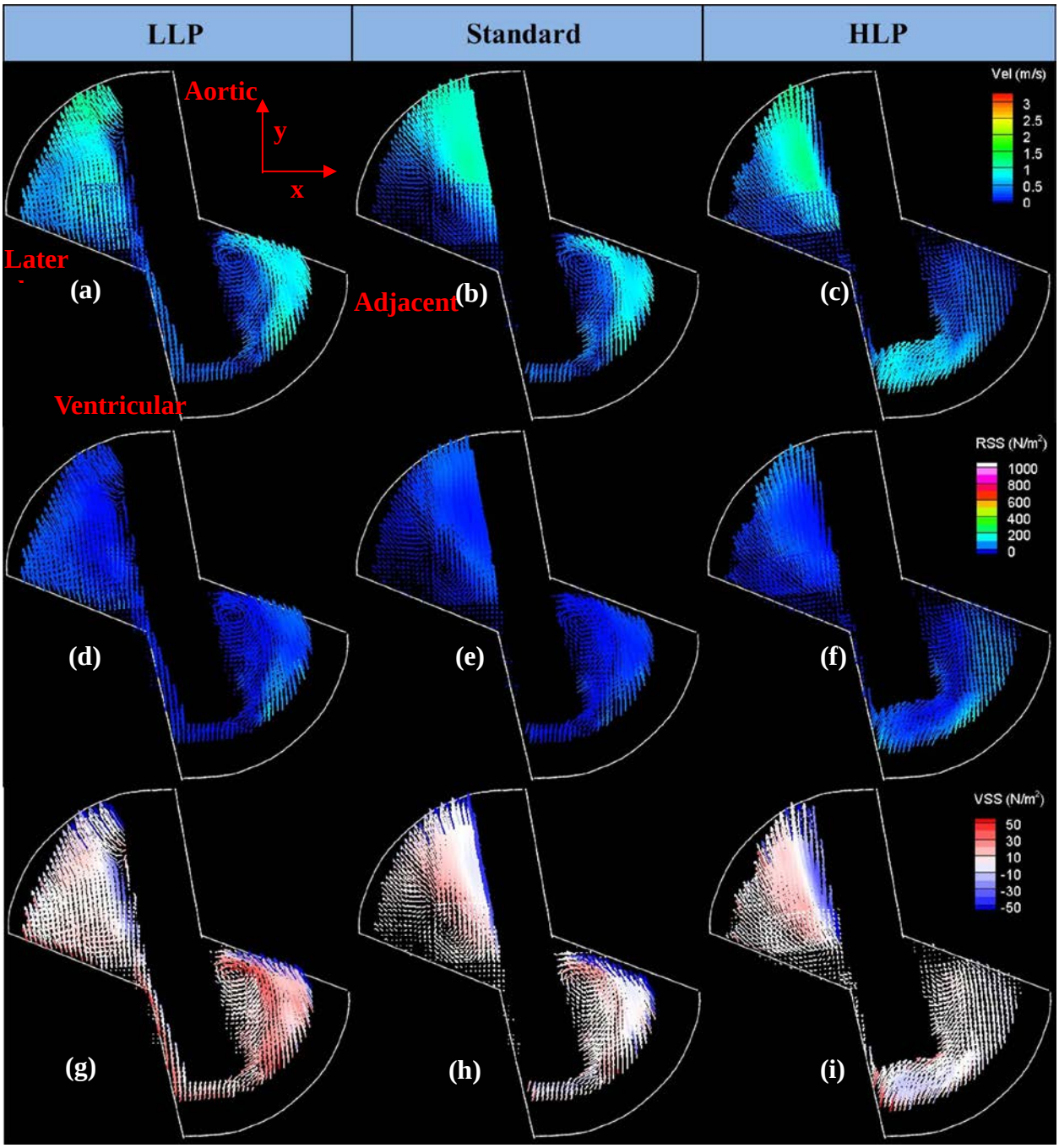

Figure 6.7: Ensemble averaged flow fields acquired from PIV for the three valves (FLAT plane) at the peak systolic phase. Velocity field from (a) LLP, (b) Standard, and (c) HLP. Apparent Reynolds shear stress field from (d) LLP, (e) Standard, and (f) HLP. Viscous shear stress field from (g) LLP, (h) Standard, and (i) HLP

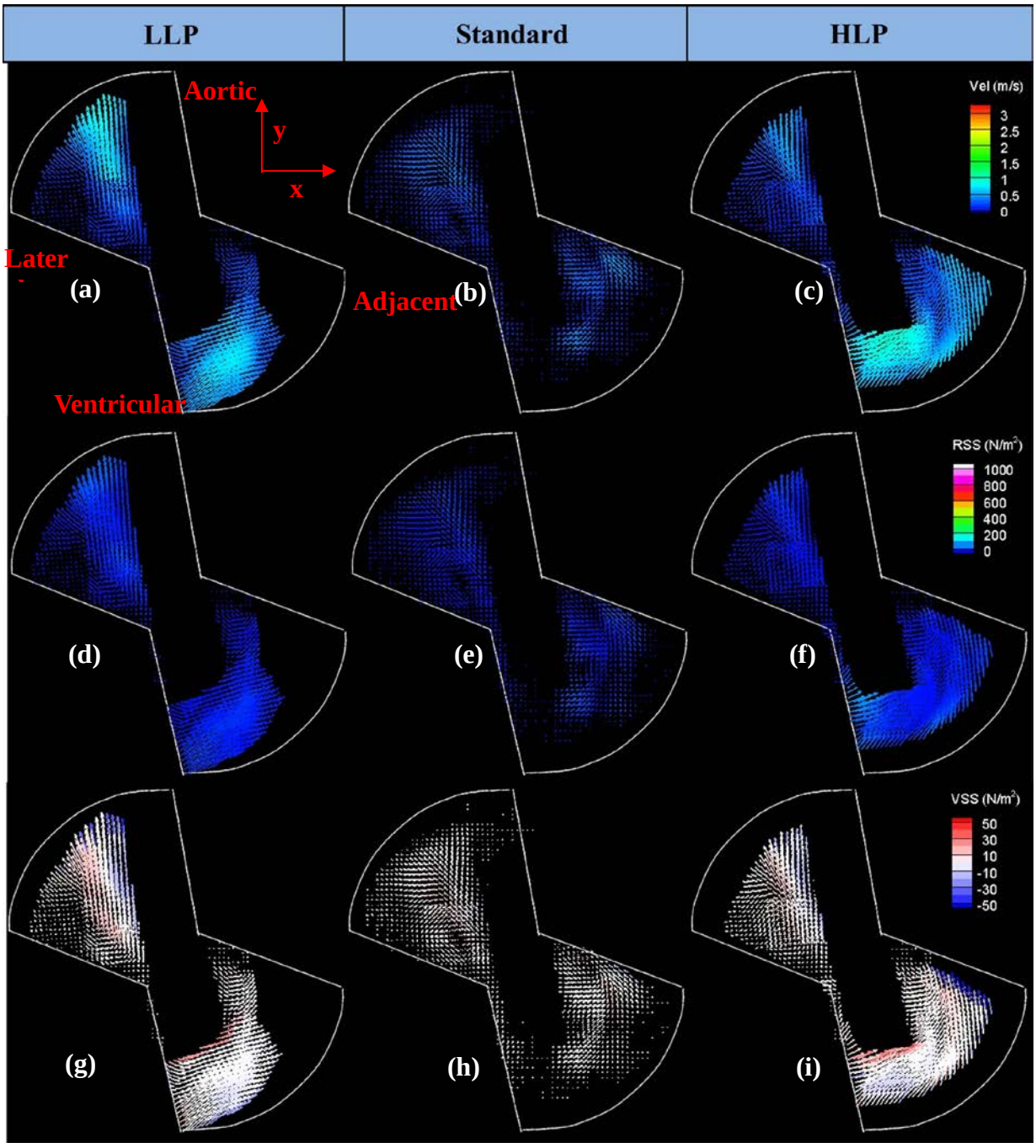

Figure 6.8: Ensemble averaged flow fields acquired from PIV for the three valves (195µm plane) at the peak systolic phase. Velocity field from (a) LLP, (b) Standard, and (c) HLP. Apparent Reynolds shear stress field from (d) LLP, (e) Standard, and (f) HLP. Viscous shear stress field from (g) LLP, (h) Standard, and (i) HLP

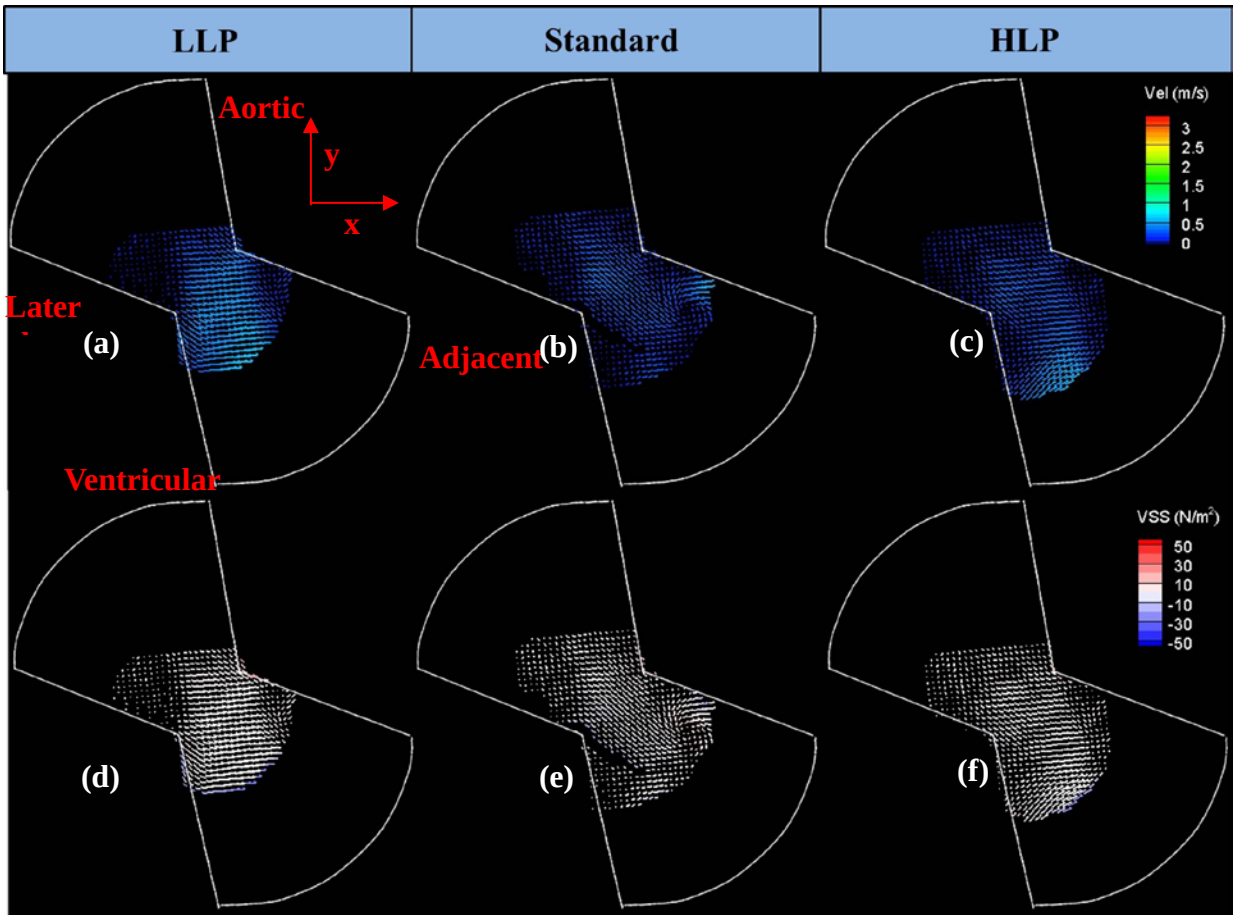

Figure 6.9: Ensemble-correlation averaged flow fields acquired from PIV for the three valves (390µm plane) at the peak systolic phase. Velocity field from (a) LLP, (b) Standard, and (c) HLP. Viscous shear stress field from (d) LLP, (e) Standard, and (f) HLP.

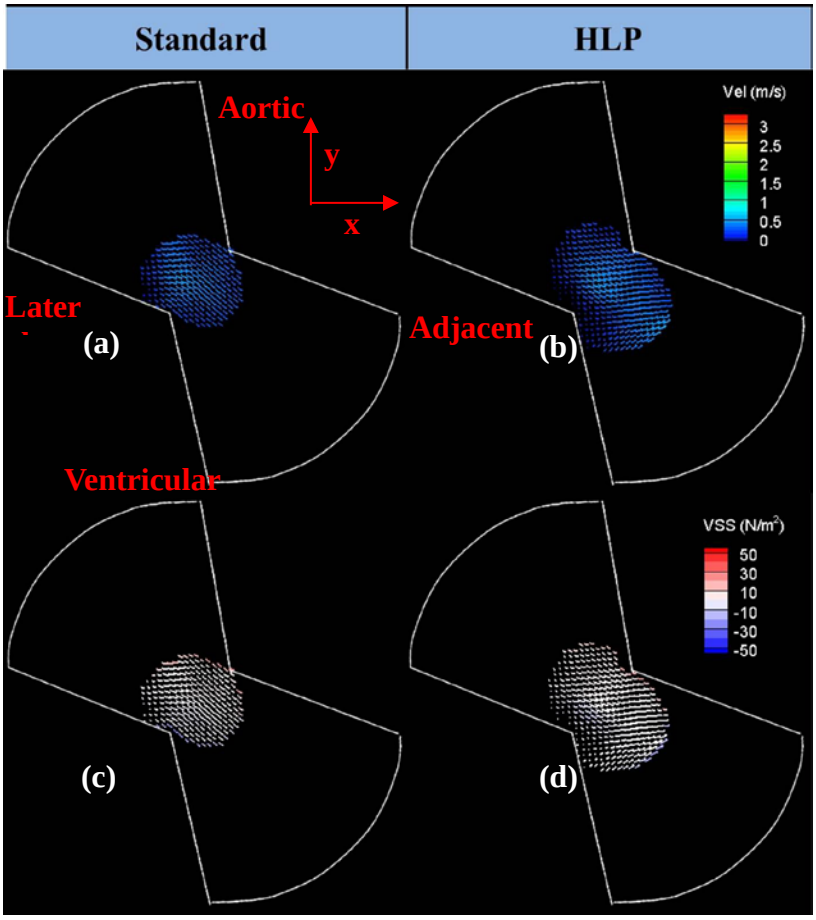

Figure 6.10: Ensemble-correlation averaged flow fields acquired from PIV for the three valves (585µm plane) at the peak-systolic phase. Velocity field from (a) Standard, and (b) HLP. Viscous shear stress field from (c) Standard, and (d) HLP.

The diastolic phase began at 380 ms with fully closed leaflets with low velocity (Vel < 0.1m/s) across all measurement planes. A sharp increase in transvalvular pressure gradient results in reversal of flow. A significant increase in velocity (Vel_{peak} > 3 m/s) for the leakage flow fields was observed at 420 ms across all measurement planes. The transvalvular pressure gradient reached a maximum value (150 mmHg) at this time point, and then gradually decreased to 120 mmHg at 480 ms, at which it remained until the end of diastole. Leakage flow fields at the mid-diastolic phase across all measurement planes (Fig. 6.11 – 6.14) looked very similar to the steady leakage flow fields presented by Jun *et al.* (2013). Lower measurement planes showed a high velocity jet (Vel > 1m/s) along the arc of the housing from the adjacent and ventricular corners

with presence of a low flow region near the leaflet center on the ventricular side. From the aortic corner, incoming flow with a low velocity (Vel < 0.1 m/s) diverged towards the lateral corner with increased velocity (Vel~0.8m/s) as the leaflet ear was obstructing the incoming flow. In the upper measurement planes which are deeper into the hinge recess, incoming flow from the aortic side convected across the leaflet ear and accelerated as particles passed through the narrow gap of the hinge.

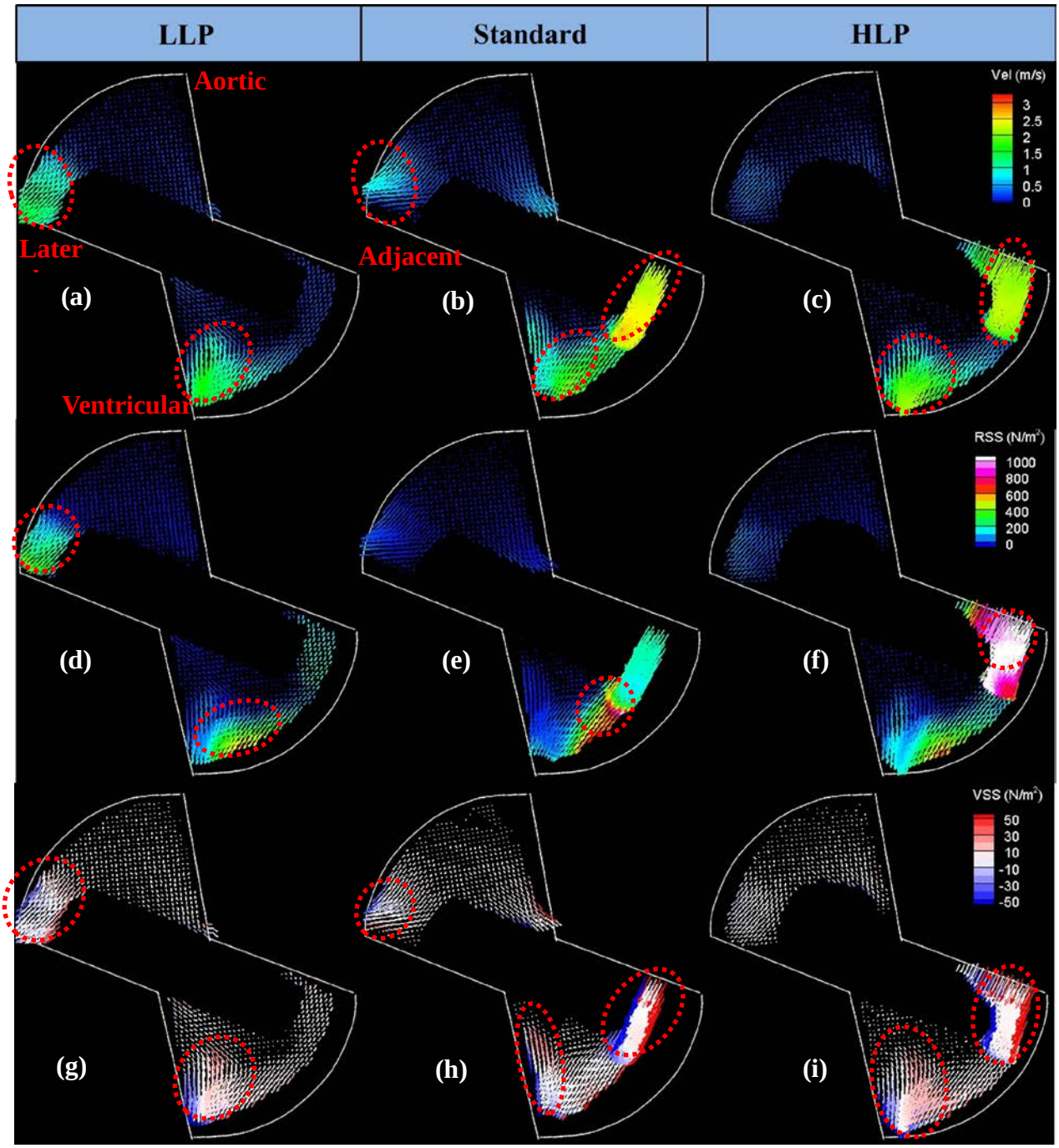

Figure 6.11: Ensemble averaged flow fields acquired from PIV for the three valves (FLAT plane) at the mid-diastolic phase. Velocity field from (a) LLP, (b) Standard, and (c) HLP. Apparent Reynolds shear stress field from (d) LLP, (e) Standard, and (f) HLP. Viscous shear stress field from (g) LLP, (h) Standard, and (i) HLP

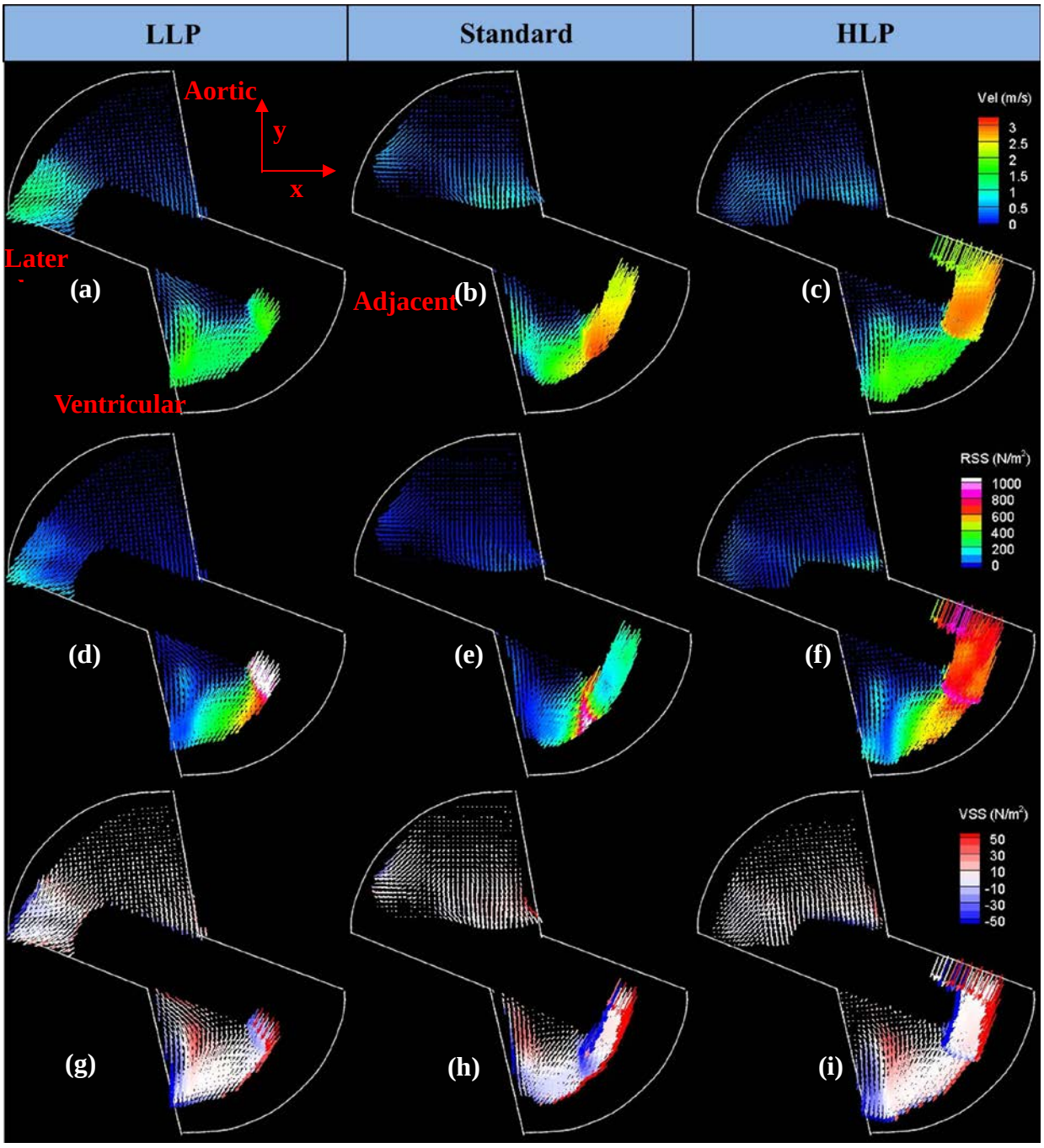

Figure 6.12: Ensemble averaged flow fields acquired from PIV for the three valves (195µm plane) at the mid-diastolic phase. Velocity field from (a) LLP, (b) Standard, and (c) HLP. Apparent Reynolds shear stress field from (d) LLP, (e) Standard, and (f) HLP. Viscous shear stress field from (g) LLP, (h) Standard, and (i) HLP

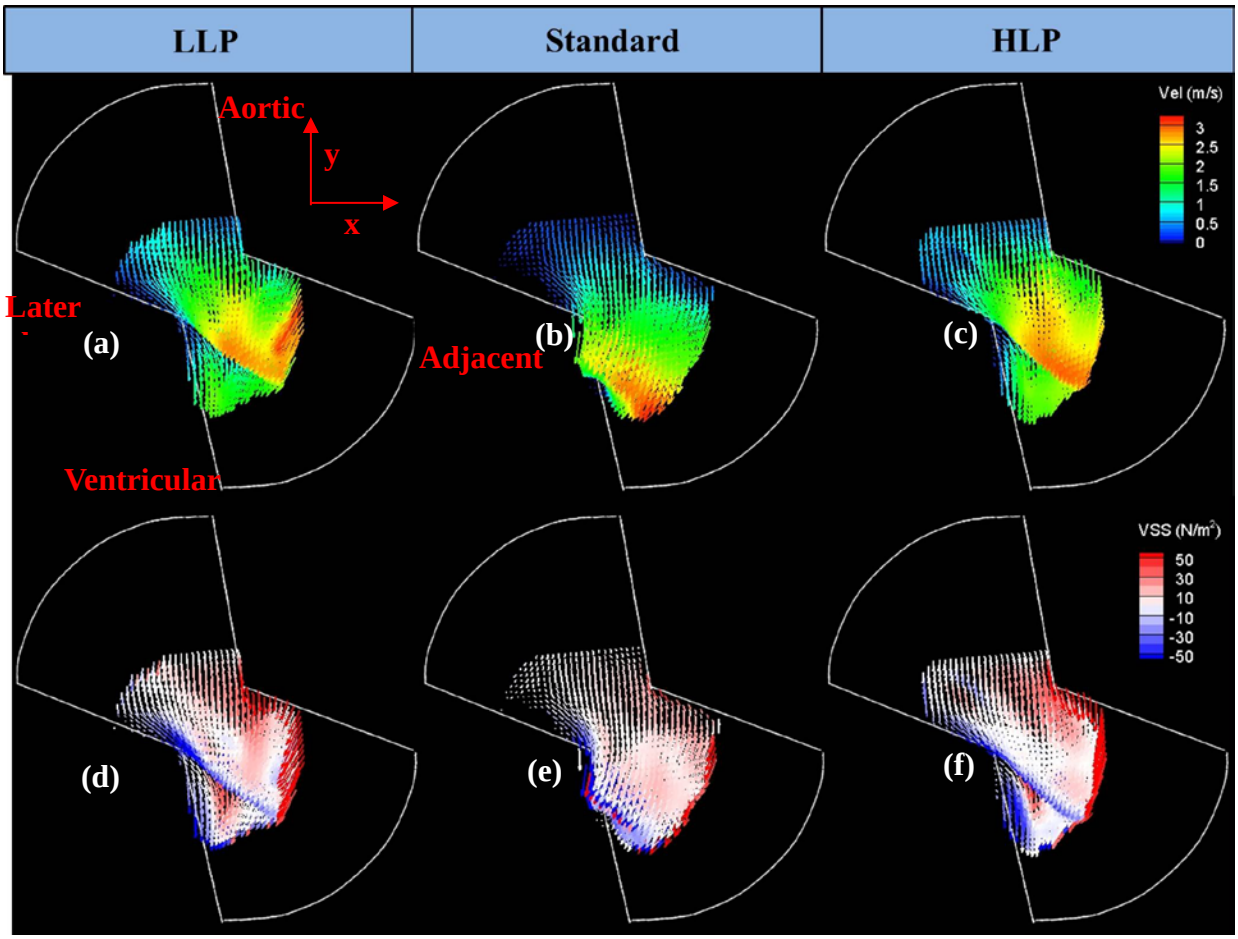

Figure 6.13: Ensemble-correlation averaged flow fields acquired from PIV for the three valves (390µm plane) at the mid-diastolic phase. Velocity field from (a) LLP, (b) Standard, and (c) HLP. Viscous shear stress field from (d) LLP, (e) Standard, and (f) HLP.

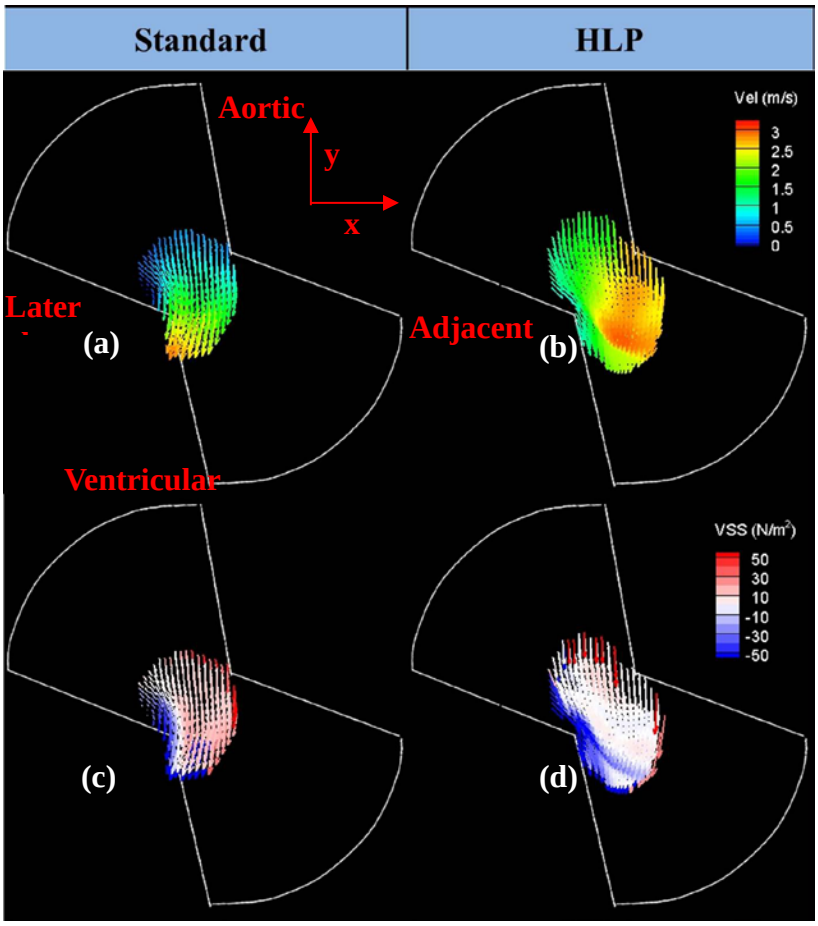

Figure 6.14: Ensemble-correlation averaged flow fields acquired from PIV for the three valves (585µm plane) at the mid-diastolic phase. Velocity field from (a) Standard, and (b) HLP. Viscous shear stress field from (c) Standard, and (d) HLP.

6.3.3 Velocity comparison of three valve models

6.3.3.1 Systole

All three valves showed similar flow features across all measurement planes (Table 6.3 and Figure 6.7-a,b,c). In the lower measurement planes (Figures 6.7 and 6.8), recirculating flow and forward flow jet structures built up towards the peak systolic phase (t = 200ms) then gradually dissipated as the leaflets started closing. For all three valves, Vel_{peak} = 1 – 1.2m/s occurred at the FLAT level (t = 200ms), near the leaflet on the lateral side. In the upper measurement planes (Figures 6.9 and 6.10), low flow regions (Vel < 0.3m/s) were present without any coherent jet or

recirculation zones. Overall, no significant qualitative or quantitative differences were observed during systole among three valves.

6.3.3.2 Diastole

The velocity magnitude during diastole was greater than during systole across all measurement planes for the three valves (Table 6.3). Figures 6.11-a,b,c and 6.12-a,b,c compares the velocity fields measured from the HLP, Standard, and LLP valves at the mid-diastolic phase which represents the most dominant leakage flow structure with fully closed leaflets. At the start of reverse flow near the aortic side at the FLAT plane, all three valves showed lateral jets diverging away from the leaflet ear, but with different velocity magnitudes. The LLP valve showed the strongest lateral jet with a maximum velocity magnitude of up to 1.1m/s, the Standard valve jet was weaker (Vel_{peak} = 0.7m/s) and the HLP valve showed the weakest lateral jet (Vel_{peak} < 0.4m/s).

In the ventricular side at FLAT plane, a reverse flow was directed along the arc of the housing exiting towards the ventricular corner, where differences were observed in terms of jet structure and velocity magnitude across the three valves. The HLP and Standard valves showed two coherent jets at the adjacent and ventricular corners, while the LLP valve exhibited a jet structure at the ventricular and lateral corners (Fig. 6.11-a). The peak velocity magnitude of these jets increased with respect to the hinge gap width (Table 6.4) at 195, 390, and 585µm plane. At the 195µm plane, similar trends and jet structures such as the lateral, ventricular and adjacent jets were present with slight reduction in flow area.

Table 6.3: Comparison of the ensemble averaged velocity (Vel), viscous shear stress (VSS), and apparent Reynolds shear stress (RSS_{app}) magnitude ranges for the three valve types at the lateral, adjacent and ventricular jets at the peak systolic and mid-diastolic phases (FLAT level).

		LLP			**Standard**			**HLP**		
		Vel range (m/s)	VSS Range (N/m^2)	RSS_{app} range (N/m^2)	Vel range (m/s)	VSS range (N/m^2)	RSS_{app} range (N/m^2)	Vel range (m/s)	VSS range (N/m^2)	RSS_{app} range (N/m^2)
Forward jets (t=160ms)	Lateral Corner	0.19-1.1	7.3-44	2.0-94	0.15-1.1	4.4-45	1.8-65	0.2-1.2	5.2-40	3.0-110
	Adjacent Corner	0.26-0.98	2.5-35	4.5-152	0.25-0.90	6.5-41	5.9-97	0.23-0.79	5.1-45	2.0-173
Leakage jets (t=600ms)	Lateral Corner	1.1-1.4	6.4-38	226-341	0.42-0.86	0.3-28	4.5-62	0.24-0.34	0.5-2.2	27-88
	Adjacent Corner	0.22-0.37	0.4 - 3.3	125-164	2.35-2.57	10-44	160-938	2.0-2.2	9.2-48	768-1142
	Ventricular Corner	1.2-1.7	9-46	79-429	0.96-1.8	8.2-34	62-327	1.7-2.1	8.0-42	191-419

In the upper measurement planes (Figs. 6.13-6.14), a strong reverse flow with uniform jet structure across the leaflet ear was observed across all three valves. The LLP valve showed flow stasis on the ventricular side near the leaflet ear. This flow stasis region was also observed in the HLP valve, but with a much reduced area.

Table 6.4: Peak phase averaged velocity (m/s) across all measurement planes and RSS_{app} (N/m^2) comparison at the lower measurement planes from the three valve prototypes.

Measurement plane	LLP	Standard	HLP
Flat	**1.67 m/s (430 N/m^2)**	**2.57 m/s (938 N/m^2)**	**2.26 m/s (1142 N/m^2)**
195µm above flat level	**1.77 m/s (885 N/m^2)**	**2.73 m/s (944 N/m^2)**	**2.86 m/s (967 N/m^2)**
390µm above flat level	**2.51 m/s**	**2.52 m/s**	**2.91 m/s**
585µm above flat level	**NA**	**2.70 m/s**	**2.99 m/s**

6.3.4 Shear stress comparison of the three valves

Animations (AVI format) of the shear stress fields obtained within the SJM hinge region are given in appendix C.

6.3.4.1 Systole

The highest shear stress levels during systole were recorded at the peak systolic phase (t = 200 ms) from the three valves at FLAT level based on the observation from the velocity fields. All three valves presented a similar magnitude and distribution for RSS_{app} and VSS surrounding the lateral jet and recirculating flow structure in the adjacent corner (Figure 6.7-d,e,f,g,h,i). Unlike VSS plots, where similar levels of VSS were observed between the lateral jet and recirculation zones, RSS_{app} plots showed about ~100 N/m^2 higher RSS_{app} levels at the recirculation zones in the adjacent corner (Table 6.3). This indicates that VSS due to the velocity gradients was similar at these two pockets, but RSS_{app} was higher in the recirculating flow. Overall, shear stress distribution and magnitude from the three valves did not show significant differences. The

maximum VSS and RSS_{app} levels were around ~40 N/m^2 and ~200 N/m^2, respectively (Table 6.3).

6.3.4.2 Diastole

RSS_{app} levels observed from the three valves in diastole were three or more times greater than at the peak systolic phase, indicating higher RSS_{app} in the leakage flow. Figures 6.11-d,e,f,g,h,i and 6.12-d,e,f,g,h,i represent comparison of the Vel, RSS_{app} and VSS fields at the mid-diastolic phase (lower measurement planes). Table 6.4 compares the maximum RSS_{app} among three valve models. The HLP valve reported the highest RSS_{app} magnitude (~1000 N/m^2) among the three valves at the adjacent corner. The highest RSS_{app} region (~900 N/m^2) for the Standard valve was roughly halfway between the adjacent and ventricular corners. The LLP valve showed highest RSS_{app} magnitude (~400 N/m^2) near the ventricular corner as well as the presence of another high level of RSS_{app} (~300 N/m^2) at the lateral corner, which was not observed in the other valves. Overall, the RSS_{app} magnitudes increased with increasing hinge gap width, and locations of high RSS_{app} varied among the three valves.

All three valves indicated high VSS magnitude (VSS > 30 N/m^2) at the ventricular corner. Additionally, the HLP and Standard valves indicated regions of highest VSS magnitude (~50 N/m^2) near the adjacent corner, which was not present in the LLP valve. In the lateral corner, the VSS level increased with respect to the valve with smaller hinge gap width. Subsequently, the LLP valve indicated VSS magnitudes up to 30 N/m^2 at this region. Accordingly, the high VSS regions were similar between the HLP and Standard valves in terms of magnitude and locations.

The LLP valve reported the lowest VSS magnitude among the three valves, but with an additional high VSS region at the lateral corner.

6.3.5 Leaflet Sliding Motion

In addition to the rotational motion of the leaflets, the mating tolerance between the curved leaflet ear and the hinge recess allows translational motion along radial and axial directions [Leo, 2006; Simon, 2009]. The methodology of analysis of this phenomenon is described in Chapter 5: Experimental Protocol. This section describes the leaflet translation motion and its fluid dynamics effects.

The location of the leaflet ear within the hinge recess at the end of valve closure varies from cycle to cycle. Analysis of velocity vector fields indicated two dominant modes of leaflet positions during diastole of cardiac cycle. Figure 6.15 illustrates this phenomenon where the location of the leaflet ear relative to the hinge housing changed across various cycles during the diastolic phase. The sliding motion was identified by tracking a reference point on the leaflet ear (Standard valve) across all cycles during diastole. The Standard valve had fluorescent particles adhered to the surface of the leaflet adjacent to the sharp corner of the hinge housing that served as the reference location. The adherence of fluorescent particles at the small region can be caused by wearing of a coated leaflet surface due to an excessive use of high powered laser during experiments. Subsequently, changes to a surface roughness at certain regions can potentially trap micron-scale seeding particles. Unlike the Standard valve, HLP and LLP valves showed clean and smooth leaflet ear image with no regions of particle adherence to be tracked, most likely due to lower exposure to high-powered-laser. Therefore, quantitative analysis of the flow field comparison with respect to the leaflet position was possible from PIV images obtained from the

Standard valve. The analysis of the sliding motion for the HLP and LLP valves were conducted based on the binning of distinct patterns in the flow fields that was qualitatively observed.

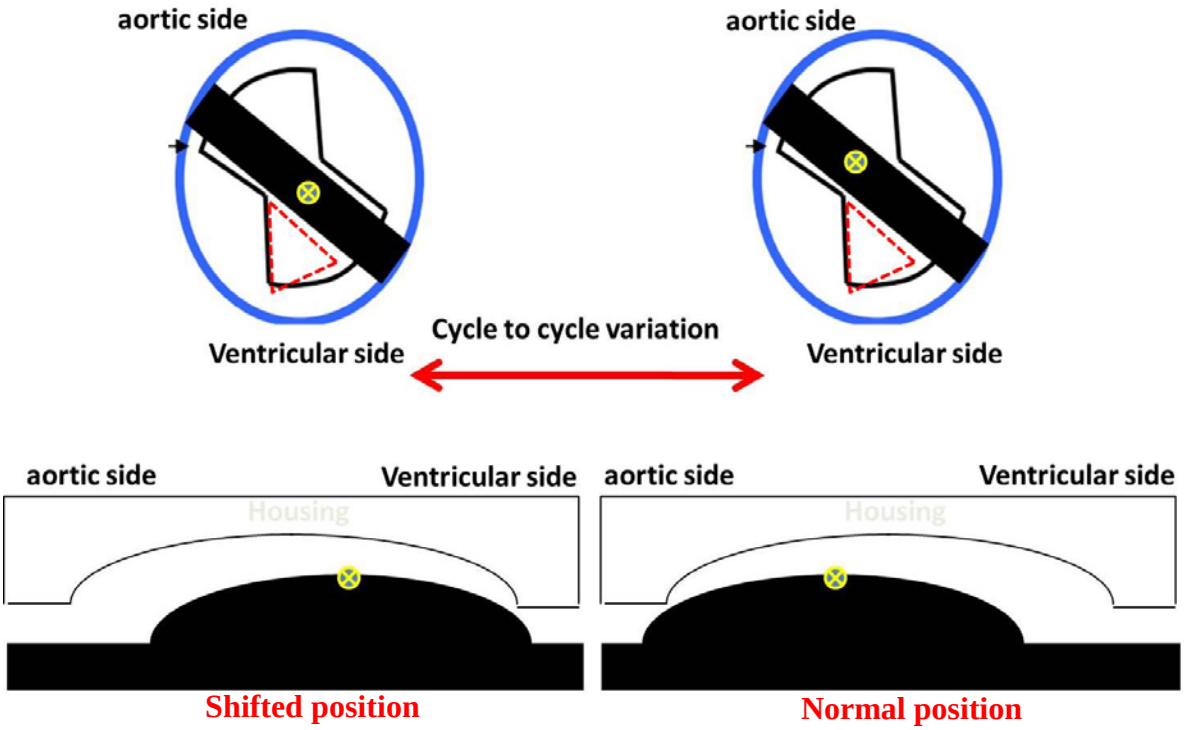

Figure 6.15: Schematic showing the translation motion of the leaflet ear inside a hinge recess

Table 6.5 represents the distribution of this motion throughout the 200 successive instantaneous flow fields at early diastole (420 – 600ms). Transvalvular pressures ranging from 120 – 150 mmHg was experienced across the valve during this phase. The mid to end-diastole phase (640 – 860ms) was not examined since transvalvular pressure during this phase was steady at 120 mmHg (Figure 6.6).

Table 6.5: Frequency of occurrence of sliding positions across 200 flow fields during diastole (Standard)

Sliding position	Time point in cardiac cycle(ms)					
	420	**440**	**480**	**520**	**560**	**600**
Shifted	70	54	72	67	74	68
Normal	130	146	128	133	126	132

The leaflet ear position at aortic side (normal position) was more frequently observed than the ventricular (shifted) position (Figure 6.15 and Table 6.5). It should be noted that the 200 instantaneous flow fields were binned into only two prominent groups by a visual assessment, even though sliding displacement of the leaflet ear in the hinge varied from 0 to 100μm.

Figure 6.16 represents mid-diastolic flow fields (Standard valve at 600ms) with two different jet patterns based on the leaflet position. For the normal position, a high velocity jet along the arc of the housing in the ventricular corner was observed, which was similar to the ensemble-averaged leakage flow fields. For the shifted position, the ventricular jet had a smaller spatial area with vertical orientation. This difference was most likely due to narrowing of the gap width allowing fewer particles to flow through the adjacent corner of the hinge when a leaflet ear was in the shifted position. Figures 6.16-b,c,e,f,h,i show the velocity, RSS_{app} and VSS comparison between two patterns associated with these two positions. There was no noticeable difference in peak RSS_{app} values between normal and shifted position (Figure 6.16-e,f). Similar to the velocity field, the normal position indicated larger region of RSS_{app} greater than 100 N/m^2 than the shifted position. Unlike the velocity and RSS_{app} fields, the VSS fields between two patterns showed negligible qualitative and quantitative differences (Figures 6.16-g,h,i).

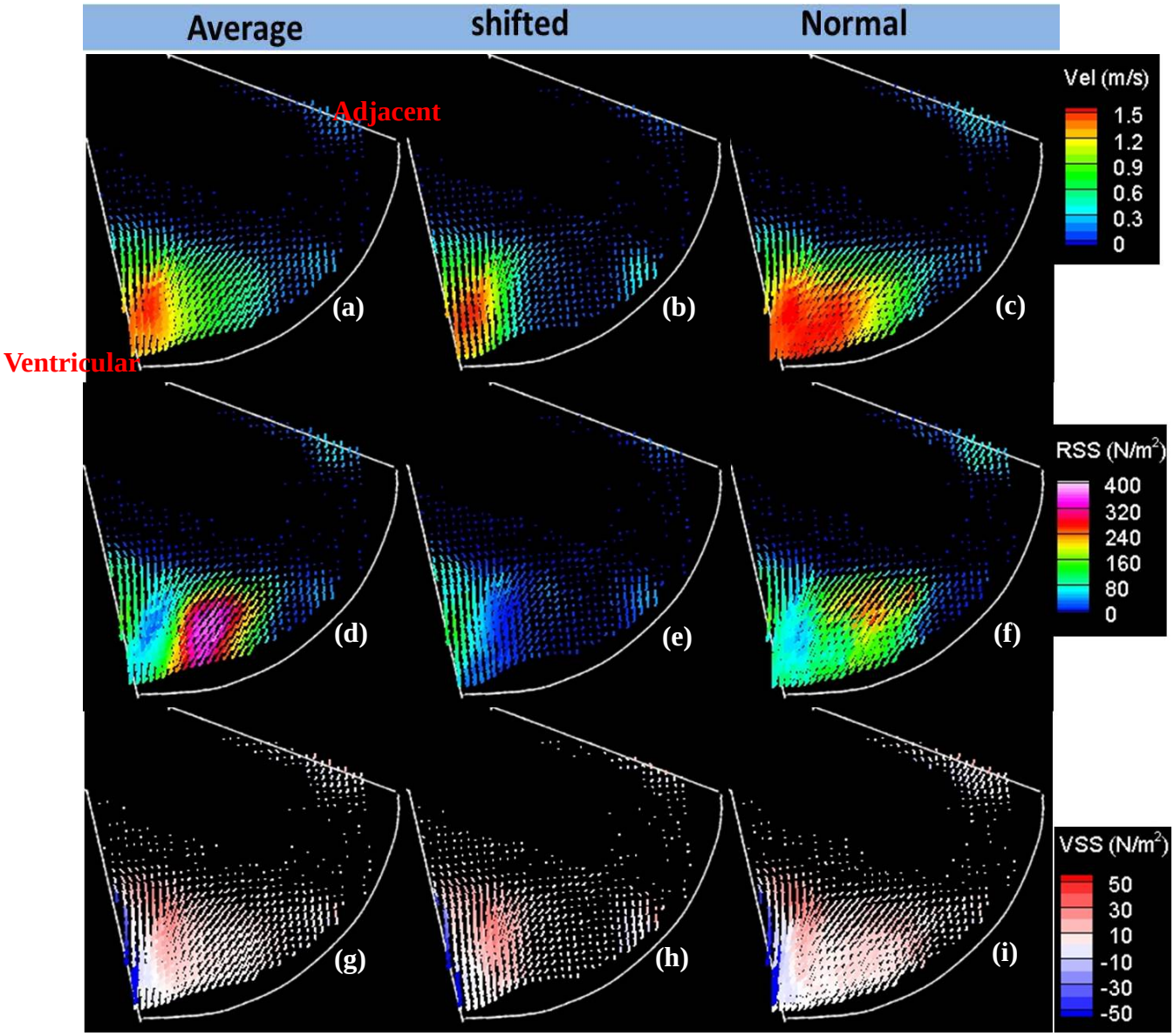

Figure 6.16: Ensemble averaged flow fields acquired from PIV for the three groups at the mid-diastolic phase (Standard). Velocity field from (a) average, (b) shifted position, and (c) normal position. Apparent Reynolds shear stress field from (d) average, (e) shifted position, and (f) normal position. Viscous shear stress field from (g) average, (h) shifted position, and (i) normal position.

Similarly, Tables 6.6-6.7 and Figures 6.17-6.18 represent the sliding motion analysis conducted on LLP and HLP valves. These results from HLP and LLP valves also demonstrated analogous

patterns between two positions where the ventricular jet had a smaller spatial area with vertical orientation in the shifted position. Subsequently, the normal position indicated RSS_{app} greater than ~100 N/m^2 than the shifted position. The LLP valve showed comparable counts of shifted position to the Standard valve as indicated on Table 6.6.

Table 6.6: Frequency of occurrence of sliding positions across 200 flow fields during diastole (LLP)

Sliding position	**Time points (ms)**					
	420	**440**	**480**	**520**	**560**	**600**
Shifted	53	40	78	79	44	56
Normal	147	160	122	121	156	144

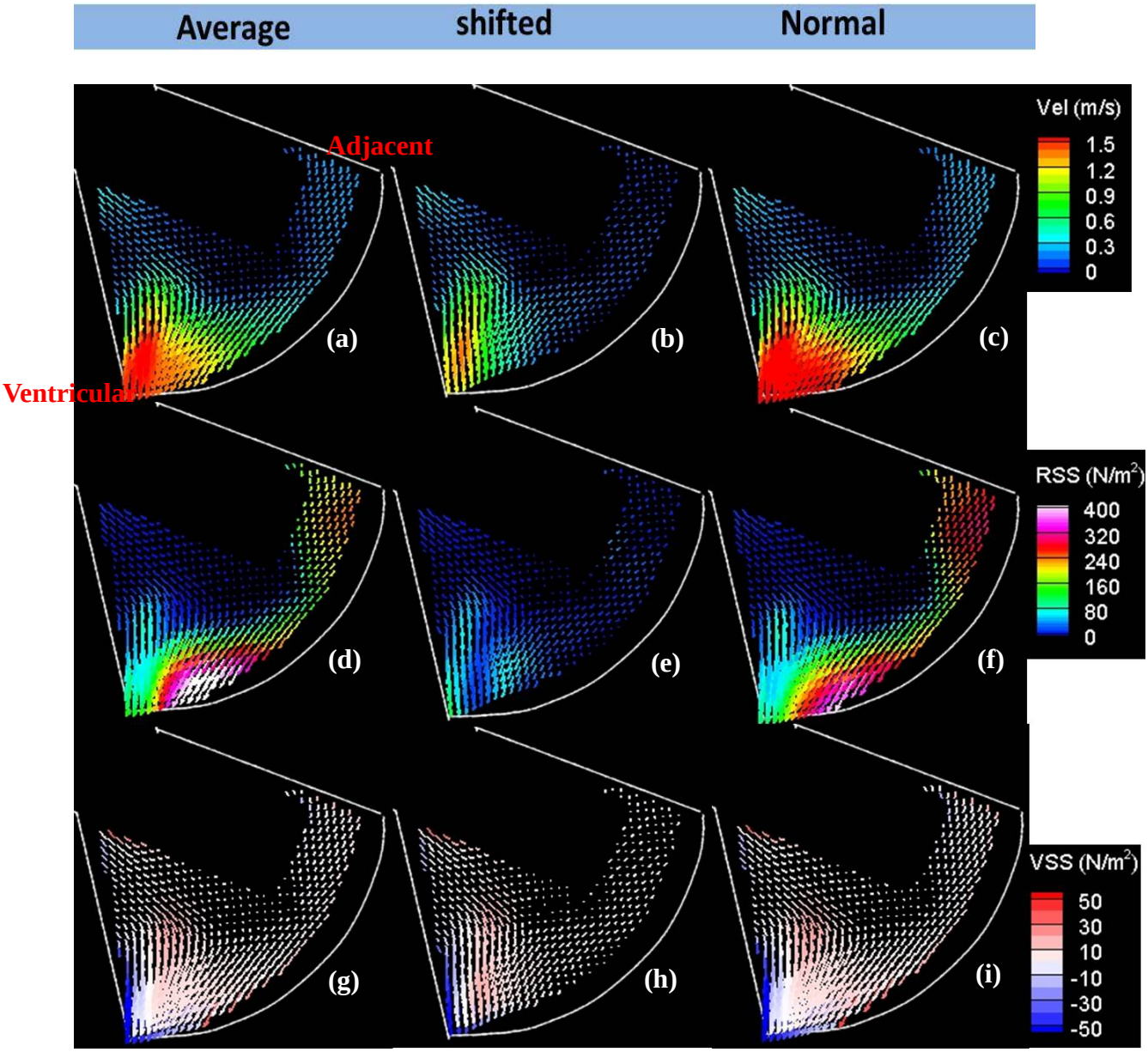

Figure 6.17: Ensemble averaged flow fields acquired from PIV for the three groups at the mid-diastolic phase (LLP). Velocity field from (a) average, (b) shifted position, and (c) normal position. Apparent Reynolds shear stress field from (d) average, (e) shifted position, and (f) normal position. Viscous shear stress field from (g) average, (h) shifted position, and (i) normal position.

As represented in Figure 6.18, the flow fields obtained from the HLP valve showed more coherent jets at the adjacent corner of the hinge. This was likely due to the large hinge gap width allowing greater number of particles to flow over to this location of the hinge with much higher velocity than the other valves. Subsequently, the normal position indicated velocity and RSS_{app} greater than 1 m/s and 200 N/m^2, respectively, than the shifted position at the adjacent corner of the hinge. This difference was most likely due to the narrowing of the gap width allowing fewer particles to flow through the adjacent corner when a leaflet ear is shifted towards the ventricular side of the hinge. The distinct pattern observed in the ventricular corner of the hinge was qualitatively and quantitatively similar to the Standard and LLP valves. However, the number of occurrences of shifted position counted from the HLP valve was much less than the other valves, as indicated on Table 6.7. Such a discrepancy might be attributed to a large hinge gap width (200μm) from the HLP valve. The velocity jet observed at the adjacent corner of the HLP valve's hinge had a strongest magnitude among the three valves, which may prevent the shifting motion of the leaflet.

Table 6.7: Frequency of occurrence of sliding positions across 200 flow fields during diastole (HLP)

Sliding position	**Time points (ms)**					
	420	**440**	**480**	**520**	**560**	**600**
Shifted	15	19	16	29	21	15
Normal	185	181	184	171	179	185

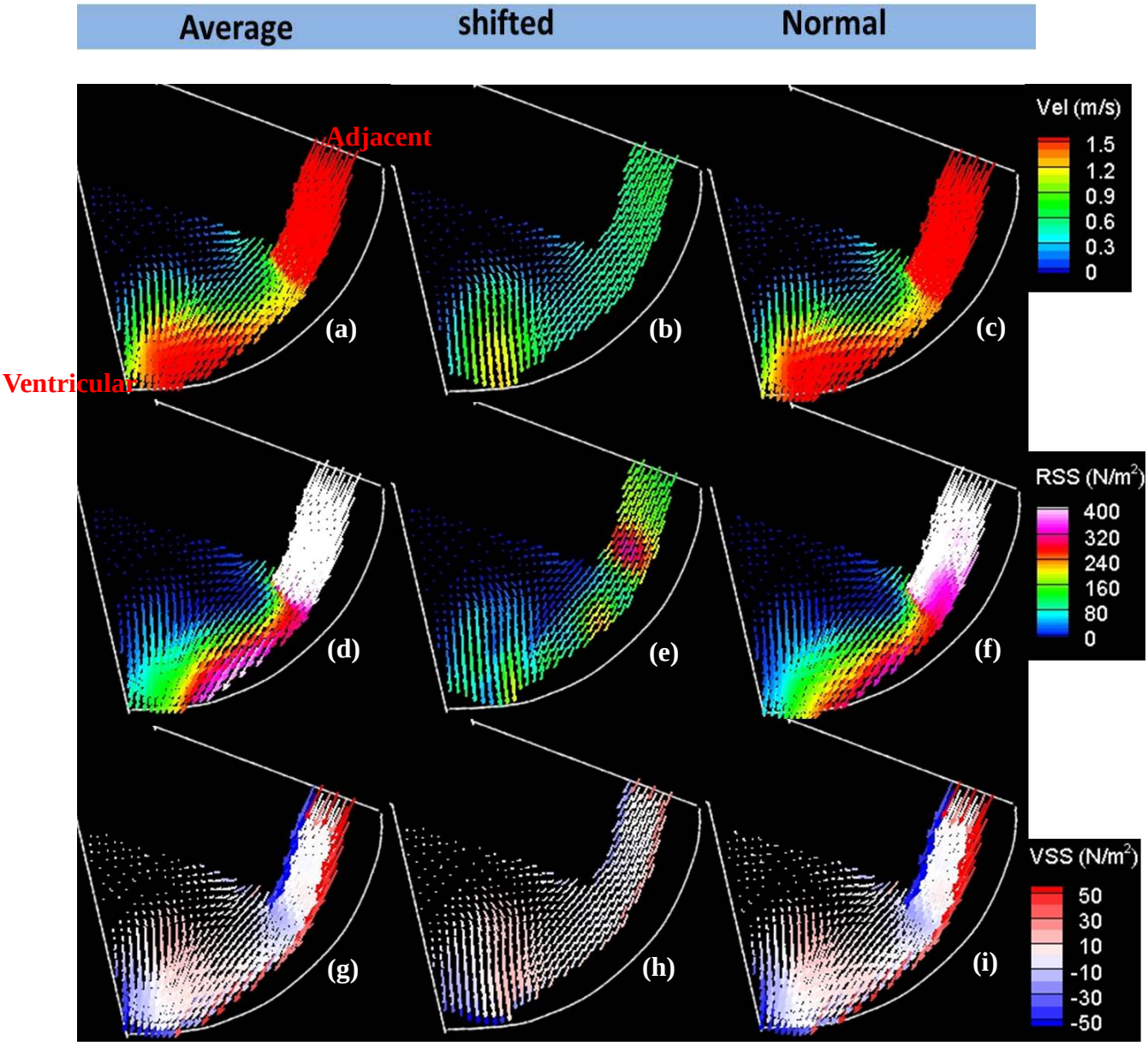

Figure 6.18: Ensemble averaged flow fields acquired from PIV for the three groups at the mid-diastolic phase (HLP). Velocity field from (a) average, (b) shifted position, and (c) normal position. Apparent Reynolds shear stress field from (d) average, (e) shifted position, and (f) normal position. Viscous shear stress field from (g) average, (h) shifted position, and (i) normal position.

CHAPTER 7

DISCUSSION

7.1 Hinge Study – Steady Flow

7.1.1 Global velocity fields in the hinge

As shown in Table 7.1, V_{peak} on the ventricular side increased with higher dP as expected. The flow field within the hinge region had a reverse flow pattern with presence of a high velocity jet and low flow regions on the ventricular side, but no coherent vortex structures were observed.

Table 7.1: V_{peak} (m/s) from ensemble correlation of 50 image pairs.

	FLAT plane	**195µm** plane	**390µm** plane	**585µm** plane
dP = 80mmHg	1.47	2.73	2.68	2.69
dP = 120mmHg	2.62	3.21	3.24	3.11
LDV (**dP** = 120mmHg)	1.64	1.96	2.27	0.49

For FLAT and 195 µm planes, reverse flow was observed in the adjacent corner and low flow regions were present at the ventricular corner due to the obstruction from the leaflet ear. At deeper levels within the hinge recess (390 µm and 585 µm planes), low flow regions were reduced and reverse flow jet was observed at the ventricular corner near the center location as reverse flow was directed across the hinge recess gap.

Higher velocity jets were measured at deeper levels within the hinge recess with V_{peak} = 3.24 m/s. The VSS fields across all four measurement planes indicate that VSS was higher on the ventricular side due to the interaction between a high velocity jet at the adjacent corner and low flow regions at the ventricular corner.

The global velocity maps at the FLAT and 195 μm planes suggested the potential for platelet activation and their longer residence time, due to the coexistence of the high VSS and the larger low flow region than the upper measurement planes. In the 390 μm plane, regions of low flow were reduced and the fluid jet traveled over to the ventricular side from the aortic side, exiting the hinge region. VSS magnitude of up to 60 N/m^2 was still observed along the edge of the jet similar to the lower measurement planes.

At 585 μm, low flow regions were minimal and the direction of the high velocity jet was most uniform compared to the other planes, which can be associated with the low hinge Reynolds number. These flow patterns indicate strong washout in the deeper levels of hinge recess, which is a favorable design feature. The strong jet with uniform direction can potentially wash out activated platelets and even RBCs that may get trapped in the small regions of the hinge recess. This aspect may be a primary advantage leading to clinical success of the SJM BMHV.

7.1.2 Comparison to previous studies

The current study is the first experimental study to obtain the complete flow fields within the hinge region of a SJM BMHV in the aortic position under steady leakage flow conditions. The four measurement planes and transvalvular pressure conditions were selected for the purpose of comparison with previous experimental and computational studies of hinge flows (Simon, 2004; Leo, 2005; Simon, 2010; Yun, 2012). Among these studies, detailed qualitative and quantitative comparisons with LDV and CFD studies by Simon *et al*. (Simon, 2004; Simon, 2010) were

conducted, due to the methodological similarity with the current study. However, several differences exist between the two methods that should to be clarified.

The LDV study was conducted under physiological pulsatile flow conditions at the aortic position whereas the current PIV study was performed under steady leakage flow at fixed dP values representing two time points in diastole. The depth of correlation of the PIV measurement was between 120.2 μm and 317.4 μm whereas the LDV setup had an ellipsoid probe volume with major and minor axes of 21 μm and 140 μm respectively (Leo, 2005). Despite the differences between these two methods, the general qualitative leakage flow fields were quite similar (Figures 7.1 – 7.3), where reverse flow from the aortic side was squeezed through the ventricular side. Additionally, good agreement was shown in terms of the location of the high velocity jet and low flow region in the ventricular side. The leakage jet at the lateral corner on the aortic side that was seen from LDV study at flat level was not observed from the current PIV results. This is due to scattered laser light in the PIV image at the lateral corner, which limited the visibility of the PIV particles at this particular location.

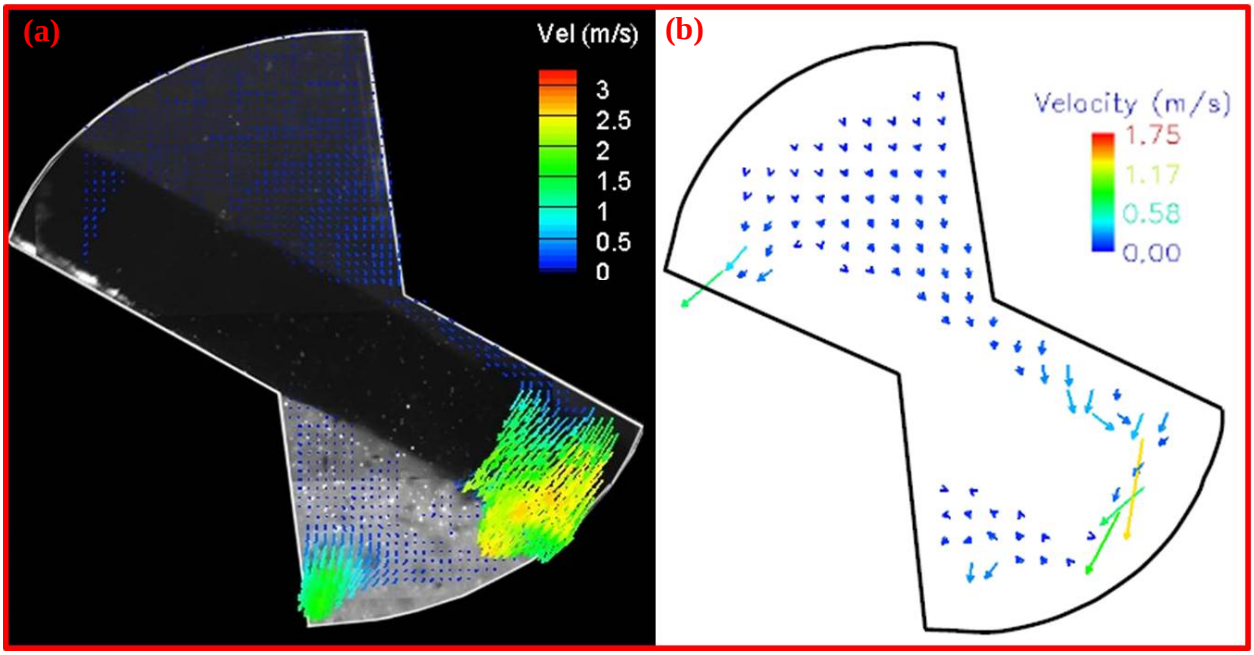

Figure 7.1: Comparison of the two-dimensional leakage flow velocity field at flat level in 23 mm SJM BMHV hinge among different methods, (a) µPIV, and (b) LDV.

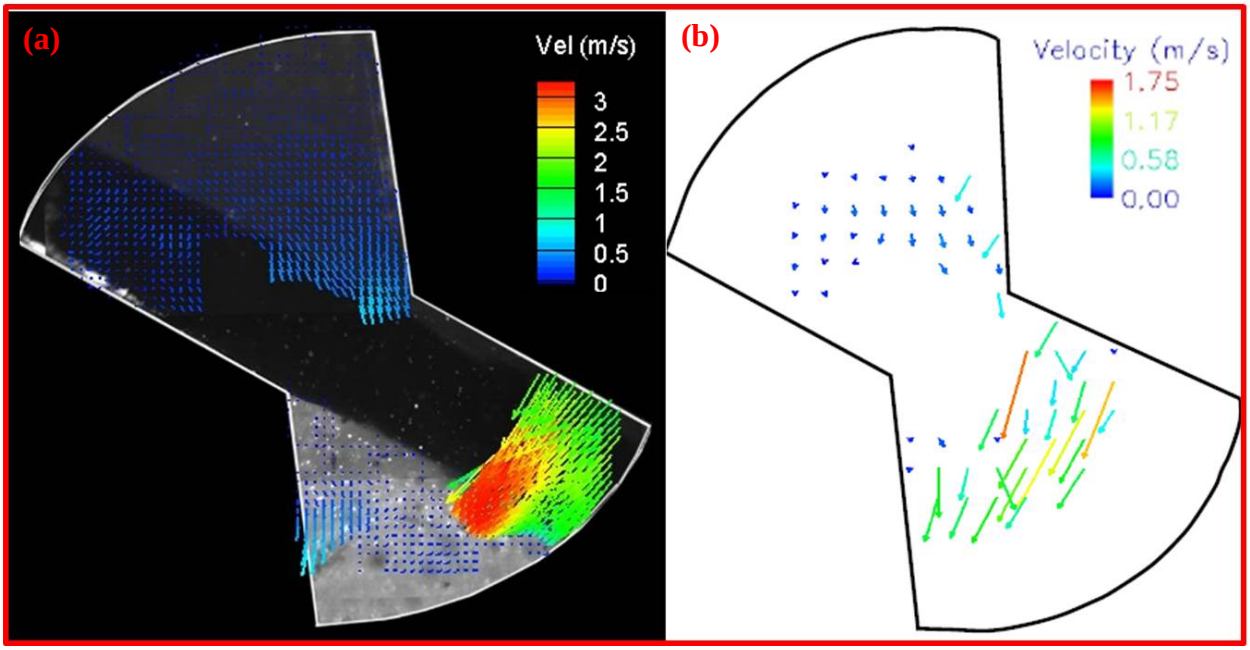

Figure 7.2: Comparison of the two-dimensional leakage flow velocity field at 195µm above flat level in 23 mm SJM BMHV hinge among different methods, (a) µPIV, and (b) LDV.

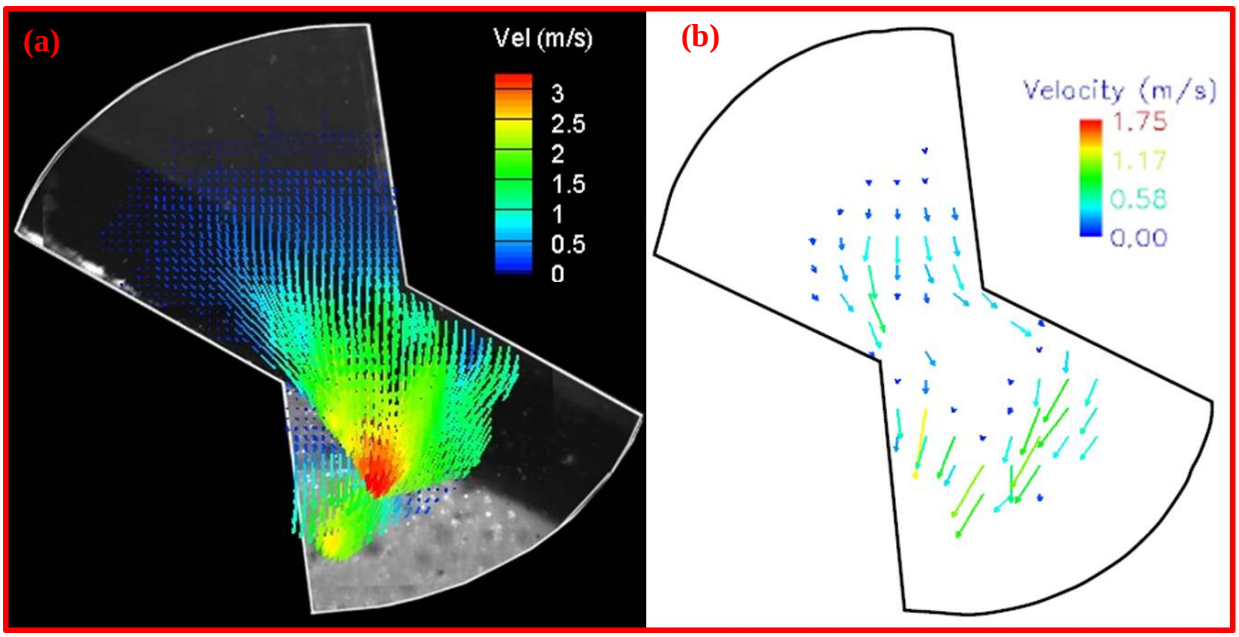

Figure 7.3: Comparison of the two-dimensional leakage flow velocity field at 390µm above flat level in 23 mm SJM BMHV hinge among different methods, (a) µPIV, and (b) LDV.

Table 7.1 compares V_{peak} from the LDV and current PIV study at dP = 120 mmHg across all four measurement planes. The LDV values presented in this table were chosen from the mid-diastolic phase where dP across the valve was approximately 120 mmHg based on the pulsatile pressure waveforms (Simon, 2004). As the aortic side has an incoming jet with much lower flow velocities than the jets in the ventricular side, the peak velocity values at these regions were close to the LDV results. On the ventricular side, V_{peak} obtained from PIV was higher than the corresponding LDV measurements across all planes. The higher V_{peak} from PIV is likely due to the enhanced spatial resolution (64 um vs. 203 um) as well as much fewer number of velocity vectors present in the LDV study, particularly in upper measurement planes (only three points were measured at 585µm plane) due to the difficulty of locating the LDV probe near the wall of the hinge housing.

The current PIV results showed good qualitative agreement with the CFD study across all measurement planes (Simon, 2010). In the FLAT and 195 μm planes, similar high velocity jets were observed in both studies - along the arc of housing near the adjacent corner and in the near end of the ventricular corner (Figure 7.4-c). The location of low flow regions on the ventricular side matched closely between the two studies, where the vertical distance of this region estimated from the sharp corner in the center was 1.19 mm and 1.16 mm from the CFD and PIV studies, respectively at the FLAT level.

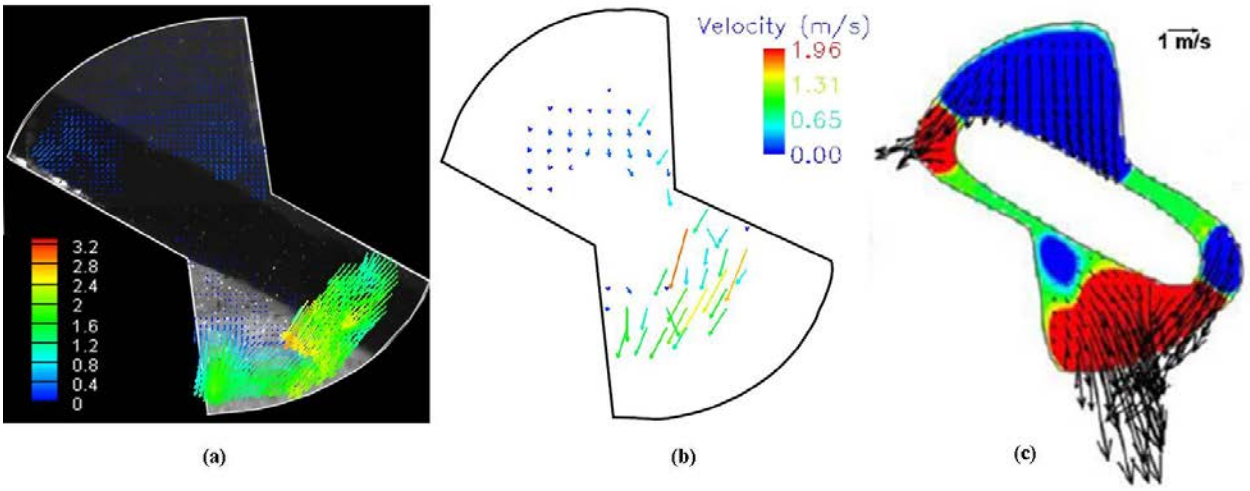

Figure 7.4: Comparison of the two-dimensional leakage flow velocity field at 390μm above flat level in 23 mm SJM BMHV hinge among different methods, (a) μPIV, (b) LDV (Simon, 2004), and (c) CFD (Simon, 2010).

The CFD study showed a leakage jet at the lateral corner on the aortic side that was not observed from the PIV study due to the aforementioned scattered laser light in the PIV images. In the upper measurement planes, both studies showed the presence of a uniform ventricular jet exiting the hinge at high velocity.

This suggests that the CFD studies are able to capture the relevant flow structures that have been characterized here using PIV. From a quantitative standpoint, peak velocity values obtained from

CFD studies were closer to the current PIV results than to the previous LDV study. Nonetheless, the peak velocity magnitude from CFD studies were still greater than PIV results, potentially due to the limitations associated with numerical study, such as idealized boundary conditions and a smaller degree of freedom with leaflet motion.

One aspect that is lacking in the CFD study is the true representation of the mating between the leaflet and hinge housing. In the numerical study, the only degree of freedom provided in the fluid-structure interaction model is rotational motion. The current experimental setup allows visualizing the actual leaflet within the hinge recess during the valve closure, which cannot be obtained from the previous LDV techniques. Such new feature provides more detailed characterization of the hinge flow fields.

7.1.3 Blood damage potential

These fluid mechanical assessments can be tied to what has been clinically observed with MHVs. Two important fluid dynamic parameters associated with thromboembolic complications in BMHVs are high shear stress and low flow recirculation regions (Yun, 2012). The shear stress imposed on the surface of platelets can lead to platelet activation, and low flow regions exacerbate this process by providing longer residence time for these activated platelets, ultimately resulting in thromboembolism. Gross *et al.* (Gross, 1996) reported that the viscous shear stress level at 10 N/m^2 can be defined as a threshold for the platelet activation. The threshold level for the hemolysis was near 100 N/m^2 according to Leverett *et al.* (Leverett, 1972), which is greater than the peak viscous shear stresses reported in this study. Thus, it is expected that the valve model studied here showed greater potential for the platelet activation

than the hemolysis across all conditions, which may lead to sublethal damage to blood elements. In particular, the coexistence of the high VSS and low flow regions from the lower measurement planes may favor thromboembolic complications.

7.2 Hinge Study – Pulsatile Flow

7.2.1 Effect of hinge gap width on the global flow field

The results presented in this study demonstrate that the hinge gap width had a more significant influence during leakage flow compared to forward flow, in terms of the washout and shear stress characteristics. During systole, the flow in the three SJM valves was governed by the rapid flow ejection from the piston. This resulted in similar velocity and acceleration profiles for all three cases within the hinge regions. In addition, only the FLAT plane had a dominant flow structure at the peak systolic phase. Measurement planes located deeper in the hinge recess had low flow regions (Vel < 0.3m/s) without any coherent structures to be differentiated among the three valves. Also, the VSS and RSS_{app} fields were not considerably different among the three valves, as these parameters were calculated based on the measured velocity field. Therefore, the hinge gap width had minimal effect on the flow inside the hinge during the forward flow.

Previous hinge studies reported that the leakage flow in the SJM BMHV induces a much stronger jet in the hinge region than the forward flow which can potentially wash out stagnant blood elements (Simon, 2004; Leo, 2006; Simon, 2010). This was apparent for all three valves based on the measured flow fields. In diastole, the HLP valve revealed the strongest washout potential across all measurement planes. This was likely due to the large hinge gap width allowing particles to flow over to the ventricular side with much higher velocity than the other

valves. The Standard valve also showed strong velocity jets at the adjacent and ventricular corners, but with lower magnitude than the HLP valve at the 195, 390, and 585μm planes.

The LLP valve exhibited the weakest washout potential among the three valves across all measurement planes in diastole. At lower measurement planes, the LLP valve indicated a stronger lateral jet structure than the other valves. However, a high velocity jet at this location will be less likely to contribute to the washout of blood elements located deep in the hinge recess. Even at the 390μm plane, the low flow region near the ventricular pocket was larger in area than for the other valves. This indicates that small blood elements such as platelets (~2μm diameter) can recirculate in this region and may not be washed out effectively either in systole or in diastole.

The hinge gap width altered locations of high VSS and RSS_{app} regions in the leakage flow. The highest RSS_{app} level was observed at the adjacent corner of the HLP valve. At this location, the high velocity jet squeezed from the hinge recess gap impinged on the sharp corner of the hinge housing, which may contribute to the unsteady flow in this region. The other potential factor could be the sliding motion of the leaflet ear which occurs naturally in diastole as a result of the rapid sweeping motion under pulsatile flow conditions. The RSS_{app} in the flow field at the adjacent corner can be easily affected by the sliding motion due to the close contact with the leaflet ear. This phenomenon is discussed in more detail in section 7.2.4.

The hinge gap width also appeared to influence the locations of high VSS and RSS_{app} regions across the three valves. The high RSS_{app} regions were found near the edges of the strongest

leakage jets on the ventricular corner of the hinge. The HLP and Standard valves had similar magnitudes and distributions of VSS during the leakage flow, with the highest VSS occurring at the adjacent corner. Alternatively, the LLP valve showed high VSS at the lateral and ventricular corners, but with lower VSS levels than the other two valves. These observations indicate that the gap width difference between the HLP and Standard valves had a negligible effect on the VSS fields, but the smallest hinge gap width from the LLP valve induced lower VSS values at the adjacent corner. This is due to it having the smallest area that would allow fluid to flow along the adjacent corner of the hinge.

7.2.2 Cycle-to-Cycle Variations in the Velocity Measurements

The flow field in the hinge region exhibits cycle to cycle fluctuations which arise due to experimental artifacts such as the variations in the pulsatile flow as well as valve leaflet dynamics. The pulse duplicator used in the current study generates rapid forward and backward motions of the piston, which give rise to the cycle-to-cycle fluctuations in the flow and pressures. In addition, the opening and closing dynamics of valve leaflets will affect the instantaneous position of the leaflet from one cycle to another. Similar cycle-to-cycle fluctuations were observed in previous studies with biological valves as well (Yap, 2010; Saikrishnan, 2012). These observations from the *in-vitro* experiments can reflect physiological phenomenon taking place in the human heart, as heart rate and blood pressure changes continuously over cardiac cycles. Subsequently, the blood elements near the surface of the leaflet will experience different magnitudes of shear stress and exposure time from cycle-to-cycle, which may affect the blood damage potential. As shown from the current study, even small variations in the leaflet position (~100μm) in diastole can contribute to the velocity fluctuations in the hinge region. Therefore, it

is important to investigate the cycle to cycle velocity fluctuations in the hinge region quantified in the form of RSS.

7.2.3 Blood damage potential

The blood damage potential from each valve model was estimated in this study using threshold levels investigated from previous studies (Leverett, 1972; Lu, 2001; Simon, 2007). Leakage flow fields obtained from the HLP and Standard valve showed RSS_{peak} values of 1140 N/m^2 (HLP) and 950 N/m^2 (Standard), which were above threshold levels for hemolysis suggested from Lu et al. (Lu, 2001). The LLP valve had RSS_{peak} value of 430 N/m^2 which did not exceed RSS threshold levels for hemolysis. VSS_{peak} values reported from all three valves exceeded VSS threshold levels for platelet activation but not hemolysis based on critical values suggested by Leverett et al. and Lu et al. (Leverett, 1972; Lu, 2001)

For washout potential during leakage flow, the LLP valve demonstrated the "worst case" scenario among the three valves, in terms of velocity magnitude and regions of flow stasis. This scenario could lead to the accumulation of activated platelets due to increased residence times within the hinge. Therefore, even though the LLP valve had lower levels of RSS_{app} and VSS than the other two valves, the poor washout potential increases the chances for accumulation of activated blood elements for this hinge gap. Subsequently, the Standard valve had a more optimal gap width among the three valves based on the shear stress levels and washout potential.

7.2.4 Comparison to previous studies

The LDV and μPIV studies were both conducted under physiological pulsatile flow conditions. The depth of correlation of the PIV measurement was between 120.2 μm and 317.4 μm whereas the LDV setup had an ellipsoid probe volume with major and minor axes of 21 μm and 140 μm respectively (Leo, 2005). Despite the differences between these two methods, the general qualitative forward and leakage flow fields were quite similar (Figures 7.5 – 7.9). A good agreement was shown in terms of the location of the high velocity jet and low flow region in the aortic and ventricular side.

Similar to the comparison between the pulsatile flow LDV (Simon, 2004) and steady flow μPIV (Jun, 2013) measurements, the largest discrepancy was observed at the upper measurement planes (Figure 7.7). The primary reason is likely due to the differences in measurement depth and spatial resolution between two methods, as described in section 7.1.2.

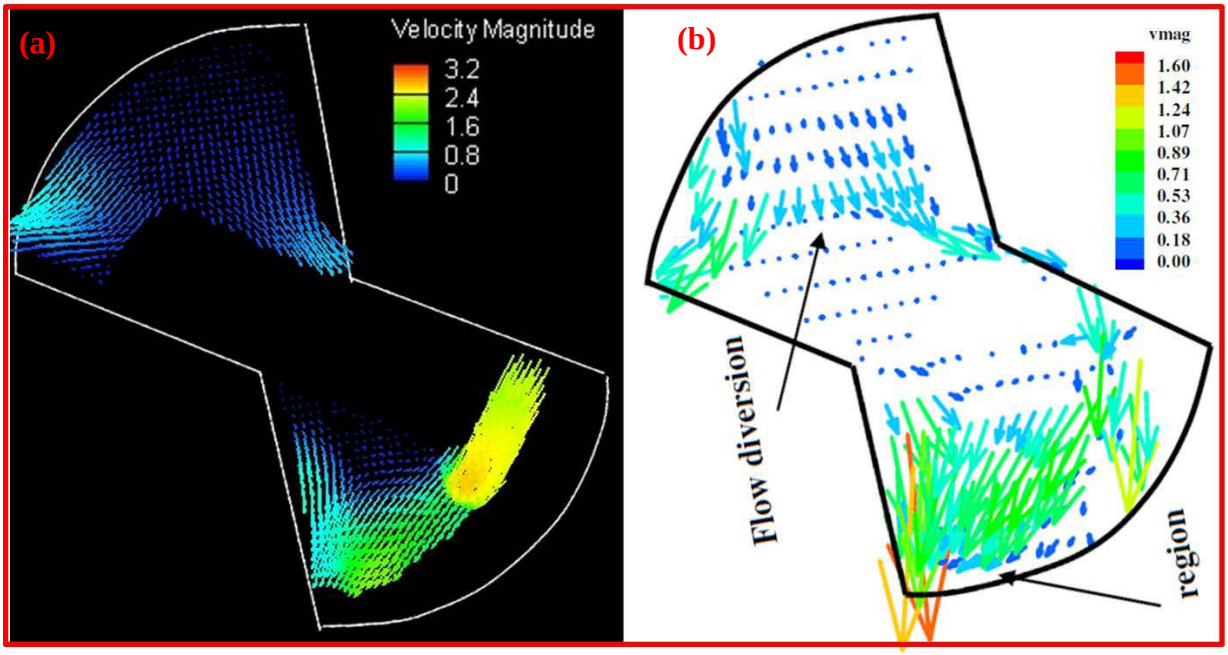

Figure 7.5: Comparison of the two-dimensional leakage flow velocity field at flat level in Standard valve among different methods, (a) μPIV, and (b) LDV (Leo, 2005).

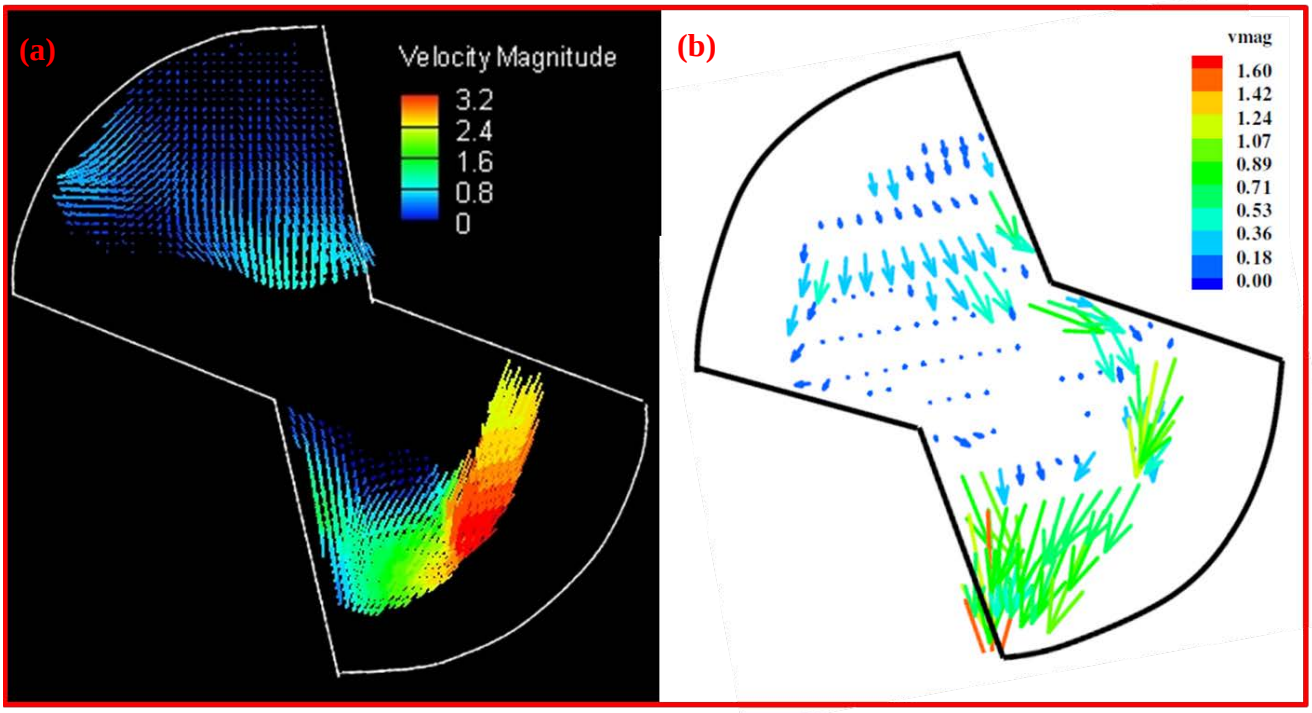

Figure 7.6: Comparison of the two-dimensional leakage flow velocity field at flat level in Standard valve among different methods, (a) µPIV, and (b) LDV (Leo, 2005).

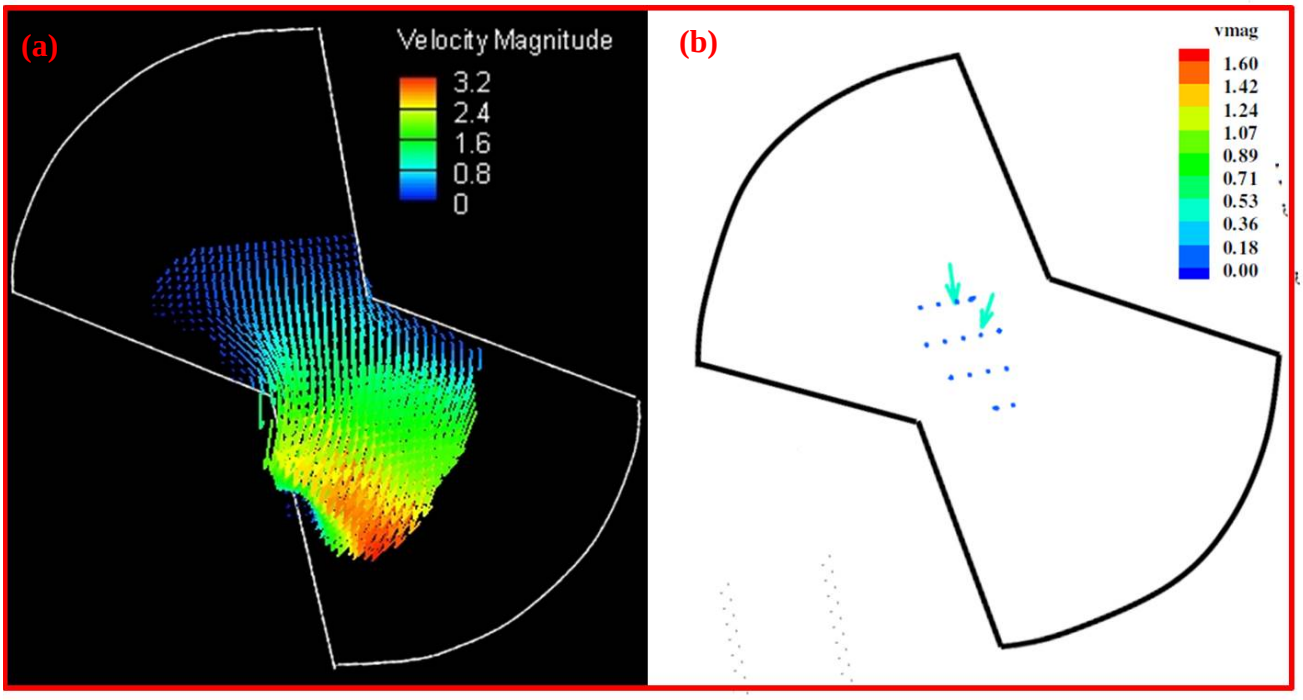

Figure 7.7: Comparison of the two-dimensional leakage flow velocity field at flat level in Standard valve among different methods, (a) µPIV, and (b) LDV (Leo, 2005).

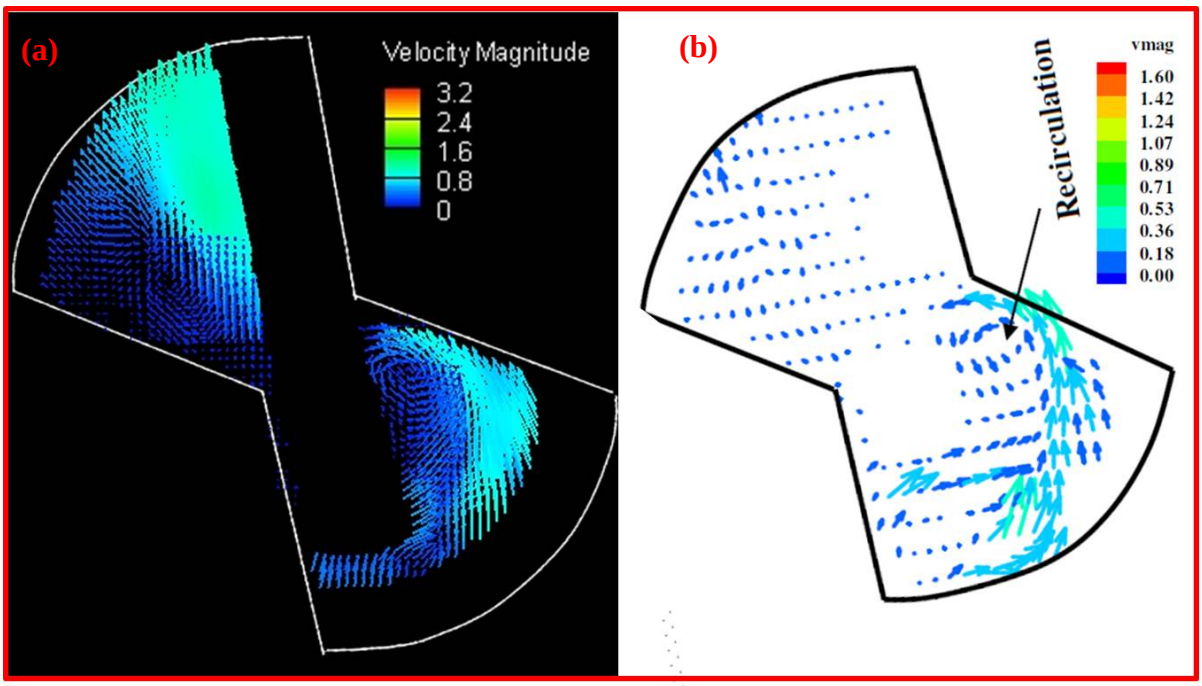

Figure 7.8: Comparison of the two-dimensional peak systolic flow velocity field at flat level in Standard valve among different methods, (a) µPIV, and (b) LDV (Leo, 2005).

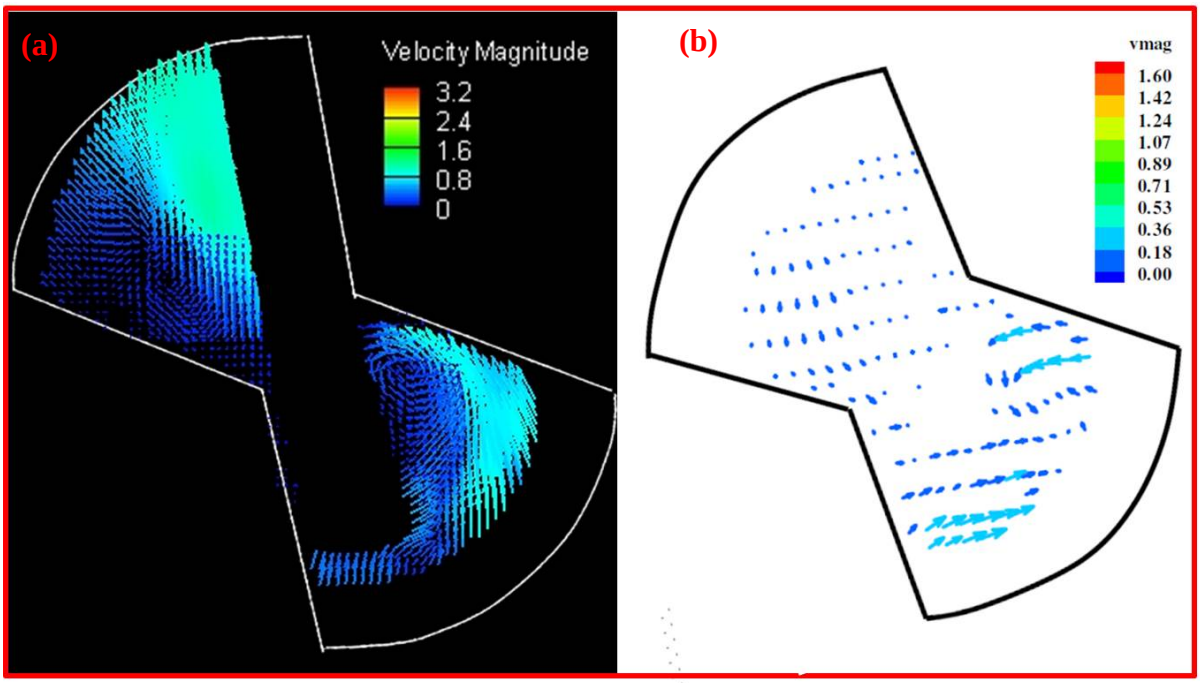

Figure 7.9: Comparison of the two-dimensional peak systolic flow velocity field at 195µm above flat level in Standard valve among different methods, (a) µPIV, and (b) LDV (Leo, 2005).

Figures 7.10 – 7.15 illustrate the comparison of representative flow fields between the µPIV and Computational Fluid Dynamics (CFD) results (Standard valve) obtained by Simon *et al*. (Simon, 2009; Simon, 2010). For the peak systolic phase (Figures 7.10 – 7.11), both results were consistent in structure and orientation of jets, which included a recirculating flow and a high velocity jet from the adjacent and lateral corner, respectively. The Vel_{peak} from the µPIV study at this phase was 1.1 m/s which was comparable to the Ve_{peak} (1.5 m/s) from the CFD study.

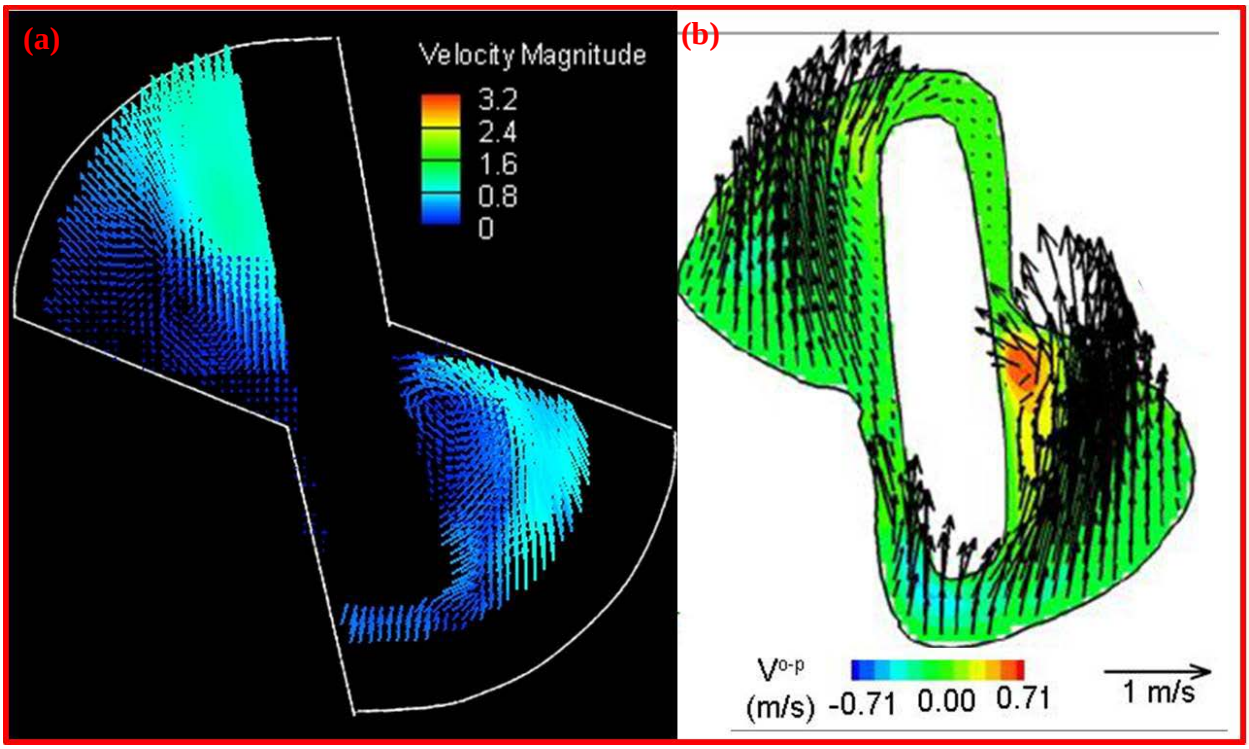

Figure 7.10: Comparison of the two-dimensional peak systolic flow velocity field at flat level in Standard valve among different methods, (a) µPIV, and (b) CFD (Simon, 2010).

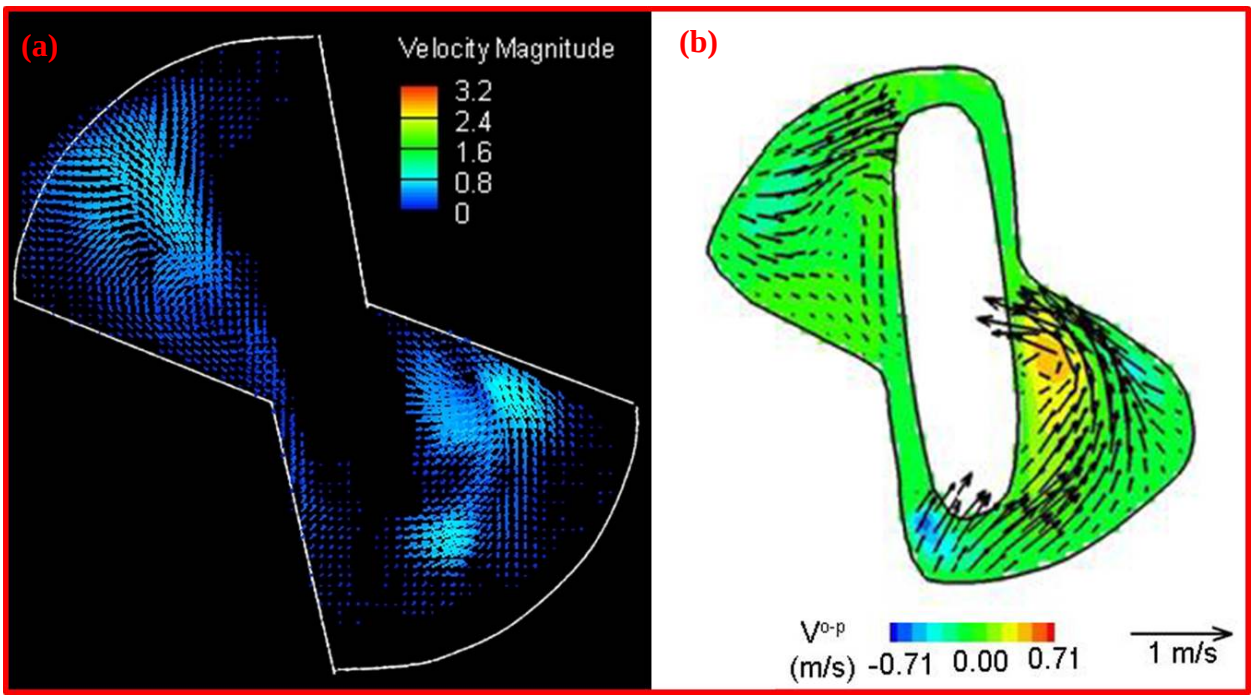

Figure 7.11: Comparison of the two-dimensional peak systolic flow velocity field at 195µm above flat level in Standard valve among different methods, (a) µPIV, and (b) CFD (Simon, 2010).

In diastole, both CFD and μPIV results showed qualitatively similar leakage flow fields across all measurement planes. In the lower measurement planes (Figures 7.12 - 7.13), both studies showed common leakage flow features including lateral, adjacent, ventricular jets and a low flow region. The velocity ranges of these three jets were higher in the CFD study (1 – 4.75 m/s) than the μPIV study (0.4 – 2 m/s). The largest difference was observed at the lateral corner, where results from the CFD study showed about two times greater velocity magnitudes than the μPIV study. The orientation of ventricular jets in the two studies was also slightly different. Two primary differences exist between the CFD simulations and the *in vitro* experiments, as discussed in a previous study by Jun *et al*. (Jun, 2013). Firstly, CFD could not capture the cycle to cycle variability in leaflet position, which was accounted for in PIV by ensemble averaging. Secondly, the depth of correlation in PIV is larger than the spatial resolution of the CFD data.

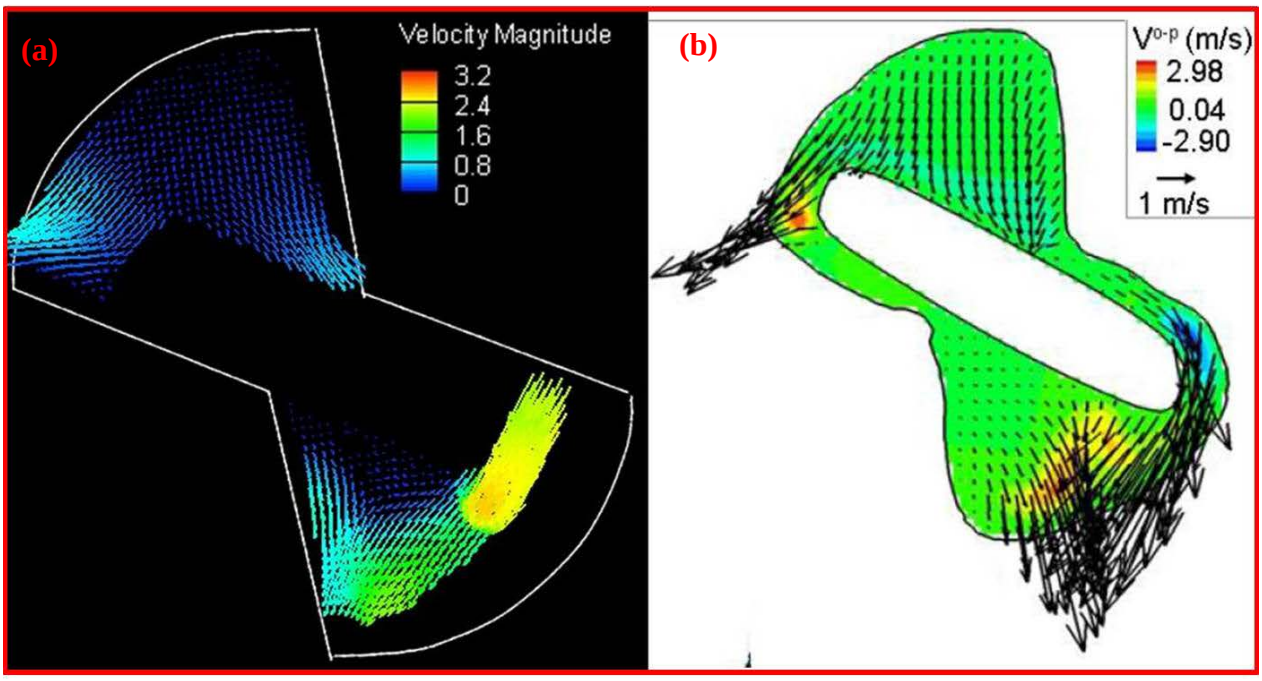

Figure 7.12: Comparison of the two-dimensional leakage flow velocity field at flat level in Standard valve among different methods, (a) µPIV, and (b) CFD (Simon, 2010).

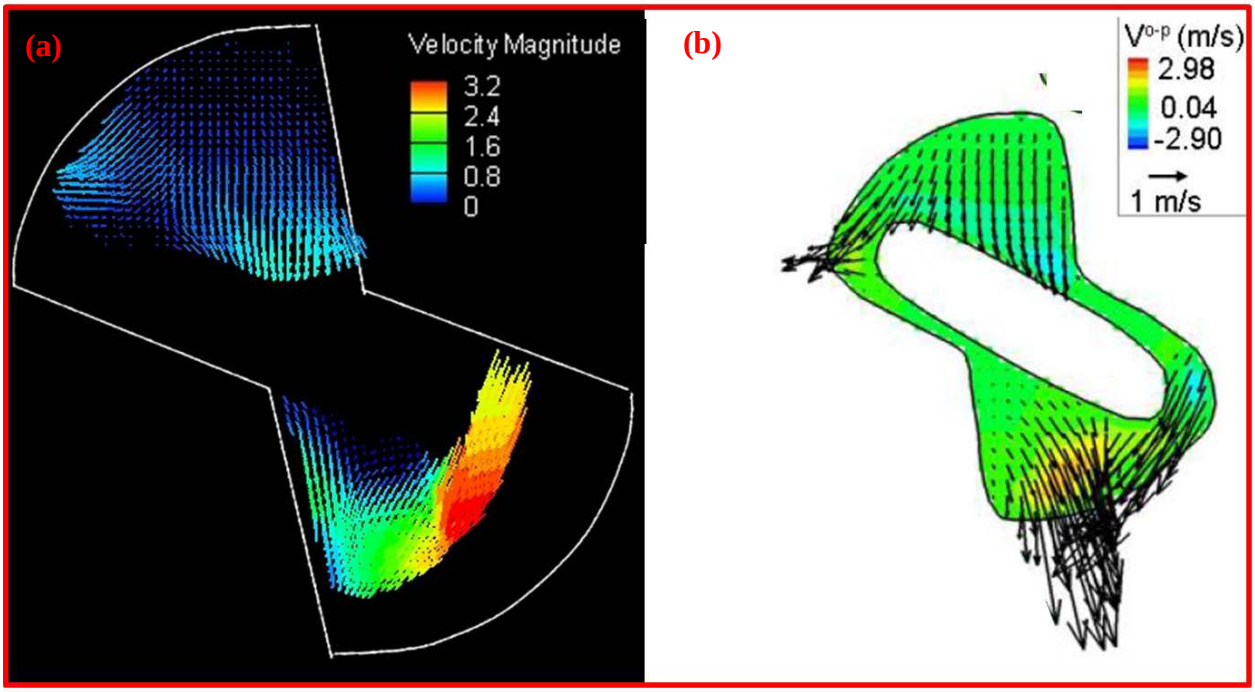

Figure 7.13: Comparison of the two-dimensional leakage flow velocity field at 195µm above flat level in Standard valve among different methods, (a) µPIV, and (b) CFD (Simon, 2010).

At the upper measurement planes (Figures 7.14 – 7.15), flow fields from both studies showed more similarities than at the lower measurement planes. A uniformly structured jet passing across the leaflet center was observed in both studies with velocities ranging from 1 to 3 m/s. These measurement planes were deeper in the hinge recess, which were less influenced by the sliding motion and spatial location of the leaflet ear, hence representing a better match between the two studies.

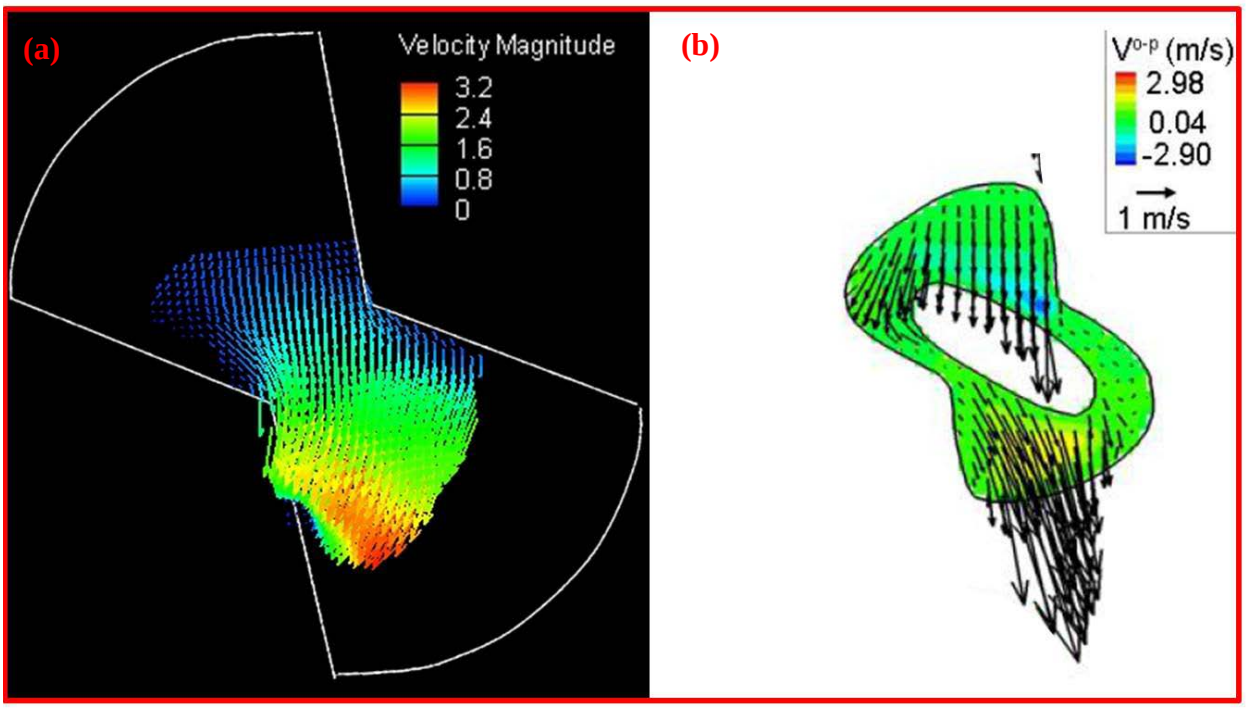

Figure 7.14: Comparison of the two-dimensional leakage flow velocity field at 390µm above flat level in Standard valve among different methods, (a) µPIV, and (b) CFD (Simon, 2010).

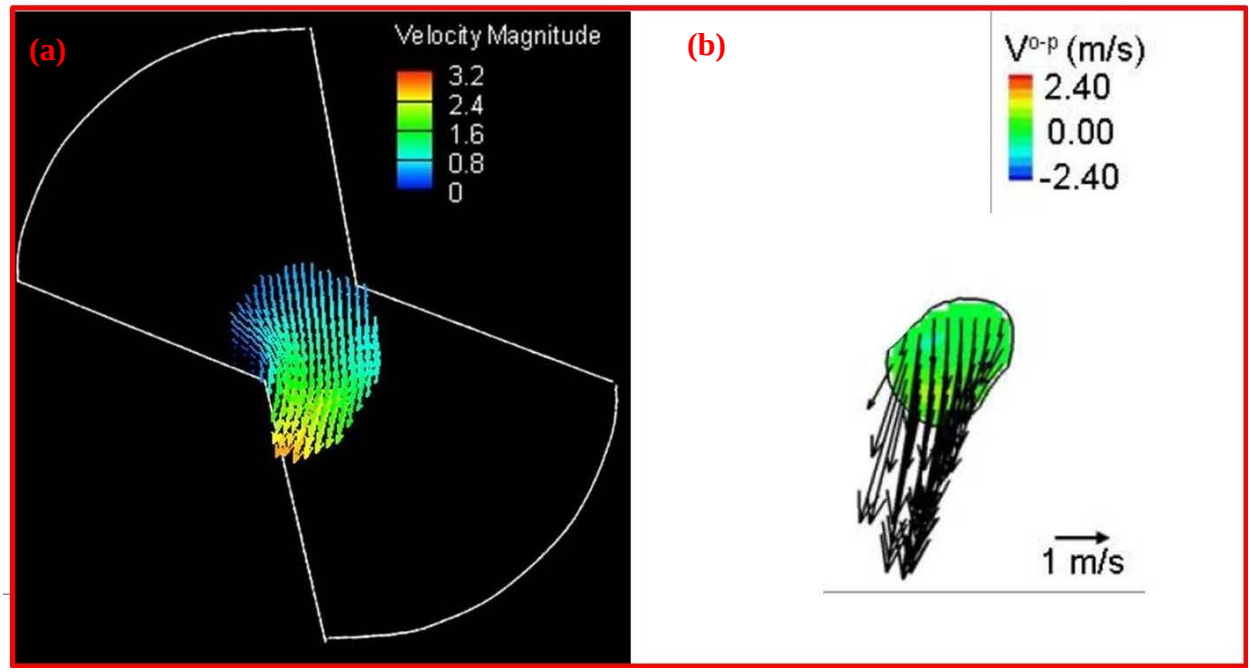

Figure 7.15: Comparison of the two-dimensional leakage flow velocity field at 585µm above flat level in Standard valve among different methods, (a) µPIV, and (b) CFD (Simon, 2010).

7.2.5 Comparison between the steady and pulsatile flow hinge studies

This study represents the first fully pulsatile flow µPIV measurements in the hinge region of a BMHV, by adapting the previously developed µPIV system for steady flow studies (Jun, 2013). In both the steady and pulsatile flow studies, the highest thromboembolic potential was observed during the leakage flow phase under aortic conditions. Nevertheless, the current pulsatile flow µPIV study revealed a number of critical aspects that would have been difficult to investigate under steady flow conditions.

In order to further differentiate flow characteristics between BMHV hinge designs, an experimental setup with low cycle-to-cycle variations in the flow conditions is necessary.

The pulsatile experimental set up allows us to investigate the dynamic acceleration effects of leaflet motion on the hinge flow fields. This cannot be achieved from the steady flow loop setup

where valve leaflets are in a static position throughout the experiment. The instantaneous velocity fields obtained from each cardiac cycle enabled calculation of RSS_{app}, representing instantaneous velocity fluctuation in the flow field in different phases, which was not identified in the steady flow study.

7.2.6 Applications of Micro-PIV hinge studies

These unique aspects of BMHV flows found in the current μPIV study such as evaluating cycle to cycle variation and global velocity maps under micron-scale flow domains are not restricted to the hinge region. Previous studies indicated that large recirculation regions are formed upstream of the valve during the leakage phase. In addition, strong regurgitant jets were observed in the B-datum plane and peripheral leakage regions located in the neighborhood of the hinge [Manning, 2003; Dasi, 2008; Dumont, 2007]. These combined factors can potentially trap damaged/activated blood elements at these locations resulting in thromboembolic complications.

The established technique from this study can be used to assess other critical regions in a BMHV such as leakage flow through the B-datum gap, and flow fields in the immediate vicinity of a hinge during the period of valve closure. This study has shown the fully pulsatile flow characteristics of the three valve models with intricate hinge flow structures, such as variations in Vel, VSS, and RSS_{app}. In addition, the study has demonstrated the application of the high-resolution μPIV system, which can aid in the design optimization of BMHVs.

7.2.7 Leaflet Sliding Motion Analysis

The leaflet sliding phenomenon was serendipitously observed during PIV analysis of the Standard valve. Typically, during PIV experiments the best practice is to avoid any seed particles adhering to the surface of the leaflet, since the particles that are not in motion will yield zero velocity. Furthermore, if particles adhere to regions on a leaflet where fluid velocity is substantial (Vel>1m/s), the velocity measurement is biased or underestimated. Though the adhered particles served as a reference for tracking the leaflet translation motion, they were omitted while processing the PIV data analysis. Subsequently, two distinct patterns of velocity field representing different levels of washout potential were observed with respect to two dominant modes of leaflet position across all three valves. As illustrated in the results chapter, the shifted position indicated larger low flow region (Vel<0.3m/s) located between the ventricular and adjacent corners. This low flow region was most likely produced due to the narrowing of the gap width allowing fewer particles to flow through the adjacent corner when a leaflet ear is shifted towards the ventricular side. This indicates that small blood elements such as platelets (~2 μm diameter) can recirculate in this region and may not be washed out effectively in diastole than the normal position.

The peak velocity, VSS, and RSS_{app} values across three valves between two positions were not significantly different. This is likely due to the occurrence of strong leakage flow deeper in the hinge recess irrespective of the leaflet sliding effect, where interactions between particles and leaflet ear were insignificant.

The blood damage potential from each position was estimated using threshold levels investigated from previous studies [Leverett, 1972; Lu, 2001; Simon, 2007; Murphy, 2008]. The RSS_{peak} values obtained from both positions did not exceed threshold levels for hemolysis suggested from Lu *et al*. [Lu, 2001]. The VSS_{peak} values reported from both positions exceeded threshold levels for platelet activation but not hemolysis, based on critical values suggested from Leverett *et al*. and Lu *et al*. [Leverett, 1972; Lu, 2001].

Overall, the shifted position of the leaflet demonstrated less effective washout potential than the normal position, in terms of velocity magnitude and regions of low flow. This particular position was observed more frequently from the Standard and LLP valves, as discussed in the results chapter. This scenario could lead to accumulation of activated platelets due to increased residence times within the ventricular side of the hinge. However, the leaflet alternates between the positions, allowing adequate washout of blood elements in the hinge recess across multiple cycles. The altering position of the leaflet may produce effective washout of blood elements with velocity jets in different direction and magnitude in locations where the flow is potentially stagnant in the hinge during diastole.

7.2.8 Summary of Flow Topology in the hinges of three SJM valves

In summary, hinge flow characterization of three SJM valves using Micro-PIV revealed a number of parameters which play a critical role in blood damage potential during diastole of cardiac cycle.

In the lower measurement planes across all three valves (LLP, Standard, and HLP), five different regions were identified based on levels of blood damage potential (predicted based on velocity, VSS, and RSS_{app} fields), as illustrated in Figure 7.16.

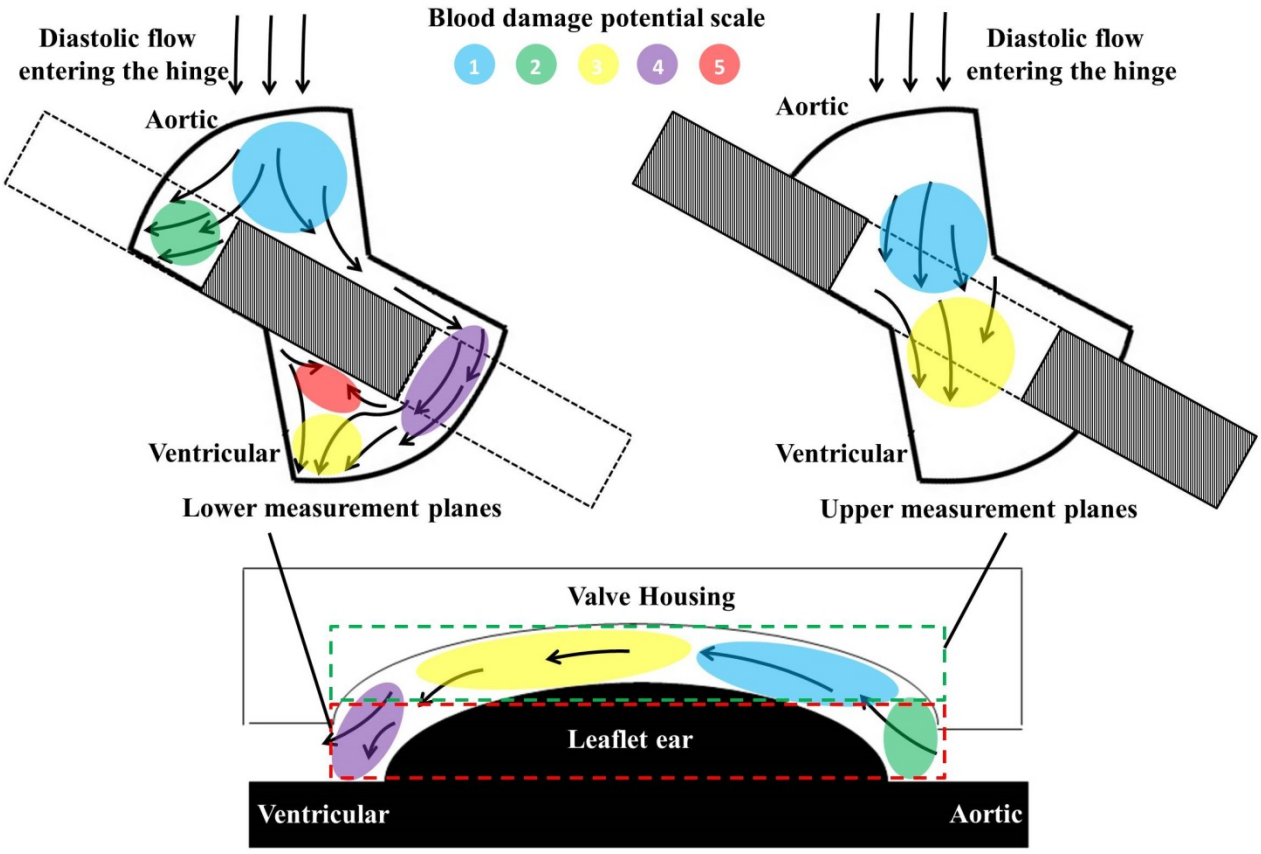

Figure 7.16: Blood damage potential assessment in the hinge (LLP, Standard, and HLP valves) from the Micro-PIV characterization

The hinge gap width influences the shear stress level and washout potential in the green and purple regions, where a moderate to high level of blood damage potential was predicted. The flow field in the yellow region was observed to be influenced predominantly by the leaflet resting position, which changes the orifice area in the purple region. The highest level of blood damage potential was observed in the red region, regardless of the leaflet resting position and the hinge gap width. The red region represents the low flow zone, where highly sheared blood elements passing through the purple region may get trapped and sustain long residence times. In

the upper measurement planes across all three valves (LLP, Standard, and HLP), a moderate level of blood damage was predicted in the yellow region due to the high velocity and VSS magnitudes, but with better washout potential than in the lower measurement planes. This is likely due to minimal curvature and level of interaction between the flow field and leaflet ear in the upper measurement planes. All measurement planes indicated the lowest level of blood damage potential in the blue regions, as blood elements did not experience high levels of shear stress at the aortic side of the hinge.

These findings provide a better understanding of the regions of potential blood element damage within the BMHV hinge, together with previous results from *in vitro* LDV studies (Simon, 2004; Leo, 2006).The current micro-PIV technique enables the measurement of high-spatial resolution flow fields together with visualization of the leaflet resting position. The leaflet translational motion in diastole provides a potential explanation for the high RSS_{app} observed in the purple region using both LDV and micro-PIV techniques. In addition, the new PIV flow field data may be used for the validation of the CFD approaches developed for characterizing the BMHV hinge flow fields (Simon, 2010; Yun, 2012).

7.2.9 Implications for Valve Design

The results drawn from the current experiments provide additional guidance in the design optimization of bileaflet mechanical heart valves. The hinge gap width had a more significant influence during leakage flow as compared to forward flow, in terms of washout and shear stress characteristics. Subsequently, another novel finding of this study was that the hinge gap width also appeared to influence the locations of high VSS and RSS_{app} regions across the three valves.

These traits found in the current study can be used as valuable sources to predict locations of platelet aggregation and the propagation of the coagulation cascade with respect to the valve design factors. The high-resolution μPIV system allowed identification of specific variations of fluid dynamic parameters (Vel, VSS, and RSS_{app}) across the three valves from the global velocity maps. The results obtained from this study demonstrated that the Standard valve had a more optimal gap width than the other valves based on the shear stress levels and washout potential during diastole. Previous in-vitro and ex-vivo hinge studies conducted by Travis, Leo, and Fallon et al. (Travis, 2001; Leo, 2005; Fallon, 2006) also reported the superior performance of the standard SJM valve in terms of platelet damage and fluid dynamic performance compared to other valves with different gap widths. This agreement found across different studies highlights the importance of hinge gap width in determining the blood damage potential of a BMHV, and these methodologies can be used as guidance to prosthetic heart valve designs where mating tolerances may significantly impact the potential for thrombus formation. The numerical hinge flow studies conducted by Simon et al and Yun et al [Simon, 2010; Yun, 2012] are also an additional powerful tool and resource to be used in conjunction with in-vitro and ex-vivo techniques. Numerical methods allow investigations of blood damage potential in BMHVs under finer spatial and temporal resolution conditions, which are difficult to achieve with experimental techniques. Use of these resources can help to further evaluate the BMHV designs tested in the current study and lead to better designs.

CHAPTER 8

LIMITATIONS

A few limitations exist in this study due to the experimental factors encountered during the investigation of complex hinge flows. First, due to the limited seeding density at the upper measurement planes, the ensemble averaging technique was only used at the FLAT and 195µm plane to calculate RSS_{app} values. However based on previous studies, the lower measurement planes have been shown to indicate the highest thromboembolic potential [Leo, 2006; Simon, 2007; Simon, 2010] which was investigated in detail in this study.

Secondly, a cyclic variation in velocity measurement exists primarily due to the cycle-to-cycle variation of the leaflet kinematics as well as fluctuations introduced by the flow and pressure in the system. Although it is difficult to isolate the cycle-to-cycle variations of the loop, a precisely controlled pulsatile flow system was used in this study in an effort to keep these fluctuations to a minimum. Subsequently, the cycle-to-cycle variation in velocity was captured from the RSS_{app} fields. In order to rigorously investigate the cyclic variations arising due to leaflet dynamics, future studies should characterize the cycle to cycle variations in the pulsatile flow system by quantifying the fluctuations in the flow field upstream of the valve (ventricular side). Such information will allow estimation of the velocity fluctuation in the free stream region where cycle-to-cycle fluctuations arise from the use of pulse duplicator alone.

Finally, the 2D global velocity maps presented in this study represent the dominant velocity components in each of the imaging planes across the hinge, caused by a reverse axial flow across the semi-circular geometry of the hinge. Nevertheless, as the hinge region is a complex 3D structure, out-of-plane flow will also be an important variable to be studied [Simon, 2010]. However, measurement of the third velocity component is difficult due to limited optical access with the clinical valve model used in this study. It was ensured that the imaging plane is oriented such that the dominant velocity components are captured in this study. To reduce the effect of out-of-plane particles on velocity calculation, images were pre-processed using a sliding background subtraction filter to eliminate defocused particles. Further studies should use a particle tracking and/or stereoscopic PIV technique to resolve unknown parameters such as full exposure time and the third velocity component.

CHAPTER 9

CONCLUSIONS

In the current study, a μPIV system was developed to characterize the global flow fields in the hinge region of BMHVs. The present studies were conducted under steady leakage and fully pulsatile flow conditions, representing physiological aortic valve hemodynamic conditions. The flow dynamics in the hinge were very complex across all measurement planes during steady diastolic leakage flow conditions. At lower levels within the hinge recess, a leakage jet and low flow regions were seen at the ventricular side of the hinge region, which can be correlated to the shear stress-induced blood damage leading to platelet activation in the valve. The flow fields at deeper levels within hinge recess showed strong velocity jets with uniform direction that can aid washout of blood elements. These particular traits compare very closely to previous LDV and CFD studies conducted with similar valve models (Simon, 2004; Leo, 2006; Simon, 2010; Yun, 2012).

Experiments with fully pulsatile flow conditions investigated the effect of hinge gap width on flow fields in SJM bileaflet mechanical heart valves. The hinge gap width was found to alter shear stress levels and washout potential during leakage flow but had minimal effect during the forward flow. Reynolds shear stress levels increased with respect to the larger hinge gap width with altered location of high fluctuation regions in the three valves.

The results from this study suggest that the BMHV hinge design is a fine balance between reduction of fluid shear stresses and areas of flow stasis during leakage flow, and needs to be optimized to ensure minimal thromboembolic complications.

Overall, the current study demonstrates the ability of high-resolution μPIV in characterizing whole flow fields in the micron-scale domain compared to other experimental methods. The methodology established in this paper can be extended to different MHV designs and other implantable cardiovascular devices, where micro-scale flow studies may be critical to assessing the potential for hemolytic and thromboembolic complications.

CHAPTER 10

RECOMMENDATIONS

The current work has proven the novel features of the experimental technique developed in this study to characterize the global hinge flow fields. Nevertheless, few improvements can be made in the following aspects of the study. First, further work with μPIV measurements taken in the plane of the B-datum and peripheral gaps, however, would be required for the complete assessment of the blood damage potential in a BMHV. Such information can also be linked with the findings from this study such as the leaflet translational motion.

Second improvement of this study would be the modification of the clear housing BMHV model to allow measurement of the out-of-plane velocity field. The clear housing BMHV model used in this study as well as previous experimental studies were specifically machined to vertically see through the butterfly-shaped hinge cavity. Subsequently, the optical access of the side view of the hinge with a semi-circular leaflet ear is extremely limited. To date, no experimental study has focused on investigating the out-of-plane flow measurement within the valve hinges. Use of micro-CT scans of BMHV hinge to redesign such prototype would be very feasible, since complete dimension of the hinge region has been measured and reconstructed by Simon et al (Simon, 2009). Another improvement with the BMHV model would be to embed a small reference point on the leaflet surface in order to more efficiently track the cycle-to-cycle variation of the leaflet translational motion. Such modification will allow precise measurement of the leaflet position with respect to the instantaneous flow field, rather than binning flow fields into two dominant groups.

At last, the inclusion of full exposure times of individual particles into the current study would provide more accurate prediction of the blood damage potential. Such improvement would be possible with incorporating high speed-PIV and/or Lagrangian particle tracking techniques into the current experimental system.

APPENDIX A

METHODS-RELATED MATERIALS

A1. Micro-CT scans of BMHV

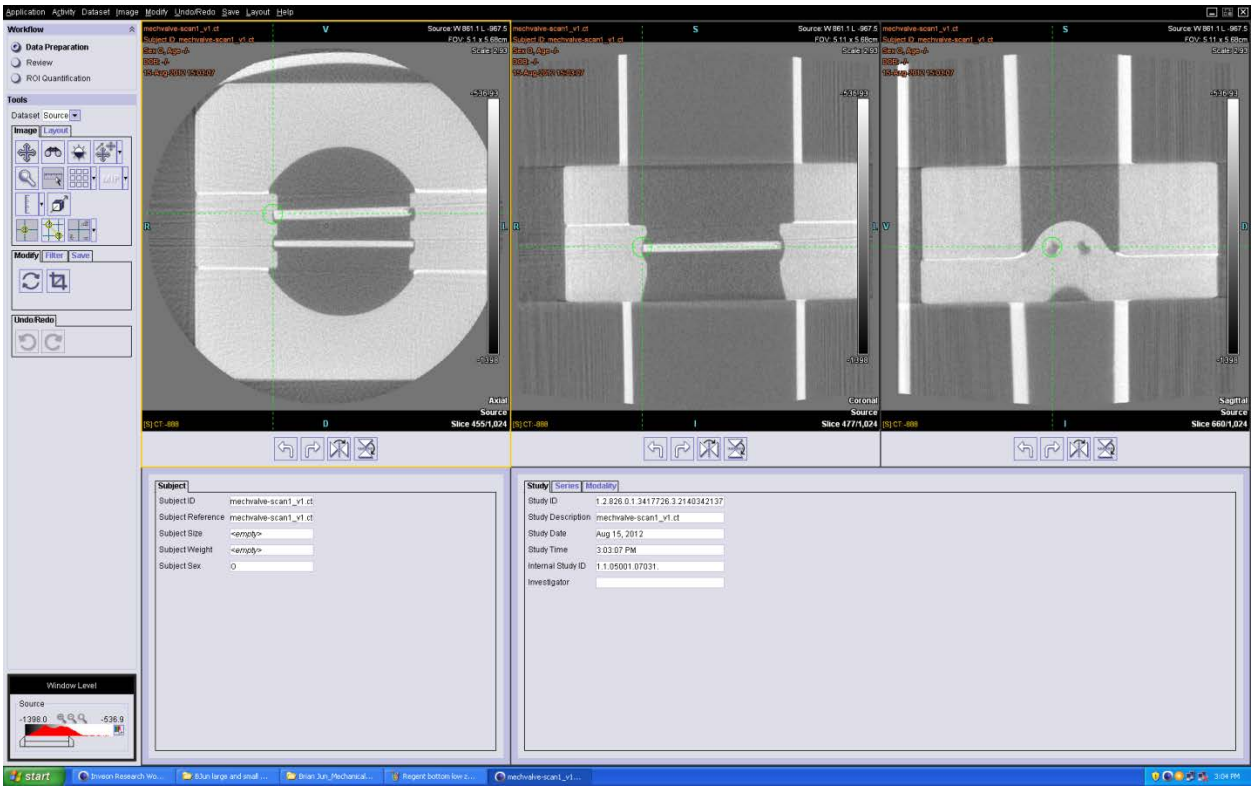

Figure A.1.1: Illustration of measuring the hinge gap width from µCT scan images

1. Import µCT scan images from Inveon Research Workplace (µCT facility in IBB)
2. Adjust cursors from three windows shown above to select the region of interest
3. Zoom in the region of interest in order to use the measurement tool
4. Click the “measurement” option from the tool box, drag a line within the region of interest as represented on Figure A.1.2 below. The measured distance is displayed in millimeter.

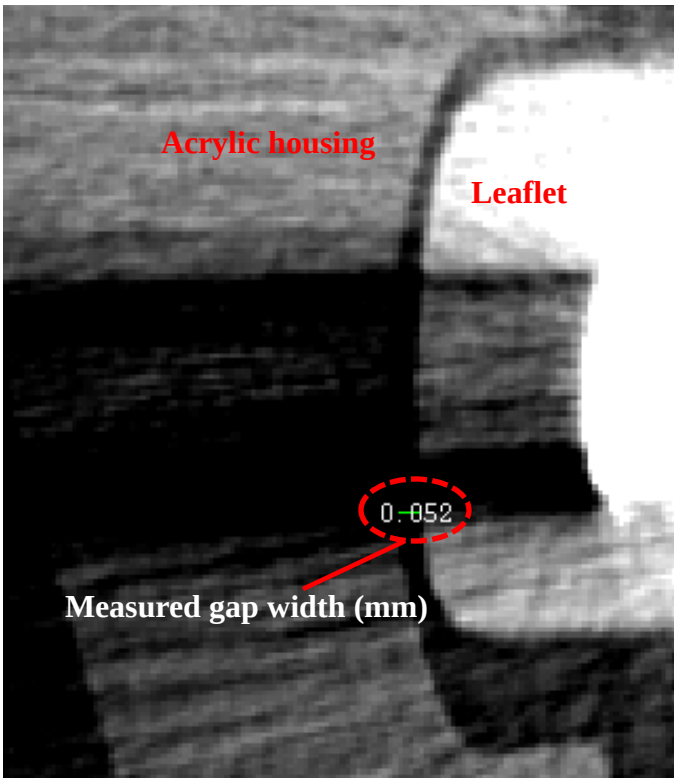

Figure A.1.2: Measuring BMHV hinge gap width from Inveon Research Workplace.

A2. Setting up the Velmax motor-driven traverse system

1. Launch FlowSizer (TSI Inc, USA)
2. Select “Traverse” from the top window (Figure A.2.1)
3. “Traverse manager” window will appear as represented on Figure A.2.2
4. Select “Setup” menu from the lower right corner
5. This window allows to select desired unit (mm or inch) for the traverse motion as represented on Figure A.2.3
6. Go back to the “Traverse manager” window, and input distances into X and Y position boxes.
7. Click “Move to”, to enable operation of the traverse.

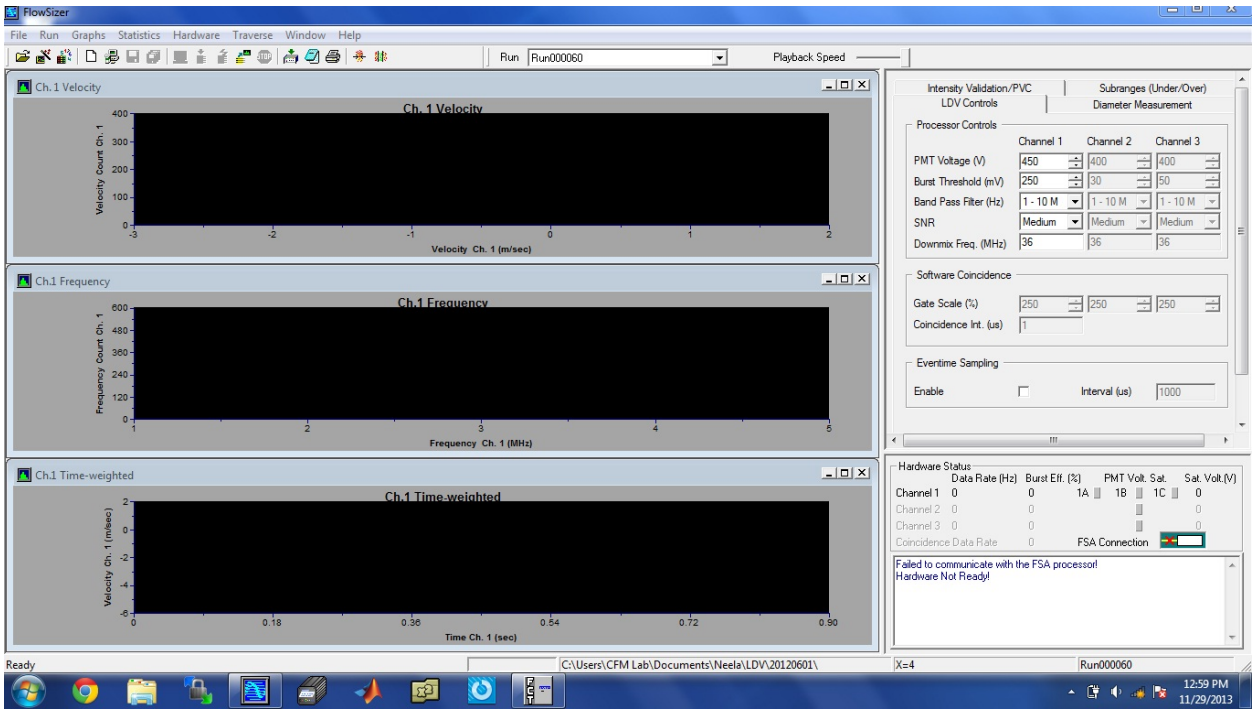

Figure A.2.1: FlowSizer main screen

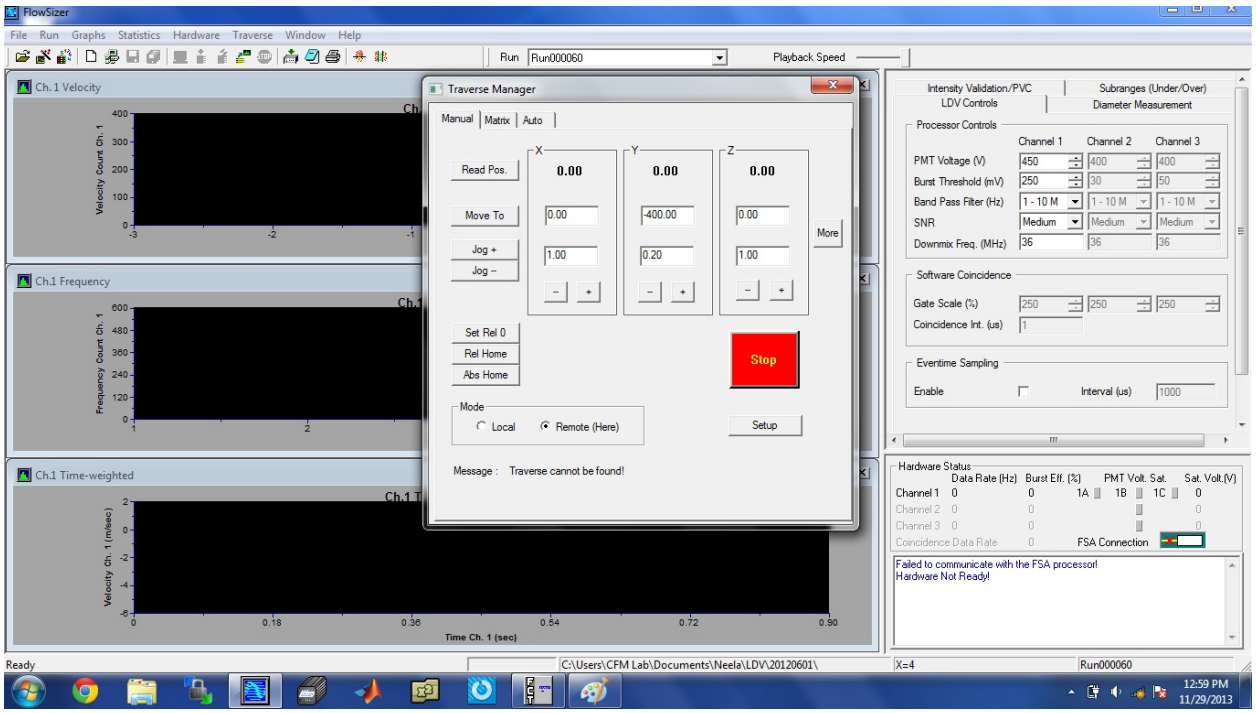

Figure A.2.2: FlowSizer traverse menu

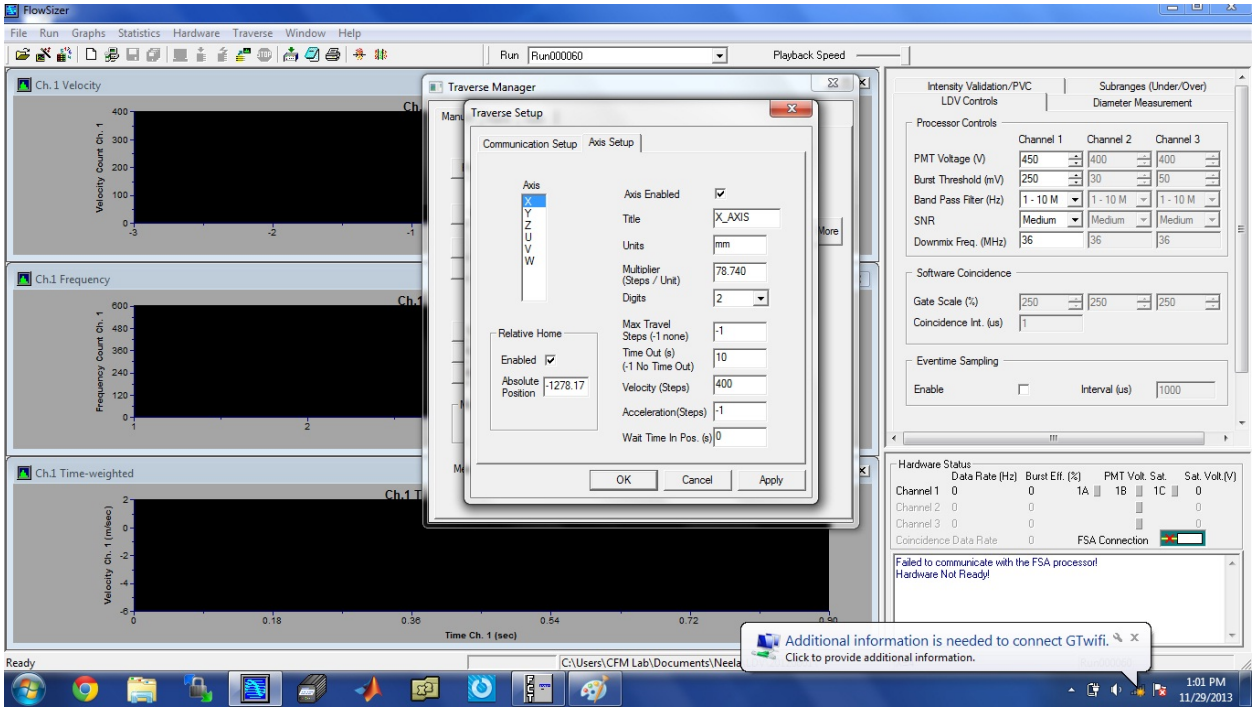

Figure A.2.3: FlowSizer traverse menu – Axis setup

APPENDIX B

EXPERIMENTAL PROTOCOL-RELATED MATERIALS

B1. FESTO linear actuator motion profile during the cardiac cycle

Table B.1.1: Forward stroke motion.

position(mm)	Velocity (mm/s)	Accel (m/s^2)	Flow rate (L/min)	time (ms)
0	0	13	0	0
0.0065	13	13	0.2510586	1
0.026	26	13	0.5021172	2
0.0585	39	13	0.7531758	3
0.104	52	13	1.0042344	4
0.1625	65	13	1.255293	5
0.234	78	13	1.5063516	6
0.3185	91	13	1.7574102	7
0.416	104	13	2.0084688	8
0.5265	117	13	2.2595274	9
0.65	130	13	2.510586	10
0.7865	143	13	2.7616446	11
0.936	156	13	3.0127032	12
1.0985	169	13	3.2637618	13
1.274	182	13	3.5148204	14
1.4625	195	13	3.765879	15
1.664	208	13	4.0169376	16
1.8785	221	13	4.2679962	17
2.106	234	13	4.5190548	18
2.3465	247	13	4.7701134	19
2.6	260	13	5.021172	20
2.8665	273	13	5.2722306	21
3.146	286	13	5.5232892	22
3.4385	299	13	5.7743478	23
3.744	312	13	6.0254064	24
4.0625	325	13	6.276465	25
4.394	338	13	6.5275236	26
4.7385	351	13	6.7785822	27
5.096	364	13	7.0296408	28
5.4665	377	13	7.2806994	29
5.85	390	13	7.531758	30
6.2465	403	13	7.7828166	31
6.656	416	13	8.0338752	32
7.0785	429	13	8.2849338	33

7.514	442	13	8.5359924	34
7.9625	455	13	8.787051	35
8.424	468	13	9.0381096	36
8.8985	481	13	9.2891682	37
9.386	494	13	9.5402268	38
9.8865	507	13	9.7912854	39
10.4	520	13	10.042344	40
10.9265	533	13	10.2934026	41
11.466	546	13	10.5444612	42
12.0185	559	13	10.7955198	43
12.584	572	13	11.0465784	44
13.1625	585	13	11.297637	45
13.754	598	13	11.5486956	46
14.3585	611	13	11.7997542	47
14.976	624	13	12.0508128	48
15.6065	637	13	12.3018714	49
16.25	650	13	12.55293	50
16.9065	663	13	12.8039886	51
17.576	676	13	13.0550472	52
18.2585	689	13	13.3061058	53
18.954	702	13	13.5571644	54
19.6625	715	13	13.808223	55
20.384	728	13	14.0592816	56
21.1185	741	13	14.3103402	57
21.866	754	13	14.5613988	58
22.6265	767	13	14.8124574	59
23.4	780	13	15.063516	60
24.1865	793	13	15.3145746	61
24.986	806	13	15.5656332	62
25.7985	819	13	15.8166918	63
26.624	832	13	16.0677504	64
27.4625	845	13	16.318809	65
28.314	858	13	16.5698676	66
29.1785	871	13	16.8209262	67
30.056	884	13	17.0719848	68
30.9465	897	13	17.3230434	69
31.85	910	13	17.574102	70
32.7665	923	13	17.8251606	71
33.696	936	13	18.0762192	72
34.6385	949	13	18.3272778	73
35.594	962	13	18.5783364	74
36.5625	975	13	18.829395	75
37.544	988	13	19.0804536	76

38.5385	1001	13	19.3315122	77
39.546	1014	13	19.5825708	78
40.5665	1027	13	19.8336294	79
41.6	1040	13	20.084688	80
42.6465	1053	13	20.3357466	81
43.706	1066	13	20.5868052	82
44.7785	1079	13	20.8378638	83
45.864	1092	13	21.0889224	84
46.9625	1105	13	21.339981	85
48.074	1118	13	21.5910396	86
49.1985	1131	13	21.8420982	87
50.336	1144	13	22.0931568	88
51.4865	1157	13	22.3442154	89
52.65	1170	13	22.595274	90
53.8265	1183	13	22.8463326	91
55.016	1196	13	23.0973912	92
56.2185	1209	13	23.3484498	93
57.434	1222	13	23.5995084	94
58.6625	1235	13	23.850567	95
59.904	1248	13	24.1016256	96
61.1585	1261	13	24.3526842	97
62.426	1274	13	24.6037428	98
63.7065	1287	13	24.8548014	99
65	1300	13	25.10586	100
66.3	1300	0	25.10586	101
67.6	1300	0	25.10586	102
68.9	1300	0	25.10586	103
70.2	1300	0	25.10586	104
71.5	1300	0	25.10586	105
72.8	1300	0	25.10586	106
74.1	1300	0	25.10586	107
75.4	1300	0	25.10586	108
76.7	1300	0	25.10586	109
78	1300	0	25.10586	110
79.3	1300	0	25.10586	111
80.6	1300	0	25.10586	112
81.9	1300	0	25.10586	113
83.2	1300	0	25.10586	114
84.5	1300	0	25.10586	115
85.8	1300	0	25.10586	116
87.1	1300	0	25.10586	117
88.4	1300	0	25.10586	118
89.7	1300	0	25.10586	119

91	1300	0	25.10586	120
92.3	1300	0	25.10586	121
93.6	1300	0	25.10586	122
94.9	1300	0	25.10586	123
96.2	1300	0	25.10586	124
97.5	1300	0	25.10586	125
98.8	1300	0	25.10586	126
100.1	1300	0	25.10586	127
101.4	1300	0	25.10586	128
102.7	1300	0	25.10586	129
104	1300	0	25.10586	130
105.3	1300	0	25.10586	131
106.6	1300	0	25.10586	132
107.9	1300	0	25.10586	133
109.2	1300	0	25.10586	134
110.5	1300	0	25.10586	135
111.8	1300	0	25.10586	136
113.1	1300	0	25.10586	137
114.4	1300	0	25.10586	138
115.67	1292	-8	24.9513624	139
116.958	1284	-8	24.7968648	140
118.238	1276	-8	24.6423672	141
119.51	1268	-8	24.4878696	142
120.774	1260	-8	24.333372	143
122.03	1252	-8	24.1788744	144
123.278	1244	-8	24.0243768	145
124.518	1236	-8	23.8698792	146
125.75	1228	-8	23.7153816	147
126.974	1220	-8	23.560884	148
128.19	1212	-8	23.4063864	149
129.398	1204	-8	23.2518888	150
130.598	1196	-8	23.0973912	151
131.79	1188	-8	22.9428936	152
132.974	1180	-8	22.788396	153
134.15	1172	-8	22.6338984	154
135.318	1164	-8	22.4794008	155
136.478	1156	-8	22.3249032	156
137.63	1148	-8	22.1704056	157
138.774	1140	-8	22.015908	158
139.91	1132	-8	21.8614104	159
141.038	1124	-8	21.7069128	160
142.158	1116	-8	21.5524152	161
143.27	1108	-8	21.3979176	162

144.374	1100	-8	21.24342	163
145.47	1092	-8	21.0889224	164
146.558	1084	-8	20.9344248	165
147.638	1076	-8	20.7799272	166
148.71	1068	-8	20.6254296	167
149.774	1060	-8	20.470932	168
150.83	1052	-8	20.3164344	169
151.878	1044	-8	20.1619368	170
152.918	1036	-8	20.0074392	171
153.95	1028	-8	19.8529416	172
154.974	1020	-8	19.698444	173
155.99	1012	-8	19.5439464	174
156.998	1004	-8	19.3894488	175
157.998	996	-8	19.2349512	176
158.99	988	-8	19.0804536	177
159.974	980	-8	18.925956	178
160.95	972	-8	18.7714584	179
161.918	964	-8	18.6169608	180
162.878	956	-8	18.4624632	181
163.83	948	-8	18.3079656	182
164.774	940	-8	18.153468	183
165.71	932	-8	17.9989704	184
166.638	924	-8	17.8444728	185
167.558	916	-8	17.6899752	186
168.47	908	-8	17.5354776	187
169.374	900	-8	17.38098	188
170.27	892	-8	17.2264824	189
171.158	884	-8	17.0719848	190
172.038	876	-8	16.9174872	191
172.91	868	-8	16.7629896	192
173.774	860	-8	16.608492	193
174.63	852	-8	16.4539944	194
175.478	844	-8	16.2994968	195
176.318	836	-8	16.1449992	196
177.15	828	-8	15.9905016	197
177.974	820	-8	15.836004	198
178.79	812	-8	15.6815064	199
179.598	804	-8	15.5270088	200
180.398	796	-8	15.3725112	201
181.19	788	-8	15.2180136	202
181.974	780	-8	15.063516	203
182.75	772	-8	14.9090184	204
183.518	764	-8	14.7545208	205

184.278	756	-8	14.6000232	206
185.03	748	-8	14.4455256	207
185.774	740	-8	14.291028	208
186.51	732	-8	14.1365304	209
187.238	724	-8	13.9820328	210
187.958	716	-8	13.8275352	211
188.67	708	-8	13.6730376	212
189.374	700	-8	13.51854	213
190.07	692	-8	13.3640424	214
190.758	684	-8	13.2095448	215
191.438	676	-8	13.0550472	216
192.11	668	-8	12.9005496	217
192.774	660	-8	12.746052	218
193.43	652	-8	12.5915544	219
194.078	644	-8	12.4370568	220
194.718	636	-8	12.2825592	221
195.35	628	-8	12.1280616	222
195.974	620	-8	11.973564	223
196.59	612	-8	11.8190664	224
197.198	604	-8	11.6645688	225
197.798	596	-8	11.5100712	226
198.39	588	-8	11.3555736	227
198.974	580	-8	11.201076	228
199.55	572	-8	11.0465784	229
200.118	564	-8	10.8920808	230
200.678	556	-8	10.7375832	231
201.23	548	-8	10.5830856	232
201.774	540	-8	10.428588	233
202.31	532	-8	10.2740904	234
202.838	524	-8	10.1195928	235
203.358	516	-8	9.9650952	236
203.87	508	-8	9.8105976	237
204.374	500	-8	9.6561	238
204.87	492	-8	9.5016024	239
205.358	484	-8	9.3471048	240
205.838	476	-8	9.1926072	241
206.31	468	-8	9.0381096	242
206.774	460	-8	8.883612	243
207.23	452	-8	8.7291144	244
207.678	444	-8	8.5746168	245
208.118	436	-8	8.4201192	246
208.55	428	-8	8.2656216	247
208.974	420	-8	8.111124	248

209.39	412	-8	7.9566264	249
209.798	404	-8	7.8021288	250
210.198	396	-8	7.6476312	251
210.59	388	-8	7.4931336	252
210.974	380	-8	7.338636	253
211.35	372	-8	7.1841384	254
211.718	364	-8	7.0296408	255
212.078	356	-8	6.8751432	256
212.43	348	-8	6.7206456	257
212.774	340	-8	6.566148	258
213.11	332	-8	6.4116504	259
213.438	324	-8	6.2571528	260
213.758	316	-8	6.1026552	261
214.07	308	-8	5.9481576	262
214.374	300	-8	5.79366	263
214.67	292	-8	5.6391624	264
214.958	284	-8	5.4846648	265
215.238	276	-8	5.3301672	266
215.51	268	-8	5.1756696	267
215.774	260	-8	5.021172	268
216.03	252	-8	4.8666744	269
216.278	244	-8	4.7121768	270
216.518	236	-8	4.5576792	271
216.75	228	-8	4.4031816	272
216.974	220	-8	4.248684	273
217.19	212	-8	4.0941864	274
217.398	204	-8	3.9396888	275
217.598	196	-8	3.7851912	276
217.79	188	-8	3.6306936	277
217.974	180	-8	3.476196	278
218.15	172	-8	3.3216984	279
218.318	164	-8	3.1672008	280
218.478	156	-8	3.0127032	281
218.63	148	-8	2.8582056	282
218.774	140	-8	2.703708	283
218.91	132	-8	2.5492104	284
219.038	124	-8	2.3947128	285
219.158	116	-8	2.2402152	286
219.27	108	-8	2.0857176	287
219.374	100	-8	1.93122	288
219.47	92	-8	1.7767224	289
219.558	84	-8	1.6222248	290
219.638	76	-8	1.4677272	291

219.71	68	-8	1.3132296	292
219.774	60	-8	1.158732	293
219.83	52	-8	1.0042344	294
219.878	44	-8	0.8497368	295
219.918	36	-8	0.6952392	296
219.95	28	-8	0.5407416	297
219.974	20	-8	0.386244	298
219.99	12	-8	0.2317464	299
219.998	4	-8	0.0772488	300

Table B.1.2: Bakcward stroke motion.

position(mm)	Velocity (mm/s)	Accel (m/s^2)	Flow rate (L/min)	time (ms)
0	0	9	0	301
0.0045	9	9	0.1738098	302
0.018	18	9	0.3476196	303
0.0405	27	9	0.5214294	304
0.072	36	9	0.6952392	305
0.1125	45	9	0.869049	306
0.162	54	9	1.0428588	307
0.2205	63	9	1.2166686	308
0.288	72	9	1.3904784	309
0.3645	81	9	1.5642882	310
0.45	90	9	1.738098	311
0.5445	99	9	1.9119078	312
0.648	108	9	2.0857176	313
0.7605	117	9	2.2595274	314
0.882	126	9	2.4333372	315
1.0125	135	9	2.607147	316
1.152	144	9	2.7809568	317
1.3005	153	9	2.9547666	318
1.458	162	9	3.1285764	319
1.6245	171	9	3.3023862	320
1.8	180	9	3.476196	321
1.9845	189	9	3.6500058	322
2.178	198	9	3.8238156	323
2.3805	207	9	3.9976254	324
2.592	216	9	4.1714352	325
2.8125	225	9	4.345245	326
3.042	234	9	4.5190548	327
3.2805	243	9	4.6928646	328
3.528	252	9	4.8666744	329

3.7845	261	9	5.0404842	330
4.05	270	9	5.214294	331
4.3245	279	9	5.3881038	332
4.608	288	9	5.5619136	333
4.9005	297	9	5.7357234	334
5.202	306	9	5.9095332	335
5.5125	315	9	6.083343	336
5.832	324	9	6.2571528	337
6.1605	333	9	6.4309626	338
6.498	342	9	6.6047724	339
6.8445	351	9	6.7785822	340
7.2	360	9	6.952392	341
7.5645	369	9	7.1262018	342
7.938	378	9	7.3000116	343
8.3205	387	9	7.4738214	344
8.712	396	9	7.6476312	345
9.1125	405	9	7.821441	346
9.522	414	9	7.9952508	347
9.9405	423	9	8.1690606	348
10.3205	430	9	8.304246	349
10.7505	430	9	8.304246	350
11.1805	430	9	8.304246	351
11.6105	430	9	8.304246	352
12.0405	430	9	8.304246	353
12.4705	430	9	8.304246	354
12.9005	430	9	8.304246	355
13.3305	430	9	8.304246	356
13.7605	430	9	8.304246	357
14.1905	430	9	8.304246	358
14.6205	430	9	8.304246	359
15.0505	430	9	8.304246	360
15.4805	430	9	8.304246	361
15.9105	430	9	8.304246	362
16.3405	430	9	8.304246	363
16.7705	430	9	8.304246	364
17.2005	430	9	8.304246	365
17.6305	430	9	8.304246	366
18.0605	430	9	8.304246	367
18.4905	430	9	8.304246	368
18.9205	430	9	8.304246	369
19.3505	430	9	8.304246	370
19.7805	430	9	8.304246	371
20.2105	430	9	8.304246	372

20.6405	430	9	8.304246	373
21.0705	430	9	8.304246	374
21.5005	430	9	8.304246	375
21.9305	430	9	8.304246	376
22.3605	430	9	8.304246	377
22.7905	430	9	8.304246	378
23.2205	430	9	8.304246	379
23.6505	430	-9	8.304246	380
24.0805	430	-9	8.304246	381
24.5105	430	-9	8.304246	382
24.9405	430	-9	8.304246	383
25.3705	430	-9	8.304246	384
25.8005	430	-9	8.304246	385
26.2305	430	-9	8.304246	386
26.6605	430	-9	8.304246	387
27.0905	430	-9	8.304246	388
27.5205	430	-9	8.304246	389
27.9505	430	-9	8.304246	390
28.3805	430	-9	8.304246	391
28.8105	430	-9	8.304246	392
29.2405	430	-9	8.304246	393
29.6705	430	-9	8.304246	394
30.1005	430	-9	8.304246	395
30.5305	430	-9	8.304246	396
30.9605	430	-9	8.304246	397
31.3905	430	-9	8.304246	398
31.8205	430	-9	8.304246	399
32.2505	430	-9	8.304246	400
32.6805	430	-9	8.304246	401
33.1105	430	-9	8.304246	402
33.5405	430	-9	8.304246	403
33.9705	430	-9	8.304246	404
34.4005	430	-9	8.304246	405
34.8305	430	-9	8.304246	406
35.2605	430	-9	8.304246	407
35.6905	430	-9	8.304246	408
36.1205	430	-9	8.304246	409
36.5505	430	-9	8.304246	410
36.9805	430	-9	8.304246	411
37.4105	430	-9	8.304246	412
37.8405	430	-9	8.304246	413
38.2705	430	-9	8.304246	414
38.7005	430	-9	8.304246	415

39.1305	430	-9	8.304246	416
39.5605	430	-9	8.304246	417
39.9905	430	-9	8.304246	418
40.4205	430	-9	8.304246	419
40.8505	430	-9	8.304246	420
41.2805	430	-9	8.304246	421
41.7105	430	-9	8.304246	422
42.1405	430	-9	8.304246	423
42.5705	430	-9	8.304246	424
43.0005	430	-9	8.304246	425
43.4305	430	-9	8.304246	426
43.8605	430	-9	8.304246	427
44.2905	430	-9	8.304246	428
44.7205	430	-9	8.304246	429
45.1505	430	-9	8.304246	430
45.5805	430	-9	8.304246	431
46.0105	430	-9	8.304246	432
46.4405	430	-9	8.304246	433
46.8705	430	-9	8.304246	434
47.3005	430	-9	8.304246	435
47.7305	430	-9	8.304246	436
48.1605	430	-9	8.304246	437
48.5905	430	-9	8.304246	438
49.0205	430	-9	8.304246	439
49.4505	430	-9	8.304246	440
49.8805	430	-9	8.304246	441
50.3105	430	-9	8.304246	442
50.7405	430	-9	8.304246	443
51.1705	430	-9	8.304246	444
51.6005	430	-9	8.304246	445
52.0305	430	-9	8.304246	446
52.4605	430	-9	8.304246	447
52.8905	430	-9	8.304246	448
53.3205	430	-9	8.304246	449
53.7505	430	-9	8.304246	450
54.1805	430	-9	8.304246	451
54.6105	430	-9	8.304246	452
55.0405	430	-9	8.304246	453
55.4705	430	-9	8.304246	454
55.9005	430	-9	8.304246	455
56.3305	430	-9	8.304246	456
56.7605	430	-9	8.304246	457
57.1905	430	-9	8.304246	458

57.6205	430	-9	8.304246	459
58.0505	430	-9	8.304246	460
58.4805	430	-9	8.304246	461
58.9105	430	-9	8.304246	462
59.3405	430	-9	8.304246	463
59.7705	430	-9	8.304246	464
60.2005	430	-9	8.304246	465
60.6305	430	-9	8.304246	466
61.0605	430	-9	8.304246	467
61.4905	430	-9	8.304246	468
61.9205	430	-9	8.304246	469
62.3505	430	-9	8.304246	470
62.7805	430	-9	8.304246	471
63.2105	430	-9	8.304246	472
63.6405	430	-9	8.304246	473
64.0705	430	-9	8.304246	474
64.5005	430	-9	8.304246	475
64.9305	430	-9	8.304246	476
65.3605	430	-9	8.304246	477
65.7905	430	-9	8.304246	478
66.2205	430	-9	8.304246	479
66.6505	430	-9	8.304246	480
67.0805	430	-9	8.304246	481
67.5105	430	-9	8.304246	482
67.9405	430	-9	8.304246	483
68.3705	430	-9	8.304246	484
68.8005	430	-9	8.304246	485
69.2305	430	-9	8.304246	486
69.6605	430	-9	8.304246	487
70.0905	430	-9	8.304246	488
70.5205	430	-9	8.304246	489
70.9505	430	-9	8.304246	490
71.3805	430	-9	8.304246	491
71.8105	430	-9	8.304246	492
72.2405	430	-9	8.304246	493
72.6705	430	-9	8.304246	494
73.1005	430	-9	8.304246	495
73.5305	430	-9	8.304246	496
73.9605	430	-9	8.304246	497
74.3905	430	-9	8.304246	498
74.8205	430	-9	8.304246	499
75.2505	430	-9	8.304246	500
75.6805	430	-9	8.304246	501

76.1105	430	-9	8.304246	502
76.5405	430	-9	8.304246	503
76.9705	430	-9	8.304246	504
77.4005	430	-9	8.304246	505
77.8305	430	-9	8.304246	506
78.2605	430	-9	8.304246	507
78.6905	430	-9	8.304246	508
79.1205	430	-9	8.304246	509
79.5505	430	-9	8.304246	510
79.9805	430	-9	8.304246	511
80.4105	430	-9	8.304246	512
80.8405	430	-9	8.304246	513
81.2705	430	-9	8.304246	514
81.7005	430	-9	8.304246	515
82.1305	430	-9	8.304246	516
82.5605	430	-9	8.304246	517
82.9905	430	-9	8.304246	518
83.4205	430	-9	8.304246	519
83.8505	430	-9	8.304246	520
84.2805	430	-9	8.304246	521
84.7105	430	-9	8.304246	522
85.1405	430	-9	8.304246	523
85.5705	430	-9	8.304246	524
86.0005	430	-9	8.304246	525
86.4305	430	-9	8.304246	526
86.8605	430	-9	8.304246	527
87.2905	430	-9	8.304246	528
87.7205	430	-9	8.304246	529
88.1505	430	-9	8.304246	530
88.5805	430	-9	8.304246	531
89.0105	430	-9	8.304246	532
89.4405	430	-9	8.304246	533
89.8705	430	-9	8.304246	534
90.3005	430	-9	8.304246	535
90.7305	430	-9	8.304246	536
91.1605	430	-9	8.304246	537
91.5905	430	-9	8.304246	538
92.0205	430	-9	8.304246	539
92.4505	430	-9	8.304246	540
92.8805	430	-9	8.304246	541
93.3105	430	-9	8.304246	542
93.7405	430	-9	8.304246	543
94.1705	430	-9	8.304246	544

94.6005	430	-9	8.304246	545
95.0305	430	-9	8.304246	546
95.4605	430	-9	8.304246	547
95.8905	430	-9	8.304246	548
96.3205	430	-9	8.304246	549
96.7505	430	-9	8.304246	550
97.1805	430	-9	8.304246	551
97.6105	430	-9	8.304246	552
98.0405	430	-9	8.304246	553
98.4705	430	-9	8.304246	554
98.9005	430	-9	8.304246	555
99.3305	430	-9	8.304246	556
99.7605	430	-9	8.304246	557
100.1905	430	-9	8.304246	558
100.6205	430	-9	8.304246	559
101.0505	430	-9	8.304246	560
101.4805	430	-9	8.304246	561
101.9105	430	-9	8.304246	562
102.3405	430	-9	8.304246	563
102.7705	430	-9	8.304246	564
103.2005	430	-9	8.304246	565
103.6305	430	-9	8.304246	566
104.0605	430	-9	8.304246	567
104.4905	430	-9	8.304246	568
104.9205	430	-9	8.304246	569
105.3505	430	-9	8.304246	570
105.7805	430	-9	8.304246	571
106.2105	430	-9	8.304246	572
106.6405	430	-9	8.304246	573
107.0705	430	-9	8.304246	574
107.5005	430	-9	8.304246	575
107.9305	430	-9	8.304246	576
108.3605	430	-9	8.304246	577
108.7905	430	-9	8.304246	578
109.2205	430	-9	8.304246	579
109.6505	430	-9	8.304246	580
110.0805	430	-9	8.304246	581
110.5105	430	-9	8.304246	582
110.9405	430	-9	8.304246	583
111.3705	430	-9	8.304246	584
111.8005	430	-9	8.304246	585
112.2305	430	-9	8.304246	586
112.6605	430	-9	8.304246	587

113.0905	430	-9	8.304246	588
113.5205	430	-9	8.304246	589
113.9505	430	-9	8.304246	590
114.3805	430	-9	8.304246	591
114.8105	430	-9	8.304246	592
115.2405	430	-9	8.304246	593
115.6705	430	-9	8.304246	594
116.1005	430	-9	8.304246	595
116.5305	430	-9	8.304246	596
116.9605	430	-9	8.304246	597
117.3905	430	-9	8.304246	598
117.8205	430	-9	8.304246	599
118.2505	430	-9	8.304246	600
118.6805	430	-9	8.304246	601
119.1105	430	-9	8.304246	602
119.5405	430	-9	8.304246	603
119.9705	430	-9	8.304246	604
120.4005	430	-9	8.304246	605
120.8305	430	-9	8.304246	606
121.2605	430	-9	8.304246	607
121.6905	430	-9	8.304246	608
122.1205	430	-9	8.304246	609
122.5505	430	-9	8.304246	610
122.9805	430	-9	8.304246	611
123.4105	430	-9	8.304246	612
123.8405	430	-9	8.304246	613
124.2705	430	-9	8.304246	614
124.7005	430	-9	8.304246	615
125.1305	430	-9	8.304246	616
125.5605	430	-9	8.304246	617
125.9905	430	-9	8.304246	618
126.4205	430	-9	8.304246	619
126.8505	430	-9	8.304246	620
127.2805	430	-9	8.304246	621
127.7105	430	-9	8.304246	622
128.1405	430	-9	8.304246	623
128.5705	430	-9	8.304246	624
129.0005	430	-9	8.304246	625
129.4305	430	-9	8.304246	626
129.8605	430	-9	8.304246	627
130.2905	430	-9	8.304246	628
130.7205	430	-9	8.304246	629
131.1505	430	-9	8.304246	630

131.5805	430	-9	8.304246	631
132.0105	430	-9	8.304246	632
132.4405	430	-9	8.304246	633
132.8705	430	-9	8.304246	634
133.3005	430	-9	8.304246	635
133.7305	430	-9	8.304246	636
134.1605	430	-9	8.304246	637
134.5905	430	-9	8.304246	638
135.0205	430	-9	8.304246	639
135.4505	430	-9	8.304246	640
135.8805	430	-9	8.304246	641
136.3105	430	-9	8.304246	642
136.7405	430	-9	8.304246	643
137.1705	430	-9	8.304246	644
137.6005	430	-9	8.304246	645
138.0305	430	-9	8.304246	646
138.4605	430	-9	8.304246	647
138.8905	430	-9	8.304246	648
139.3205	430	-9	8.304246	649
139.7505	430	-9	8.304246	650
140.1805	430	-9	8.304246	651
140.6105	430	-9	8.304246	652
141.0405	430	-9	8.304246	653
141.4705	430	-9	8.304246	654
141.9005	430	-9	8.304246	655
142.3305	430	-9	8.304246	656
142.7605	430	-9	8.304246	657
143.1905	430	-9	8.304246	658
143.6205	430	-9	8.304246	659
144.0505	430	-9	8.304246	660
144.4805	430	-9	8.304246	661
144.9105	430	-9	8.304246	662
145.3405	430	-9	8.304246	663
145.7705	430	-9	8.304246	664
146.2005	430	-9	8.304246	665
146.6305	430	-9	8.304246	666
147.0605	430	-9	8.304246	667
147.4905	430	-9	8.304246	668
147.9205	430	-9	8.304246	669
148.3505	430	-9	8.304246	670
148.7805	430	-9	8.304246	671
149.2105	430	-9	8.304246	672
149.6405	430	-9	8.304246	673

150.0705	430	-9	8.304246	674
150.5005	430	-9	8.304246	675
150.9305	430	-9	8.304246	676
151.3605	430	-9	8.304246	677
151.7905	430	-9	8.304246	678
152.2205	430	-9	8.304246	679
152.6505	430	-9	8.304246	680
153.0805	430	-9	8.304246	681
153.5105	430	-9	8.304246	682
153.9405	430	-9	8.304246	683
154.3705	430	-9	8.304246	684
154.8005	430	-9	8.304246	685
155.2305	430	-9	8.304246	686
155.6605	430	-9	8.304246	687
156.0905	430	-9	8.304246	688
156.5205	430	-9	8.304246	689
156.9505	430	-9	8.304246	690
157.3805	430	-9	8.304246	691
157.8105	430	-9	8.304246	692
158.2405	430	-9	8.304246	693
158.6705	430	-9	8.304246	694
159.1005	430	-9	8.304246	695
159.5305	430	-9	8.304246	696
159.9605	430	-9	8.304246	697
160.3905	430	-9	8.304246	698
160.8205	430	-9	8.304246	699
161.2505	430	-9	8.304246	700
161.6805	430	-9	8.304246	701
162.1105	430	-9	8.304246	702
162.5405	430	-9	8.304246	703
162.9705	430	-9	8.304246	704
163.4005	430	-9	8.304246	705
163.8305	430	-9	8.304246	706
164.2605	430	-9	8.304246	707
164.6905	430	-9	8.304246	708
165.1205	430	-9	8.304246	709
165.5505	430	-9	8.304246	710
165.9805	430	-9	8.304246	711
166.4105	430	-9	8.304246	712
166.8405	430	-9	8.304246	713
167.2705	430	-9	8.304246	714
167.7005	430	-9	8.304246	715
168.1305	430	-9	8.304246	716

168.5605	430	-9	8.304246	717
168.9905	430	-9	8.304246	718
169.4205	430	-9	8.304246	719
169.8505	430	-9	8.304246	720
170.2805	430	-9	8.304246	721
170.7105	430	-9	8.304246	722
171.1405	430	-9	8.304246	723
171.5705	430	-9	8.304246	724
172.0005	430	-9	8.304246	725
172.4305	430	-9	8.304246	726
172.8605	430	-9	8.304246	727
173.2905	430	-9	8.304246	728
173.7205	430	-9	8.304246	729
174.1505	430	-9	8.304246	730
174.5805	430	-9	8.304246	731
175.0105	430	-9	8.304246	732
175.4405	430	-9	8.304246	733
175.8705	430	-9	8.304246	734
176.3005	430	-9	8.304246	735
176.7305	430	-9	8.304246	736
177.1605	430	-9	8.304246	737
177.5905	430	-9	8.304246	738
178.0205	430	-9	8.304246	739
178.4505	430	-9	8.304246	740
178.8805	430	-9	8.304246	741
179.3105	430	-9	8.304246	742
179.7405	430	-9	8.304246	743
180.1705	430	-9	8.304246	744
180.6005	430	-9	8.304246	745
181.0305	430	-9	8.304246	746
181.4605	430	-9	8.304246	747
181.8905	430	-9	8.304246	748
182.3205	430	-9	8.304246	749
182.7505	430	-9	8.304246	750
183.1805	430	-9	8.304246	751
183.6105	430	-9	8.304246	752
184.0405	430	-9	8.304246	753
184.4705	430	-9	8.304246	754
184.9005	430	-9	8.304246	755
185.3305	430	-9	8.304246	756
185.7605	430	-9	8.304246	757
186.1905	430	-9	8.304246	758
186.6205	430	-9	8.304246	759

187.0505	430	-9	8.304246	760
187.4805	430	-9	8.304246	761
187.9105	430	-9	8.304246	762
188.3405	430	-9	8.304246	763
188.7705	430	-9	8.304246	764
189.2005	430	-9	8.304246	765
189.6305	430	-9	8.304246	766
190.0605	430	-9	8.304246	767
190.4905	430	-9	8.304246	768
190.9205	430	-9	8.304246	769
191.3505	430	-9	8.304246	770
191.7805	430	-9	8.304246	771
192.2105	430	-9	8.304246	772
192.6405	430	-9	8.304246	773
193.0705	430	-9	8.304246	774
193.5005	430	-9	8.304246	775
193.9305	430	-9	8.304246	776
194.3605	430	-9	8.304246	777
194.7905	430	-9	8.304246	778
195.2205	430	-9	8.304246	779
195.6505	430	-9	8.304246	780
196.0805	430	-9	8.304246	781
196.5105	430	-9	8.304246	782
196.9405	430	-9	8.304246	783
197.3705	430	-9	8.304246	784
197.8005	430	-9	8.304246	785
198.2305	430	-9	8.304246	786
198.6605	430	-9	8.304246	787
199.0905	430	-9	8.304246	788
199.5205	430	-9	8.304246	789
199.9505	430	-9	8.304246	790
200.3805	430	-9	8.304246	791
200.8105	430	-9	8.304246	792
201.2405	430	-9	8.304246	793
201.6705	430	-9	8.304246	794
202.1005	430	-9	8.304246	795
202.5305	430	-9	8.304246	796
202.9605	430	-9	8.304246	797
203.3905	430	-9	8.304246	798
203.8205	430	-9	8.304246	799
204.2505	430	-9	8.304246	800
204.6805	430	-9	8.304246	801
205.1105	430	-9	8.304246	802

205.5405	430	0	8.304246	803
205.9705	430	0	8.304246	804
206.4005	430	0	8.304246	805
206.8305	430	0	8.304246	806
207.2605	430	0	8.304246	807
207.6905	430	0	8.304246	808
208.1205	430	-9	8.304246	809
208.5505	430	-9	8.304246	810
208.9805	430	-9	8.304246	811
209.4105	430	-9	8.304246	812
209.68	430	-9	8.304246	813
210.1055	421	-9	8.1304362	814
210.522	412	-9	7.9566264	815
210.9295	403	-9	7.7828166	816
211.328	394	-9	7.6090068	817
211.7175	385	-9	7.435197	818
212.098	376	-9	7.2613872	819
212.4695	367	-9	7.0875774	820
212.832	358	-9	6.9137676	821
213.1855	349	-9	6.7399578	822
213.53	340	-9	6.566148	823
213.8655	331	-9	6.3923382	824
214.192	322	-9	6.2185284	825
214.5095	313	-9	6.0447186	826
214.818	304	-9	5.8709088	827
215.1175	295	-9	5.697099	828
215.408	286	-9	5.5232892	829
215.6895	277	-9	5.3494794	830
215.962	268	-9	5.1756696	831
216.2255	259	-9	5.0018598	832
216.48	250	-9	4.82805	833
216.7255	241	-9	4.6542402	834
216.962	232	-9	4.4804304	835
217.1895	223	-9	4.3066206	836
217.408	214	-9	4.1328108	837
217.6175	205	-9	3.959001	838
217.818	196	-9	3.7851912	839
218.0095	187	-9	3.6113814	840
218.192	178	-9	3.4375716	841
218.3655	169	-9	3.2637618	842
218.53	160	-9	3.089952	843
218.6855	151	-9	2.9161422	844
218.832	142	-9	2.7423324	845

218.9695	133	-9	2.5685226	846
219.098	124	-9	2.3947128	847
219.2175	115	-9	2.220903	848
219.328	106	-9	2.0470932	849
219.4295	97	-9	1.8732834	850
219.522	88	-9	1.6994736	851
219.6055	79	-9	1.5256638	852
219.68	70	-9	1.351854	853
219.7455	61	-9	1.1780442	854
219.802	52	-9	1.0042344	855
219.8495	43	-9	0.8304246	856
219.888	34	-9	0.6566148	857
219.9175	25	-9	0.482805	858
219.938	16	-9	0.3089952	859
219.9495	7	-9	0.1351854	860

B2. FESTO linear actuator motion tracking option

1. Launch “Festo Configuration Tool”.
2. From the main window (Figure B.2.1), select “Trace configuration” (Figure B.2.2)
3. From the “Trace configuration” window, select the variables of interest to be traced (position, velocity, and time)
4. Variables will be traced and acquired while the linear actuator is in motion
5. Select “Trace Data” from the main menu (Figure B.2.1)
6. Velocity, position, and time values are displayed by using cursors on the left side (Figure B.2.3 – B.2.4)

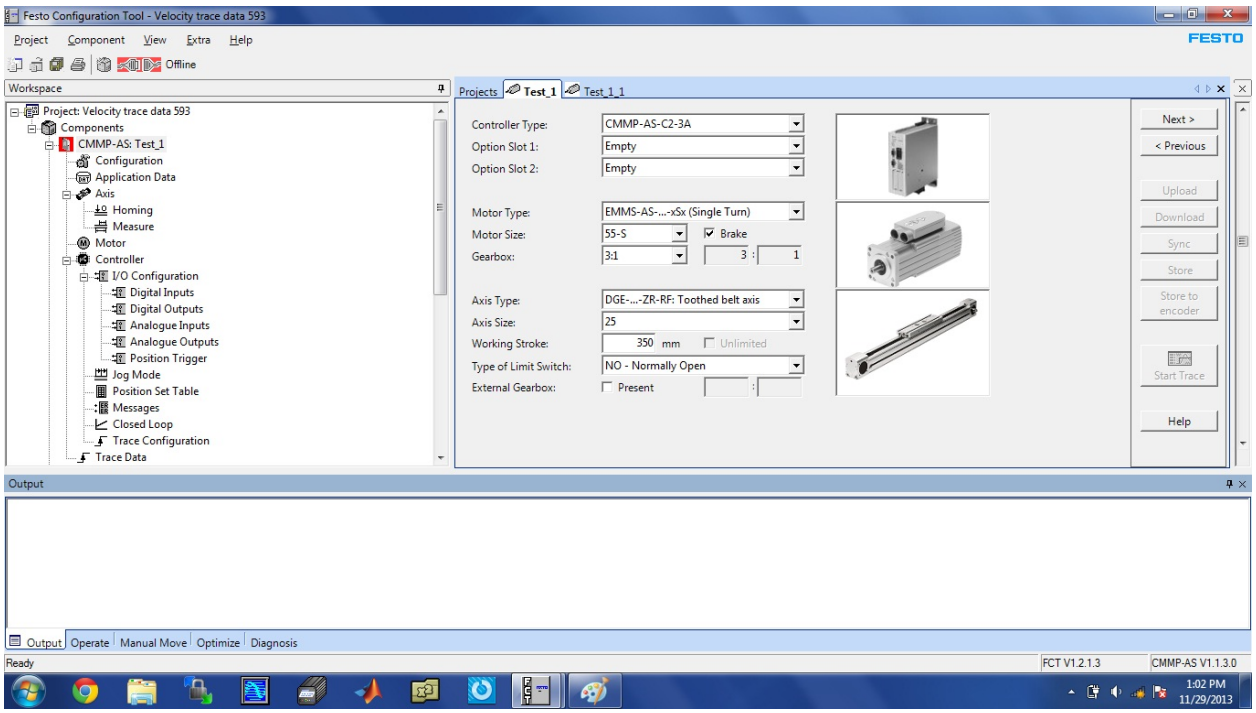

Figure B.2.1: FESTO Configuration Tool main screen

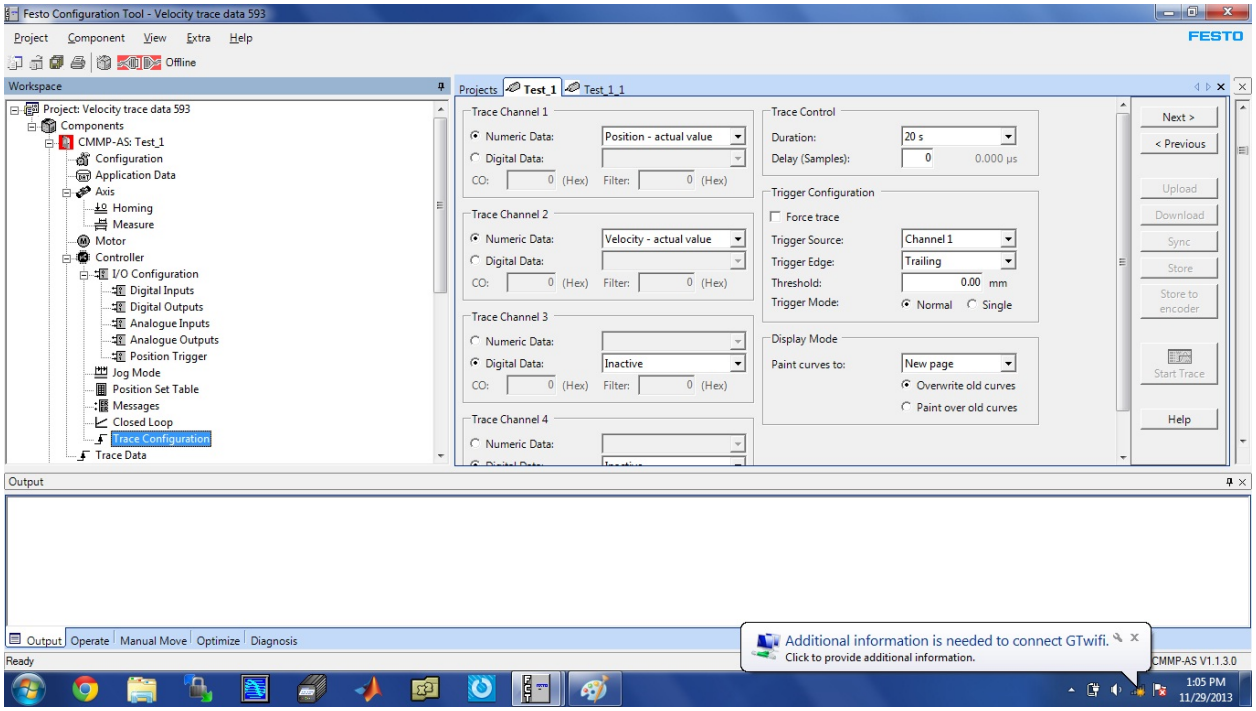

Figure B.2.2: FESTO Configuration Tool – Trace Configuration menu

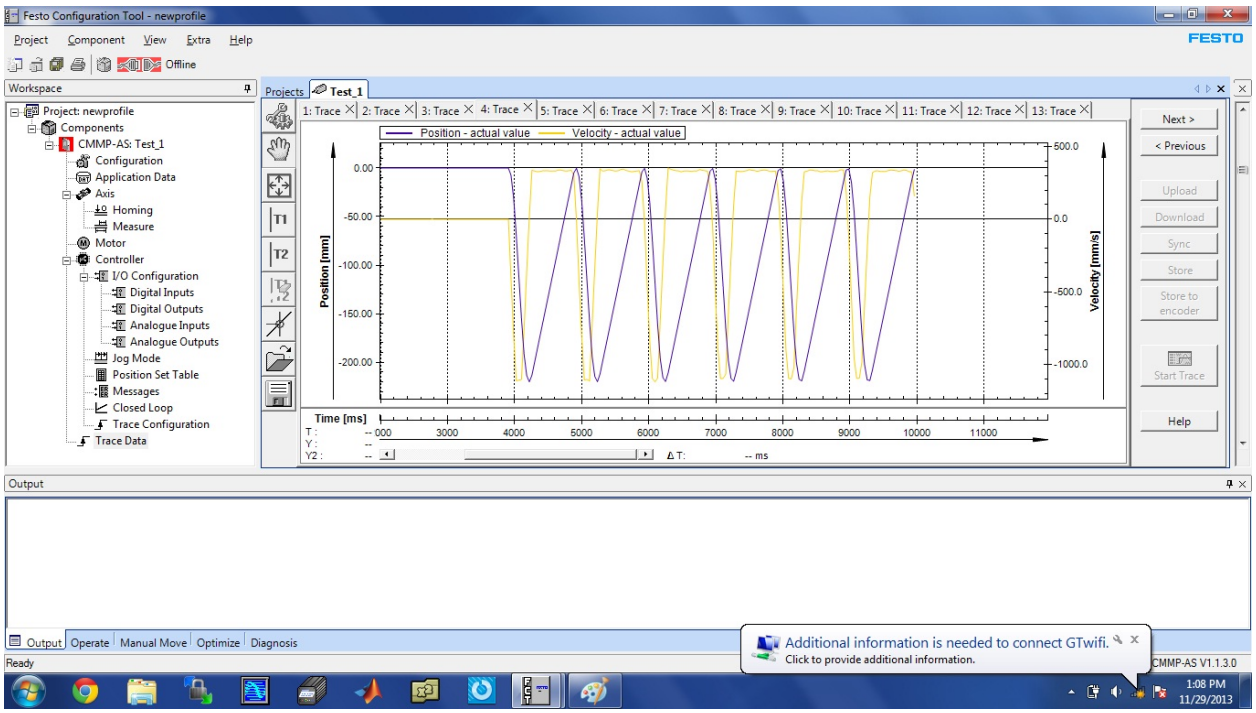

Figure B.2.3: Position and velocity trace from the Trace Configuration menu

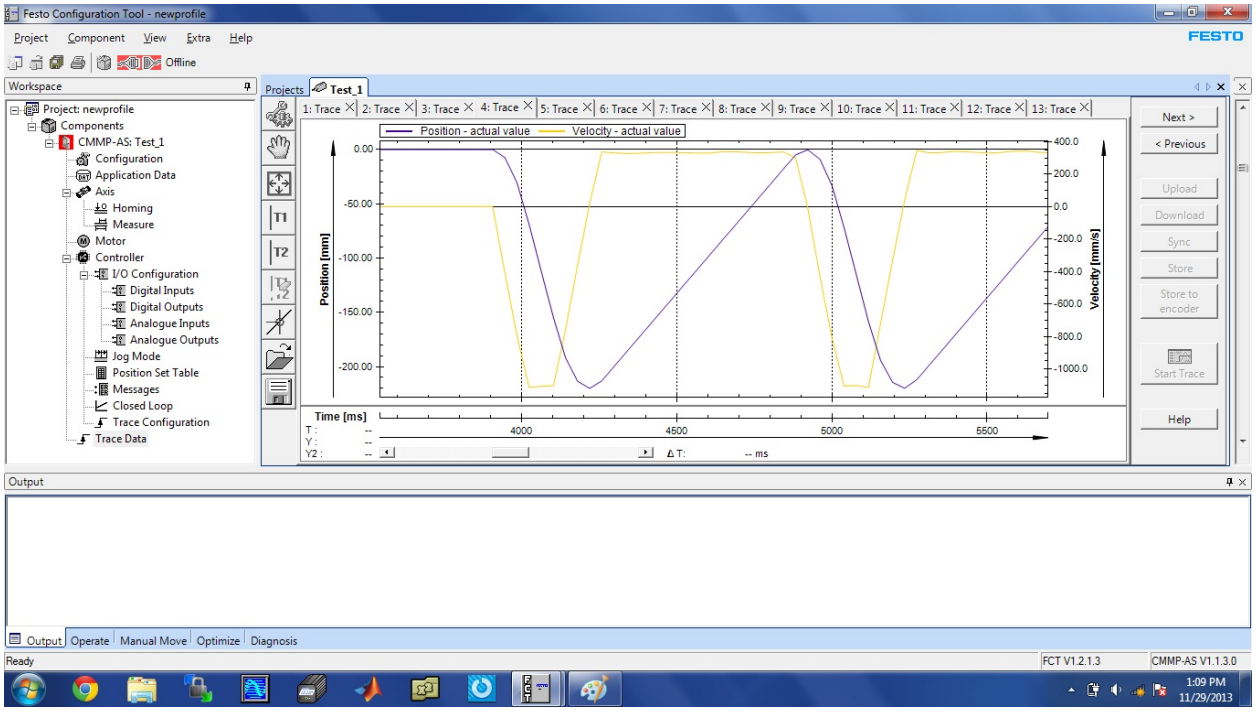

Figure B.2.4: Zoom-in window of Position and velocity trace

B3. FESTO trigger setup

1. Launch “FESTO Configuration Tool”

2. Select “Application Data”

3. Ensure “Position trigger” box is checked as represented on Figure B.3.1

4. Selection “Position Trigger” from the main menu

5. Enter the trigger signal range as represented on Figure B.3.2

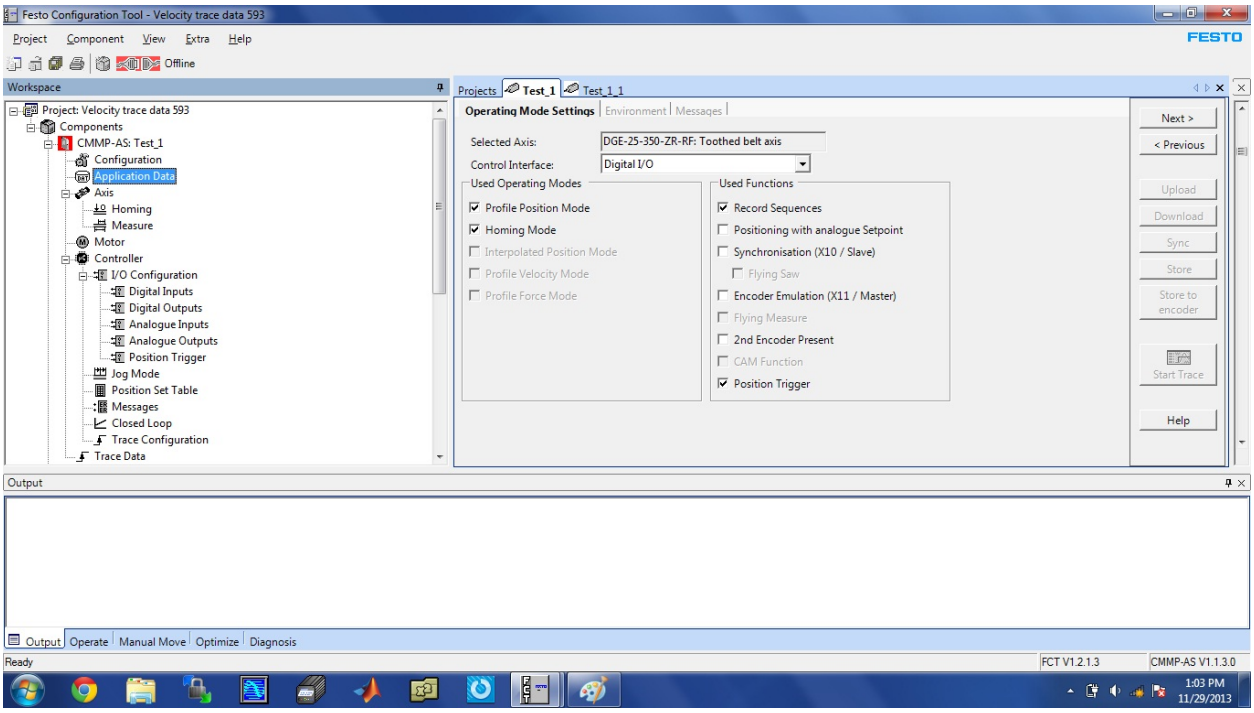

Figure B.3.1: Festo Configuration Tool – Application Data menu

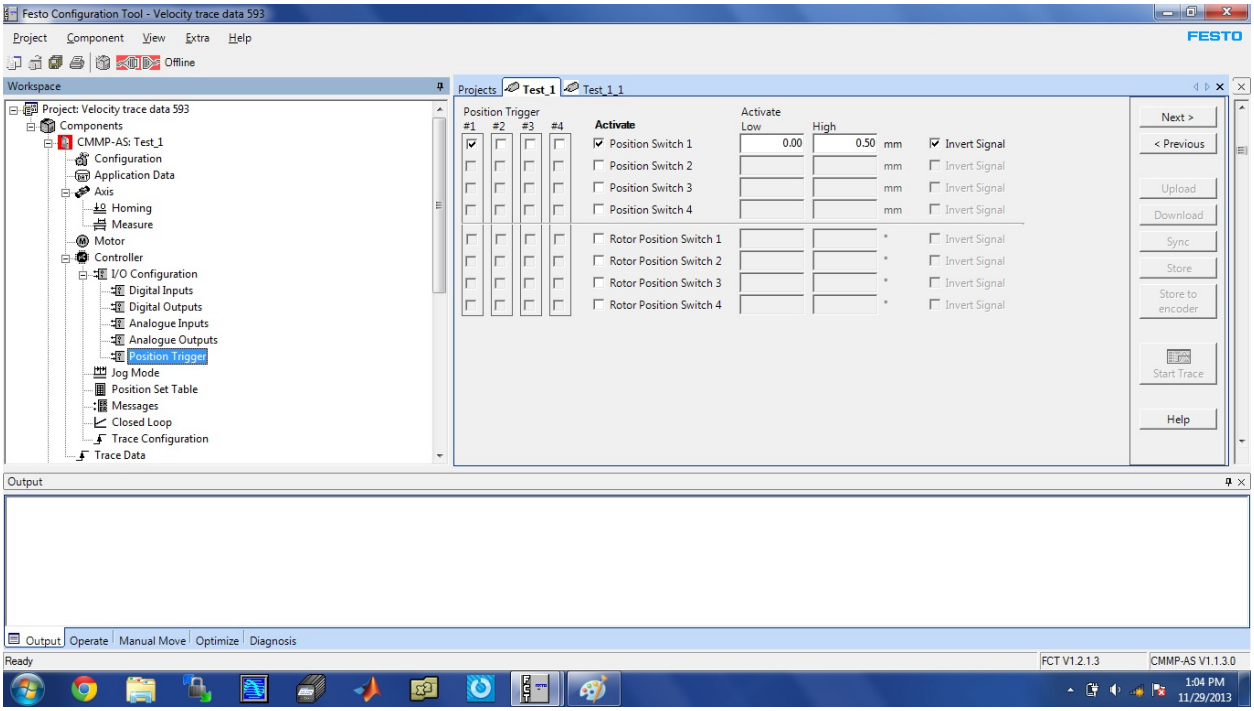

Figure B.3.2: Festo Configuration Tool – Position Trigger

B4. DaVis 7.2 Image pre-processing

The image preprocessing allows filtering the particle image before the vector calculation is performed. Often this helps to improve the quality of the results, especially when working with high or locally changing background intensities. Two preprocessing options used in this study are subtracting an offset and a sliding background.

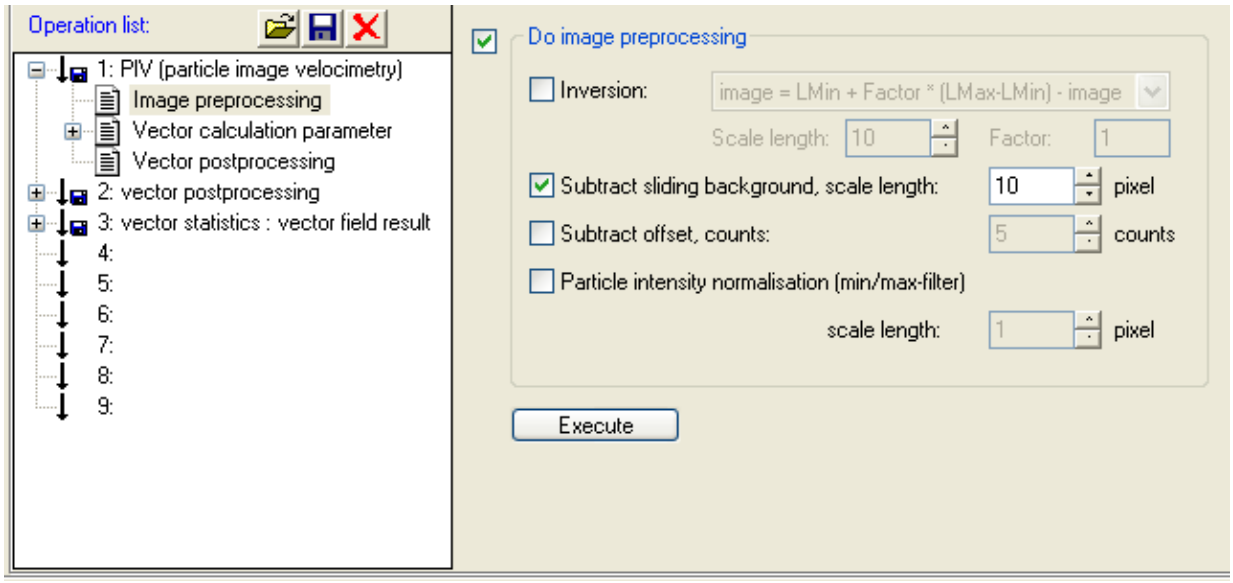

Figure B.4.1: Image pre-processing tool frm DaVis 7.2

Subtract a sliding background

This can be useful in preventing intensity fluctuation in the background due to reflections. This option allows filtering out large intensity fluctuations in the background while the small intensity fluctuations of the particle signal will pass through. The scale length in pixel dimensions should be at least double the size of the mean particle diameter. In this study, scale length of 10 pixels was used for a sliding background subtraction (Fig B.4.2).

Subtract an offset

The offset may be specified in counts (intensity) in the corresponding textbox as represented on Figur B.4.1. This feature is useful for eliminating illuminations from de-focused particles, as represented on Figure B.4.3. In this study, 10 offset counts were subtracted from PIV images.

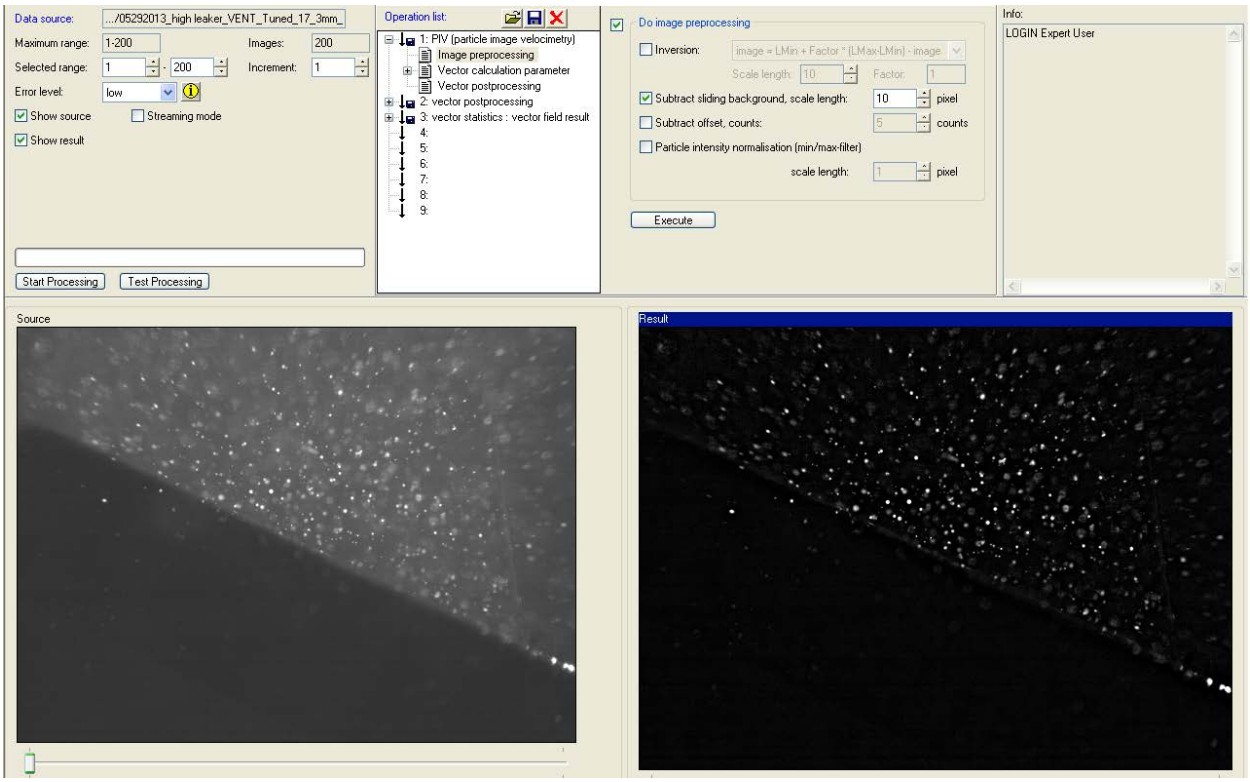

Figure B.4.2: A sliding back ground subtraction (right image) from DaVis 7.2

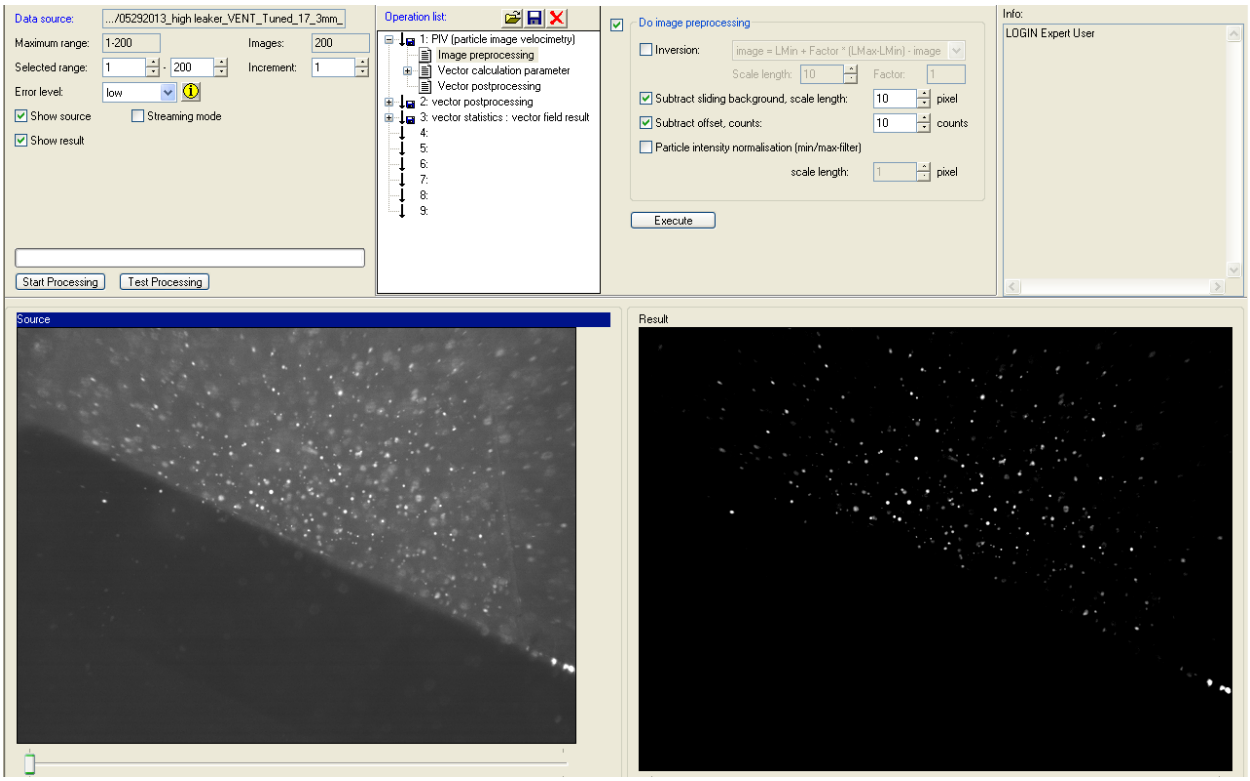

Figure B.4.3: A sliding back ground and offset subtractions (right image) from DaVis 7.2

B5. Superimposing vector fields from Tecplot

1. Open Tecplot.
2. Create a new blank layout.
3. In the active frame, go to “Insert” and select “Image.” Select your hinge outline from the menu, then press Okay.
4. Double click on the placed image to bring up the Image dialogue. Set the image to a size which is large enough for the height to take up much of the vertical workspace. It is suggested to set the width to 60 units and to maintain the aspect ratio from the original image.

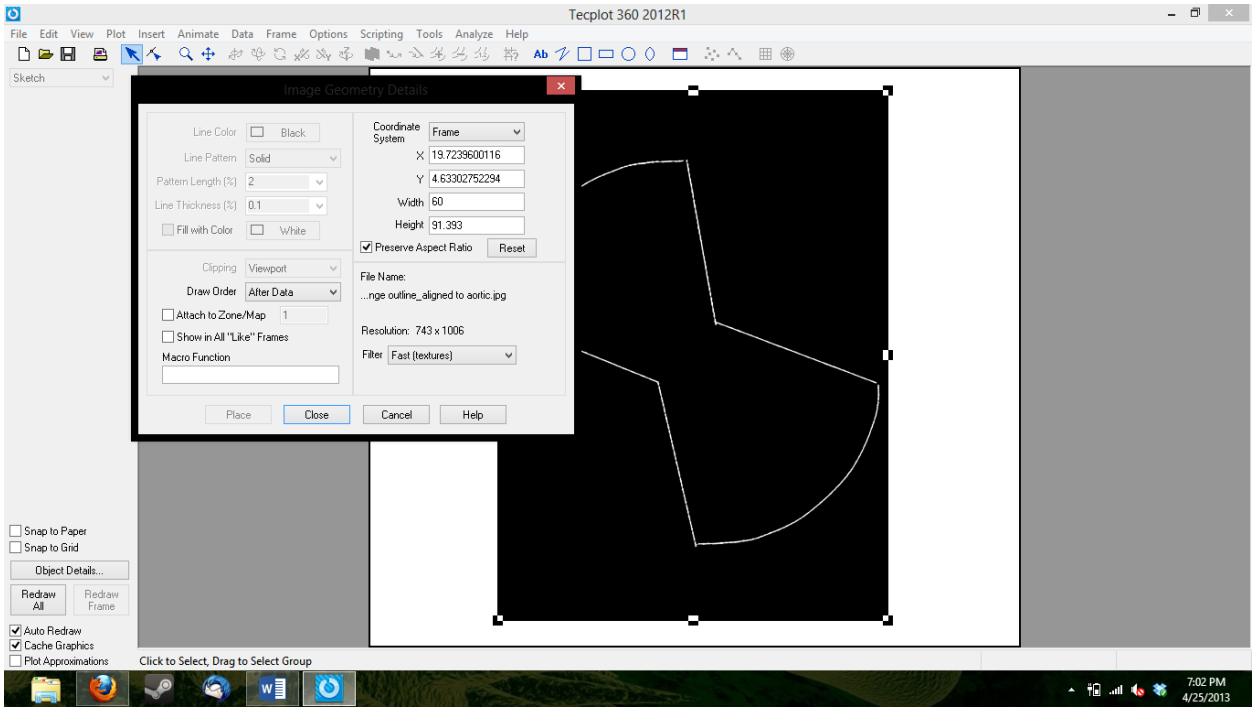

5. Go to “Frames.” Select “Edit Active Frame” from the drop down. Deselect “Show Background” and “Show Border.”
6. Go to “Tools.” Select “Create Multiple Frames” from the dropdown menu. Create a 2x2 square of frames (this should be the default).

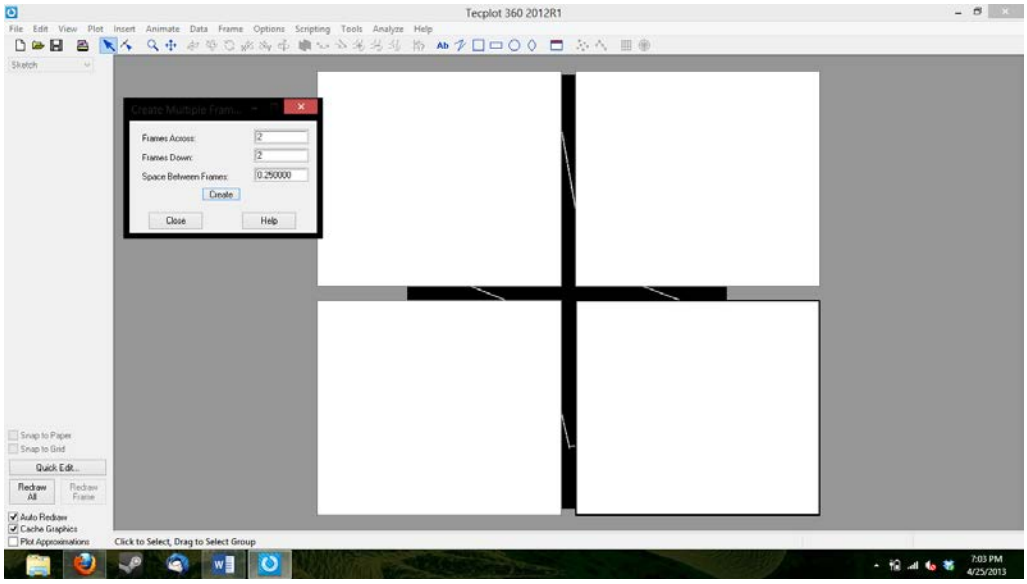

7. Make one of the frames active (the bottom right frame is a good candidate), and then go to the “Frames” drop down and select “Delete Active Frame.” If your image will only include two data areas (such as aortic and ventricular only) then you should make another frame active and delete it as well.
8. Select the frame where you will plot the first area. Push all other frames to the back by activating them and going to the “Frames” dropdown and selecting “Push Active Frame”

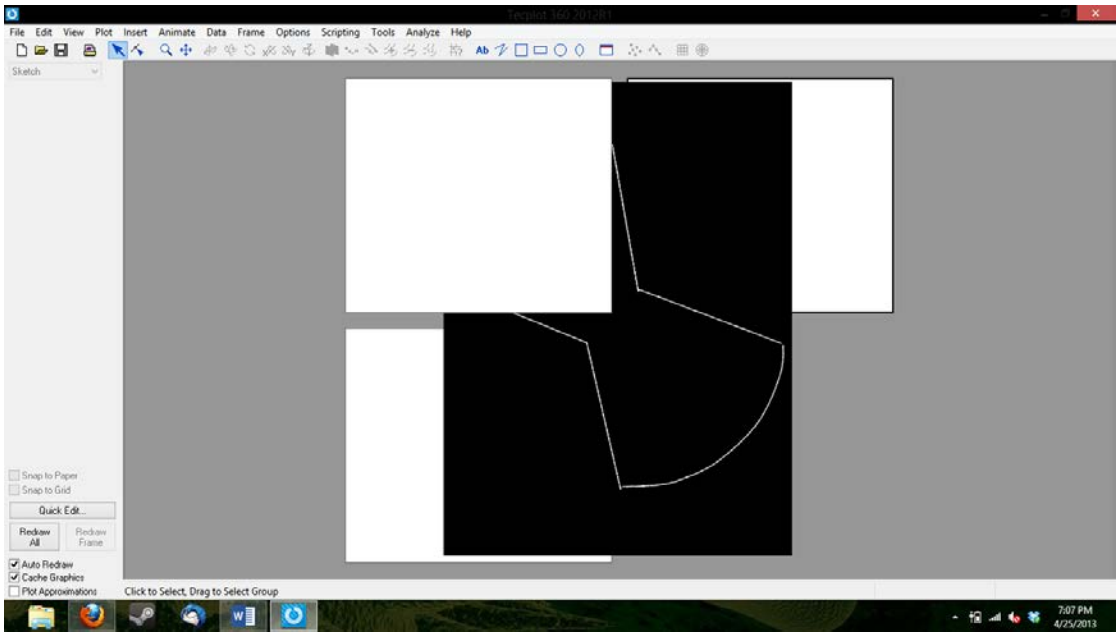

9. Activate the frame where you will plot the first area. From the “File” dropdown, select “Load Data File”. Select Tecplot Data File, and find your data file in the browser.
10. Deactivate Shade and Edge in the sidebar. Activate Vectors in the sidebar. Plot U and V.
11. In the “Zone Style” menu located at the bottom of the side bar, navigate to the vector tab and select the coloration to be “Multi 1.” Set the Line thickness to the value which you prefer, make sure it’s consistent with your other plots.
12. In the “Plot” dropdown, select Axis and deactivate the X and Y axis for the plot. Also in the “Plot” menu set your values for length of vector and arrowhead length.
13. Using the “Edit Active Frame” Dialogue, move your plot roughly into place on top of the hinge outline. The “Left Side” denotes the distance of the left edge of the frame from the edge of the paper, and the “Top Side” denotes the distance of the top edge of the frame from the edge of the paper. You may then use the translation tool to fine tune the position of the plot within the frame. Keep in mind that the frame’s width controls the overall size of the image, however the height may give you more room to move your plot area to fine tune the position. It is suggested to keep the width at the default value (should be 4.125), and to set the height to a larger size, for instance, 6 units, so as to expose the maximal amount of the plot area. If you do this, it will recenter the plot to the center of the frame, but will preserve where the frame exists on the paper, meaning you will need to go back and adjust the “Top Side” and “Left Side” as needed to position the plot appropriately.

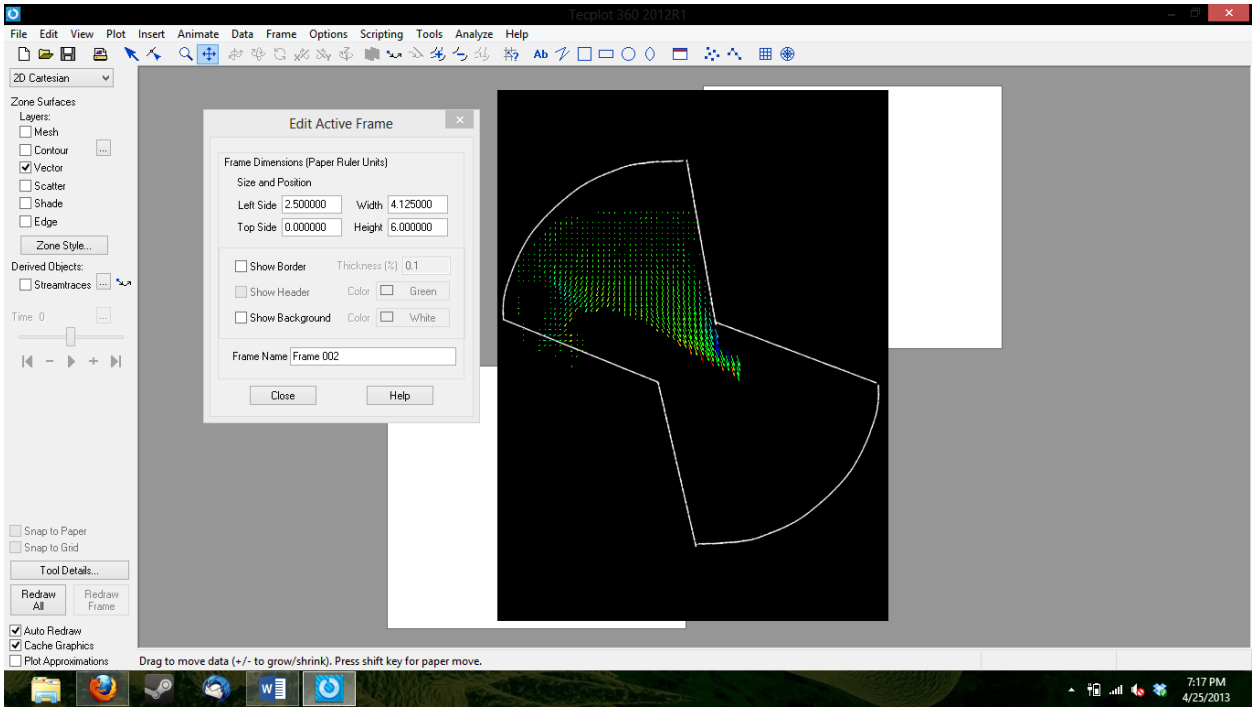

14. Repeat this process for all other plots in the image.
15. Go back into the “Plot” dropdown dialogue and select “Contour and Multicoloring.” Select the data set from the drop down on the upper right corner, and set levels to be consistent with other plots.
16. If you are creating an image with the aortic side on the top rather than the bottom, you will have to rotate the plot 180 degrees in the portion of the hinge outline where it is to go. Go to “Data” then “Alter Data” then “Rotate.” Enter 180 for the value and select the data set, then confirm.

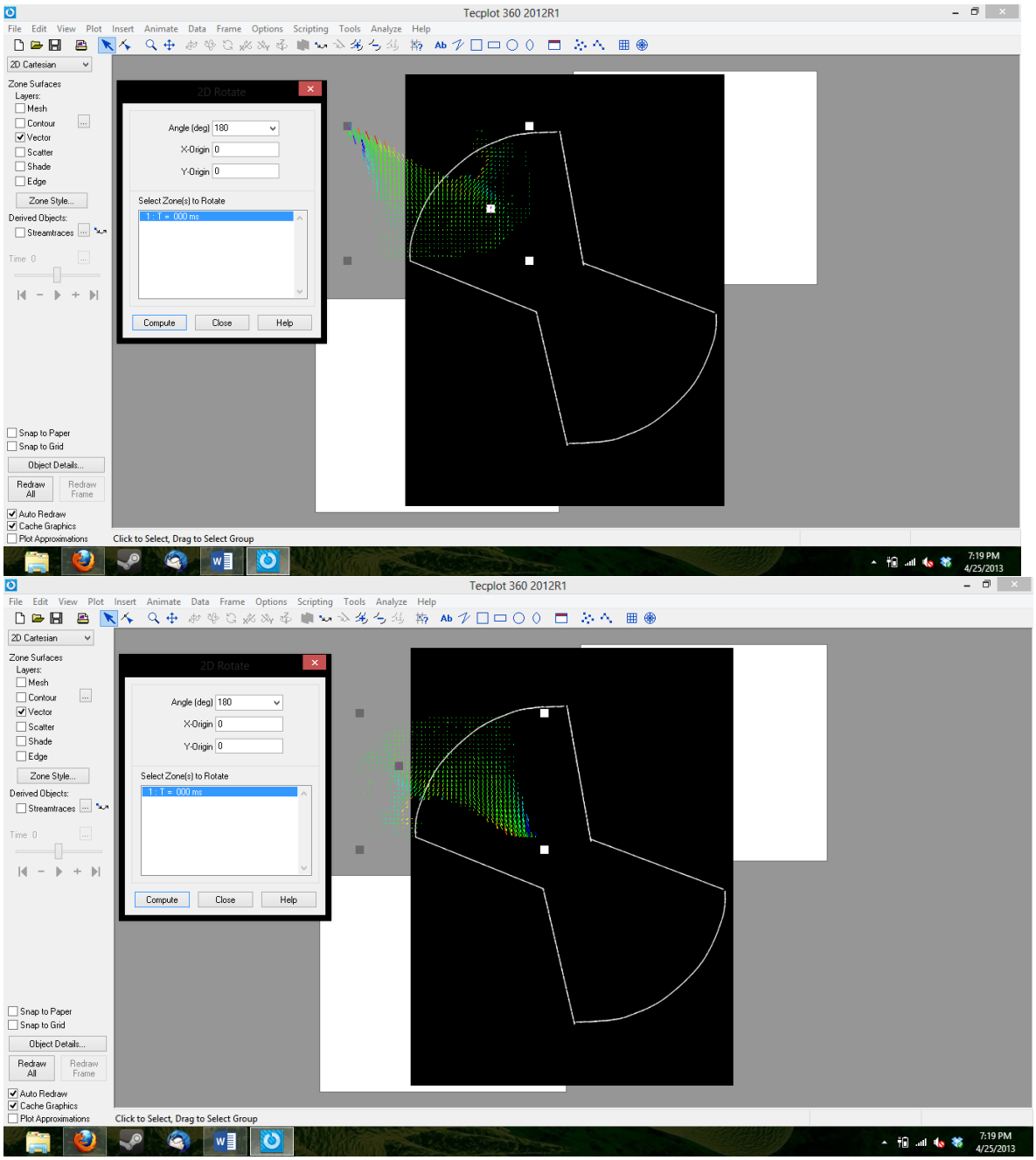
Tecplot 360 2012R1
File Edit View Plot Insert Animate Data Frame Options Scripting Tools Analyze Help
2D Cartesian
Zone Surfaces
Layers:
Mesh
Contour
Vector
Scatter
Shade
Edge
Zone Style...
Derived Objects:
Streamtraces
Time 0
2D Rotate
Angle (deg) 180
X-Origin 0
Y-Origin 0
Select Zone(s) to Rotate
1: T = 000 ms
Compute
Close
Help
Snap to Paper
Snap to Grid
Object Details...
Redraw All
Redraw Frame
Auto Redraw
Cache Graphics
Plot Approximations
Click to Select, Drag to Select Group
7:19 PM
4/25/2013

B6. MATLAB scripts

PIV data analysis – VSS & RSS_{app} calculation

```
clear all

cd 'C:\Documents and Settings\cfmlab.GEORGIA-5C792A9\Desktop\MATLAB Files\PIV
Processing\'
%%%%%%%%%%%%%%%%%%%%%%%%%%%%%%%%%%%%%%%%%%%%%%%%%%%%%%%%%%%%%%%%%%%%%%%%%%%
% MASTER PROGRAM FOR PIV PROCESSING
% CURRENT AS OF 12/19/2012
% ASSUME NUMBER OF FILES IS NFILE
% THIS PROGRAM CREATES TWO FILES:
% 1. B00001-NFILE.DAT
% 2. MEAN FILES CREATING FROM THE AVERAGING PROGRAM
% THE INPUT FILE FOR THIS PROGRAM IS input.txt
% input.txt - List of data folders, exported from Davis
% THIS PROGRAM ASSUMES THAT THE DATAFILES ARE STORED AS B*****.DAT, WHERE
% ***** RANGES FROM 1-NFILE.
%%%%%%%%%%%%%%%%%%%%%%%%%%%%%%%%%%%%%%%%%%%%%%%%%%%%%%%%%%%%%%%%%%%%%%%%%%%
% File containing the list of data directories
inpf = 'C:\Documents and Settings\cfmlab.GEORGIA-5C792A9\Desktop\MATLAB
Files\PIV Processing\input.txt';
% Directory for writing the output files
outdir = 'C:\Documents and Settings\cfmlab.GEORGIA-5C792A9\Desktop\MATLAB
Files\PIV Processing\';
% Number of data files
nfile = 100;
% Size of data array in one file
sz = [43 32];
% Density of solution in kg/m3
rho = 1600.0;
% Kinematic viscosity in m2/s
nu = 3.5E-6;
% z-location of plane of interest;
% For BAV, z=5.0 for pl1, z=0.0 for pl2 and z=2.5 for pl3
% For Normal, z=2.5 for pl1, z=0.0 for pl2 and z=5.0 for pl3
z = 0.0;
% Flag for coordinates
% Flag = 1, write out coordinates, use only for pl2 of all datasets
% Flag = 2, read coordinates
flag = 1;
% Path of coordinates file
coordfile = strcat(outdir,'coordfile.dat');
% Length of string for output files
lencur = 6;
% Time points of data acquisitions
tp = [240];
% flag_del = 1 deletes the file named B00001-NFILE.DAT.
% Any other value keeps the file in the folder
flag_del = 2;
%%%%%%%%%%%%%%%%%%%%%%%%%%%%%%%%%%%%%%%%%%%%%%%%%%%%%%%%%%%%%%%%%%%%%%%%%%%
% Total number of elements
tot = sz(1)*sz(2);

% Open the file containing the list of data directories
```

```
fid1 = fopen(inpf,'r');
dirs = textscan(fid1,'%s','Delimiter','\n');
dirs = dirs{1};
fclose(fid1);

% Create file for writing time points of measurements
A = exist(strcat(outdir,'Mean'));
if (A~=7)
    mkdir(outdir,'Mean');
end
outf = strcat(outdir,'Mean\tpts.txt');
fid5 = fopen(outf,'w');

% Scan through the list of directories
for i=1:size(dirs,1)
    curr = char(dirs(i));
    mean_term = zeros(8,tot);

    if (nfile>99)
        nfile_nam = num2str(nfile,'%3d');
    else if (nfile>9)
            nfile_nam = num2str(nfile,'%2d');
        else
            nfile_nam = num2str(nfile,'%1d');
        end
    end
% Create the output file name for writing
    outf = strcat(curr,'B00001-',nfile_nam,'.dat');
    fid3 = fopen(outf,'w');
    fprintf('%s%s\n','Writing file: ',outf);

    for l=1:nfile
        fprintf('%s%s\n','Processing file:
',strcat(curr,'B',sprintf('%05d\n',l),'.dat'));
%   CREATE FILENAME
        fnam = strcat(curr,'B',sprintf('%05d\n',l),'.dat');
%   OPEN FILE
        fid2 = fopen(fnam,'r');
%   READ HEADER
        head = fgetl(fid2);
        fgetl(fid2);
        tem = fgetl(fid2);
        sz = sscanf(tem,['ZONE T="Frame 0", I=','%d',', J=','%d'],[1 Inf]);
%   READ DATA
        dat = fscanf(fid2,'%f %f %f %f\n',[4 inf]);
        fclose(fid2);

%   VELOCITY MAGNITUDE
        vel_mag = sqrt(dat(3,:).^2+dat(4,:).^2);

%   RESHAPING DATA
        X = reshape(dat(1,:),sz(1),sz(2));
        Y = reshape(dat(2,:),sz(1),sz(2));
        U = reshape(dat(3,:),sz(1),sz(2));
        V = reshape(dat(4,:),sz(1),sz(2));
```

```
%   VECTOR SPACING
        dx = (X(2,1)-X(1,1));
        dy = (Y(1,1)-Y(1,2));

        dUdx = zeros(sz(1),sz(2));
        dUdy = zeros(sz(1),sz(2));
        dVdx = zeros(sz(1),sz(2));
        dVdy = zeros(sz(1),sz(2));
        w_z = zeros(sz(1),sz(2));

%   CALCULATING GRADIENTS AND WALL-NORMAL GRADIENTS
        for j=2:sz(1)-1
            for k=2:sz(2)-1
                dUdx(j,k) = (U(j+1,k)-U(j-1,k))/(X(j+1,k)-X(j-1,k));
                dUdy(j,k) = (U(j,k+1)-U(j,k-1))/(Y(j,k+1)-Y(j,k-1));
                dVdx(j,k) = (V(j+1,k)-V(j-1,k))/(X(j+1,k)-X(j-1,k));
                dVdy(j,k) = (V(j,k+1)-V(j,k-1))/(Y(j,k+1)-Y(j,k-1));
                w_z(j,k) = dVdx(j,k)-dUdy(j,k);
            end
        end

        dUdx = reshape(dUdx,1,tot);
        dUdy = reshape(dUdy,1,tot);
        dVdx = reshape(dVdx,1,tot);
        dVdy = reshape(dVdy,1,tot);
        w_z = reshape(w_z,1,tot);

% If it is the first file, write the common header, else only write zone
% header
        if (l==1)
            fprintf(fid3,'%s\n',head);
            fprintf(fid3,'%s\n','VARIABLES = "X (mm)", "Y (mm)", "U (m/s)",
"V (m/s)", "Vel (m/s)" "dUdX" "dUdY" "dVdX" "dVdY" "Z vorticity"');
        end
        fprintf(fid3,'%s%s%s%d%s%d%s\n','ZONE
T="',strcat('B',sprintf('%05d\n',i),'.dat'),'", I=',sz(1),'
J=',sz(2),',DATAPACKING=POINT');
        for j=1:tot

fprintf(fid3,'%8.4f %8.4f %8.4f %8.4f %8.4f %8.4f %8.4f %8.4f %8.4f %8.4f\n',
dat(1,j),dat(2,j),dat(3,j),dat(4,j),vel_mag(j),dUdx(j),dUdy(j),dVdx(j),dVdy(j
),w_z(j));
        end
% Calculate mean quantities for the N files
        mean_term(1,:) = mean_term(1,:) + dat(3,:)/double(nfile);
        mean_term(2,:) = mean_term(2,:) + dat(4,:)/double(nfile);
        mean_term(3,:) = mean_term(3,:) + vel_mag/double(nfile);
        mean_term(4,:) = mean_term(4,:) + dUdx/double(nfile);
        mean_term(5,:) = mean_term(5,:) + dUdy/double(nfile);
        mean_term(6,:) = mean_term(6,:) + dVdx/double(nfile);
        mean_term(7,:) = mean_term(7,:) + dVdy/double(nfile);
        mean_term(8,:) = mean_term(8,:) + w_z/double(nfile);
    end
% Conversion of units from m/s/mm to 1/s
    for j=4:8
```

```
        mean_term(j,:) = mean_term(j,:)*1000;
    end
    fclose(fid3);

% Open the newly created file for further calculations
    fid3 = fopen(outf,'r');
    fprintf('%s%s\n','Reading file for mean calculations: ',outf);
%   READ HEADER
    for l=1:2
        head = fgetl(fid3);
    end

    uu = zeros(1,tot);
    vv = zeros(1,tot);
    uv = zeros(1,tot);
    tke = zeros(1,tot);
    rss = zeros(1,tot);
    vss = zeros(1,tot);

% Calculation of quantities
    for l=1:nfile
        head = fgetl(fid3);
        dat = fscanf(fid3,'%f %f %f %f %f %f %f %f %f %f\n',[10,tot]);
        for j=1:tot
            uu(1,j) = uu(1,j) + rho*(dat(3,j)-mean_term(1,j))^2/double(nfile);
            vv(1,j) = vv(1,j) + rho*(dat(4,j)-mean_term(2,j))^2/double(nfile);
            uv(1,j) = uv(1,j) + rho*(dat(4,j)-mean_term(2,j))*(dat(3,j)-
mean_term(1,j))/double(nfile);
        end
    end
% Calculation of TKE and RSS
    for j=1:tot
        tke(1,j) = 0.5*(uu(1,j) + 2*vv(1,j));
        rss(1,j) = sqrt(((uu(1,j)-vv(1,j))/2)^2+(uv(1,j))^2);
        vss(1,j) = nu*rho*(mean_term(7,j)+mean_term(8,j));
    end
    fclose(fid3);

% Read or write coordinates file depending on flag
    if (flag==1)
        fid4 = fopen(coordfile,'w');
        for j=1:tot
            fprintf(fid4,'%8.4f %8.4f\n',dat(1,j),dat(2,j));
        end
        flag = 2;
        fclose(fid4);
    else
        fid4 = fopen(coordfile,'r');
        tem = fscanf(fid4,'%f %f\n',[1 inf]);
        fclose(fid4);
        dat(1,:) = tem(1:2:tot*2);
        dat(2,:) = tem(2:2:tot*2);
    end


% Write results of mean calculations
```

```
    slash = find(curr=='\');
    fnam = strcat(outdir,'Mean\T= ',sprintf('%03d',tp(i)),'.dat');
    fid6 = fopen(fnam,'w');
    fprintf(fid5,'%s%s%s\n','T=',sprintf('%03d',tp(i)),'.dat');
    fprintf('%s%s\n','Writing file: ',fnam);

    fprintf(fid6,'%s %s %s\n','TITLE = "T = ',sprintf('%03d',tp(i)),'ms"');
    fprintf(fid6,'%s\n','VARIABLES = "X (mm)", "Y (mm)", "Z (mm)", "U (m/s)",
"V (m/s)", "Vel (m/s)", "dU/dx (s<sup>-1</sup>)", "dU/dy (s<sup>-1</sup>)",
"dV/dx (s<sup>-1</sup>)", "dV/dy (s<sup>-1</sup>)", "w_z (s<sup>-1</sup>)",
"VSS (N/m<sup>2</sup>)", "<greek>r</greek>u\''u\'' (N/m<sup>2</sup>)",
"<greek>r</greek>v\''v\'' (N/m<sup>2</sup>)", "<greek>r</greek>u\''v\''
(N/m<sup>2</sup>)", "TKE (N/m<sup>2</sup>)", "RSS (N/m<sup>2</sup>)"');
    fprintf(fid6,'%s %s %s %d %s %d\n','ZONE T=" T =
',sprintf('%03d',tp(i)),'ms", I=',sz(1), 'J=',sz(2));
    for j=1:tot

fprintf(fid6,'%8.4f %8.4f %8.4f %8.4f %8.4f %8.4f %8.4f %8.4f %8.4f %8.4f %8.
4f %8.4f %8.4f %8.4f %8.4f %8.4f %8.4f %8.4f\n',dat(1,j),dat(2,j),z,mean_term(1,j),
mean_term(2,j),mean_term(3,j),mean_term(4,j),mean_term(5,j),mean_term(6,j),me
an_term(7,j),mean_term(8,j),vss(1,j),uu(1,j),vv(1,j),uv(1,j),tke(1,j),rss(1,j
));
    end
    fclose(fid6);
    if (flag_del==1)
        delete(outf);
    end
end
fclose(fid5);
```

Error analysis – Normalized Median Test

```
%PIV Outlier Detection Code (Courtesy of Westerweel, 2005)
[J,I]=size(U);
Medianres=zeros(J,I);
Normfluct=zeros(J,I,2);
b=1;
eps=0.1;
%
for c=1:2
 if c==1; VelComp=U; else; VelComp=V; end;
  for i=1+b:I-b
   for j=1+b:J-b
       Neigh=VelComp(j-b:j+b,i-b:i+b)
       NeighCol=Neigh(:)
       NeighCol2=[NeighCol(1:(2*b+1)*b+b);NeighCol((2*b+1)*b+b+2:end)]
       Median=Median(NeighCol2)
       Fluct=VelComp(j,i)-Median;
       Res=NeighCol2-Median
       Medianres=Median(abs(Res))
       Normfluct(j,i,c)=abs(Fluct/(Medianres+eps))
   end
  end
 end
info1=(sqrt(Normfluct(:,:,1).^2+Normfluct(:,:,2).^2)>Thr)

%converting array for Vx
%Matrix A = raw DAT file
```

APPENDIX C

RESULTS-RELATED MATERIALS

Table C.1: Description of the pulsatile hinge flow animation files – Standard valve

Valve type	**Measurement plane**	**Flow field**	**File label**
Standard	FLAT	Velocity field	Standard_FLAT_Vel.avi
	390µm	Velocity field	Standard_390um_Vel.avi
	FLAT	VSS field	Standard_FLAT_VSS.avi
	390µm	VSS field	Standard_390um_VSS.avi
	FLAT	RSS_{app} field	Standard_FLAT_RSS.avi

Table C.2: Description of the pulsatile hinge flow animation files – HLP valve

Valve type	**Measurement plane**	**Flow field**	**File label**
HLP	390µm	Velocity field	HLP_390um_Vel.avi
	585µm	Velocity field	HLP_585um_Vel.avi
	390µm	VSS field	HLP_390um_VSS.avi
	585µm	VSS field	HLP_585um_VSS.avi

Table C.3: Description of the pulsatile hinge flow animation files – LLP valve

Valve type	**Measurement plane**	**Flow field**	**File label**
LLP	390µm	Velocity field	LLP_390um_Vel.avi
	390µm	VSS field	LLP_390um_VSS.avi

REFERENCES

1. Baskurt, O.K., H.J. Meiselman. Blood rheology and hemodynamics. Semin Thromb Hemost. 2003;29:435-50.

2. Baudet, E.M., Puel, V., McBride, J.T., Grimaud, J.P., Roques, F., Clerc, F., Roques, X., and Laborde, N., Long-term results of valve replacement with the St. Jude Medical prosthesis. *J Thorac Cardiovasc Surg*. 109(5): p. 858-70, 1995.

3. Bellofiore, A., E.M. Donohue, N.J. Quinlan. Scale-up of an unsteady flow field for enhanced spatial and temporal resolution of PIV measurements: application to leaflet wake flow in a mechanical heart valve. Experiments in Fluids. 2011;51:161-176.

4. Black, M.M. and Drury, P.J., Mechanical and other problems of artificial valves. *Curr Top Pathol*. 86: p. 127-59, 1994.

5. Blackman, B.R., Barbee, K.A., and Thibault, L.E. In vitro cell shearing device to investigate the dynamic response of cells in a controlled hydrodynamic environment. Ann Biomed Eng. 2000; 28(4): 363-72.

6. Chandran, K.B., A.P. Yoganathan., S.E. Rittgers. The Human Circulation. 1 ed. Boca Raton, FL.: CRC Press, 2007.

7. Cooper, B.T., B.N. Roszelle, T.C. Long, S. Deutsch, K.B. Manning. The 12 cc Penn State pulsatile pediatric ventricular assist device: Fluid dynamics associated with valve selection. J Biomech Eng-T Asme. 2008;130.

8. Dasi, L.P., D.W. Murphy, A. Glezer, A.P. Yoganathan. Passive flow control of bileaflet mechanical heart valve leakage flow. J Biomech. 2008;41:1166-73.

9. DeWall, R.A., Qasim, N., and Carr, L., Evolution of mechanical heart valves. *Ann Thorac Surg*. 69(5): p. 1612-21, 2000.

10. Dumont, K., J. Vierendeels, R. Kaminsky, G. van Nooten, P. Verdonck, D. Bluestein. Comparison of the hemodynamic and thrombogenic performance of two bileaflet mechanical heart valves using a CFD/FSI model. J Biomech Eng. 2007;129:558-65.

11. Fallon, A.M., N. Shah, U.M. Marzec, J.N. Warnock, A.P. Yoganathan, S.R. Hanson. Flow and thrombosis at orifices simulating mechanical heart valve leakage regions. J Biomech Eng-T Asme. 2006;128:30-39.

12. Giersiepen, M., L.J. Wurzinger, R. Opitz, H. Reul. Estimation of shear stress-related blood damage in heart valve prostheses--in vitro comparison of 25 aortic valves. Int J Artif Organs. 1990;13:300-6.

13. Gross, J.M., M.C.S. Shu, F.F. Dai, J. Ellis, A.P. Yoganathan. Microstructural flow analysis within a bileaflet mechanical heart valve hinge. J Heart Valve Dis. 1996;5:581-590.

14. Jun, B.H., N. Saikrishnan, A.P. Yoganathan. Micro Particle Image Velocimetry Measurements of Steady Diastolic Leakage Flow in the Hinge of a St. Jude Medical Regent Mechanical Heart Valve. Ann Biomed Eng. 2014;42(3):526-540.

15. Jun, B.H., N. Saikrishnan, S. Arjunon, B.M. Yun, A.P. Yoganathan. Effect of hinge gap width of a St. Jude Medical Bileaflet Mechanical Heart Valve on blood damage potential - An *In vitro* Micro-PIV study. J Biomech Eng-T Asme (under revision)

16. Keane, R.D., R.J. Adrian. Theory of Cross-Correlation Analysis of Piv Images. Appl Sci Res. 1992;49:191-215.

17. Kline, S.J., McClintock, F. A. Describing uncertainties in single-sample experiments. Mech Eng. 1953;75:3-8.

18. Ku, D.N., D.P. Giddens, C.K. Zarins, S. Glagov. Pulsatile flow and atherosclerosis in the human carotid bifurcation. Positive correlation between plaque location and low oscillating shear stress. Arteriosclerosis. 1985;5:293-302.

19. Leo, H.-L. An In Vitro Investigation of the Flow Fields Through Bileaflet and Polymeric Prosthetic Heart Valves. Biomedical Engineering Department. Atlanta: Georgia Institute of Technology, 2005.

20. Leo, H.L., Z.M. He, J.T. Ellis, A.P. Yoganathan. Microflow fields in the hinge region of the CarboMedics bileaflet mechanical heart valve design. J Thorac Cardiovasc Surg. 2002;124:561-574.

21. Leo, H.L., H.A. Simon, L.P. Dasi, A.P. Yoganathan. Effect of hinge gap width on the microflow structures in 27-mm bileaflet mechanical heart valves. J Heart Valve Dis. 2006;15:800-808.

22. Leverett, L.B., E.C. Lynch, C.P. Alfrey, J.D. Hellums. Red Blood-Cell Damage by Shear-Stress. Biophys J. 1972;12:257-273.

23. Lu, P.C., H.C. Lai, J.S. Liu. A reevaluation and discussion on the threshold limit for hemolysis in a turbulent shear flow. J Biomech. 2001;34:1361-1364.

24. Manning, K.B., V. Kini, A.A. Fontaine, S. Deutsch, J.M. Tarbell. Regurgitant flow field characteristics of the St. Jude bileaflet mechanical heart valve under physiologic pulsatile flow using particle image velocimetry. Artif Organs. 2003;27:840-846.

25. MedlinePlus [Internet]. Bethesda (MD): National Library of Medicine (US); [updated 2013 March 22]. Hematocrit; [updated 2012 Feb 8; reviewed 2013 Aug 28; cited 2013

Aug 28]; [about 2 p.]. Available from: http://www.nlm.nih.gov/medlineplus/ency/article/003646.htm

26. Meinhart, C.D., S.T. Wereley, J.G. Santiago. A PIV algorithm for estimating time-averaged velocity fields. J Fluid Eng-T Asme. 2000;122:285-289.

27. Meinhart, C.D., S.T. Wereley, J.G. Santiago. PIV measurements of a microchannel flow. Experiments in Fluids. 1999;27:414-419.

28. Murphy, D. The Application of Passive Flow Control to Bileaflet Mechanical Heart Valve Leakage Jets School of Mechanical Engineering. Atlanta: Georgia Institute of Technology, 2009.

29. Nkomo, V.T., J.M. Gardin, T.N. Skelton, J.S. Gottdiener, C.G. Scott, M. Enriquez-Sarano. Burden of valvular heart diseases: a population-based study. Lancet. 2006;368:1005-11.

30. Olsen, M.G., R.J. Adrian. Out-of-focus effects on particle image visibility and correlation in microscopic particle image velocimetry. Experiments in Fluids. 2000;29:S166-S174.

31. On-X Life Technologies Inc. 2013. http://www.onxlti.com/patient-guide/comparison-mechanical-tissue-heart-valve-performance/

32. Raffel, M., C.E. Willer., S.T. Wereley, J. Kompenhans. Particle Image Velocimetry A Practical Guide. Berlin Heidelberg: Springer-Verlag, 2007.

33. Ross, D., M.H. Yacoub. Homograft replacement of the aortic valve. A critical review. Progress in Cardiovascular Diseases. 11(4): p. 275-293, 1969.

34. Saikrishnan, N., C.H. Yap, N.C. Milligan, N.V. Vasilyev, A.P. Yoganathan. In Vitro Characterization of Bicuspid Aortic Valve Hemodynamics Using Particle Image Velocimetry. Ann Biomed Eng. 2012;40:1760-1775.

35. Simon, H.A. Influence of the Implant Location on the Hinge and Leakage Flow Fields Through Bileaflet Mechanical Heart Valves. Chemical & Biomolecular Engineering Department. Atlanta: Georgia Institute of Technology, 2004.

36. Simon, H.A. Numerical simulations of the micro flow field in the hinge region of bileaflet mechanical heart valves. Chemical & Biomolecular Engineering Department. Atlanta: Georgia Institute of Technology, 2009.

37. Simon, H.A., L.P. Dasi, H.L. Leo, A.P. Yoganathan. Spatio-temporal flow analysis in bileaflet heart valve hinge regions: potential analysis for blood element damage. Ann Biomed Eng. 2007;35:1333-46.

38. Simon, H.A., L. Ge, F. Sotiropoulos, A.P. Yoganathan. Simulation of the Three-Dimensional Hinge Flow Fields of a Bileaflet Mechanical Heart Valve Under Aortic Conditions. Ann Biomed Eng. 2010;38:841-853.

39. Simon, H.A., H.L. Leo, J. Carberry, A.P. Yoganathan. Comparison of the hinge flow fields of two bileaflet mechanical heart valves under aortic and mitral conditions. Ann Biomed Eng. 2004;32:1607-1617.

40. Starr, A., Fessler, C.L., Grunkemeier, G., and He, G.W., Heart valve replacement surgery: past, present and future. *Clin Exp Pharmacol Physiol*. 29(8): p. 735-8, 2002.

41. Travis, B.R., U.M. Marzec, H.L. Leo et al. Bileaflet aortic valve prosthesis pivot geometry influences platelet secretion and anionic phospholipid exposure. Ann Biomed Eng. 2001;29:657-664.

42. Vennemann, P., K.T. Kiger, R. Lindken et al. In vivo micro particle image velocimetry measurements of blood-plasma in the embryonic avian heart. J Biomech. 2006;39:1191-1200.

43. Vongpatanasin, W., Hillis, L.D., and Lange, R.A., Prosthetic heart valves. *N Engl J Med*. 335(6): p. 407-16, 1996.

44. Wereley, S.T., C.D. Meinhart. Recent Advances in Micro-Particle Image Velocimetry. Annu Rev Fluid Mech. 2010;42:557-576.

45. Westerweel, J., Scarano, F. . Universial Outlier Detection for PIV data. Experiments in Fluids. 2005;39:1096-1100.

46. Yoganathan, A.P., H.-L. Leo, Travis, B. R, Teoh, H. S. Encyclopedia of Comprehensive Structural Integrity. Amsterdam: Elsevier. 2003:795-796.

47. Yun, B.M., J.S. Wu, H.A. Simon et al. A Numerical Investigation of Blood Damage in the Hinge Area of Aortic Bileaflet Mechanical Heart Valves During the Leakage Phase. Ann Biomed Eng. 2012;40:1468-1485.